SCUOLA DI DOTTORATO
UNIVERSITÀ DEGLI STUDI DI MILANO-BICOCCA

Dipartimento di / Department of

Scienze dell'Ambiente e della Terra

Dottorato di Ricerca in / PhD program **SCGA** Ciclo / Cycle **36°**

Curriculum in (se presente / if it is) **Geologia**

Rockfall Volume Distribution, Fragmentation, and Frequency in the Context of Climate Change

Cognome / Surname **Lanfranconi** Nome / Name **Camilla**

Matricola / Registration number **784298**

Tutore / Tutor: **prof. Frattini Paolo**

Supervisor: **prof. Crosta Giovanni Battista**

Coordinatore / Coordinator **prof. Marco Malusà**

ANNO ACCADEMICO / ACADEMIC YEAR **2022-2023**

Thesis objectives

This doctoral research project, titled **Rockfall Volume Distribution, Fragmentation, and Frequency in the Context of Climate Change**, investigates various facets of rockfall phenomena. It comprises the analysis of real case studies to understand fragment distribution in relation to volume and topography, numerical simulations to assess fragmentation's impact on hazard analysis, and in-situ and laboratory experiments to enhance fragmentation dynamics understanding. This multifaceted approach provides valuable insights into rockfall behavior, fragmentation, and their implications for hazard assessment and risk management in mountainous regions.

More specifically, the thesis is focused on four main objectives:

1. Analysis of rockfall case studies, specifically examining block size distributions in the final deposit of rockfall fragments. This investigation allowed to propose indicators that provide insights into the dynamics of fragmentation during rockfall events. Three key indicators related to fragmentation in rockfalls are described in Chapter 1: travel distance vs fragment size, power-law scaling in deposit vs fragment size, reach angle and lateral dispersion. These indicators provide insights into the occurrence of dynamic fragmentation during rockfall events, distinguish between primary deposit characteristics and blocks/fragments, and highlight the mobility and energy consumption associated with fragmentation

2. Quantification and evaluation of fragmentation in rockfall dynamics and hazard through detailed modeling and analysis of real case studies. This analysis is described in Chapter 2, and explores how fragmentation processes, such as trajectory diversion, dispersion, and kinetic energy variations, impact rockfall hazards, and the importance of explicitly modeling fragmentation for hazard assessments.

3. Analysis of the fragmentation process through experiments conducted at different scales (real scale and laboratory scale) to investigate the rockfall fragmentation behaviors observed in real case studies, concerning rockfall dispersion, deposition, and mobility, and to explore the impacts of discontinuities on fragmentation. This research presented in Chapter 3 underscores the necessity of grasping the fundamental laws governing fragmentation to enhance existing models.

Despite the inherent complexity and existing gaps in knowledge, the analysis of fragmentation remains extremely important for several significant reasons. Firstly, it pushes geologists to move beyond descriptive accounts and explore the realm of physical laws, providing a deeper understanding of observable facts. Secondly, as populations continue to live in risky areas, the practical need to predict landslide characteristics such as how far they will travel, the extent of damage, the energy involved, and their path becomes increasingly crucial. Accurate predictive models have the potential to save lives and safeguard property. This thesis takes steps in this direction, aiming to enhance our understanding of the subject.

Brief introduction

Rockfalls

A landslide can be defined as the displacement of rock, debris, or soil under the influence of gravity. Various classification systems have been proposed for classifying landslides, including those developed by Varnes (1978), Hungr et al. (2001), and Hutchinson (1988). The EPOCH classification system, which has evolved from Hutchinson's system (1998), comprises seven distinct classes and three material types, resulting in a total of 21 possible classifications, as outlined in Table 1. The rockfalls discussed in this thesis are categorized as "Falls". Falls involve the displacement of material from a steep headwall or cliff, typically comprising limited volumes of material, most commonly rock. This material descends freely under the influence of gravity, making contact with the ground primarily towards the end of its trajectory, often resulting in fragmentation.

Table 1 Classification of landslides adopted from the EPOCH system (Dikau et al., 1996). In boldface the most common types.

	Material		
Movement	Rock	Debris	Soil or earth
Fall	**Rockfall**	Debris fall	Soil fall
Topple	**Rock topple**	Debris topple	Soil topple
Translational slide	**Rock slide**	Debris slide	Soil slide
Rotational slide or “slump”	Rock slump	**Debris slump**	**Soil slump**
Lateral spreading	**Lateral rock spreading**	Lateral debris spreading	**Lateral soil spreading**
Flow	**Rock flow or “sacking”**	**Debris flow**	**Soil flow**
Complex			

Rock falls are sudden detachments of rock material that include single or multiple blocks detaching more or less simultaneously and propagating downslope with only a minor reciprocal interaction (Cancelli and Crosta, 1993; Evans and Hungr, 1993). Their rapid detachment, high associated energy and dispersed trajectories can cause casualties and important damage to structures, infrastructures, lifelines and cultural heritage. Hence, the analysis of rockfall hazard and risk requires the description of all the phases starting from the pre-detachment down to the runout and the final deposition, passing through the series of possible interactions with natural and artificial elements.

While rockfalls typically involve relatively small masses, they manifest as exceptionally swift events characterized by substantial kinetic energies, extensive runout distances, and potential for significant damage (Corominas et al., 2017). Numerical modeling of rockfalls is indispensable for hazard and risk assessment (Corominas et al., 2005; Agliardi et al., 2009; Lari et al., 2014; Wang et al., 2014; De Biagi et al., 2017; Farvacque et al., 2019, 2021; Hantz et al., 2021) as well as for the design of protective structures (Volkwein et al., 2009). This modeling serves to evaluate key parameters of block dynamics, including velocity, kinetic energy, and bouncing height, along with lateral and longitudinal dispersion (Agliardi & Crosta, 2003). It is relevant to account for both slope characteristics (e.g., topography, material properties, and presence of forests) and the nature of the rockfall event (e.g., whether it involves fragmentation) during modeling. These factors collectively influence the extent of rockfall potential and hazard zoning in mountainous regions (Frattini et al., 2012). They can significantly alter the trajectories, extent, and dynamics of rockfall events, as well as the frequency and likelihood of impact. The likelihood of rockfall impact is often expressed as the proportion of blocks of a certain volume that reach a specific location (Guzzetti et al., 2002; Jaboyedoff et al., 2005). However, real-scale testing has demonstrated that a single block can disintegrate into numerous fragments (Gili et al., 2016; Ruiz-Carulla et al., 2016), leading to alterations in probability.

Fragmentation

We use the term "fragmentation" in situations where stiff and strong rock blocks hit a hard impact substratum or other blocks of comparable size like a talus deposit, and they may fragment and explode (Crosta et al., 2015). The rockfall fragmentation process is defined as the separation of the initial rock mass into smaller pieces generally upon the first impact on the ground (Evans & Hungr, 1993). Subsequently, these resulting fragments follow trajectories different from that trajectory followed by the initial block in absence of fragmentation. It is important to note that the fragmentation is stochastic due to the internal weakening of the parent block, introducing an element of unpredictability into modeling efforts aimed at assessing the hazards associated with rockfall events. In recent decades, research has concentrated on various aspects of the fragmentation process such as block shape characterization, terrain description, roughness analysis, and parameters related to the rebound of fragments, among others. These investigations are crucial for advancing on our understanding of fragmentation and the comprehensive prediction of the entire fragment size distribution, which has significant implications for hazard analysis.

The flight bullets phenomenon is another fascinating result of fragmentation. When objects break apart explosively, smaller fragments are shot out at high speeds, following paths that can go over obstacles and travel long distances. This increases significantly the area affected by fragments, causing a major chance of collisions and risk of impacts to human or man-made objects, rather than the case of rockfall in absence of fragmentation. Although the comprehension of dynamic fragmentation and the cracks propagation is not completely understood yet, the consequences of fragment generation by breaking off a larger object are well known in literature especially for their dangerous consequences. The energy required to fragment a block (fragmentation energy) depends on the new surface generated by the block splitting, and the remaining energy content can cause a speeding up of the generated fragments. Other variables involved in the fragmentation process like fragments' flying heights, kinetic energies, how they spread sideways, and their ability to move will also be discussed in this thesis. Another important complex aspect is that during an in-situ rockfall, many impact points can happen simultaneously when a block impacts along the edge or face. These occurrences affect significantly the crack propagation due to their relative orientation of initial rock's natural cracks or weak spots. The type of rock also matters: rocks can have multiple weak spots due to how they formed and the stresses they have experienced. The number of these weak spots and the shape of the block affect the chances of a random impact fragment direction. This behavior has been observed in in-situ tests conducted by researchers like Giacomini et al. (2009), Gili et al. (2016), and Ruiz-Carulla et al. (2016).

Despite the recognition of fragmentation's pivotal role in rockfall risk analysis, a complete understanding of the fragmentation process during rockfall events remains elusive. Remarkably, this phenomenon has largely been overlooked in numerical modeling efforts. Indeed, only a limited number of numerical simulation codes explicitly incorporate fragmentation into their models (Crosta et al., 2003; Frattini et al., 2012; Matas et al., 2017; Ruiz-Carulla, 2018). These models will be examined in more detail in the upcoming chapter, Chapter 2.

Thesis structure

This thesis comprehensively investigate rockfalls, both conventional and those featuring fragmentation, with a focus on enhancing our understanding of these phenomena and quantifying their significance for risk mitigation. It consists of three main chapters, structured as scientific articles in terms of layout. Each chapter includes a research background section before the paper, where the main themes or the theory underlying the paper are analyzed.

Of these scientific papers, the following have already been published:

- **Rockfalls, fragmentation and dust clouds: analysis of the 2017 Pousset event (Northern Italy)** – *Chapter 2*
- **Accounting for the effect of forest and fragmentation in probabilistic rockfall hazard** – *Chapter 2*

and the following are currently in preparation:

- **Field evidence and indicators of rockfall fragmentation and implications for mobility** – *Chapter 1*
- **Investigating fragmentation patterns in rockfall events: a comparative analysis of in-situ and laboratory experiments** – *Chapter 3*
- **Investigating the influence of discontinuities on fragmentation: experimental insights** – *Chapter 3*

I certify that I have made a substantial contribution to the papers of which I am a joint author, and I have included a preamble in which I describe my role and contribution to each paper before the paper itself.

Table of contents

Thesis objectives 1
Brief introduction 2
  Rockfalls 2
  Fragmentation 3
Thesis structure 3
Chapter 1: From rockfall deposit analysis to rockfall event characterization 9
  Research background 9
    The organization of rockfall deposits 9
    The analysis of Rockfall Block Size Distributions and their significance in risk assessment and protective design 10
    Distinguishing disaggregation and fragmentation 11
    The analysis of rockfall mobility and lateral dispersion 11
    Background Bibliography 12
Field evidence and indicators of rockfall fragmentation and implications for mobility 15
  Abstract 15
  Introduction 15
  Case studies 16
  Methods 18
  Analysis and results 20
    Mapping and density of blocks within the deposits 20
  Discussion 27
    Blocks and fragments mapping 27
    Fragmentation and block size distribution 27
    Fragmentation and block size trend with distance 27
    Fragmentation and rockfall mobility 28
    Identification of fragmentation from post-event field evidences 28
  Conclusions 28

Acknowledgments 29
References 29
Chapter 2: Numerical simulations of case studies with fragmentation 32
Research background 32
The rockfall motion 32
The phases of rockfall events 32
Impact modelling 33
Hy-Stone 34
The Extremely Energetic Rockfalls 36
The importance of RBSD analysis and fragmentation energy calculation 37
The generation and propagation of dust 38
Background Bibliography 39
Rockfalls, fragmentation and dust clouds: analysis of the 2017 Pousset event (Northern Italy) 41
Abstract 41
Introduction 41
The 2017 Pousset rock fall 42
Geological setting 43
The 2017 event 44
Dust sampling and analysis 47
Rockfall simulation 50
HyStone code 50
Model settings 51
Rockfall simulation results 51
Dust cloud analysis 55
Fragmentation energy 55
Dust cloud propagation 58
Cloud settling 60
Conclusions 62
Acknowledgements 63
References 63
Supplementary materials 66
HyStone motion equations 66
Bond’s law for fragmentation energy 67
Rockfall events during which the processes of fragmentation and impact with trees played a decisive role . 71
Research background 71
The restitution coefficients 71
The distinction between hazard and risk in the assessment and management of landslide risk 72
Assessing impact frequency of fragmental rockfalls 73

The strategies for mitigating rockfall hazards 75

Quantifying the contribution of fragmentation and tree impact on rockfall dynamics and hazard 76

Background Bibliography 76

Accounting for the effect of forest and fragmentation in probabilistic rockfall hazard 80

Abstract 80

Introduction 80

Methods 81

Rockfall analysis 81

Rockfall hazard assessment 83

Demonstration case studies 84

Analysis and results 85

Calibration by back-analysis 85

Effect of tree-impact and fragmentation sub-models on kinetic energy 87

Rockfall Hazard 91

Discussion 94

Tree impact 94

Fragmentation 95

Probabilistic rockfall hazard 95

Conclusions 95

Acknowledgments 96

References 96

Chapter 3: Fragmentation tests 99

Fragmentation tests | in-situ and laboratory experiments 99

Research Background 99

Numerical studies on fragmentation upon impact 99

Fragmentation modelling and real-scale tests 100

Background Bibliography 101

Investigating fragmentation patterns in rockfall events: a comparative analysis of in-situ and laboratory experiments 103

Introduction 103

Methods 104

In-Situ Test 104

Laboratory Test 105

Analysis and results 108

In-situ quarry test 108

Laboratory test 113

Discussion 117

Conclusions 118

  References 118
  Supplementary materials 120
    Ground Dispersion of Fragments Resulting from Impacts 122
    Simplified fragment tracking results and Exit angles calculation 129
Fragmentation tests | in-situ and laboratory experiments 136
  Research Background 136
    Impact loading behavior and fragmentation patterns 136
    Background Bibliography 138
Investigating the influence of discontinuities on fragmentation: experimental insights 139
  Abstract 139
  Introduction 139
  Methodology 140
    Experimental setup 140
    Materials 141
    Procedures for preparing dental plaster mixtures 142
    Preparation of the spheres 142
    Material Characterization through UCS, Brazilian, and Shear Tests 144
    The fragmentation tests 145
  Analysis and results 145
    Qualitative analysis of sphere fracture modes and fragment characteristics 145
    Mass-frequency analysis 149
  Discussion 150
  Conclusion 151
  References 151
Final reflections 152

Chapter 1: From rockfall deposit analysis to rockfall event characterization

Rockfall fragmentation plays a crucial role in hazard mitigation and the design of protective measures. However, the current lack of modeling tools that incorporate rock fragmentation mechanics is a limitation. This chapter aims to investigate the fragmentation patterns of rockfalls and analyze the resulting distribution of fragment sizes within the deposit, with a specific focus on small fragments, which can be used as input for numerical modeling and also provide insights into the dynamics of the rockfall event. We analyzed multiple rockfall events from various locations worldwide, each exhibiting different levels of fragmentation. By employing image analysis techniques, we mapped all visible blocks, determined their volumes, and measured the distances they traveled from the point of impact. A key finding is the identification of three indicators of fragmentation. Firstly, in cases where significant fragmentation was absent, we observed a trend of increasing block size with distance from the impact point or source area, which aligns with existing scientific literature. However, for energetic rockfall events characterized by intense fragmentation, we observed that small fragments exhibited longer travel distances compared to larger ones. This distinction allowed us to differentiate blocks primarily resulting from the disaggregation process from blocks primarily resulting from dynamic fragmentation, with interesting implications for rockfall mobility. Secondly, we observed that the main deposit exhibits power-law scaling for larger volumes, while fragments show either an absence or smaller threshold, indicating distinct fragmentation patterns. Thirdly, we found that rockfalls with fragmentation experience higher reach angles indicating reduced mobility and the energy-consuming nature of fragmentation, and higher lateral dispersion indicating a wider dispersion of trajectories. In addition, topography has been evaluated, which is an important factor to consider when studying the distribution of fragments in rockfall events because it can significantly influence the movement and deposition of falling rocks. Steeper slopes generally result in faster and more chaotic rockfall events, which can cause fragments to scatter over a larger area, while flatter slopes may cause fragments to accumulate in a more localized area. Moreover, the presence of natural or man-made barriers, such as trees or buildings, can also affect the distribution of fragments by altering their trajectory or slowing their movement. These findings underline the importance of understanding the dominant fragmentation mechanisms in rockfall events to accurately predict the behavior of falling rocks and assess the potential risks they pose.

Research background

The paper presented below primary objective is to investigate the fragmentation patterns of rockfalls and the resulting distribution of the deposit, with a particular emphasis on the behavior of small fragments. The study highlights the need to analyze not only the distribution of blocks in the main talus deposit but also the small fragments that may travel further than larger ones during intense rockfall events. By incorporating the distribution of both large and small fragments, a different power-law distribution can be obtained, with relevant implications for hazard mitigation. Furthermore, we explored the topic of rockfall mobility by examining the H/L ratio and planimetric lateral dispersion.

The organization of rockfall deposits

The central theme of this chapter revolves around rockfall deposits, which are often referred to as talus. A talus is the product of rockfalls which often takes the form of a pile of rocks at the base of mountain slopes. The formation of a talus is due to the energy released by the falling blocks. When a block loses its energy while traveling down the slope and is not balanced out by the energy gained from gravity, it stops and contributes to steepening the slope. On the other hand, if the energy gain from gravity is greater than the energy loss, the block will accelerate and decrease the slope angle. The smaller fragments tend to get trapped in between the larger blocks due to the irregular surface of the talus, while larger fragments travel longer and have a lower rolling friction coefficient, which allows them to avoid being trapped by the roughness of the surface. This results in a longitudinal sorting of the talus (De Blasio, 2018).

In the long run, the path for the succeeding blocks is determined by the position of the fallen blocks in the talus. This leads to a self-organization of the talus, resulting in a stripe-like pattern where small blocks are found at the top and boulders at the bottom, creating a longitudinal grading. Although taluses may seem like chaotic heaps, they are often stratified, and geophysical methods have demonstrated this (Sass 2006; Van Stejin et al. 1995). The deposit is poorly consolidated, and the angles at the highest part of the talus range from 30° to 40°, decreasing to 30–35° in the middle and less than 20° at the foot. The lengths of taluses range from a few meters to hundreds of meters.

Several studies have been conducted to experimentally recreate the formation of taluses (Statham 1972; Statham, 1976; Sæter, 2008; De Blasio and Sæter, 2009b). These studies show that at the beginning of the experiment, small grains tend to stop at the apex, while larger ones roll down to the slope break. However, in a later stage, a superficial creep is observed, followed by a series of avalanches (De Blasio and Sæter, 2009b). Avalanching is preceded by vertical segregation, where small particles move to the bottom, resulting in instability and observed avalanches. Rockfall deposits exhibit fahrboschungs between 32° and 45°, making them less mobile than rock avalanches but far more common.

The analysis of Rockfall Block Size Distributions and their significance in risk assessment and protective design

In the study of rockfalls, data analysis typically begins with available information, which may include knowledge of the characteristics of the blocks that have fallen, but more commonly includes the distribution of blocks within talus deposit that have already fallen. This is because information on the material that has detached requires surveys with drones, laser scanners, or other investigations prior to the event. The material that is still on the wall and then involved in the event is defined as the In Situ Block Size Distribution (ISBD) (Lu & Latham, 1999), while the material that has collapsed and forms the deposit of the event is defined as the Rock Block Size Distribution (RBSD). The RBSD refers to the distribution of rock block sizes on the ground, which includes both blocks derived from the fragmentation process and the disaggregation process. Grain size analysis of rockfall deposits requires multi-scale methods using airborne and UAV imagery (Carbonneau et al., 2004; Woodget & Austrums, 2017), and field survey activities (Ruiz-Carulla et al., 2015).

The relationship between frequency and magnitude generally follows a power-law trend, as reported in previous studies (Dussauge et al., 2003; Malamud et al., 2004). The distributions exhibit nearly linear behavior in log-log space for volumes larger than case-specific thresholds, while a downward deviation from linearity is observed for smaller volumes, indicating a censoring effect (Dussauge et al., 2003; Strunden et al., 2015). The choice of the cutoff volume is based on manual selection, guided by the shape of the distribution. Subsequently, a power-law distribution is fitted to the observed cumulative volume distribution.

The RBSD parameter is crucial in assessing the risk of rockfall events, as block sizes significantly influence detachment frequency and kinetic energy (Hungr et al., 1999; Lari et al., 2014; Wang et al., 2014). Rockfall block volume also affects mitigation measures and forest protection efficiency (Lanfranconi et al., 2020). Knowledge of the RBSD can then be used to design protective structures, such as barriers and containment nets, which must be adequately sized to withstand falls of different block sizes (Brunetti et al., 2009; Corominas et al., 2017a, 2017b; Crosta et al., 2015; De Biagi et al., 2017; Dussauge et al., 2003; Dussauge-Peisser et al., 2002; Lambert and Bourrier, 2013; Lari et al., 2014; Malamud et al., 2004). Numerical modelling of rockfalls is conducted to assess the dynamics of the blocks (i.e., velocity, kinetic energy, impact forces, and bouncing height) and the lateral and longitudinal spreading (Agliardi & Crosta, 2003). To perform numerical modelling, a distribution of blocks volume is needed, so the analysis of rockfall deposits plays a crucial role in selecting appropriate volume distributions for event propagation simulations (Melzner et al, 2020). Very few rockfall simulation codes incorporate fragmentation process modelling (Crosta et al., 2003; Frattini et al, 2012; Matas et al., 2017; Ruiz-Carulla, 2018), for which the additional volume distribution of fragments is an important parameter. Therefore, it is essential to gather a second volume distribution specifically for fragments. In this article, we propose that comprehensive analysis of the rockfall deposit through image analysis, combined with ground validation, enables insights into the dynamics of rockfall events. The availability of high-resolution images facilitates detailed examination. To investigate fragmentation patterns of rockfalls, the resulting distribution of the deposit was studied, with particular emphasis on the behavior of small fragments.

Distinguishing disaggregation and fragmentation

When studying rockfall deposits, it is important to differentiate the processes that determine the distribution of blocks within them. Depending on the volume and energy possessed by the block at the time of impact, three situations may occur: the material may remain intact, may break along pre-existing planes of weakness, or may break generating volumes. These two distinct processes will be referred to as disaggregation and fragmentation, respectively. The resulting RBSD can be used to characterize the fragmentation phenomenon and to identify the predominant mechanism as disaggregation, pure breakage, or a combination of both. In this thesis I refer to disaggregation when, after its detachment from the rock wall and/or due to a low energy impact on the ground, the rock mass disaggregates. In this case, the block fragments are bounded by the preexisting joints and the RBSD generated is similar to the initial in-situ block size distribution (IBSD) (Ruiz-Carulla et al., 2017). If the impact energy is enough to fragment the blocks, the generated RBSD will differ from the initial IBSD and we refer to that process as fragmentation. The latter process is still debated and unclear in its dynamic, even if understanding the fragmentation process is key to rockfall hazard analysis (Jaboyedoff et al. 2005; Corominas et al. 2019) as it affects volume, trajectory, spread of rock fragments, and the encounter probability with the elements at risk (Nocilla et al., 2009; Ruiz-Carulla et al., 2016). While for energy of the order of 100 J/kg a block may break into few pieces, for much greater energies of the order of some MJ the block disintegrates into a myriad of smaller grains, often including powder-size broken rock, producing seismic waves (Deparis et al., 2008), damaging trees (Crosta et al., 2023) and producing a temporary darkness (De Blasio, 2011).

Several parameters influence the fragmentation process and the RBSD, such as the presence and persistence of discontinuities, the impact energy, the rigidity of the ground, and the impact angle (Dussauge et al., 2003; Wang & Tonon, 2011; Hantz et al., 2014). Obtaining the RBSD requires counting and measuring the blocks and fragments on the ground, which can be challenging for large rockfall deposits due to the high number of blocks involved. Ruiz-carulla et al. (2018) propose counting and measuring block fragments in selected sampling plots within homogeneous zones in the young debris cover generated by the rockfall, along with all the large scattered rock blocks. The obtained size distribution of the blocks can be well-fitted by a power law distribution, indicating the scale-invariant character of the fragmentation process (Hantz et al., 2014; Hartmann, 1969; Turcotte, 1986). The total volume of the rockfall fragments should be compared to the volume of the rockfall source, which can be calculated by comparing 3D digital surface models before and after the event. In this chapter a new methodology to distinguish between the two contributions of disaggregation and fragmentation within rockfall deposits is proposed.

The analysis of rockfall mobility and lateral dispersion

Another crucial and straightforward variable for characterizing landslide mobility (Crosta et al., 2018) is the H/L ratio (Heim's ratio or Fahrböschung), which expresses the maximum vertical-to-horizontal landslide displacement fraction (from the crown of the starting zone to the tip of the talus deposit).

It represents a good indicator of the friction coefficient the landslide encounters during its movement (Scheidegger, 1973). A low H/L ratio suggests that the landslide traveled a long distance with a relatively small fall height. Typically, mobility is evaluated by studying the main deposit or by including the extremely distant blocks resulting from fragmentation (also depending on conservativeness). An issue related to the mobility of rockfall is whether fragmentation can enhance the mobility, as observed by some authors (Jin et al, 2023) or should be considered an energy-consuming process (Crosta et al., 2007, De Blasio et al., 2018; De Blasio & Crosta, 2015). Moreover, the lateral dispersion of trajectories also offers valuable insights into the mobility and dynamics of a rockfall event. The deviation of downslope blocks from the maximum slope due to rolling in concavities and oblique surface impacts causes a disorder effect in the paths of falling blocks (Crosta & Agliardi, 2004; Azzoni et al., 1995; Evans and Hungr, 1993; Jaboyedoff et al., 2005). This effect becomes more significant with longer fall paths as errors from various controlling parameters spread through multiple impacts and encountered morphological changes (Crosta & Agliardi, 2004; Azzoni et al., 1995). In this chapter, the topic of rockfall mobility has been explored by examining the H/L ratio and planimetric lateral dispersion.

The resulting angles show that rockfalls without fragmentation exhibit a lower percentage of lateral dispersion for the main body series, while those with fragmentation show significantly higher values for the more distal deposit series. This indicates a greater mobility in fragmented rockfalls.

The research question underlying the paper reported below was: *Is it possible to describe the dynamic of a rockfall event just studying the rockfall deposit?* To answer this question, I analyzed the rockfall events and the resulting deposits from the following case studies: Villeneuve (Italy), Saint-Oyen (Italy), Novate Mezzola (Italy), Gallivaggio (Italy), Cárcavos (Spain), Parkline (USA), El Capitan (USA). I would like to express my gratitude to the Geological Survey of Valle d'Aosta, ARPA Lombardia, the Spanish IGME Research Group, and the United States Geological Survey (USGS) for their collaboration and for providing valuable data. The Yosemite data have been collected between January and March 2022, during which I had the opportunity to spend a few months abroad working at the USGS.

I’m author of the paper below, for which I contributed to the conceptualisation of the project, I dealt with formal analysis, investigation, methodology, visualisation, and writing of the original draft. Currently it is in the very last review-phase before submission.

Background Bibliography

Agliardi, F., & Crosta, G. B. (2003). High resolution three-dimensional numerical modelling of rockfalls. International Journal of Rock Mechanics and Mining Sciences, 40(4), 455-471

Agliardi, F., Crosta, G.B., Frattini, P., 2009. Integrating rockfall risk assessment and countermeasure design by 3D modelling techniques. Nat. Hazard. Earth Syst. Sci. 9, 1059 Katlenburg-Lindau.

Azzoni, A., La Barbera, G., & Zaninetti, A. (1995, October). Analysis and prediction of rockfalls using a mathematical model. In International journal of rock mechanics and mining sciences & geomechanics abstracts (Vol. 32, No. 7, pp. 709-724). Pergamon.

Brunetti, M. T., Guzzetti, F., & Rossi, M. J. N. P. I. G. (2009). Probability distributions of landslide volumes. Nonlinear Processes in Geophysics, 16(2), 179-188.

Carbonneau, P. E., Bergeron, N., & Lane, S. N. (2005). Automated grain size measurements from airborne remote sensing for long profile measurements of fluvial grain sizes. Water resources research, 41(11).

Corominas J, Lantada N, Gili J, Ruiz R, Matas G, Mavrouli O, Núñez-Andrés MA, Moya J, Buill F, Abellán A, Puig-Polo C, Prades A, Martinez-Bofill J, Salo L (2017b) The RockRisk project: rockfall risk quantification and prevention. Proceedings of ROCEXS 2017, 6th Interdisciplinary Workshop on Rockfall Protection, May 2017, Barcelona (Spain). pp 39–42. Available at: http://congress.cimne.com/rocexs2017/frontal/Doc/Ebook.pdf.

Corominas J, Mavrouli O, Ruiz-Carulla R (2017a) Rockfall occurrence and fragmentation. In: Sassa K, Mikoš M, Yin Y (Eds): Advancing Culture of Living with Landslides. World Landslide Forum, WLF 2017, Ljubljana. Springer, Cham. pp 75–97. https://doi.org/10.1007/978-3-319-59469-9_4

Corominas J, Mavrouli O, Santana D, Moya J (2012) Simplified approach for obtaining the block volume distribution of fragmental rockfalls. In: Eberhardt E, Froese C, Turner AK, Leroueil S (eds) Landslides and engineered slopes, 2, pp 1159–1164

Corominas, J., Matas, G., & Ruiz-Carulla, R. (2019). Quantitative analysis of risk from fragmental rockfalls. Landslides, 16(1), 5-21

Crosta, G. B., Agliardi, F., Frattini, P., & Imposimato, S. (2004). A three-dimensional hybrid numerical model for rockfall simulation. In Geophys Res Abstr (Vol. 6, p. 04502).

Crosta, G. B., De Blasio, F. V., & Frattini, P. (2018). Global scale analysis of Martian landslide mobility and paleoenvironmental clues. Journal of Geophysical Research: Planets, 123(4), 872-891.

Crosta, G. B., Frattini, P., & Fusi, N. (2007). Fragmentation in the Val Pola rock avalanche, Italian alps. Journal of Geophysical Research: Earth Surface, 112(F1).

Crosta, G.B.; Agliardi, F.; Frattini, P.; Lari, S. Key Issues in Rock Fall Modeling, Hazard and Risk Assessment for Rockfall Protection. In Engineering Geology for Society and Territory - Volume 2; 2015

De Biagi, V., Napoli, M. L., & Barbero, M. (2017). A quantitative approach for the evaluation of rockfall risk on buildings. Natural hazards, 88, 1059-1086.

De Blasio FV, Sæter M-B (2009b) Small-scale experimental simulation of talus evolution. Earth Surf Process Land 34:1685–1692

De Blasio, F. V. (2011). Introduction to the physics of landslides: lecture notes on the dynamics of mass wasting. Springer Science & Business Media.

De Blasio, F. V., & Crosta, G. B. (2015). Fragmentation and boosting of rock falls and rock avalanches. Geophysical Research Letters, 42(20), 8463-8470.

De Blasio, F. V., Dattola, G., & Crosta, G. B. (2018). Extremely energetic rockfalls. Journal of Geophysical Research: Earth Surface, 123(10), 2392-2421.

Deparis, J., Jongmans, D., Cotton, F., Baillet, L., Thouvenot, F., & Hantz, D. (2008). Analysis of rock-fall and rock-fall avalanche seismograms in the French Alps. Bulletin of the Seismological Society of America, 98(4), 1781-1796.

Dikau R, Brunsden D, Schrott L, Ibsen M-L (eds) (1996) Landslide recognition. Identification, movement and causes. Wiley, Chichester

Dussauge, C., Grasso, J. R., & Helmstetter, A. (2003). Statistical analysis of rockfall volume distributions: Implications for rockfall dynamics. Journal of Geophysical Research: Solid Earth, 108(B6).

Dussauge-Peisser, C., Helmstetter, A., Grasso, J. R., Hantz, D., Desvarreux, P., Jeannin, M., & Giraud, A. (2002). Probabilistic approach to rock fall hazard assessment: potential of historical data analysis. Natural hazards and earth system sciences, 2(1/2), 15-26.

Evans, S.G.; Hungr, O. The Assessment of Rockfall Hazard at the Base of Talus Slopes. Can. Geotech. J. 1993, 30, 620–636.

Frattini, P., Crosta, G. B., Agliardi, F., Clague, J. J., & Stead, D. (2012). 22 Rockfall characterization and modeling. Landslides: types, mechanisms and modeling, 267.

Hantz D, Rossetti JP, Servant F, D'Amato J (2014) Etude de la distribution des blocs dans un éboulement pour l'évaluation de l'aléa. Proceedings of Rock Slope Stability 2014, Marrakesh, p 10

Hantz, D., Corominas, J., Crosta, G. B., & Jaboyedoff, M. (2021). Definitions and concepts for quantitative rockfall hazard and risk analysis. Geosciences, 11(4), 158.

Hartmann, W. K. (1969). Terrestrial, lunar, and interplanetary rock fragmentation. Icarus, 10(2), 201-213.

Hungr O, Evans SG, Bovis MV, Hutchinson JN (2001) A review of the classification of landslides of the flow type. Environ Eng Geosci 7(3):221–238 Hunt ML, Zenit R, Campbell CS, Brennen CE (2002) Revisiting

Hutchinson JN (1988) General report: morphological and geotechnical parameters of landslides in relation to geology and hydrogeology. In: Bonnard C (a cura di) Proceedings of the fifth international symposium on landslides, Balkema, Rotterdam, pp 3–35

Jaboyedoff, M., Dudt, J. P., & Labiouse, V. (2005). An attempt to refine rockfall hazard zoning based on the kinetic energy, frequency and fragmentation degree. Natural Hazards and Earth System Sciences, 5(5), 621-632.

Jin, K., Xing, A., Li, B., He, K., Zhuang, Y., & Chang, W. (2023). Dynamic fragmentation characteristics of columnar rockfall: insights from discrete element method. Bulletin of Engineering Geology and the Environment, 82(8), 322.

Lambert, S., & Bourrier, F. (2013). Design of rockfall protection embankments: a review. Engineering geology, 154, 77-88.

Lanfranconi, C., Sala, G., Frattini, P., Crosta, G. B., & Valagussa, A. (2020). Assessing the rockfall protection efficiency of forests at the regional scale. Landslides, 17, 2703-2721.

Lari, S., Frattini, P., & Crosta, G. B. (2014). A probabilistic approach for landslide hazard analysis. Engineering geology, 182, 3-14.

Lu, P., & Latham, J. P. (1999). Developments in the assessment of in-situ block size distributions of rock masses. Rock mechanics and rock engineering, 32, 29-49.

Malamud, B. D., Turcotte, D. L., Guzzetti, F., & Reichenbach, P. (2004). Landslide inventories and their statistical properties. Earth Surface Processes and Landforms, 29(6), 687-711.

Matas, G.; Lantada, N.; Corominas, J.; Gili, J. A.; Ruiz-Carulla, R.; Prades, A., RockGIS: a GIS-based model for the analysis of fragmentation in rockfalls. Landslides 2017, 14 (5), 1565-1578.

Melzner, S., Rossi, M., & Guzzetti, F. (2020). Impact of mapping strategies on rockfall frequency-size distributions. Engineering Geology, 272, 105639.

Nocilla, N., Evangelista, A., & Scotto di Santolo, A. (2009). Fragmentation during rock falls: Two Italian case studies of hard and soft rocks. Rock mechanics and rock engineering, 42, 815-833.

Ruiz-Carulla, R., Corominas, J., & Mavrouli, O. (2015). A methodology to obtain the block size distribution of fragmental rockfall deposits. Landslides, 12(4), 815-825.

Ruiz-Carulla, R., Corominas, J., & Mavrouli, O. (2017). A fractal fragmentation model for rockfalls. Landslides, 14(3), 875-889.

Ruiz-Carulla, R., Corominas, J., & Mavrouli, O. (2018). Comparison of block size distribution in rockfalls. In Landslides and engineered slopes. Experience, theory and practice (pp. 1767-1774). CRC Press

Sass O (2006) Determination of the internal structure of alpine talus deposits using different geophysical methods (Lechtaler Alps, Austria). Geomorphology 80:45–58

Scheidegger, A. E. (1973). On the prediction of the reach and velocity of catastrophic landslides. Rock mechanics, 5(4), 231-236.

Strunden, J., Ehlers, T.A., Brehm, D., Nettesheim, M., 2015. Spatial and temporal variations in rockfall determined from TLS measurements in a deglaciated valley, Switzerland. J. Geophys. Res. Earth Surf. 120, 1251–1273. https://doi.org/10.1002/2014JF003274.

Turcotte, D. L. (1986). Fractals and fragmentation. Journal of Geophysical Research: Solid Earth, 91(B2), 1921-1926.

Van Steijn H, Bertran P, Francou B, Hetu B, Texier JP (1995) Models for genetic and environmental interpretation of stratified slope deposits: review. Permafrost Periglac 6:125–146

Volkwein, A., Roth, A., Gerber, W., & Vogel, A. (2009). Flexible rockfall barriers subjected to extreme loads. Structural engineering international, 19(3), 327-332.

Wang, X., Frattini, P., Crosta, G. B., Zhang, L., Agliardi, F., Lari, S., & Yang, Z. (2014). Uncertainty assessment in quantitative rockfall risk assessment. Landslides, 11, 711-722.

Wang, Y., & Tonon, F. (2011). Discrete element modeling of rock fragmentation upon impact in rock fall analysis. Rock mechanics and rock engineering, 44, 23-35.

Woodget, A. S., & Austrums, R. (2017). Subaerial gravel size measurement using topographic data derived from a UAV-SfM approach. Earth Surface Processes and Landforms, 42(9), 1434-1443.

Field evidence and indicators of rockfall fragmentation and implications for mobility

Camilla Lanfranconi[1], Paolo Frattini[1], Federico Agliardi[1], Greg M. Stock[2], Brian Collins[2], Giovanni Crosta[1]

[1] Università degli studi di Milano – Bicocca, DISAT, Dept. of Earth and Environmental Sciences, Milano 20126, Italy

[2] U.S. National Park Service, Yosemite National Park, El Portal California 95318, United States

Abstract

Rockfall fragmentation plays a important role in hazard studies and the design of protective measures. However, the current lack of modeling tools that incorporate rock fragmentation mechanics is a limitation. This research investigates the fragmentation patterns of rockfalls and analyses the resulting distribution of fragment sizes within the deposit, with a specific focus on small fragments, which can be used as input for numerical modeling and also provide insights into the dynamics of the rockfall event. We analyzed multiple rockfall events from locations worldwide, each exhibiting different levels of fragmentation. Using image analysis techniques, we mapped all visible blocks, determined their volumes, and measured the distances they traveled from the point of impact. A key finding is the identification of three indicators of fragmentation. Firstly, in cases where significant fragmentation was absent, we observed a trend of increasing block size with distance from the impact point or source area, which aligns with existing scientific literature. However, for energetic rockfall events characterized by intense fragmentation, we observed that small fragments exhibited longer travel distances compared to larger ones. This distinction allowed us to differentiate blocks primarily resulting from the disaggregation process from blocks primarily resulting from dynamic fragmentation, with interesting implications for rockfall mobility. Secondly, while the size distribution of rockfall deposit exhibits a power-law scaling for volumes larger than a minimum size threshold corresponding to a rollover of the distribution, in some case studies a deviation from power is observed, indicating a process of larger block comminution due to fragmentation. Thirdly, we found that rockfalls with fragmentation experience higher reach angles, indicating reduced mobility, and higher lateral dispersion, indicating a wider dispersion of trajectories. We interpret these findings to be related directly to the energy-consuming nature of fragmentation which prevents longer deposition.

Introduction

Rockfall events pose significant risks to infrastructure and human safety, necessitating the implementation of effective rockfall protection measures or other risk mitigation strategies. Understanding the behavior and characteristics of rockfalls is crucial for the design and planning of such protective measures (Agliardi et al., 2009; Volkwein et al., 2009; Lanfranconi et al, 2023). When stiff and strong rock blocks impact a hard substratum or other blocks of comparable size such as a talus deposit, they may either disaggregate into smaller blocks delimited by pre-existing or latent discontinuities in the initial mass (Corominas et al. 2012; Ruiz-Carulla, 2018) or undergo an explosive dynamic fragmentation when the energy is sufficient (De Blasio et al., 2018; Crosta et al., 2015). In both cases, the resultant fragments propagate downslope following trajectories and different dynamics compared to the source block (Collins et al., 2022), posing a significant challenge for numerical modelling of rockfall propagation (Crosta et al., 2004; Frattini et al, 2012; Matas et al., 2017; Ruiz-Carulla, 2018; Sala et al, 2019).

A first issue addressed by this study is whether fragmentation should be considered an energy-consuming process (Crosta et al., 2007, De Blasio et al., 2018; De Blasio & Crosta, 2015), or it can enhance the mobility

(Jin et al, 2023), and the lateral dispersion of the trajectories (Crosta & Agliardi, 2004; Azzoni et al., 1995; Evans and Hungr, 1993; Jaboyedoff et al., 2005). A second issue is the characterization of the rock block size distributions of rockfall deposits. This distribution exhibits nearly linear behavior in log-log space for volumes larger than case-specific thresholds (Dussauge et al., 2003; Malamud et al., 2004), while a downward deviation from linearity is observed for smaller volumes, indicating a censoring effect (Dussauge et al., 2003; Strunden et al., 2015). The choice of the cutoff volume is based on manual selection, guided by the shape of the distribution. Subsequently, a power-law distribution is fitted to the observed cumulative volume distribution. The block size distribution parameter is critical in assessing the risk of rockfall events, as block size significantly influences detachment frequency and kinetic energy (Hungr et al., 1999; Lari et al., 2014; Wang et al., 2014), the latter of which can entirely govern the proper selection of mitigation methods and forest protection efficiency (Lanfranconi et al., 2020). Knowledge of the block size distribution can thus be used to design protective structures, such as barriers and containment nets, that must be adequately sized to withstand falls of different block sizes (Brunetti et al., 2009; Corominas et al., 2017a, 2017b; Crosta et al., 2015; De Biagi et al., 2017; Dussauge et al., 2003; Dussauge-Peisser et al., 2002; Lambert and Bourrier, 2013; Lari et al., 2014; Malamud et al., 2004). A characterization of the block size distribution requires a multi-scale method, which includes airborne and UAV high-resolution imagery (Carbonneau et al., 2004; Woodget & Austrums, 2017) and field survey activities (Ruiz-Carulla et al., 2015).

This study aims to advance our understanding of rockfall events through detailed deposit characterization and the exploration of fragmentation indicators in frequency size distributions. The focus is on analyzing rockfall deposits to study the distribution of blocks in the main talus deposit and the behavior of small fragments. By investigating fragmentation patterns through the block size distribution and comparing it with the main deposit's distribution, our study aims to identify potentially different and distinct fragmentation behaviors. Additionally, we explore rockfall mobility using the H/L ratio and lateral dispersion to assess whether rockfall fragmentation enhances mobility or acts as an energy-consuming process, with a higher lateral dispersion suggesting greater mobility in fragmented rockfalls. Understanding fragmentation is crucial for conducting realistic numerical simulations of rockfall runout, assessing risks from rockfalls, and designing effective protection structures. The findings from this study are aimed to be make progress to these ends.

Case studies

We selected seven rockfall case studies characterized by largely different volumes involved, lithology, soil morphology at the impact site, and fall height. Four of the rockfalls are located in Northern Italy: Villeneuve (45°42'02.8"N 7°12'29.9"E) and Saint-Oyen (45°48'59.0"N 7°12'21.0"E) in the Aosta Valley region (western Italian Alps), and Novate Mezzola (46°13'35.4"N 9°27'20.9"E) and Gallivaggio (46°21'46.8"N 9°22'08.2"E) in the Lombardy region (central Italian Alps). The geological Alpine domain of these case studies is the Penninic zone with the first two in the Gran San Bernardo nappe and the latter two in the Lepontine Dome. The fifth case study is located in Carcavos, in the Spanish municipality of Ayna (38°32'36.5"N 2°07'46.4"W) within the Sierra de Alcaraz domain, while the sixth and seventh are the Parkline (37°40'47.5"N 119°44'54.9"W) and El Capitan case studies (37°43'50.4"N 119°37'33.5"W) in Yosemite National Park, California (USA), within the west-central portion of the Sierra Nevada batholith. These rockfalls capture a suite of different detachment mechanisms, energy levels, morphological settings, and volumes which provides a robust suite of case studies for exploration of fragmentation effects (Chapter 1 – Table 1).

In the **Villeneuve** case study, approximately 650 m^3 of Piemontese-Zone carbonate-silicate schist detached during the night of 27 December 2019, destroying a rockfall barrier constructed in the late 1990s. A total volume of 15-20 m^3 reached the buildings at the foot of the slope without causing casualties. Most of the material stopped along the slope in a generally stable condition. Moreover, about 15 m^3 of debris along the slope was remobilized during the night of 1 January 2020, causing additional damages to the houses.

In the **Saint-Oyen** case study, about 17,500 m^3 of Ruitor micascists detached in March 2020, and reached a service road and playing field in the lower part of the slope, passing through a mature fir forest. No injuries were reported (Lanfranconi et al., 2023).

Novate Mezzola village is located at the foot of the Mount Avedèe. The affected cliff consists of leucogranite related to the Novate pluton. In January 2021, the detachment of a large portion of rock (1080 m^3) occurred at an altitude of about 550 m a.s.l. A considerable amount of material stopped at the foot of the slope and on the wall at an altitude between 430 and 410 m a.s.l., due to the presence of a large ledge. The residual part of the blocks crossed the embankment at the cliff foot, and the projections of some blocks reached houses located at a distance of between 250 and 300 meters from the toe of the talus, causing damage to the structures. One month after the event, a second detachment of 30 m^3 occurred and impacted on the loose debris on the wall, mobilising it and resulting in a rock dust cloud. The dust cloud did not result in building damage.

The 600 m high **Gallivaggio** cliff consists of locally mylonitic orthogneiss pertaining to the Truzzo granite. On 29 May 2018, a major rockfall reached and damaged the village and the XVI century sanctuary located there after crossing an 8-meter-high embankment and 5-meter-high elasto-plastic retaining nets at the foot of the slope. The volume has been estimated between 6,700 m^3 (Dei Cas et al., 2018) and 7400 m^3 (Crosta et al, in preparation). The rockfall produced a large dust cloud that rapidly spread and damaged a bell tower located just 50 m beyond the embankment.

Cárcavos is located in the south of the Albacete province, in the Castilla-La Mancha region of Spain (Chapter 1 – Figure 1). From a geological point of view, the area belongs to the domain of the Sierra de Alcaraz, in the external zone of the Betic Cordillera (Fallot, 1948). The rockfall event occurred on 17 November 2018 originated at the uppermost portion of a sub-vertical limestone cliff about 80 m high and involved a single 260 m^3 block. Due to impact, the block broke into more than 600 boulders of various sizes causing a great social alarm as some infrastructure was affected (Gallo et al. 2021).

The 650 m^3 **Parkline** rockfall event occurred on 12 June 2017 when large exfoliation sheets of Bass Lake Tonalite detached from the cliff (Chapter 1 - Figure 1). The rockfall source was located about 120 m above the cliff base and 180 m above El Portal Road which provides a main entrance to Yosemite National Park in California, USA. Detached rockfall debris slid down the cliff, hit a ledge, and broke into many pieces and spread over 300 m, eventually reaching the Merced River below. Of the total volume of material that fell from the cliff, roughly 30% of that landed on the El Portal Road, covering the road under 5-6 m of material for a distance of about 50 m. Most of the rock debris resulting from this rock fall was deposited along the slope above the road with the remainder located below the road.

The 900 m tall southeast face of **El Capitan** (Chapter 1 - Figure 1) in Yosemite National Park is composed predominantly of El Capitan Granite (Calkins et al., 1985; Peck, 2002; Putnam et al., 2015). On 27 September 2017 a series of seven rockfalls totaling 453 m^3 detached from 230 m up the southeast face of El Capitan, killing one person and seriously injuring another. The following day, a much larger rockfall (9,811 m^3) occurred from the same location. A massive slab fell from just above the previous day's rockfalls, fragmenting on impact and generating a large dust cloud. A rock fragment struck a vehicle, puncturing the sunroof and injuring the driver (Stock et al., 2018 and Guerin et al., 2020).

Chapter 1 - Table 1 Data on rockfall case studies.

	Year of the event	Volume [m^3]	Free fall height [m]	Lithology
Villeneuve (ITA)	2019	650	15	carbonate-silicate schist
Saint-Oyen (ITA)	2020	17,500	50	micascists
Novate Mezzola (ITA)	2021	1,080	270	granite
Gallivaggio (ITA)	2018	7,380	475	orthogneiss

Càrcavos (ES)	2018	260	85	limestone
Parkline (USA)	2017	650	125	tonalite
El Capitan (USA)	2017	10,700	460	granite
Novate Mezzola (ITA)	2021	1,080	270	granite
Gallivaggio (ITA)	2018	7,380	475	orthogneiss

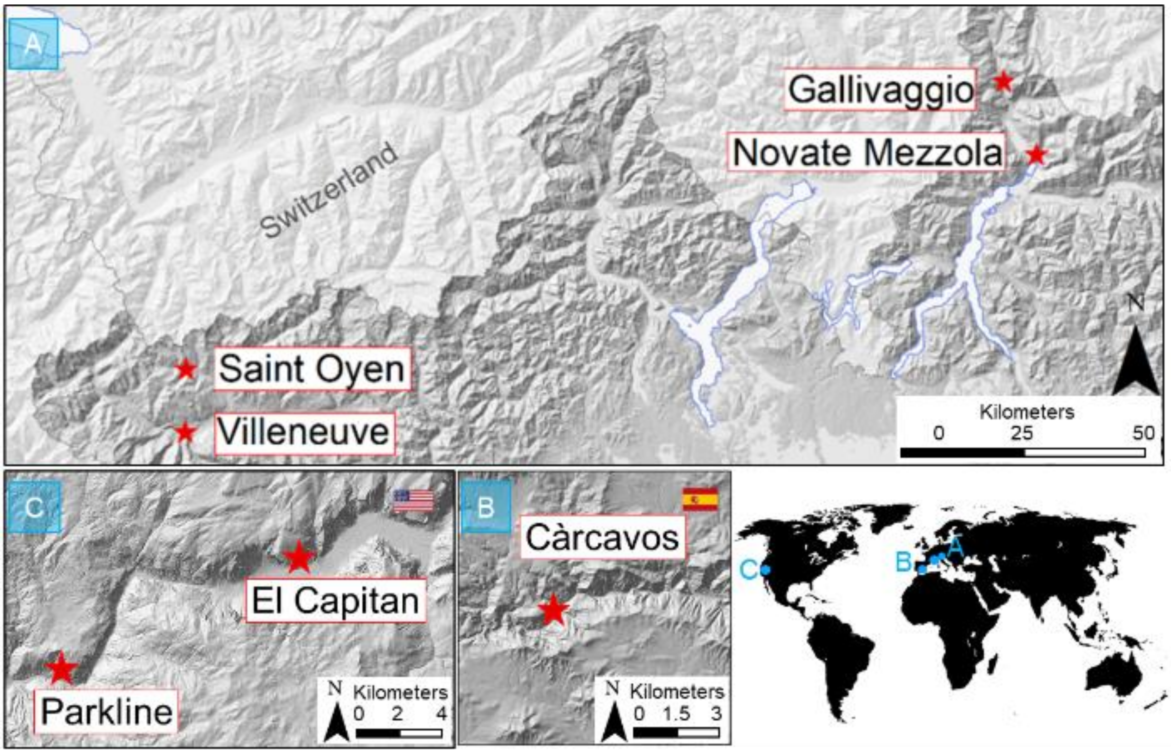

Chapter 1 - Figure 1 Study areas: A) Lombardy and Aosta Valley study areas (Italy), B) Albacete province (Spain), C) Yosemite Valley (California, USA).

Methods

The methodology adopted to study the pattern that characterize rockfalls dynamics includes: *i)* characterization of the talus deposit by image analysis **mapping** of all visible blocks; *ii)* calculation of the **volumes** of the blocks after choosing the geometric shape that fits best (since the available data often come from orthophoto images and thus when mapping in 2D the third axis size is unknown); *iii)* calculation of the **distance** traveled from the source area and from the main site where fragmentation occurred; *iv)* calculation of the block size distribution; *v)* calculation of the HL ratio.

Thanks to increasing resolution of orthophoto images and the availability of new advanced image analysis tools, the characterization of the deposit and the mapping of all the visible blocks, even centimetric, is becoming easier. However, the mapping of the deposit is highly dependent on the quality of the images, the presence of preexisting talus deposits, and the possible obstruction of trees; all these issues may cause the undersampling of the smaller sized elements.

In this study, the mapping of the blocks was supported by UAV very-high resolution images for all case studies, except El Capitan, where UAV images of the deposit were not available. Here the block size distribution of the main talus deposit was obtained in the field through a grid by number approach, measuring a block every 5 meters along scanlines parallel to the rock wall, and spaced every 10 meters. In the sparser deposit outside of the talus, we manually measured each block in the field. We georeferenced the positions of the measuring stations both within and outside the main deposit through a Garmin GPSMAP 86i.

For the case studies presented in this paper, we analyzed high-resolution post-event UAV images (Chapter 1 - Figure 2) and we used a semi-automatic mapping approach through Split-Desktop software to delineate the blocks within the deposit (panel 1 and 2 in Chapter 1 - Figure 1). SplitDesktop is based on a four-step 2D image processing routine: *i)* scale definition, *ii)* automatic or manual digitization of the outline of each individual block, *iii)* extraction of the particle size distribution curve, and *iv)* extraction of the two main axes of each block. Comparing to a manual mapping approach performed in GIS (assumed as more reliable), this semi-automatic approach using Split-Desktop is comparable up to a specific size threshold that depends on the quality of the images used for delineating blocks. Over that threshold, the software overestimates the frequency of smaller blocks (Figure 2).

The shape that we adopted for the calculation of the volume is the ellipsoid, with the invisible third axes assumed to be as long as the second intermediate axis (panel 3 in Figure 1 shows the Minimum Bounding Geometry that we adopted to define the first two axes). More specifically, we used the rectangle of the smallest area enclosing each block polygon to calculate the maximum diameter (Walton, 1948), and then we selected a volume threshold equal to 10^{-3} m^3, thereby counting only the blocks larger than that limit (Chapter 1 - Figure 2).

We finally calculated the Euclidean distance of the centroid of each block (panel 3 in Chapter 1 – Figure 2) from the base of the rockfall source wall or from the ledges or overhangs when identified as the likely major impact zone through field survey. To characterize the trend of block size with distance, we adopted the 99th percentile of volume for 10-m distance classes. This allows to evaluate the runout of blocks with different size, removing the effects of outliers form the analysis.

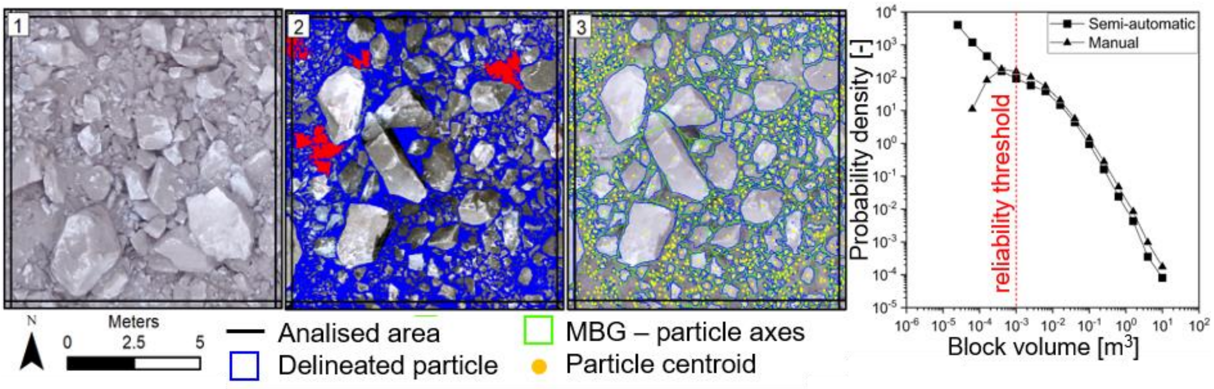

Chapter 1 - Figure 2 Example of semi-automatic mapping approach for the Gallivaggio case study. 1) original image, 2) delineation of blocks performed by Split-Desktop software, 3) centroids and main axes obtained in GIS from the minimum bounding geometry of the particles. Last graph on the right is a comparison between the distribution of boulder delineated from the semi-automatic approach and the manual mapping approach performed in GIS for a sample area in the Gallivaggio case study. The two approaches are similar up to a reliability threshold that is function of the quality of the analyzed image.

For the analysis of the block size distribution of the rockfall deposits, we developed non-cumulative log-binned magnitude frequency relationships, with the probability density, p, as a function of block volume, V (Chapter 1 – Figure 2):

$$p(V) = \frac{\partial N}{\partial V}\frac{1}{N_{tot}} \tag{1}$$

where N is the number of blocks with volume between V and $V+\partial A$, and N_{tot} is the total number of blocks.

A power law scaling for volumes larger than a threshold (Chapter 1 - Figure 2) is observed for all deposits, while for smaller volumes, we observe a downward departure from the linear behavior that is typical of a censoring effect (Dussauge et al., 2003; Strunden et al., 2015). We fitted the probability density with a Pareto distribution by using different thresholds of landslide size:

$$p(V) = \alpha c^{\alpha} V^{-(\alpha+1)} \qquad c > 0, \quad \propto > 0, \quad V \in [c, \infty) \qquad (2)$$

where $\propto$, and c are the parameters of the Pareto distribution, and $\beta=\alpha+1$ is the power-law scaling exponent of the non-cumulative distribution. The corresponding scaling exponent of the cumulative distribution would be α. We estimated the distribution parameters by least square algorithm for different thresholds, and we selected for each deposit the thresholds that maximize the fitting R^2.

Finally, for the analysis of rockfall mobility we calculated the H/L ratio (Heim's ratio or Fahrböschung) expresses the maximum vertical-to-horizontal landslide displacement fraction (from the crown of the starting zone to the tip of the talus deposit) and is a straightforward variable for characterizing landslide mobility (Crosta et al., 2018). Generally speaking, it can be used as an indicator of the friction coefficient that a landslide encounters during its movement (Scheidegger, 1973). A low H/L ratio suggests that the landslide traveled a long distance with a relatively small fall height.

Analysis and results

Mapping and density of blocks within the deposits

We mapped the deposits and the rock block concentration of each case study (Chapter 1 – Figure 3). For Villeneuve, Saint-Oyen, Cárcavos and Parkline we observe an elongated main deposit, with the higher block density in the area at the foot of the slope. For El Capitan, Novate Mezzola and Galivaggio, a second more external deposit is visible for each case study, with, for example, a density of up to 5 blocks per square meter in Gallivaggio. The numbers of mapped blocks are reported in Chapter 1 – Figure 3 The small number of blocks within the main talus deposit in El Capitan is due to the different sampling methodology. The slope profiles of the case studies and of the areas below the cliffs are shown in Chapter 1 – figure 6. We believe that the presence of two distinct and well populated deposits may indicate a process of disaggregation and fragmentation of the blocks.

Chapter 1 - Table 2 Resolution of the mapped UAV images, and number of blocks mapped within ([B] in Chapter 1 – figure 5) and outside ([F] in Chapter 1 – figure 5) the main talus deposit.

	UAV images resolution [cm/pixel]	number of blocks within the main talus deposit	number of blocks outside the main talus deposit
Villeneuve (ITA)	2	2,989	-
Saint-Oyen (ITA)	4	33,488	-
Novate Mezzola (ITA)	2	6,678	4,982
Gallivaggio (ITA)	2	18,401	38,053
Càrcavos (ES)	3	2,767	-
Parkline (USA)	6	4,730	-
El Capitan (USA)	-	175 (grid by number)	1,851

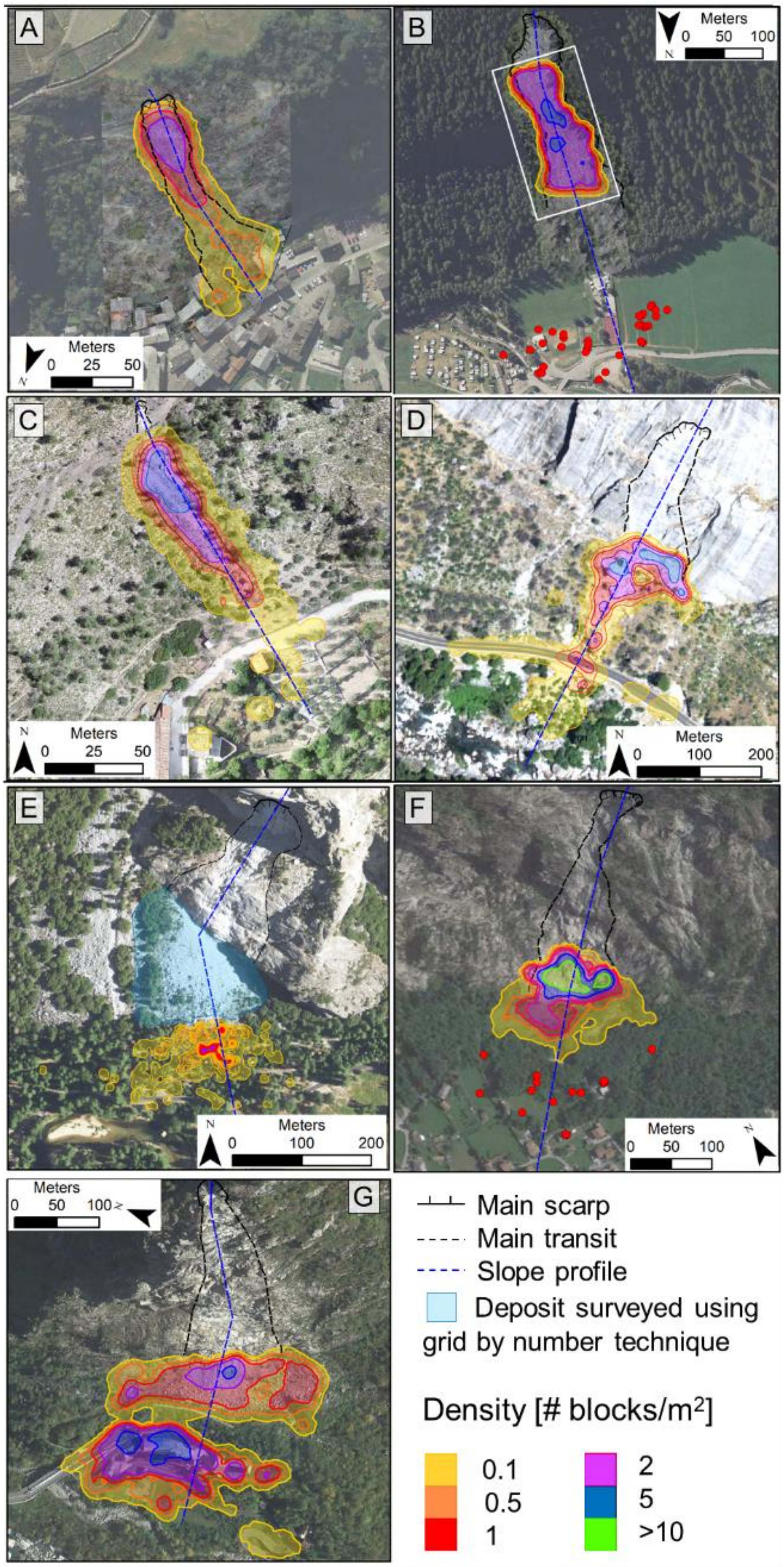

Chapter 1 - Figure 3 Density of mapped blocks per square meters. A) Villeneuve, B) Saint-Oyen, C) Cárcavos, D) Parkline, E) El Capitan, F) Novate Mezzola, G) Gallivaggio. When few blocks occurred external to the mapped deposits, these are indicated by red dots. The density of blocks is not calculated for El Capitan main deposit due to a different mapping approach. Panel B) also shows the sampling window for Saint-Oyen case study (white square).

Trend inversion of blocks size with distance

To examine the relationship between block size and distance, we plot the distance-size trend for each case study considering the 99th percentile of block volume distribution within 10-meters distance classes (Chapter 1 - Figure 5). Some trends show an exponential increase of the volume of the blocks as the distance increases, with a typical talus longitudinal sorting (Villeneuve, Saint-Oyen, Cárcavos and Parkline), while others show an increase of volume in the proximal part (direct sorting) and a decrease after a certain distance, leading to an inverse sorting (El Capitan, Novate Mezzola and Gallivaggio).

The limit between the two zones is gradual and corresponds to the end of the talus cone, 360 m in plan from the source area, as in the El Capitan case study. However, in the presence of embankments, as in the Novate Mezzola and Gallivaggio case studies, the transition occurs sharply at the edge of the defensive work, 290 m and 300 m in plan from the source area, respectively. We consider this evidence as an indicator of fragmentation occurrence.

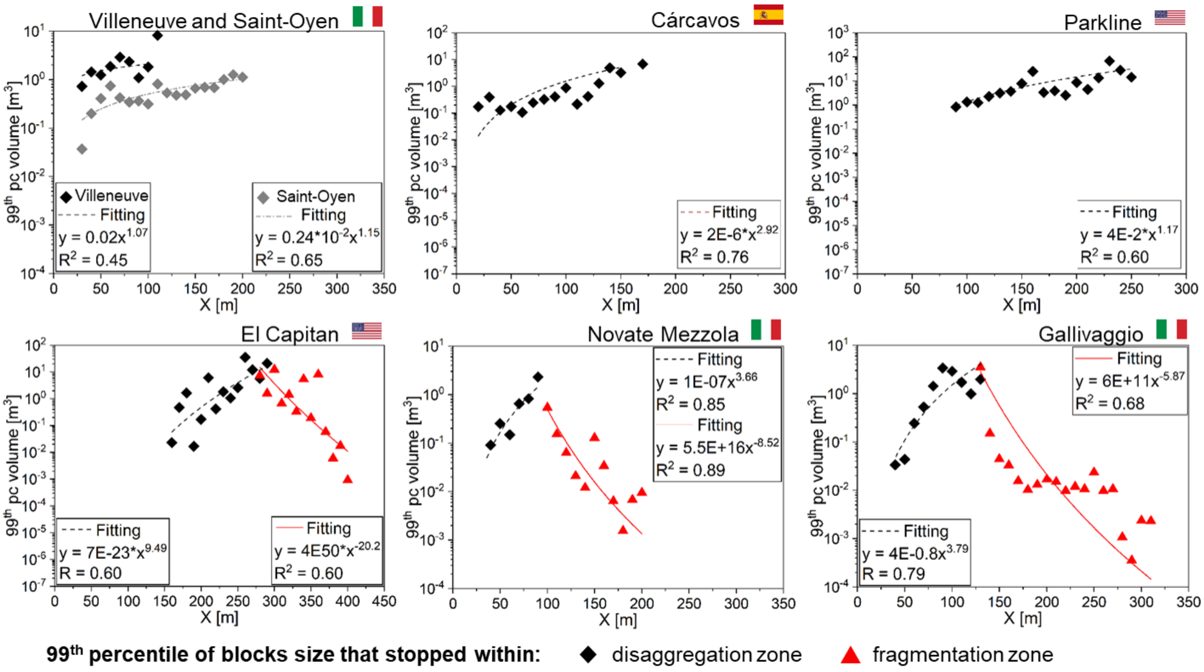

Chapter 1 - Figure 4 Relationships between the 99th percentile of volumes of blocks within individual 10-meter cells and their longitudinal travelled distance. Euclidean distances were calculated from the source area. We grouped Villeneuve and Saint-Oyen case studies in the same panel, as they belong to the same region and show similar behaviour.

Frequency size distribution

For the analysis of the frequency size distribution, we distinguished between the main body of the rockfall deposit (namely **B** in Chapter 1 – Figure 6) and blocks/fragments mapped within a more distal and sparse deposit (namely **F** in Chapter 1 – Figure 6). The latter are visible in 3 out of 7 of the case studies: Gallivaggio, Novate Mezzola and El Capitan. The limits of these two zones corresponds to the distance where the trend inversion is observed (Chapter 1 – Figure 5).

In the main deposit (B), we observe a power-law scaling for volumes larger than a threshold, which changes in each case study, according to the quality of the mapping. This threshold is always larger than the reliability threshold used for image-analysis ($V = 0.001$ m^3), and varies from 10^{-2} m^3 (Novate Mezzola) to 10 m^3 (Gallivaggio), with the exception of El Capitan, where the threshold is very small (10^{-3} m^3), but where the sampling methodology is not comparable with the other case studies. For the blocks/fragments (F) the threshold is absent (Gallivaggio and Novate Mezzola) or much smaller than the one used for the distribution obtained by image analysis. In some cases (Parkline, El Capitan, Gallivaggio, and Novate Mezzola) we also observed a deviation from the power law relationship for volumes larger than a second threshold, which is approximately located between 1 and 10 m^3. We consider this evidence as a potential indicator of fragmentation occurrence, even in the Parkline case study. The scaling exponent β (Equation 1) for all the frequency size distributions obtained for each case study (Chapter 1 –Figure 6) is shown in Table 3.

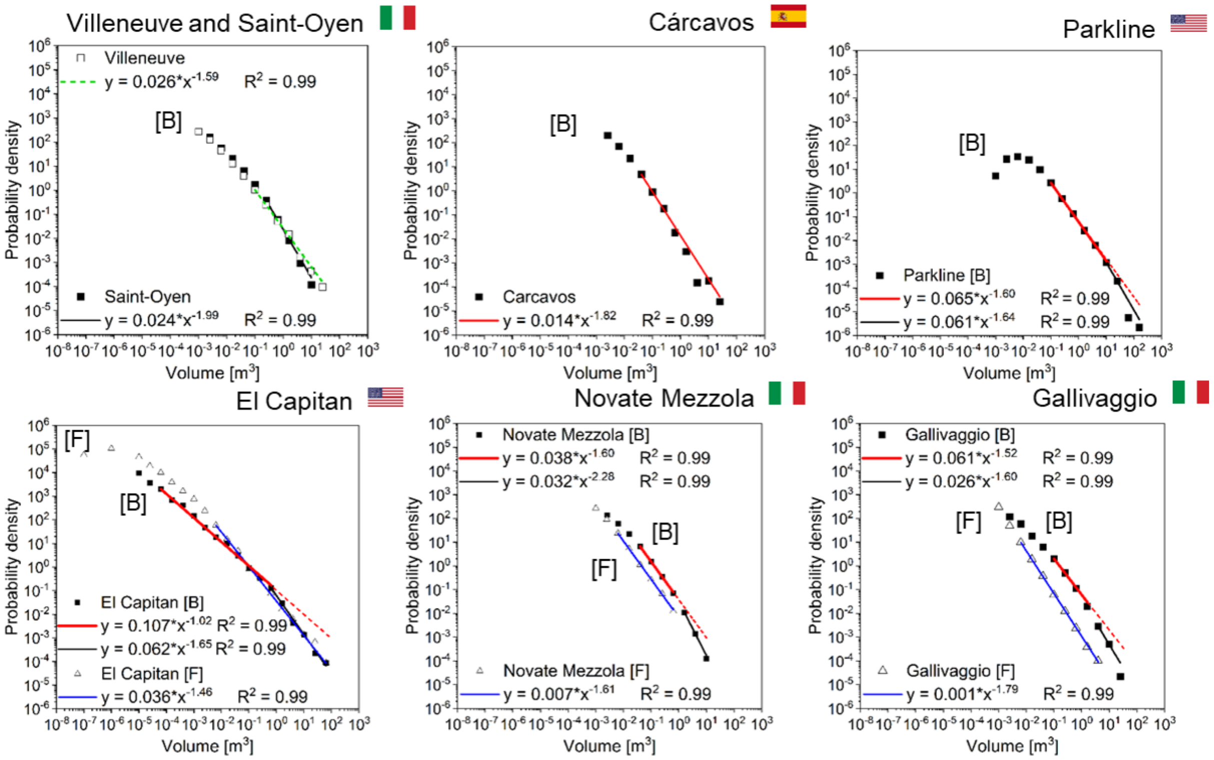

Chapter 1 - Figure 5 Size distribution of the blocks mapped within [B] and outside [F] the main deposit. For Novate Mezzola case study, the [F] series contain also the intermediate blocks. El Capitan [B] series is less numerous because of the adopted mapping techniques (grid by number). The number of mapped blocks for each case study is reported in Chapter 1 – Table 2. We grouped Villeneuve and Saint-Oyen case studies in the same panel, as they belong to the same region and they show a similar behaviour.

Chapter 1 - Table 3 Scaling factors b that characterize each curve in Chapter 1 – Figure 5, and additional data on rockfall case studies.

	1st exponent β for [B] series	2nd exponent β for [B] series	R^2 for [B] series	Exponent β for [F] series	R^2 for [F] series
Villeneuve (ITA)	**1.59**	-	0.99	-	-
Saint-Oyen (ITA)	**1.99**	-	0.99	-	-
Cárcavos (ES)	**1.82**	-	0.99	-	-
Parkline (USA)	**1.60**	**1.64**	0.99	-	-
El Capitan (USA)	**1.02**	**1.65**	0.99	**1.46**	0.99
Novate Mezzola (ITA)	**1.60**	**2.28**	0.99	**1.61**	0.99
Gallivaggio (ITA)	**1.52**	**1.60**	0.99	**1.79**	0.99

Rockfall mobility

H/L ratio

To examine the relationship between rockfall behaviour and rockfall mobility, we plot the elevation profiles of all the case studies and different shadow angles (Chapter 1 - Figure 7) along the actual path followed by the rockfalls (Chapter 1 – Figure 6). We also report the maximum distance in plan view reached by the furthest block of both the main deposit and the outer sparse deposit for El Capitan, Novate Mezzola and Gallivaggio in Table 3. For reference in the following comparison, rockfalls typically exhibit values of reach angle (arctan(H/L)) between 32° and 45° (Evans and Hungr 1993). For El Capitan, Novate Mezzola and Gallivaggio case studies, the reach angle is higher than these values when considering the main deposit (45.7°, 47.1°, and 47.2°, respectively) but it decreases by 17%, 33% and 19%, respectively, when considering the furthest fragments. If we consider the top of fragmentation ledges as the starting point to calculate the reach angle for the furthest fragments, the resulting values are much lower, i.e., 24.8°, 22.2°, and 19° respectively.

Chapter 1 – Figure 7 shows a comparison between literature H/L ratio (Scheidegger, 1973; Corominas 1996; 1998 USGS report; Copons et al., 2009; Massey et al., 2012a; Ruiz-Carulla et al., 2018) and the values of this study. We observe that the H/L values follow the same trend of literature data. However, when the main deposit only is considered, the H/L ratio of El Capitan, Novate Mezzola and Gallivaggio are higher than expected from the literature, meaning a reduced mobility.

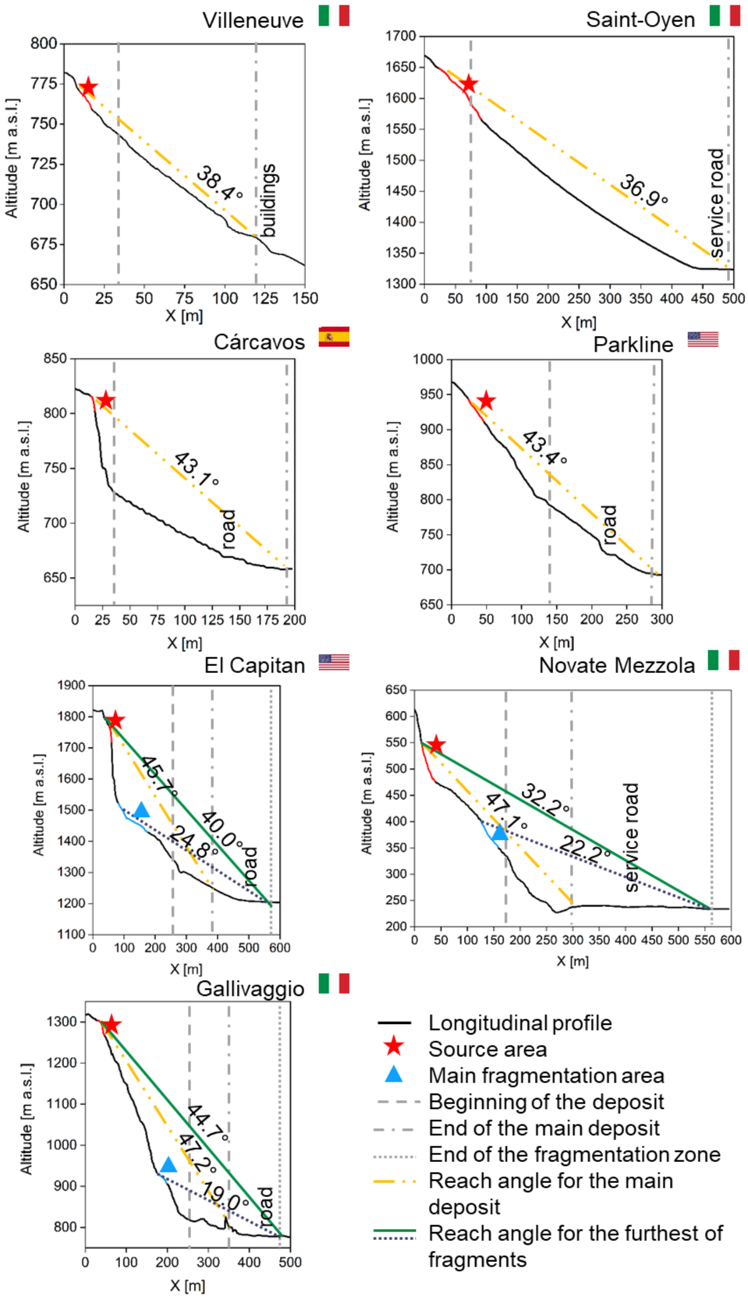

Chapter 1 - Figure 6 Slope Profiles (see Chapter 1 - Figure 4), source areas, main fragmentation areas and reach angles for each case study.

Chapter 1 - Table 4 H/L ratio and maximum distances travelled by blocks within and outside the main fragmentation zone.

	H/L for [B] series	**H/L for [B+F] series**	**Maximum distance travelled block within the main talus deposit [m]**	**Maximum distance travelled for block outside the main talus deposit [m]**
Villeneuve (ITA)	0.79	-	130	-
Saint-Oyen (ITA)	0.75	-	450	-
Cárcavos (ES)	0.93	-	170	-
Parkline (USA)	0.95	-	250	-
El Capitan (USA)	1.03	0.84	360	460
Novate Mezzola (ITA)	1.08	0.63	290	490
Gallivaggio (ITA)	1.08	0.99	300	530

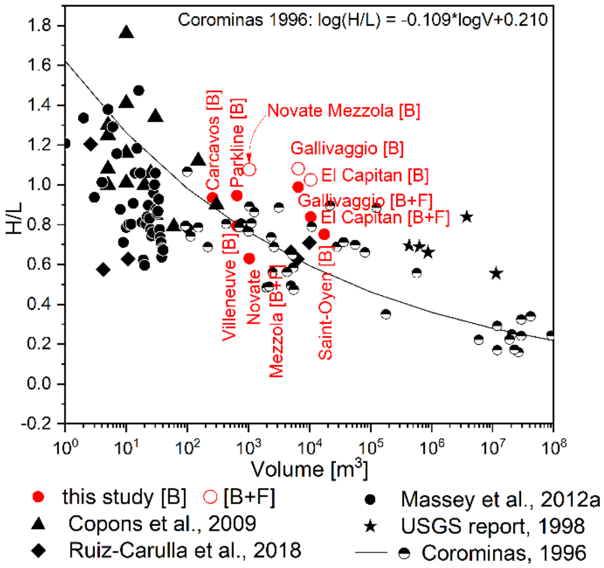

Chapter 1 - Figure 7 Comparison between literature data (black symbols) and this paper case studies (red circles). Diamonds are from Ruiz-Carulla et al. 2018, triangles from Copons et al. 2009, black circles from Massey et al., 2012a, stars from a 1998 USGS report, and half black circles from Corominas 1996. Fitting line from Corominas 1996.

Lateral dispersion

Another parameter that provides information about the mobility and the dynamics of the event is the lateral dispersion of the trajectories. The path of a downslope block can deviate from the maximum slope due to rolling in concavities and oblique surface impacts, causing a disorder effect in fall paths. This effect grows with longer fall paths as the errors from variable controlling parameters spread through numerous impacts and morphological changes encountered by the block (Crosta & Agliardi, 2004; Azzoni et al., 1995; Evans and Hungr, 1993; Jaboyedoff et al., 2005), and can also be limited but topography in many cases.

We calculated the planimetric lateral dispersion as the angle between the lines that laterally bound the source area and the deposit. These angles were positioned to encompass both the source of the collapse and the blocks on the ground in the case of the main body (series labelled [B]), while also encompassing the blocks of the more distal deposit in correspondence to the main fragmentation areas (see Chapter 1 –Figure 3) (series [F]). The results of this analysis are reported in Chapter 1 – Table 5. It can be noticed that rockfalls characterized by fragmentation have a dispersion lower than 50% for [B] series, with the exception of Parkline, while these for [F] series are much higher, showing a larger lateral spreading, probably due to topographic effects. We consider this evidence as a potential indicator of fragmentation, which may contribute to dispersion in addition to the macro- and micro-topography factors (Crosta & Agliardi, 2004).

Chapter 1 - Table 5 Planimetric lateral dispersion observed for the different case studies.

	Lateral dispersion for [B] series	**Lateral dispersion for [F] series**
Villeneuve (ITA)	49°	-
Saint-Oyen (ITA)	25°	-
Càrcavos (ES)	41°	-
Parkline (USA)	66°	-
El Capitan (USA)	35°	58°
Novate Mezzola (ITA)	37°	101°
Gallivaggio (ITA)	55°	76°

Discussion

Blocks and fragments mapping

It is rare to recognize small fragments and other blocks outside of main rockfall deposit areas because the talus below cliff walls either already include blocks from other events, or because the blocks stop in forested areas are unrecognizable. Using high quality UAV images with sufficient resolution to allow mapping at the centimetric scale, we found that at two of our case studies (Gallivaggio and Novate Mezzola), the areas external to the main deposit were nearly clear of blocks and fragments. At El Capitan, although the existing talus did not allow the same level of detail in mapping the blocks of the main deposit, we were able to mapped the fragments beyond the main deposit in extreme detail by physically mapping them on the ground one by one. These features of the deposits are therefore extremely relevant and should be taken into consideration in the context of studying the field evidence to define the dynamics of the rockfall event. The weather conditions at the time of the event are also relevant, especially in the case of deep snow at the base of the cliff, which could potentially cover the ground surface and would dampen the impact precluding the fragmentation phenomenon, and in cases control the block dynamics.

Fragmentation and block size distribution

As expected from the literature (Hantz et al., 2021), the probability density –size of blocks follows a power law distribution for volumes larger than a threshold (Chapter 1 – Figure 5). The scaling exponents are larger for the distribution of fragments ([F] series) with respect to that of blocks in the main deposit ([B] series). In certain cases, the scaling exponent β of blocks in the main deposit changes for larger volumes. This occurs especially for the Novate Mezzola and Gallivaggio rockfalls that are recognized to be subjected to a strong process of fragmentation, as witnessed by the fragments beyond the main deposit. We interpret this behavior as a direct recognizable effect of fragmentation, which reduces blocks larger than a certain size into smaller fragments. In fact, the more intense the fragmentation, the more abrupt is the change (i.e., Gallivaggio). If this interpretation is correct, the volume where the scaling exponent changes can be interpreted as the minimum volume at which volume fragmentation is effective. A small change in the exponent for larger blocks was observed also for the Parkline event, suggesting that fragmentation may have occurred also in this case study, although to a lesser extent compared to other cases. In any case, at Parkline it was impossible to clearly recognize a deposition of fragments out of the main body, because the possible fragmentation would have occurred up on the slope, and the related fragments would have been masked by the main deposit itself. Even for El Capitan, fragmentation occurred up on the slope, but the extent of this fragmentation observed during the event was huge, and clearly visible in the change of the exponent for larger blocks.

Fragmentation and block size trend with distance

As shown in Chapter 1 – Figure 4, we observe two different trends in the relationship between distance and block size for different case studies. Some events show an exponential increase in block volume with distance, indicating typical talus longitudinal sorting. However, other curves demonstrate a direct sorting pattern with increasing volume in the proximal part, followed by a decrease after a certain distance, resulting in inverse sorting. The latter behavior occurs for rockfalls that were subjected to intense dynamic fragmentation, as confirmed by eye witnesses and by the formation of dust powder clouds (De Blasio et al, 2018). Therefore, this trend inversion is interpreted as a transition between a main deposit that behaves as typical talus with longitudinal sorting, and a more distal and sparse deposit that shows an inverse sorting and derives from a process of dynamic fragmentation. Therefore, this inversion of the block size trend with distance may be used as a good indicator of fragmentation for rockfalls lacking direct observations. However, the mapping of the deposit, including blocks and fragments in the more dispersed areas, through image analysis is a time-consuming task, which is highly reliant on the availability and resolution of the images.

Fragmentation and rockfall mobility

The fragmentation process in rock avalanches is a highly debated subject in the scientific literature. Some researchers believe that fragmentation acts as an energy sink, resulting in a shorter mean travel distance (Crosta et al., 2007; Haug et al., 2016; Locat et al., 2006), whereas others argue that it can introduce new mechanical processes that increase mobility (Bowman et al., 2012; Davies et al., 1999; Davies & McSaveney, 2009; De Blasio & Crosta, 2015; Zhao et al., 2017; Jin et al, 2023). Rockfalls, however, are impulsive phenomena and cannot therefore be described with the same narrative as rock avalanches. What we have observed empirically from our case studies is that, in the presence of an inversion of trend of block and fragment size with distance within the deposit, the Fahrböschung angle (Shreve 1968) is very high for the main body, suggesting less mobility, due to energy consumption by fragmentation. This lower mobility is partially compensated by the ejection of fragments out of the main deposit, which in some cases may reach long distances, as in Novate Mezzola and El Capitan, giving the impression of a larger mobility with respect to actual one. On the other hand, the analysis of lateral dispersion of the trajectories shows a larger lateral spreading when fragmentation occurs. This is not related to an increase of mobility, but simply to the large aperture of the cone of fragmentation at impact.

Identification of fragmentation from post-event field evidences

We can summarize the results obtained from our analysis of field evidence presented herein by looking at several characteristics that may allow detection of rockfall fragmentation: i) the trend inversion of block size with distance; ii) the multi-fractal behaviour in the frequency size distribution; and iii) the lateral-dispersion increase of the trajectories. The Villeneuve, Saint-Oyen and Cárcavos case studies do not show any evidence of these features of fragmentation, confirming field observations, while El Capitan, Novate Mezzola and Gallivaggio case studies show all indicators indicators of fragmentation (Chapter 1 - Table 6). Whereas the Parkline case study shows a multi-fractal behaviour in the frequency size distribution (Chapter 1 – Figure 5), with a deviation from power law, and a larger lateral dispersion than would be otherwise expected, it completely lacks a trend inversion. We believe that these indicators are innovative in enabling post-event analysis of rockfall dynamics.

Chapter 1 - Table 6 Summary table of proposed indicators to identify the occurrence of fragmentation.

	Trend inversion of blocks size with distance	**Multi-fractal behavior in the frequency size distribution**	**Reduced mobility and increased lateral-dispersion increase of the trajectories**
Villeneuve (ITA)	N	N	N
Saint-Oyen (ITA)	N	N	N
Càrcavos (ES)	N	N	N
Parkline (USA)	N	Y	Y/N
El Capitan (USA)	Y	Y	Y
Novate Mezzola (ITA)	Y	Y	Y
Gallivaggio (ITA)	Y	Y	Y

Conclusions

Detailed characterization of rockfall deposits can significantly advance our understanding of rockfall processes. We showed that a trend inversion in the longitudinal distribution of blocks size within a rockfall deposit can reveal whether dynamic fragmentation has occurred during propagation. In particular, we propose that the transition from the typical longitudinal sorting of talus (where larger blocks travel further due to higher energy and inertia, and less impact from deposit roughness) to inverse sorting (where smaller fragments travel further) is indicative of dynamic fragmentation. This is clearly seen in plots of block volume versus longitudinal distance, where dynamic fragmentation can be recognized by a rollover of the distribution of the 99th percentiles of block volumes. An additional indicator of fragmentation identified by our study is the multi-fractal behavior in the frequency size distributions of blocks and fragments. The size distribution of the main deposit without fragmentation shows a typical behavior, with a power-law scaling for volumes larger than a threshold. However, in case of fragmentation, most of the case studies showed a second deviation from the power law for larger volumes, which we hypothesize as the effect of fragmentation of the largest blocks. Interestingly, if this interpretation is correct, this second rollover may indicate a characteristic size for which fragmentation becomes effective.

Finally, we found that fragmentation can also be distinguished by typical rockfall mobility indices such as the H/L ratio (reach angle) and lateral dispersion metrics. The reach angles of rockfalls known to have experienced fragmentation at three of our case studies (i.e., El Capitan, Novate Mezzola, and Gallivaggio) exceed typical values reported in the literature and thus suggest that reduced mobility of the main body of rockfall occurs. This is partially compensated by the ejection of few small fragments beyond the main deposit body. This suggests the energy-consuming nature of the fragmentation process. We interpret the ejection of fragments with random directions at impact to be related to an increased lateral dispersion observed for rockfalls with fragmentation. Collectively, these three field indicators of fragmentation offer tools to investigate both modern and historical rockfall events, furthering our understanding of rockfall processes and improving design of rockfall protection measures and other risk mitigation strategies.

Acknowledgments

We thank Simone De Monti and Fausto Nonini for supporting the mapping of blocks, and Davide Bertolo (Regione Valle d'Aosta, Italy), Massimo Ceriani (Regione Lombardia, Italy), Luca dei Cas (ARPA Lombardia, Italy), and Roberto Sarro (IGME, Spain) for making available post-event orthophotos.

References

Agliardi, F., & Crosta, G. B. (2003). High resolution three-dimensional numerical modelling of rockfalls. *International Journal of Rock Mechanics and Mining Sciences*, *40*(4), 455-471

Agliardi, F., Crosta, G.B., Frattini, P., 2009. Integrating rockfall risk assessment and countermeasure design by 3D modelling techniques. Nat. Hazard. Earth Syst. Sci. 9, 1059 Katlenburg-Lindau.

Azzoni, A., La Barbera, G., & Zaninetti, A. (1995, October). Analysis and prediction of rockfalls using a mathematical model. In *International journal of rock mechanics and mining sciences & geomechanics abstracts* (Vol. 32, No. 7, pp. 709-724). Pergamon.

Bowman, E. T., Take, W. A., Rait, K. L., & Hann, C. (2012). Physical models of rock avalanche spreading behaviour with dynamic fragmentation. Canadian Geotechnical Journal, 49(4), 460-476.

Brunetti, M. T., Guzzetti, F., & Rossi, M. J. N. P. I. G. (2009). Probability distributions of landslide volumes. *Nonlinear Processes in Geophysics*, *16*(2), 179-188.

Calkins FC, Huber NK, Roller JA. 1985. Geologic bedrock map of Yosemite Valley, Yosemite National Park, California, US Geological Survey, Map I-1639

Carbonneau, P. E., Bergeron, N., & Lane, S. N. (2005). Automated grain size measurements from airborne remote sensing for long profile measurements of fluvial grain sizes. Water resources research, 41(11).

Copons, R., Vilaplana, J. M., & Linares, R. (2009). Rockfall travel distance analysis by using empirical models (Solà d'Andorra la Vella, Central Pyrenees). Natural Hazards and Earth System Sciences, 9(6), 2107-2118.

Corominas J, Lantada N, Gili J, Ruiz R, Matas G, Mavrouli O, Núñez-Andrés MA, Moya J, Buill F, Abellán A, Puig-Polo C, Prades A, Martinez-Bofill J, Salo L (2017b) The RockRisk project: rockfall risk quantification and prevention. Proceedings of ROCEXS 2017, 6th Interdisciplinary Workshop on Rockfall Protection, May 2017, Barcelona (Spain). pp 39–42.

Corominas J, Mavrouli O, Ruiz-Carulla R (2017a) Rockfall occurrence and fragmentation. In: Sassa K, Mikoš M, Yin Y (Eds): Advancing Culture of Living with Landslides. World Landslide Forum, WLF 2017, Ljubljana. Springer, Cham. pp 75–97. https://doi.org/10.1007/978-3-319-59469-9_4

Corominas J, Mavrouli O, Santana D, Moya J (2012) Simplified approach for obtaining the block volume distribution of fragmental rockfalls. In: Eberhardt E, Froese C, Turner AK, Leroueil S (eds) Landslides and engineered slopes, 2, pp 1159–1164

Corominas, J. (1996). The angle of reach as a mobility index for small and large landslides. Canadian Geotechnical Journal, 33(2), 260-271.

Corominas, J., Matas, G., & Ruiz-Carulla, R. (2019). Quantitative analysis of risk from fragmental rockfalls. Landslides, 16(1), 5-21.

Crosta, G. B., Agliardi, F., Frattini, P., & Imposimato, S. (2004). A three-dimensional hybrid numerical model for rockfall simulation. In Geophys Res Abstr (Vol. 6, p. 04502).

Crosta, G. B., De Blasio, F. V., & Frattini, P. (2018). Global scale analysis of Martian landslide mobility and paleoenvironmental clues. Journal of Geophysical Research: Planets, 123(4), 872-891.

Crosta, G. B., Frattini, P., & Fusi, N. (2007). Fragmentation in the Val Pola rock avalanche, Italian alps. *Journal of Geophysical Research: Earth Surface*, *112*(F1).

Crosta, G.B.; Agliardi, F.; Frattini, P.; Lari, S. Key Issues in Rock Fall Modeling, Hazard and Risk Assessment for Rockfall Protection. In Engineering Geology for Society and Territory—Volume 2; 2015

Crosta, G. B., & Agliardi, F. (2004). Parametric evaluation of 3D dispersion of rockfall trajectories. Natural Hazards and Earth System Sciences, 4(4), 583-598.

Davies, T. R., & McSaveney, M. J. (2009). The role of rock fragmentation in the motion of large landslides. Engineering Geology, 109(1-2), 67-79.

Davies, T. R., McSaveney, M. J., & Hodgson, K. A. (1999). A fragmentation-spreading model for long-runout rock avalanches. Canadian Geotechnical Journal, 36(6), 1096-1110.

De Biagi, V., Napoli, M. L., & Barbero, M. (2017). A quantitative approach for the evaluation of rockfall risk on buildings. *Natural hazards*, *88*, 1059-1086.

De Blasio, F. V., & Crosta, G. B. (2015). Fragmentation and boosting of rock falls and rock avalanches. *Geophysical Research Letters*, *42*(20), 8463-8470.

De Blasio, F. V., Dattola, G., & Crosta, G. B. (2018). Extremely energetic rockfalls. *Journal of Geophysical Research: Earth Surface*, *123*(10), 2392-2421.

Dei Cas, L., Pastore, M. L., & Rivolta, C. (2018). Gallivaggio landslide: The geological monitoring, of a rock cliff, for early warning system. *Ital. J. Eng. Geol. Environ*, *18*, 41-55.

Dussauge, C., Grasso, J. R., & Helmstetter, A. (2003). Statistical analysis of rockfall volume distributions: Implications for rockfall dynamics. Journal of Geophysical Research: Solid Earth, 108(B6).

Dussauge-Peisser, C., Helmstetter, A., Grasso, J. R., Hantz, D., Desvarreux, P., Jeannin, M., & Giraud, A. (2002). Probabilistic approach to rock fall hazard assessment: potential of historical data analysis. *Natural hazards and earth system sciences*, *2*(1/2), 15-26.

Evans, S.G.; Hungr, O. The Assessment of Rockfall Hazard at the Base of Talus Slopes. Can. Geotech. J. 1993, 30, 620–636.

Fallot, P. (1948). *Les cordilléres betiques*. Sablons, France: Imprenta Elzeviriana.

Frattini, P., Crosta, G. B., Agliardi, F., Clague, J. J., & Stead, D. (2012). 22 Rockfall characterization and modeling. *Landslides: types, mechanisms and modeling*, 267.

Gallo, I. G., Martínez-Corbella, M., Sarro, R., Iovine, G., López-Vinielles, J., Hérnandez, M., Robustelli, G., Mateos, R. M., & García-Davalillo, J. C. (2021). An integration of UAV-based photogrammetry and 3D modelling for rockfall hazard assessment: the Cárcavos case in 2018 (Spain). *Remote Sensing*, *13*(17), 3450.

Guerin, A., Stock, G. M., Radue, M. J., Jaboyedoff, M., Collins, B. D., Matasci, B., Avdievitch, N., & Derron, M. H. (2020). Quantifying 40 years of rockfall activity in Yosemite Valley with historical Structure-from-Motion photogrammetry and terrestrial laser scanning. *Geomorphology, 356*, 107069.

Hantz, D., Corominas, J., Crosta, G. B., & Jaboyedoff, M. (2021). Definitions and concepts for quantitative rockfall hazard and risk analysis. Geosciences, 11(4), 158.

Hartmann, W. K. (1969). Terrestrial, lunar, and interplanetary rock fragmentation. Icarus, 10(2), 201-213.

Haug, Ø. T., Rosenau, M., Leever, K., & Oncken, O. (2016). On the energy budgets of fragmenting rockfalls and rockslides: Insights from experiments. Journal of Geophysical Research: Earth Surface, 121(7), 1310-1327.

Hungr, O., Evans, S. G., & Hazzard, J. (1999). Magnitude and frequency of rock falls and rock slides along the main transportation corridors of southwestern British Columbia. Canadian Geotechnical Journal, 36(2), 224-238.

Jaboyedoff, M., Dudt, J. P., & Labiouse, V. (2005). An attempt to refine rockfall hazard zoning based on the kinetic energy, frequency and fragmentation degree. Natural Hazards and Earth System Sciences, 5(5), 621-632.

Jin, K., Xing, A., Li, B., He, K., Zhuang, Y., & Chang, W. (2023). Dynamic fragmentation characteristics of columnar rockfall: insights from discrete element method. Bulletin of Engineering Geology and the Environment, 82(8), 322.

Lambert, S., & Bourrier, F. (2013). Design of rockfall protection embankments: a review. *Engineering geology, 154,* 77-88.

Lanfranconi, C., Frattini, P., Sala, G., Dattola, G., Bertolo, D., Sun, J., & Crosta, G. B. (2023). Accounting for the effect of forest and fragmentation in probabilistic rockfall hazard. *Natural Hazards and Earth System Sciences*, *23*(6), 2349-2363.

Lanfranconi, C., Sala, G., Frattini, P., Crosta, G. B., & Valagussa, A. (2020). Assessing the rockfall protection efficiency of forests at the regional scale. Landslides, 17, 2703-2721.

Lari, S., Frattini, P., & Crosta, G. B. (2014). A probabilistic approach for landslide hazard analysis. Engineering geology, 182, 3-14.

Locat, P., Couture, R., Leroueil, S., Locat, J., & Jaboyedoff, M. (2006). Fragmentation energy in rock avalanches. Canadian Geotechnical Journal, 43(8), 830-851.

Lu, P., & Latham, J. P. (1999). Developments in the assessment of in-situ block size distributions of rock masses. Rock mechanics and rock engineering, 32, 29-49.

Malamud, B. D., Turcotte, D. L., Guzzetti, F., & Reichenbach, P. (2004). Landslide inventories and their statistical properties. *Earth Surface Processes and Landforms*, *29*(6), 687-711.

Marquer, D. (1991). Structures et cinématique des déformations alpines dans le granite de Truzzo (Nappe de Tambo: Alpes centrales suisses). Eclogae Geologicae Helvetiae, 84(1), 107.

Massey, C.I., Gerstenberger, M., McVerry, G., &Litchfield, N. (2012a) Canterbury earthquakes2010/11 Port Hills slope stability: additionalassessment of the life-safety risk from rockfalls(boulder rolls)

Matas, G.; Lantada, N.; Corominas, J.; Gili, J. A.; Ruiz-Carulla, R.; Prades, A., RockGIS: a GIS-based model for the analysis of fragmentation in rockfalls. *Landslides 2017*, 14 (5), 1565-1578.

Melzner, S., Rossi, M., & Guzzetti, F. (2020). Impact of mapping strategies on rockfall frequency-size distributions. *Engineering Geology*, *272*, 105639.

Nocilla, N., Evangelista, A., & Scotto di Santolo, A. (2009). Fragmentation during rock falls: Two Italian case studies of hard and soft rocks. Rock mechanics and rock engineering, 42, 815-833.

Peck, D. 2002. Geologic map of the Yosemite quadrangle, central Sierra Nevada, California, U.S. Geological Survey Geologic Investigations Series, Map I-2751, scale 1:62,500

Putnam, R., Glazner, A. F., Coleman, D. S., Kylander-Clark, A. R., Pavelsky, T., & Abbot, M. I. (2015). Plutonism in three dimensions: Field and geochemical relations on the southeast face of El Capitan, Yosemite National Park, California. *Geosphere*, *11*(4), 1133-1157.

Ruiz-Carulla, R., Corominas, J., & Mavrouli, O. (2015). A methodology to obtain the block size distribution of fragmental rockfall deposits. Landslides, 12(4), 815-825.

Ruiz-Carulla, R., Corominas, J., & Mavrouli, O. (2018). Comparison of block size distribution in rockfalls. In Landslides and engineered slopes. Experience, theory and practice (pp. 1767-1774). CRC Press.

Sala, Z., Hutchinson, D. J., and Harrap, R. (2019). Simulation of fragmental rockfalls detected using terrestrial laser scans from rock slopes in south-central British Columbia, Canada, Nat. Hazards Earth Syst. Sci., 19, 2385–2404, https://doi.org/10.5194/nhess-19-2385-2019, 2019

Scheidegger, A. E. (1973). On the prediction of the reach and velocity of catastrophic landslides. Rock mechanics, 5(4), 231-236.

Shreve, R. L. (1968), Leakage and fluidization in air-layer lubricated avalanches, Geol. Soc. Am. Bull., 79(5), 653–658

Stock, G. M., Guerin, A., Avdievitch, N., Collins, B. D., & Jaboyedoff, M. (2018). Rapid 3-D analysis of rockfalls. GSA Today, 28(8), 28-29.

Strunden, J., Ehlers, T.A., Brehm, D., Nettesheim, M., 2015. Spatial and temporal variations in rockfall determined from TLS measurements in a deglaciated valley, Switzerland. J. Geophys. Res. Earth Surf. 120, 1251–1273. https://doi.org/10.1002/2014JF003274.

Volkwein, A., Roth, A., Gerber, W., & Vogel, A. (2009). Flexible rockfall barriers subjected to extreme loads. *Structural engineering international*, *19*(3), 327-332.

Walton, W. H. (1948). Feret‘s statistical diameter as a measure of particle size. Nature, 162(4113), 329-330

Wang, X., Frattini, P., Crosta, G. B., Zhang, L., Agliardi, F., Lari, S., & Yang, Z. (2014). Uncertainty assessment in quantitative rockfall risk assessment. Landslides, 11, 711-722.

Wang, Y., & Tonon, F. (2011). Discrete element modeling of rock fragmentation upon impact in rock fall analysis. Rock mechanics and rock engineering, 44, 23-35.

Wieczorek, G. F., Morrissey, M. M., Iovine, G., & Godt, J. (1998). Rockfall hazards in the Yosemite Valley. US Geol. Survey Open-File Report, 98(467), 8.

Woodget, A. S., & Austrums, R. (2017). Subaerial gravel size measurement using topographic data derived from a UAV-SfM approach. Earth Surface Processes and Landforms, 42(9), 1434-1443.

Zhao, T., Crosta, G. B., Utili, S., & De Blasio, F. V. (2017). Investigation of rock fragmentation during rockfalls and rock avalanches via 3-D discrete element analyses. Journal of Geophysical Research: Earth Surface, 122(3), 678-695.

Chapter 2: Numerical simulations of case studies with fragmentation

In this chapter, I explored the role of fragmentation in rockfall dynamics and hazard through detailed modeling and analysis. The chapter investigates how to model rockfall events and how fragmentation processes, including trajectory diversion, dispersion, and variations in kinetic energy, impact rockfall hazards and the importance of incorporating these processes in hazard assessments. The chapter addresses this topic from different perspectives through two already published articles that cover the following topics:

1. **Inferring the intensity of a fragmentation event from deposit analysis**: In the first paper, we modeled the 2017 Monte Pousset event. This event is particularly interesting because highly energetic events can result in explosive fragmentation and pulverization upon impact. The rockfall generated three distinct deposits with varying granulometry characteristics, depending on the degree of fragmentation severity, and allowing us to infer the intensity of the process.
2. **Rockfall events with emphasis on fragmentation and tree impact processes**: In the second paper we emphasize the impact of fragmentation and the presence of trees in rockfall dynamics and hazard assessment. We conducted rockfall simulations using the 3D simulator Hy-Stone, explicitly modeling tree presence and fragmentation through specialized algorithms. Comparing these simulations with traditional approaches that indirectly consider these factors, we found that explicitly accounting for these phenomena significantly alters hazard assessments.

Furthermore, the first paper also addresses the fact that large rock falls and cliff falls, marked by considerable fall distances and energetic impacts, trigger a series of phenomena such as dynamic fragmentation and dust cloud generation. These phenomena can significantly influence the propagation of rockfalls, subsequently impacting the associated hazard and risk. Availability of well described and constrained case studies is fundamental to start investigating this chain of events.

Research background

The rockfall motion

According to Descoudres (1997), the block motion is a composition of four elementary types of motion: the free fly, the sliding, the rolling and the impact/bouncing. Indeed, four main motion models are generally considered to characterize the fall of a block along a slope: free fall, bouncing, rolling, sliding, or a combination of the four motions. In early 60s' Ritchie (1963) proposed to relate the type of rockfall motion to the slope angle: the steepest the slope, the higher is the tendency of the block to move from a rolling motion to a bounce and then free fall motion. The freefall mode can be mostly observed on the upper part of a scarp and when the slope angle varies between 90° and 70°. For lower angle values, the block tends to bounce or move with a combination of bouncing and rolling motions. At impact, a significant amount of energy is usually lost, partially within the impacted soil/rock layer and partially as rebound energy and/or fragmentation energy for the block. If the slope gradient decreases downward to about 45°, the motion is generally transformed into a pure rolling motion. Sliding mainly occurs at the initial stages of the fall or near its stopping point, and thanks to the monitoring of it, it was possible to understand and predict the moment of detachment of the block: the analysis of monitoring data, particularly through the use of the velocity inversion method, allowed for the detection of early signs of acceleration in the boulder's movement.

The phases of rockfall events

The phases of rockfall events encompass various critical stages, starting with the pre-detachment phase where rock instability gradually builds up before the actual detachment occurs. Detecting this early phase often demands precise monitoring, which may only cover limited areas. Successful prediction relies heavily on the resolution and precision of measurement techniques, balancing the very slow initial phase with the rapid final evolution leading to collapse after minimal total displacements. Following detachment, the falling phase can be complex, especially for high cliffs or events involving large volumes of rock. In such cases, numerous blocks follow multiple trajectories, leading to extensive dispersion and impact areas. Some blocks may undergo energetic impacts, causing fragmentation and anomalous trajectories, while others may experience explosive fragmentation, resulting in fast and far-reaching fly-rocks and the generation of large, dense dust clouds that can rapidly spread and cause significant damage over vast areas. These exceptional behaviors challenge the performance of traditional rockfall simulation tools, necessitating a more integrated modeling approach. Additionally, effective countermeasure design requires accounting for these phenomena to estimate block size, velocity, energy, and trajectory reliably.

In the papers below, numerical simulations of case studies were conducted using Hy-Stone, which is capable of simulating free fly, rolling and sliding, impacts/bouncing, and fragmentation. A more detailed description of the model can be found in Chapter 2.

Impact modelling

Trajectory modelling is generally used to assess rockfall hazard and to estimate the impact energy for design of protection measures (Volkwein et al. 2011). Existing rockfall trajectory simulation models can be grouped according to the trajectory's spatial domain:

1. Two-dimensional (2D) models simulate the rockfall trajectory along a user-defined slope profile in a spatial domain defined by two axes (Azzoni et al. 1995).
2. 2.5D or quasi-3D trajectory models consider the direction of the rockfall trajectory in the x-y domain independent from the kinematics of the falling rock; in fact, the latter evolves in the vertical plane (Volkwein et al. 2011).
3. 3D trajectory models define the trajectory in a 3D plane (x, y, z). Models in this group include EBOUL-LMR (Descoeudres and Zimmermann 1987), STONE (Guzzetti et al. 2002), Rotomap (Scioldo 2006), DDA (Yang et al. 2004), STAR3-D (Dimnet 2002), Hy-Stone (Crosta et al. 2004) and Rockyfor3-D (Dorren et al. 2004), RAMMS: Rockfall (Christen et al. 2007), etc. The major advantage of 3D models is that they consider the slope topography and therefore they allow for more realistic trajectories within the 3D space. Nevertheless, 3D models require spatially explicit parameter maps which may involve significant time-consuming activity in the field.

A main aspect of rockfall trajectory modelling resides in the modelling of the rebound of the block upon impact with the slope, which can be very challenging. Two approach are commonly considered for this purpose: i) the lumped mass approach and ii) the rigid body approach (Giani 1992; Hungr and Evans 1988). Lumped mass methods consider the interaction of the point (in which the mass of the block is concentrated) with the slope without accounting for the shape of the blocks (Guzzetti et al. 2002; Hoek 1987; Hungr and Evans 1988; Piteau and Clayton 1977; Ritchie 1963). Instead, the rigid body methods use the fundamental equations of dynamics, including the rotation, to model the motion of the block along the slope (Azzoni et al. 1995; Cundall 1971; Descoeudres and Zimmermann 1987; Falcetta 1985). Other numerical tools are based on an hybrid approach that considers a lumped mass approach in the free fall trajectory phase and accounts for geometrical and mechanical characteristic of the block and the slope at impact (Bozzolo and Pamini 1986; Crosta et al. 2004; Dorren et al. 2004; Jones et al. 2000; Kobayashi et al. 1990; Pfeiffer and Bowen 1989; Rochet 1987).

Most of the existing rockfall trajectory models use coefficients of restitution (normal and tangential) to account for the rebound at impact with the slope surface and a friction coefficient to model the rolling motion. The rolling of a boulder along a slope can be represented by a sequence of short bounces and low flying parabolas. Rolling motion is usually well defined for spherical, cylindrical or discoid blocks for which the velocity of the boulder is low, and the boulders are moving on a medium to low terrain gradient with limited surface roughness. However, a pure rolling motion of a rock can be considered an abstraction as natural blocks do not have typical geometric shapes and the impacted surface is never completely flat (Azzoni et al. 1995; Bozzolo and Pamini 1986; Dorren 2003; Giacomini et al. 2010; Guzzetti et al. 2002). Sliding is mostly limited to the initial stage of a rockfall and the motion is characterised by low velocity and high loss of energy due to the frictional interaction with the slope surface. For large boulders, sliding may also occur at impact, with significant loss of energy.

It depends on the type of code used, but often, in rockfall modeling, it is necessary to include the ground-measured block size distribution that form the deposit as input, more than the distribution of blocks in situ (at the source).

Hy-Stone

For modelling the case studies proposed in this chapter, we used Hy-Stone (Crosta et al. 2004), which is a 3D rockfall simulator designed to analyze the dynamics of rockfall propagation. It employs multiple modeling techniques to simulate the motion of falling blocks and their interactions with the terrain. One of the key features of Hy-Stone is its ability to account for the stochastic nature of rockfall processes, incorporating variations in slope morphology, roughness, and other parameters using probability density distributions.

The simulator utilizes a triangulated vector topography derived from Digital Terrain Models (DTMs) to create a realistic representation of the terrain. It is capable of simulating blocks of various shapes, including spheres, cylinders, ellipsoids, and discs, providing flexibility in modeling different types of rock masses.

Reference systems

Hy-Stone employs for computational purposes four reference systems: geographical, absolute, relative, and mechanical. The geographical system is the DTM reference system included raster files, while the absolute system is located at the bottom left of the analyzed region. The local system, centered at the point where impact occurs whose z-axis is perpendicular to the local plane, is used to analyze impact processes when the lumped mass approach is concerned. Finally, the mechanical system computes the block's final velocity after impact in case of hybrid approach since the x-axis is orient along the velocity vector at impact.

Transitioning between these reference systems involves translation and rotation transformations carried out by means of homogeneous coordinates approach. The final transformation between two reference systems is the combination of multiple rotations and translations.

Since the modelling of the impact process is described by means of normal and tangential velocity component to the local plane, the absolute system is not suitable for the impact processes and for this reason a local system is introduced. This local reference system aligns with the local plane derived from the DTM raster model.

Motion for Lumped mass approach

The lumped mass approach primarily considers the block as a material point where its mass is concentrated. During the free-fly motion phase, the block is subject solely to gravitational forces since the air resistance is completely neglected, resulting in a ballistic trajectory that ends upon impact with the ground. Calculating the contact time, which marks the end of the ballistic trajectory, is essential. Knowing the contact time allows for determining the block's position and velocity at impact, needed for analyzing the impact process. In this approach, the block is treated as a mathematical point, eliminating the need to account for block dimensions in the equations.

After the impact process, the block velocity after the impact is computed if the distance between two subsequent impact is greater than a fixed threshold. If this condition is not met, the block begins sliding. In this state, both gravity and frictional forces act on the block, with the mathematical equations formulated in the local reference system, considering only horizontal components. The friction coefficient depends on the local topography and it is derived from a specific raster file.

The aim of the impact models for lumped mass approach is the determination of the translation velocity of the block after the impact once the impact velocity before of impact is known. These models rely on restitution coefficients, representing the ratio of post-impact to pre-impact velocity components.

Motion for Hybrid approach

In the hybrid approach, Hy-Stone considers the geometry of the block during free-fly motion, accounting for both the motion of the block's center of mass and its rotation. During free-fly motion, the block experiences only the force of gravity, resulting in a ballistic trajectory while its rotational velocity is constant. Unlike the lumped mass approach, determining the contact time in the hybrid approach is block-specific, and a specific equation is formulated for each block shape.

In the context of the hybrid approach, mathematical equations used in the model to describe the impact are referenced to the mechanical system, simplifying the problem since in this reference system two velocity vector components are non-zero, and the variation of angular velocity vector is perpendicular to the motion plane. This simplification allows for straightforward equations in this reference system. Although in reality, normal and tangential kinematics are interrelated due to block geometry, Hy-Stone simplifies the computation of the impact velocity by treating them as uncoupled. The variation in the normal velocity component is computed using the same formulas as in the lumped mass approach. However, a specific procedure is outlined for the tangential and rotational components, considering the block's geometry and that at the impact an instant rotation without sliding occurred at the impact point.

Impact modelling

Hy-Stone employs four impact modeling approaches to calculate the behavior of blocks upon impact with the ground or other surfaces. The possible models are:

1. **Constant Restitution Approach:** This model assumes constant restitution coefficients to determine the bouncing velocity components of blocks after impact. These coefficients of restitution are given from the raster files.
2. **Restitution Coefficient Dependent on Impacting Velocity**: Here, the raster restitution coefficients are adjusted according to the velocity at impact, accounting for variations in impact energy,
3. **Restitution Coefficient Dependent on Block Mass**: In this model, the raster restitution coefficients are modified according to the mass of the falling block, providing a more comprehensive impact assessment,
4. **Elasto-Visco-Plastic Rheological Model**: In this model the restitution coefficients are not considered since the impact process is the results of the integration of a rheological model describing the mechanical behavior of the impacted material (Dattola et al. 2021).

Hy-Stone's impact modeling enables a thorough assessment of block interactions with the terrain, structures, and other objects. Furthermore, it has the capability to simulate impacts with trees and the fragmentation process through two dedicated modules, which are elaborated upon in Chapter 2.

The code has the possibility to simulate the fragmentation processes. The onset of fragmentation is determined by an energy criteria (Yashima et al., 1987), and the code computes the size and velocity of resulting fragments, taking into account factors such as Young's modulus, Poisson's coefficient, stress limits, and representative volumes. To simulate fragmentation, the code requires the distribution of both blocks and fragments (Rock Block Size Distributions).

Tree impact sub-model

Within Hy-Stone's tree-impact sub-model, the simulation considers the intricate dynamics of a block encountering a forested environment. Each tree in the forest is characterized by specific attributes like stem height, total tree height, stem diameter, and crown diameter. When a block enters this forested zone, the model evaluates the probability of impact based on factors such as tree density, size, and the block's own properties. The impact can occur either on the tree's stem or within its crown, depending on the block's height above the ground. The stochastic nature of tree-block interactions is integral to this model, as it employs random factors to determine the likelihood and outcomes of impacts. Once an impact is identified, the model proceeds to calculate how the block's velocity and direction change. Two main scenarios are considered: if the block's kinetic energy is lower than a certain threshold associated with the tree's energy absorption capacity, it comes to a stop. Conversely, if the block's kinetic energy exceeds this threshold, it breaks the tree and continues on a new trajectory with reduced velocity and direction. The specific changes in direction depend on the incidence angle of impact, which is determined by a set of probabilistic parameters. Moreover, this sub-model also incorporates considerations for the spatial distribution of trees, their varying energy-absorbing capabilities, and the dynamic effects of tree impacts. The energy lost by impact on tree stems is greatest for central impacts and decreases away from the stem axis, following a Gaussian distribution. The angular deflection of the block on impact varies according to the type of impact, if central, lateral, or scour, each having distinct probabilities and consequences on the block's motion. Additionally, the model factors in block height relative to tree height and employs statistical variables to determine the direction of post-impact motion. More details regarding the algorithm can be found in Frattini et al. (2012) and Lanfranconi et al., (2020).

Fragmentation sub-model

When rocks or blocks impact the ground or other solid surfaces, they may break into smaller fragments, each moving independently. Hy-Stone's fragmentation sub-model simulates the process of fragmentation during rockfalls. This phenomenon significantly impacts the overall simulation, as the trajectories of these fragments differ from that of the original block. Fragmentation in Hy-Stone occurs when the kinetic energy of a block upon impact exceeds a specific threshold. This threshold is calculated using a mathematical theory based on a Weibull distribution, and the formula for the limit kinetic energy considers various material properties, such as Young's modulus, Poisson's coefficient, stress limits, and a representative volume. Subsequently, it calculates the distribution of fragment sizes, which is necessary for understanding how the generated fragments vary in size. Once information about the fragment sizes is available, Hy-Stone computes their velocities. At the time when the work on the articles in this chapter was conducted, the algorithm operated by evenly distributing kinetic energy among the fragments. Consequently, smaller fragments were ejected away with high velocity, which was an unrealistic behavior. However, a more flexible equation was then introduced, allowing users to adjust the distribution of kinetic energy by means of a model parameter which control the percentage of distribution according to the fragment mass. This new equation include the uniform distribution as in the original approach or proportionally to the fragment mass. Importantly, Hy-Stone applies the energy conservation principle to ensure that the sum of fragment kinetic energies does is equal to the initial block's kinetic energy reduced by the fragmentation energy. After fragments are generated, the code computes their trajectories using the same principles applied to the parent block, with defined initial positions and velocities. It is import to note that the code does not consider multiple fragmentation i.e. the fragments cannot be fragmented during their motion.

The Extremely Energetic Rockfalls

Rockfalls are a frequent occurrence on mountain slopes, with falling blocks often leaping or rolling atop talus or colluvial deposits where they lose significant energy. As a result, their kinetic energy upon impact is typically much less than the total potential energy available from the point of instability, with the exception of some interactions along and at the toe of steep cliffs. However, there are exceptional situations where unstable blocks suspended on the flanks of very steep mountain peaks may descend along extreme heights following free fall trajectories. These situations are typically observed in valleys carved by glaciers or high mountain peaks where permafrost thawing is more effective, leading to detachment of large unstable volumes (Rabatel et al., 2008; Noetzli et al., 2007). These conditions are quite common in alpine landscapes, with frequent and sequential collapses recorded in the last century (Luethi et al., 2015). Upon impact with the terrain, an enormous amount of energy on the order of 10 MJ per cubic meter of rock may be instantaneously dissipated, resulting in devastating effects. In De Blasio et al.'s (2018) work, a new terminology was proposed to define this type of phenomena: Extremely Energetic Rockfall (EER). EER events are characterized by the following sequence: detachment, free fall, impact, fragmentation, pulverization, and air blast. Afterward, on a longer time scale (minutes to hours), a dense dust cloud is formed, which travels along the valley, finally depositing as a thick dust layer. For an event to fall under the EER category, a rockfall mass carrying a total kinetic energy of at least 80 GJ is required, which is the energy released by a boulder of density 2,500 kg/m^3 and volume 10,000 m^3 falling from a height of 300 m (De Blasio et al., 2018). The paper reported below deals with an EER case study, the 2017 M.te Pousset rockfall event.

The importance of RBSD analysis and fragmentation energy calculation

By comparing the different distributions obtained from the in-situ blocks before detachment and the blocks present in the deposit generated by the event (respectively named IBSD and RBSD in Lu & Latham, 1999), it is possible to assess the degree of rock fragmentation and the effectiveness of rockfall protection measures that have been implemented or planned. As previously emphasized in Chapter 1, characterizing the RBSD is crucial for hazard and risk analysis because it affects detachment frequency and kinetic energy (Hungr et al., 1999; Lari et al., 2014; Wang et al., 2014).

The RBSD obtained by analyzing the deposit at the foot of the slope is the result of two main processes: disaggregation and fragmentation. Disaggregation occurs when the rock mass breaks away from the wall or due to a low energy impact on the ground, resulting in block fragments that are bounded by pre-existing joints and a RBSD that is similar to the initial in-situ block size distribution (IBSD) (Ruiz-Carulla et al., 2017). On the other hand, if the impact energy is high enough to fragment the blocks, the generated RBSD will differ from the initial IBSD, and this process is referred to as fragmentation. For rockfall simulation, it is common to calibrate the restitution parameters on the volume and location of some large unbreakable blocks during propagation (Gischig et al., 2015). However, fragmentation often occurs both during the impact and the propagation, and the blocks observed in the deposit are fragments from larger blocks that broke due to impacts (Ruiz-Carulla, 2018). The high energy content of the rockfall caused dynamic fragmentation, and the most severe fragmentation often leads to the formation of a rock dust that rises to form a cloud suspended in the air. The amount of energy used for block fragmentation and dust generation is an extremely interesting but still poorly investigated topic in the literature. In recent works (De Blasio et al., 2018; Crosta et al., 2022; Sun et al., 2023), a model for estimating the fragmentation energy of a rockfall has been proposed. This model is based on the analysis of the size distribution of the final clasts. The authors note that the fragmentation energy is only a significant fraction of the total potential energy of the rockfall when a sufficient amount of rock volume is reduced to small clasts that are as small as dust particles. This is because the fragmentation energy is proportional to the newly generated clast area. As a result, only the smallest particles contribute significantly to the fragmentation energy. The calculation suggested by De Blasio et al. (2018) involves fitting the measured granulometric curve with a theoretical curve, which has been used in the following work by Crosta et al. (2023). Indeed, fragmentation energy is a non-negligible fraction of the total potential energy of the rock fall when a sufficient amount of rock volume is reduced to small clasts the size of dust. There are different several rock fragmentation laws used in geology, geotechnical engineering, and related fields. Some of the most common ones are:

- The Bond's law is an empirical formula used to estimate the energy consumption in comminution apparatuses such as industrial mills and crushers. The law is based on the assumption that the energy required for size reduction of a material is proportional to the new surface area produced. The law states that the work required to break a unit volume of a material into a specified size reduction ratio is proportional to the reduction ratio. The Bond's law is widely used in the mining and mineral processing industries to design and optimize grinding circuits, as it provides a simple and reliable method for estimating the energy consumption of comminution equipment.
- Von Rittinger's law is an empirical equation used to describe the energy required for size reduction of a material, typically in the context of comminution processes such as grinding, crushing, and milling. The law states that the energy required for size reduction is directly proportional to the new surface area

produced. In other words, the energy required to break a given mass of material into smaller particles is proportional to the surface area of those particles. This law assumes that the particles are broken into fragments of equal size, and it is typically used for fine grinding or pulverization of materials. However, it may not be suitable for larger particle sizes or more complex particle size distributions.

- Kick's Law is an empirical relationship that states that the energy required for size reduction of a material is proportional to the ratio of the logarithm of the particle size before and after the size reduction process: the energy required for size reduction increases as the particle size decreases, and it is proportional to the total length of fractures generated during the fragmentation process. This law is often used to describe the behavior of brittle materials such as rocks.
- Griffith's law is based on fracture mechanics and states that the energy required to fracture a material depends on its mechanical properties and the length of the fractures generated during the fragmentation process. It states that the fracture toughness of a material is related to its surface energy and to the length of the fractures that propagate through it. This law is particularly useful in understanding the behavior of brittle materials, such as rocks, under different loading conditions.
- Hertz-Mindlin's law is based on the theory of elasticity and describes the distribution of forces between two bodies in contact, as occurs during the fragmentation process. Specifically, the law states that the contact force between two elastic spheres is proportional to their deformation and the elastic modulus of the material. The law is used to model the behavior of rocks during fragmentation processes and to predict the amount of energy required to fragment a material under certain loading and geometry conditions.

These laws are used to model the behavior of rocks during fracturing and fragmentation processes and to predict the energy required to fragment a material under certain load and geometry conditions. In the work presented below, the von Rittinger's law was initially used to calculate the fragmentation energy, but then the grain size distribution was introduced to improve the accuracy of the calculation. The authors obtained the grain size distribution from seven samples collected just after the event and analyzed through a laser granulometer.

The generation and propagation of dust

Research on dust generation and propagation, especially during rockfalls, rock avalanches, and Extremely Energetic Rockfalls (EER, De Blasio et al., 2018), has been limited, with relatively little emphasis on the formation and flow of dust clouds in these extreme events. Additionally, dust clouds deposited in the surrounding areas are frequently overlooked in the comprehensive deposition analysis. These processes involve various factors, including impact energy, rock composition, and explosive fragmentation potential, leading to the creation of dust particles. The high-energy fragmentation of rock into microns to millimeter-sized clasts can rapidly create a dust cloud, often initially in a state of high velocity, which generates a shock wave and perturbation of the air (Wieczorek et al., 2000, 2002). Millimeter-sized clasts propelled at such speeds can strip bark from vegetation and cause local structural damage (De Blasio et al., 2018). The dust cloud accelerates as it moves along the valley flank due to gravitational forces, and these particles can become suspended in the atmosphere, forming dense dust clouds that spread rapidly. Understanding and monitoring dust dynamics are crucial due to their implications for health and the environment. This research has involved analyzing dust samples and estimating dust thickness and distribution through post-event photography. Additionally, recent advancements have focused on modeling the fragmentation energy of rockfalls based on clast size distribution, revealing the significance of impact energy and clast size in dust generation.

Cloud modeling has also played a crucial role in characterizing grain size distribution and dust volume. This modeling has offered insights into grain size uniformity and its variations with distance from the source. Furthermore, estimating cloud density and assessing its impact on obstacles and propagation dynamics have contributed to a more comprehensive understanding of dust generation and propagation. Regarding the generation and propagation of dust, during rockfall and fragment impacts, dust particles are created. The quantity and size of these particles depend on factors such as impact energy, rock composition, and the occurrence of explosive fragmentation events. These dust particles can become suspended in the air and propagate through atmospheric conditions, potentially forming dense dust clouds that spread rapidly in the surrounding area. Analyzing and monitoring dust particles is crucial for assessing associated health and environmental risks. It plays a pivotal role in designing mitigation strategies, including area closures, evacuations, structural protection, and early warning systems to safeguard local populations and assets from the risks posed by rockfall-generated dust.

Quantification of cloud dimensions and thickness was conducted both in the subsequent paper. An initial simplified model was employed and will be described upon later.

The first paper reported in this chapter delves with an Extremely Energetic Rockfall event. The rockfall of Monte Pousset described below generated three distinct deposits that were differentiated based on observed differences in granulometry. Depending on the degree of fragmentation severity, deposit features ranged from small fragments covered in dust and exhibiting tree abrasion to larger fragments that were not coated in dust. Indeed, the research questions underlying the paper reported below were: *What are the factors that determine the severity of fragmentation in rockfalls and how can we determine the energy required for this process?*

I am an author in this work by Crosta et al. (2023), published in Landslides journal, for which I dealt with the analysis of the deposits, the modeling of the rockfall event, the analysis of trajectories and fragmentation points, and collaborated to the energy calculation.

https://doi.org/10.1007/s10346-023-02115-6

Background Bibliography

Azzoni, A., La Barbera, G., & Zaninetti, A. (1995, October). Analysis and prediction of rockfalls using a mathematical model. In International journal of rock mechanics and mining sciences & geomechanics abstracts (Vol. 32, No. 7, pp. 709-724). Pergamon.

Bowman, E. T., Take, W. A., Rait, K. L., & Hann, C. (2012). Physical models of rock avalanche spreading behaviour with dynamic fragmentation. Canadian Geotechnical Journal, 49(4), 460-476.

Bozzolo, D., & Pamini, R. (1986). Simulation of rock falls down a valley side. Acta Mechanica, 63(1-4), 113-130.

Christen, M., P. Bartelt and U. Gruber, 2007. Modelling Avalanches. GEOconnexion International 6, 4: 38-39.

Crosta, G. B., Agliardi, F., Frattini, P., & Imposimato, S. (2004). A three-dimensional hybrid numerical model for rockfall simulation. In Geophys Res Abstr (Vol. 6, p. 04502).

Crosta, G. B., Dattola, G., Lanfranconi, C., De Blasio, F. V., Malusà, M., & Bertolo, D. (2023). Rockfalls, fragmentation, and dust clouds: analysis of the 2017 Pousset event (Northern Italy). Landslides, 1-18.

Cundall, P. A. (1971). A computer model for simulating progressive, large-scale movement in blocky rock system. In Proceedings of the international symposium on rock mechanics (Vol. 8, pp. 129-136).

Dattola, G., Crosta, G. B., & di Prisco, C. (2021). Investigating the influence of block rotation and shape on the impact process. International Journal of Rock Mechanics and Mining Sciences, 147, 104867.

De Blasio, F. V., & Crosta, G. B. (2015). Fragmentation and boosting of rock falls and rock avalanches. Geophysical Research Letters, 42(20), 8463-8470.

De Blasio, F. V., Dattola, G., & Crosta, G. B. (2018). Extremely energetic rockfalls. Journal of Geophysical Research: Earth Surface, 123(10), 2392-2421, https://doi.org/10.1029/2017JF004327

Descoeudres, F., & Zimmermann, T. H. (1987, August). Three-dimensional dynamic calculation of rockfalls. In ISRM Congress (pp. ISRM-6CONGRESS). ISRM.

Descoeudres, F.: Aspects geomecaniques des instabilites de falaises rocheuses et des chutes de blocs, Publications de la societe Suisse de mecanique des sols et des roches, 135, 3–11, 1997.

Dimnet, E., Fremond, M., Gormaz, R., San Martin, J.: Collisions of rigid bodies, deformable bodies and fluids. In: Bathe, K. (ed.) Proceedings of 2nd MIT Conference on Computational Fluid and Solid Mechanics, Vols. 1 and 2, Amsterdam, 17–20 June, pp. 1317–1321. Elsevier/MIT Press, Cambridge (2003)

Dorren, L. K. (2003). A review of rockfall mechanics and modelling approaches. Progress in Physical Geography, 27(1), 69-87.

Dorren, L. K. A., Maier, B., Putters, U. S., and Seijmonsbergen, A. C.: Combining field and modelling techniques to assess rockfall dynamics on a protection forest hillslope in the European Alps, Geomorphology, 57, 151–167, 2004

Falcetta, J. L. (1985). Un nouveau modèle de calcul de trajectoires de blocs rocheux. Revue Française de Géotechnique, (30), 11-17.

Frattini, P., Crosta, G. B., Agliardi, F., Clague, J. J., & Stead, D. (2012). 22 Rockfall characterization and modeling. Landslides: types, mechanisms and modeling, 267.

Giacomini, A., Spadari, M., Buzzi, O., Fityus, S. G., & Giani, G. P. (2010, June). Rockfall motion characteristics on natural slopes of eastern Australia. In ISRM EUROCK (pp. ISRM-EUROCK). ISRM.

Giani, G. P. (1992). Rock slope stability analysis. CRC Press.

Gischig, V. S., Hungr, O., Mitchell, A., & Bourrier, F. (2015). Pierre3D: a 3D stochastic rockfall simulator based on random ground roughness and hyperbolic restitution factors. Canadian Geotechnical Journal, 52(9), 1360-1373.

Guzzetti, F., Crosta, G., Detti, R., & Agliardi, F. (2002). STONE: a computer program for the three-dimensional simulation of rock-falls. Computers & Geosciences, 28(9), 1079-1093.

Hoek E (1987) RockFall—a program for the analysis of rockfall from slopes. Dept. Civil Engineering, Univ. Toronto, Ontario

Hungr, O., Evans, S. G., & Hazzard, J. (1999). Magnitude and frequency of rock falls and rock slides along the main transportation corridors of southwestern British Columbia. Canadian Geotechnical Journal, 36(2), 224-238.

Hungr, O., Evans, S. G., Bovis, M., & Hutchinson, J. N. (2001). Review of the classification of landslides of the flow type: Environmental and Engineering Geoscience, v. VIIp.

Kobayashi, N., Cox, D.T., and Wurjanto, A (1990). "Irregular wave reflection and runup on rough impermeable slopes," J. Wtrway. Port, Coast., and Oc. Engrg., ASCE, 116(6), 708-726.

Lanfranconi, C., Sala, G., Frattini, P., Crosta, G. B., & Valagussa, A. (2020). Assessing the rockfall protection efficiency of forests at the regional scale. Landslides, 17, 2703-2721.

Lari, S., Frattini, P., & Crosta, G. B. (2014). A probabilistic approach for landslide hazard analysis. Engineering geology, 182, 3-14.

Lu, P., & Latham, J. P. (1999). Developments in the assessment of in-situ block size distributions of rock masses. Rock mechanics and rock engineering, 32, 29-49.

Noetzli, J., Gruber, S., Kohl, T., Salzmann, N., & Haeberli, W. (2007). Three-dimensional distribution and evolution of permafrost temperatures in idealized high-mountain topography. Journal of Geophysical Research: Earth Surface, 112(F2).

PFEIFFER, T. J., & BOWEN, T. D. (1989). Computer simulation of rockfalls. Bulletin of the association of Engineering Geologists, 26(1), 135-146.

Piteau, D., & Clayton, R. (1977). Discussion of paper Computerized design of rock slopes using interactive graphics for the input and output of geometrical databy Cundall, P. In Proceedings of the 16th Symposium on Rock Mechanics, Minneapolis, USA (pp. 62-63).

Rabatel, A., Deline, P., Jaillet, S., & Ravanel, L. (2008). Rock falls in high-alpine rock walls quantified by terrestrial lidar measurements: A case study in the Mont Blanc area. Geophysical Research Letters, 35(10).

Ritchie, A. M. (1963). Evaluation of rockfall and its control. Highway research record, (17).

Rochet, L. (1987, August). Development of numerical models for the analysis of propagation of rock-falls. In ISRM Congress (pp. ISRM-6CONGRESS). ISRM.

Ruiz-Carulla, R., Corominas, J., & Mavrouli, O. (2017). A fractal fragmentation model for rockfalls. Landslides, 14(3), 875-889.

Ruiz-Carulla, R., Corominas, J., & Mavrouli, O. (2018). Comparison of block size distribution in rockfalls. In Landslides and engineered slopes. Experience, theory and practice (pp. 1767-1774). CRC Press.

Scioldo G (2006) User guide ISOMAP & ROTOMAP—3D surface modelling and rockfall analysis. Geo&Soft International, Torino

Sun, J., Frattini, P., Wang, X., De Blasio, F. V., Lanfranconi, C., Jiao, Q., ... & Crosta, G. B. (2023). Deposit comminution in a weak variably-cemented breccia rock avalanche. Engineering Geology, 107331.

Volkwein, A., Schellenberg, K., Labiouse, V., Agliardi, F., Berger, F., Bourrier, F., ... & Jaboyedoff, M. (2011). Rockfall characterisation and structural protection–a review. Natural Hazards and Earth System Sciences, 11(9), 2617-2651.

Wang, X., Frattini, P., Crosta, G. B., Zhang, L., Agliardi, F., Lari, S., & Yang, Z. (2014). Uncertainty assessment in quantitative rockfall risk assessment. Landslides, 11, 711-722.

Wieczorek, G. F., Snyder, J. B., Waitt, R. B., Morrissey, M. M., Uhrhammer, R. A., Harp, E. L., ... & Finewood, L. G. (2000). Unusual July 10, 1996, rock fall at Happy Isles, Yosemite National Park, California. Geological Society of America Bulletin, 112(1), 75-85.

Wieczorek, G. F. (2002). Catastrophic rockfalls and rockslides in the Sierra Nevada, USA.

Yang, T. H., Tham, L. G., Tang, C. A., Liang, Z. Z., & Tsui, Y. (2004). Influence of heterogeneity of mechanical properties on hydraulic fracturing in permeable rocks. Rock mechanics and rock engineering, 37, 251-275.

Yashima, S., Kanda, Y., & Sano, S. (1987). Relationships between particle size and fracture energy or impact velocity required to fracture as estimated from single particle crushing. Powder technology, 51(3), 277-282.

Rockfalls, fragmentation and dust clouds: analysis of the 2017 Pousset event (Northern Italy)

Giovanni B. Crosta[1], Giuseppe Dattola[1], Camilla Lanfranconi[1], Fabio V. De Blasio[1], Marco Malusà[1], Davide Bertolo[2]

[1]Department of Earth and Environmental Sciences, Università degli Studi di Milano Bicocca, Italy

[2]Dipartimento programmazione, risorse idriche e territorio, Regione Valle d’Aosta, Italy

Abstract

The process and dynamics of rock fragmentation during the collapse of rock falls and rock avalanches is a poorly developed topic. The most severe fragmentation often leads to the formation of a rock dust that rises to form a cloud suspended in the air. The understanding of fragmentation processes is hampered by the environmental disturbances that alter the dust cloud deposit shortly after deposition. Here, we study the fragmentation of the October 2017 Pousset rockfall, detached from a NNE facing steep bedrock wall in the permafrost zone, that involved 8,300 m^3 of metamorphic rock and fell about 800 m. The collapse generated large boulders which rolled downslope and a thick and large dust cloud. The source and deposit were investigated, and dust cloud material was sampled at different locations to reconstruct an exponential thickness distribution and perform grain size characterization. The fragmentation energy was estimated by integrating the spectrum of the grains assuming that the fragmentation energy is proportional to the generated area. The fragmentation energy was found to be about 0.4% of the initial potential energy. Most probable fragmentation points and block deposition areas were evaluated and positioned by means of the Hy-Stone 3D rockfall simulator. Furthermore, we calculated the flow rate of the suspended powder generated by the fragmentation process and compared the results with observations available for the evolution of the phenomenon and the collected samples. The Pousset event, in its relatively simple dynamics, may be a good testing ground to address the current theories of rockfall and rock avalanche fragmentation and dust cloud behavior.

Introduction

Rock falls in high mountain environments have been reported more frequently and with more details in the last decades (Gruber et al., 2004; Gruber and Haeberli, 2007; Ravanel et al., 2017). Permafrost thaw in steep bedrock walls is considered the main cause of periglacial rock wall failures. Ice-filled joints are common under bedrock permafrost conditions and continuous ice-coated failure surfaces are frequently observed at source areas just after rock fall release (Geertsema et al., 2006; Ravanel et al., 2017; Walter et al., 2020). Ice-filled joints can be extended and opened because of ice-segregation and wedging, but also by percolating water during thawing. It has been shown in the literature that rock falls of very different volumes can be associated to such processes and this requires action of different triggering factors or of the same factor acting over different time scales. Because of the high relief of these steep rock walls, rock falls and avalanches can undergo very high drops and consequently propagate over long distances.

Although rockfalls and rock avalanches are common occurrences in the mountainous environment, they still hold many enigmatic aspects, especially regarding the dynamics and energetics of the fragmentation processes from the large portions of initially intact rock to finely comminuted clasts of wide size spectrum. Some rockfalls consist of single isolated blocks travelling downslope and colliding through successive bounces with the terrain and rolling. In this case, the frequent collisions dissipate much energy, and the block will only be partially fragmented or undergo continuous chipping. It is not unusual to observe meter or even decameter-size blocks to roll for several tens of meters, practically intact. In contrast with these rockfalls, when the terrain is very steep, a block may accelerate in the gravity field in ballistic flight or free fall for a great height, H, without continuous interaction with the ground. It will so accumulate an energy $E_0 = \rho g\, H\, V$ where ρ is the rock density and V its volume, which is released in one or few catastrophic impacts, and severe fragmentation will occur at each impact. The most extreme cases have been recently analysed under the name of Extremely Energetic Rockfalls (EER, De Blasio et al., 2018). These EERs are events in which the following two criteria are both met: high specific energy released at once (or equivalently great unimpeded fall height) and high total energy (or equivalently large mass). Thus, an EER is a falling boulder travelling mostly along ballistic trajectories along which it acquires kinetic energy without, or with little, interaction with the terrain. According to the definition proposed by De Blasio et al. (2018), EER events have sufficiently high total energy (of the order of some tens of GJ) to generate large mobile dust clouds and fragments capable to impact large areas. Altogether, 23 major documented events have been reported by De Blasio et al. (2018) worldwide even though such phenomena are believed to be much more frequent. Furthermore, there is evidence that permafrost can influence the stability of rock and debris masses in high mountain areas and consequently the progressive effects of climate change at high elevations and the consequent increase in temperature leads to destabilization of steep rock slopes triggering rockfalls, slides and avalanches (Ravanel et al., 2010, 2017; Phillips et al., 2017).

The dust cloud formation mechanisms in EERs is different from the process observed in rock avalanches, where the interaction with the terrain is more or less continuous for a long-distance. Rock avalanches fragment both at their basal layers especially via crushing along dynamical force chains, and in the interior due to surface chipping of fragments off the surface of the colliding clasts. Many observers have reported the onset of a dust cloud created by high-energy fragmentation of rock down to microns to millimetre size clasts in both EER and rock avalanches. In the most extreme cases, the dust cloud can initially be produced in a state of high velocity and create a shock wave perceived as a strong perturbation of the air (Wieczorek et al., 2000, 2002). Millimeter-sized clasts fired at such a high rate can exfoliate and debark vegetation and produce other local and structural damages (De Blasio et al., 2018). After this initial phase, the resulting dust cloud often travels as an accelerated suspension from the gravitational field along the valley flank. So far, little research has concentrated on the creation and further flow of dust clouds. Furthermore, the dust clouds deposited in the areas surrounding the event are often overlooked in the global deposition of the event.

In this work we analyze the collapse of the Cima Pousset in the north-western Italian Alps (Val D’Aosta) in October 2017. The 8,300 m^3 rock fall detached at about 3,000 m a.s.l. well within the permanent permafrost conditions (Chapter 2a – Figure 1) according to the Alpine Permafrost Index Map (Boeckli et al., 2012). It was not particularly large but yet quite energetic in terms of fall height. The runout of the main blocks reached a distance between 500 and 800 m. The initial collapse phase created numerous blocks each some cubic metres in volume, which rolled along the local slope maintaining high kinetic energy. At the end of their trajectory, blocks hit the eastern flank of the peak, disintegrating at once at the base of the cliff, producing a large dust cloud that coated the area from the slope to the main valley bottom and the opposite valley side. Hence, the identification of the events unfolding during the Pousset landslide permits a direct and controlled examination of many of the still enigmatic aspects of rock avalanche and rockfall dynamics. In the following, we describe first the geology and meteo-climatic characteristics of the area, and the dynamics and the main deposit characteristics of the 2017 event. Then, we present our modeling study of the detailed rockfall trajectories after the initial collapse. Finally, we suggest a physical explanation for the dust cloud generated by these collisions in terms of grain size distribution, energy of fragmentation, propagation and dust settling.

The 2017 Pousset rock fall

In contrast to most rock fall and avalanche occurrences, which are usually examined after weathering has altered the site condition and posing a minimal attention for the dust cloud deposit, a visit to the Pousset site was planned immediately after the event. This allowed us to sample the rock dust deposit from different points considered less exposed to risk, before rain and wind could disperse and alter the deposits. In fact, no major meteorological event occurred between the collapse and our first field trip to the location. As above mentioned, De Blasio et al. (2018) defined Extremely Energetic Rockfalls (EER) those rockfalls of large total energy falling from extreme heights, and little interaction with the terrain. The definitory values of the fall height and involved energy are somehow arbitrary, and have been set at 300 m and about 80 GJ, respectively. The Pousset event had a height the full drop height of about 800 metres (considering for the complete fragmentation of the initial rockfall volume) and energy of ca. 170 GJ, but the interaction with the terrain was continuous, thus falling outside our earlier definition of a EER.

Geological setting

The study area (Chapter 2a – Figure 1) is located in the Pennidic domain of the Italian Western Alps at the boundary between the so-called Eocene Eclogite Belt and the lower-grade Paleogene Frontal Wedge of the orogen (Malusà et al., 2015). The rockfall source area consists of serpentinites and metabasites of the Grivola-Urtier metaophiolitic Unit (Polino et al., 2015), which is part of the Eocene Eclogite Belt. These rocks underwent subduction to eclogite facies condition during the Cenozoic and were rapidly exhumed to the Earth’s surface by the end of the Eocene, now forming a tectonic envelope on top of the eclogitic gneissic dome of the Gran Paradiso Massif. In the Cogne Valley, the Grivola-Urtier metaophiolites are juxtaposed against metamorphic rocks of the Frontal wedge by the Belleface-Trajo Fault, a steeply dipping ENE-WSW post-metamorphic fault that includes slivers of marbles, calcschists and carbonate tectonic breccias (Malusà et al., 2005). This fault runs along the steep Trajo valley, representing the rockfall accumulation zone. On the north-western side of the fault are exposed Late Devonian meta-granodiorites (Bergomi et al., 2017) and associated country rocks of the Gran Nomenon Unit (Polino et al. 2015). These country rocks, which are part of the Frontal Wedge of the orogen, chiefly consist of albite-chlorite gneisses and experienced pre-Alpine metamorphism under epidote-amphibolite facies conditions followed by a greenschist facies Alpine overprint (Malusà et al., 2005). Serpentinites and metabasites of the rockfall source area show on average a main foliation dipping towards the NNE. This main foliation is cut by steep NE-dipping fault planes belonging to the Cogne Fault zone, a deformation zone including opposite-dipping fault segments that exert a strong morphological control on the landscape as confirmed by the NW-SE trend of the Cogne Valley and Upper Aosta Valley. Based on available low temperature thermochronology data, the Cogne fault was likely active during the mid Miocene (Malusà et al., 2009). This tectonic arrangement controls the sliding mechanisms in the sub-vertical dip-slope source area.

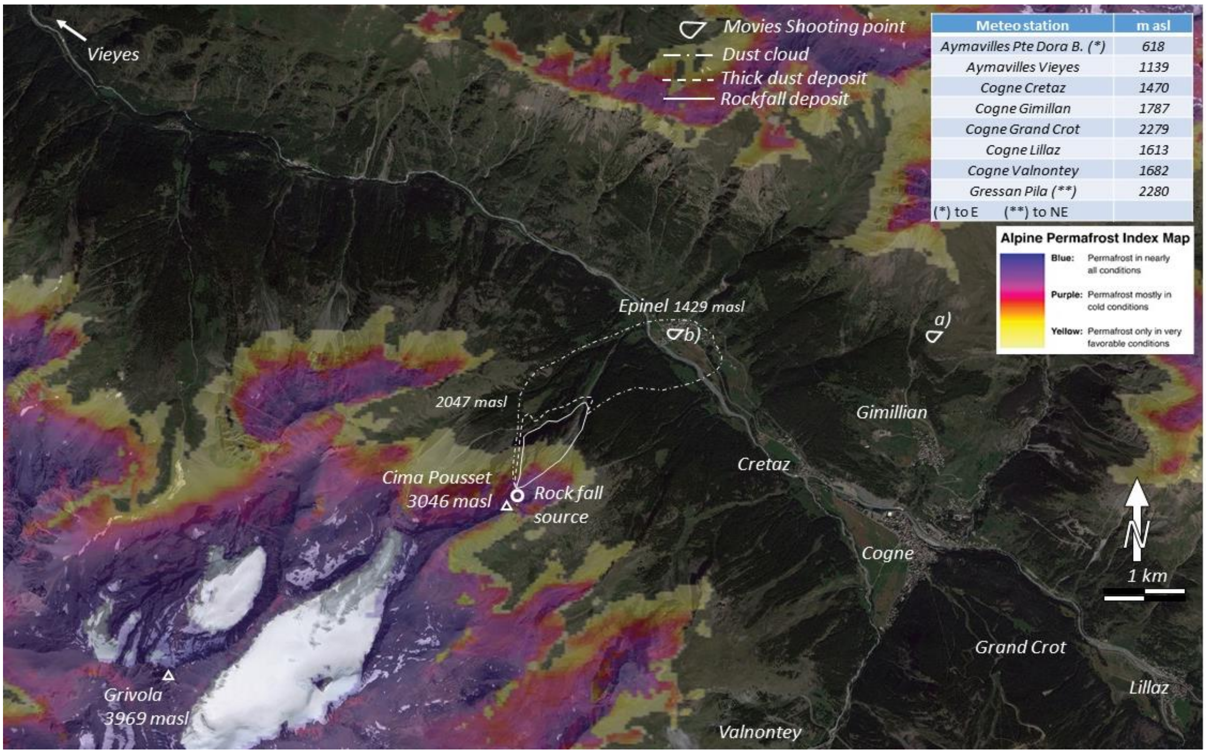

Meteo station	m asl
Aymavilles Pte Dora B. (*)	618
Aymavilles Vieyes	1139
Cogne Cretaz	1470
Cogne Gimillan	1787
Cogne Grand Crot	2279
Cogne Lillaz	1613
Cogne Valnontey	1682
Gressan Pila (**)	2280
(*) to E (**) to NE	

Chapter 2a - Figure 1 Location map of the area affected by the 2017 Pousset rock fall with position of the meteo-station and the deposits of the rockfall boulders and of the rock dusts. In colors are reported permafrost conditions according to the Alpine Permafrost Index Maps (Boeckli et al., 2012).

The 2017 event

The main event occurred on October 31 2017 at 12:17, and it was followed by a minor event at 12:43. Due to the time of the day and to the visibility from the valley bottom, it was recorded both on video and photo allowing for some detailed observations of the occurrence and of the associated effects. The Pousset (3046 m asl) is a sharp peak at the extremity of a thin NE trending ridge. The detachment occurred along a steeper part of the foliation about 80 metres below the Pousset peak (Chapter 2a – Figure 2a) along the NNE slope. Just after the event, a helicopter overflight allowed us to spot the presence of a centimetre to decimetre thick ice layer still attached along differently oriented sectors of the failure surface. The main fracture sets (K1, K2 and K3, see Chapter 2a – Figure 2a) clearly define the geometry of the volume which detached from the cliff. The fracture sets isolated the roughly pyramidal failed block with a base and height estimated at about 500 m^2 and 50 m, respectively. The finding of ice on part of the detachment surface, delimited by the three sets, points to the hypothesis of water freezing and ice thawing along well-developed rock discontinuities as one of the triggering mechanisms. The surface of the ice layer, still pasted to the scar surface, was characterized by a series of wrinkles parallel to the discontinuity direction (see Chapter 2a – Figure 2c). Ice evidence was mainly visible in the upper part of the failure surface where the block was just a few meters thick. These observations support the idea that weakening by permafrost thawing and ice melting could occur prevalently at the base of the failing block, along the contact between block and ice, by heat conduction and secondarily by advection. In general, it is expected that the maximum active layer thickness is reached late in the year (October to December, Gruber and Haeberli, 2007) and the Pousset event seems to support this critical condition. In the case of the Pousset peak, the underground temperature distribution and regime are the result of the three dimensional effects controlled by the narrow NE trending ridge, the consequent difference in spatial temperature distribution at the surface (SE, NW and NE facing slopes (see Chapter 2a – Figure 2), the seasonal transience of surface temperature, and also the thermo-physical anisotropy strongly controlled by the persistent foliation.

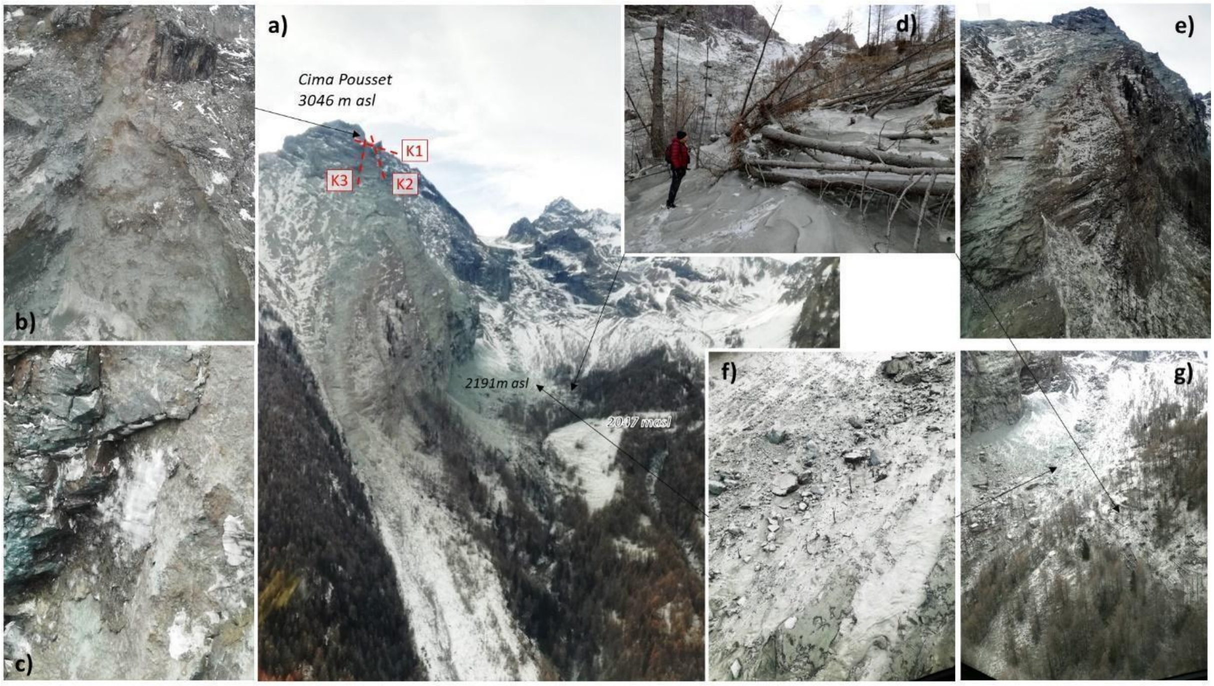

Chapter 2a - Figure 2 Pousset peak a) view with source area, the three main fracture sets controlling the detachment scar, the transit and the deposits. Three areas with different block depositional characteristics are shown (D1, D2 and D3); b) source area of the 8,300 m^3 rockfall; c) ice layer along the upper sector of the detachment plane; d) tree cluster uprooted and covered by a thick dust layer; e) upward view of the slope; f) and g) tree stumps and uprooted trees in the area of thick dust cloud and blocks propagation.

Following the initial detachment, a small dust cloud developed from the source area and along the steep cliff (see Chapter 2a –Figure 2a) but it never developed noticeably with time whereas a much larger and rapidly moving cloud was generated when a large part of the falling blocks reached the base of the cliff. This main cloud infilled the tributary valley (Trajo valley; Chapter 2a – Figure 3a and b), increasing in thickness and with its front moving against the opposite valley flank and then rapidly descending towards the main valley. In about 2 minutes after its formation the main dust cloud reached the valley bottom climbing about 100 m on the opposite valley side and enlarging along the valley bottom (see the approximate cloud limits in Chapter 2a – Figure 1). At this time the Epinel village and the main valley road were obscured hampering visibility. Then the cloud slowly evolved and stratified in air lasting for a total of circa 30 minutes. Assuming a total maximum fall height of 800m (impact velocity 125 ms^{-1}) and an initial volume of 8,300 m^3 of rock (density 2700 kg/m^3) the specific energy per unit mass results 7848 J/ kg^{-1} and a total energy 170 GJ.

Chapter 2a - Figure 3 Propagation of the dust cloud from two videos recorded during the event (photo by I. Busto, see acknowledgements for the web link). The two shooting points are shown in Chapter 2a - Figure 1 a) from above Gimillan, b) from the Epinel village. Time is from the initial time (t_0) chosen for sequence. Sequence a) show that the dust cloud in the source area and along the rocky cliff remains limited in extent during the entire falling time while it grows considerably along the gentler slope of tributary valley starting from a thickness of 50 to 100 m (t_0 to t 140 s in the video-sequence a). The cloud front at t_0 in b) reached about 300 m in thickness growing to about 500 m at t_2 = 85 s.

The trajectories of the falling blocks concentrated in the N and NE directions, the first one following a steeper path ending with a 250 m high vertical jump just before reaching the talus deposits, and the second one following a long slope controlled by the foliation planes. As a consequence, two main deposition zones were recognized (D1 and D2 in Chapter 2a – Figure 5).

The temperature records for eight stations distributed around the rockfall area were examined to look for long term and short term changes. In the 2010-2022 period, a mean increase in temperature was recorded ranging between 0.04°C/year and 0.17°C/year with a slight positive relationship with elevation (see Chapter 2a – Figure 4a). The year 2017 was not anomalous with respect to the others in the time series (Chapter 2a – Figure 4*a* and *b*). The mean daily temperature in the week before the event decreased by 1.2-1.6°C/day from about 8-12°C to 1-4°C (Chapter 2a – Figure 4c) whereas no rainfall occurred close to the event (Chapter 2a – Figure 4d). Following Paranunzio et al. (2016), we analysed temperature data collected from weather stations in the proximity of the event. The analysis of the temperatures at the stations in Vieyes and Gimillian (Chapter 2a – Figure 1) showed that the week before the rockfall was characterised by higher temperatures than those recorded in the 2010-2018 period. Analysing the 30 day interval preceding the rockfall, it was found that at the Vieyes, Gimillian and Grand Crot stations a positive anomaly was recorded. In fact, the thirty days preceding the rock fall were characterized by higher temperatures than those recorded in the 2010-2018 period. These results could indicate a relationship with the triggering of the event, but further investigation required to support this thesis is beyond the aims of this study.

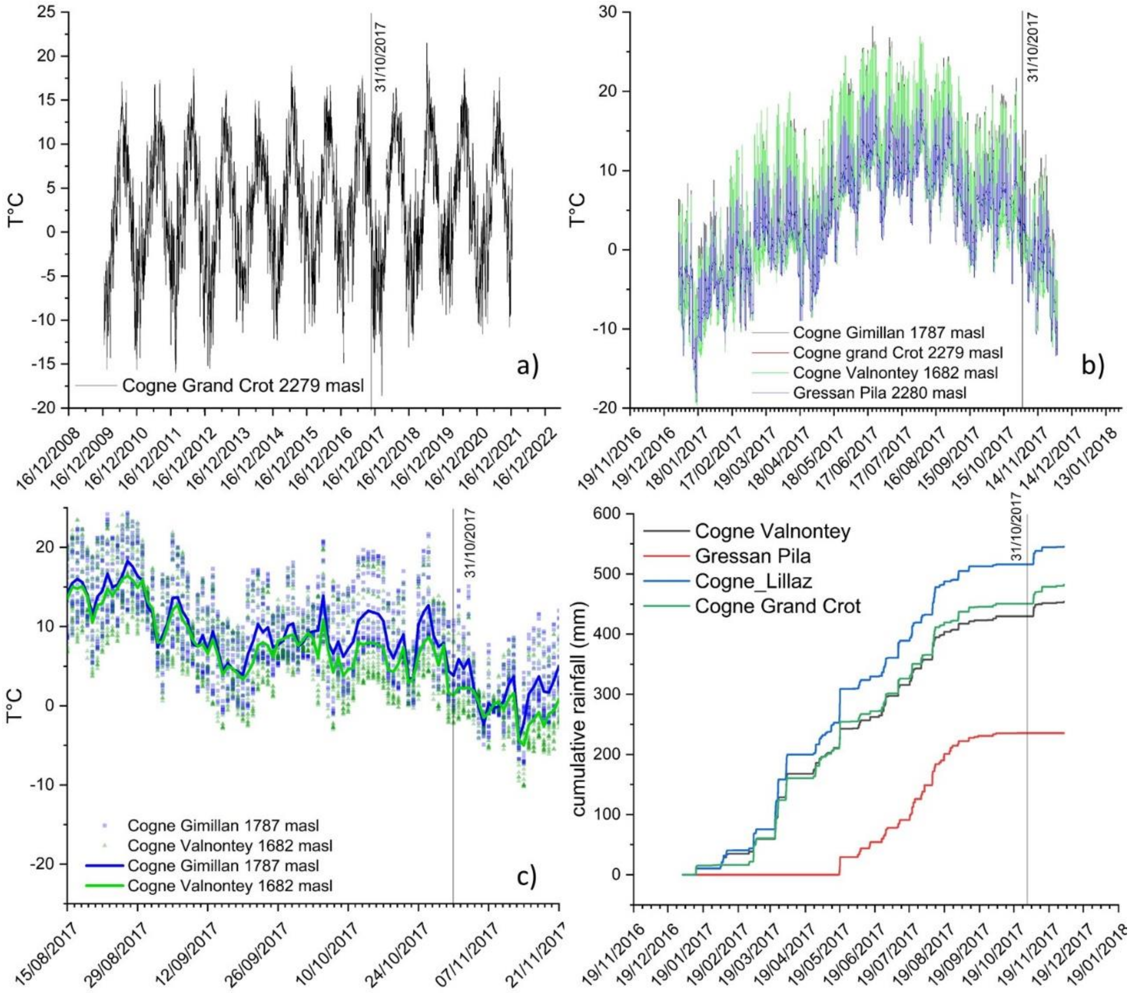

Chapter 2a - Figure 4 Temperature time series for some of the meteo-stations located close to the Pousset area (see Figure 1): a) 2010-2022 mean daily temperature time series for the Cogne Grand Crot showing a 0.17 °C/year increase; b) 2017 hourly temperature time series for four meteo stations; c) hourly and mean daily temperature time series for the period of the rockfall events. A decreasing temperature (ca 1.2-1.6°C/day) was observed in the week before the event. e) 2017 cumulative rainfall.

Dust sampling and analysis

Aspect of rock dust deposit in the field

During the Pousset rockfall a part of the rock volume was converted into a cloud of dust that settled close to the area of collapse and progressively along the path while traveling down to the main valley. The dust deposit thickness was measured and material was sampled, at different points around the collapse and main impact area (see Chapter 2a – Figure 5) and in the main valley in November 2017.

Figure 5 shows the appearance of dust deposited on trees and rockfall boulders. The rock dust was still found perfectly in place and we were able to measure the thicknesses in different places and collect samples of the material from the ground, trees and mountain hut structures. Note: i) the conspicuous thickness of the deposit up to a few centimeters, decreasing with the distance from the center of the impact area (Chapter 2a – Figure 5a) down to a thin film in the main valley and at the Epinel village (Chapter 2a – Figure 5); ii) a shielding effect, i.e., the deposit is thicker on the upwind side of obstacles , which is particularly evident along the circumference of the tree trunks; iii) the breaking of branches and trunks; iv) the deposition both on horizontal and inclined surfaces (as tree trunks), indicating that deposition was not ruled only by gravitational settling, but also by the thrust by the dust cloud.

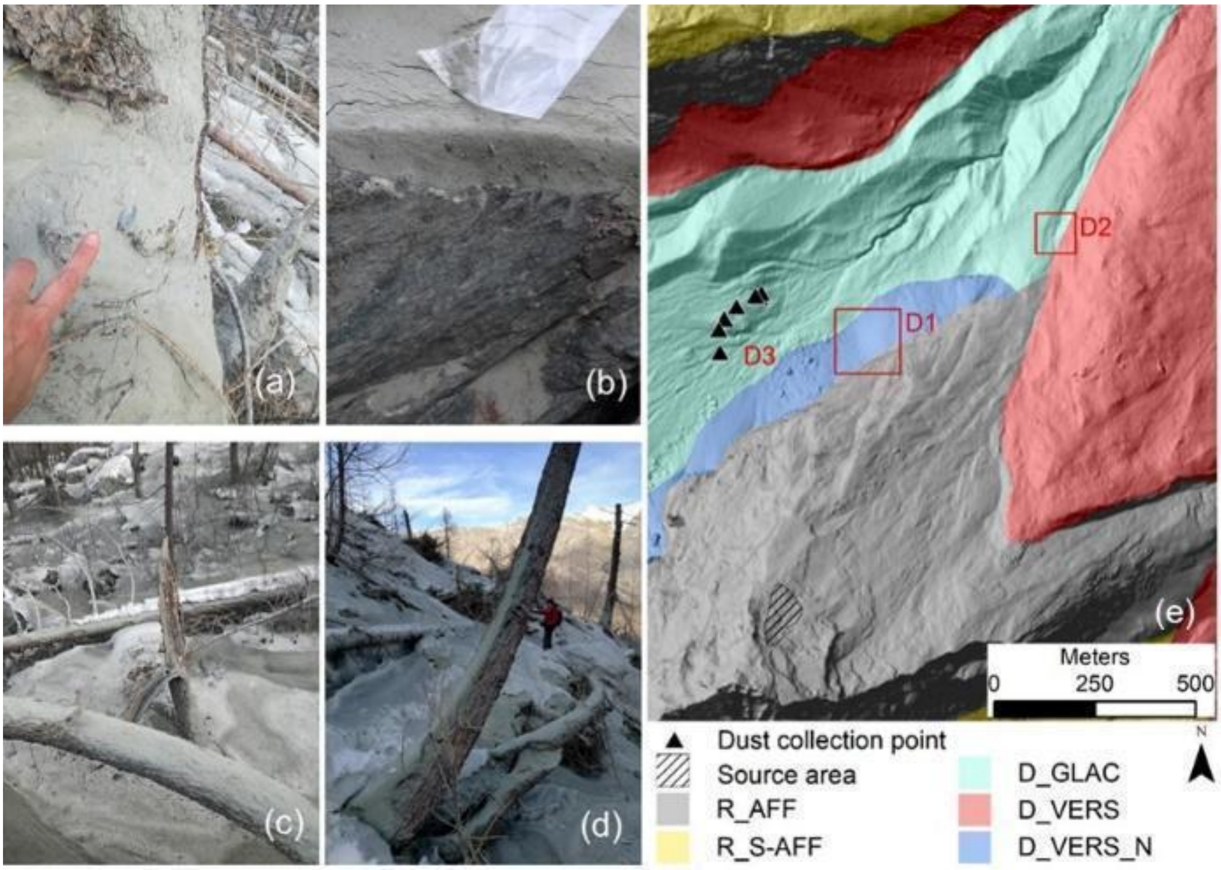

Chapter 2a - Figure 5 High density rock dust deposits on trees and large blocks at 2140-2150 m asl, a): on the upwind side of a debarked tree trunk with some centimetre sized elements immersed in a fine matrix; b) on uprooted and snapped trees laying down in the direction of the cloud motion; c) 3-4 cm thick and uniform dust layer on a rock block; d) accumulation of the rock dust along the slope and trees in a position at about 2100 m asl; e) map of the ground surface characteristics with the rockfall source area and the three main deposition zones (D1, D2 and D3) for the blocky material. Sampling points for the rock dust are also reported.

The rock dust was sampled and its thickness measured at seven different locations (Chapter 2a – Figure 5). Furthermore, in the other three locations we measured without sampling the dust thickness. Samples were collected from both loose (e.g below trees or on mountain huts) and hardened (e.g. in the upper areas on trees and blocks) deposits and sealed in plastic bags for further examination in the laboratory.

Chapter 2a – Figure 6 shows the changing of the measured deposit thickness with distance from the main impact area and the experimental granulometric curves obtained from the previous considered samples compared with other granulometric curves obtained in analog cases.

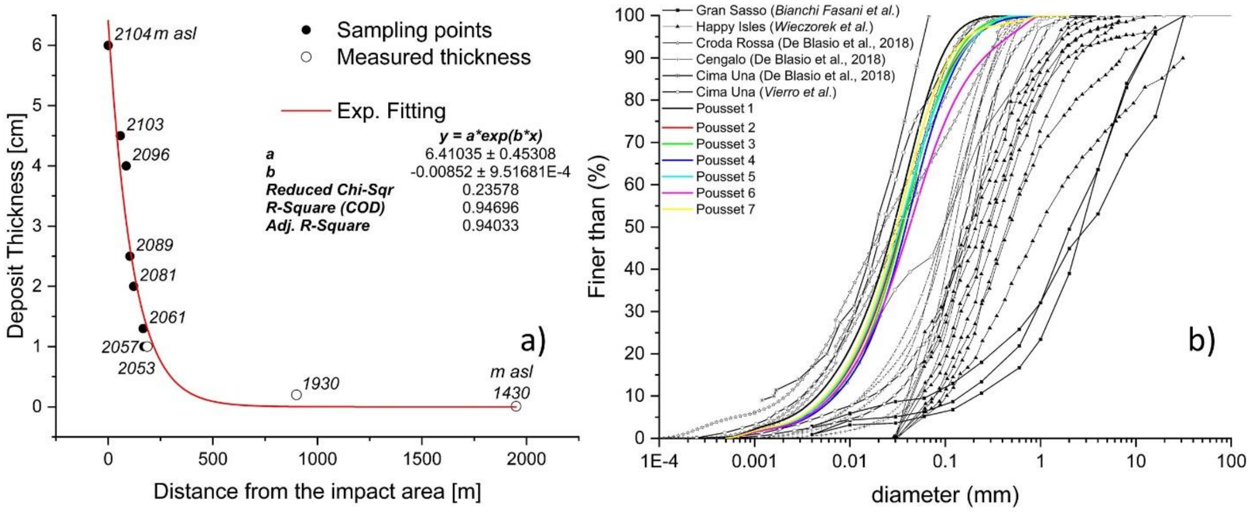

Chapter 2a - Figure 6 Characteristics of the dust layer at the Pousset site: a) thickness versus distance from the main impact area measured on sub-horizontal surfaces; the sampling points are shown in Fig. 5 except for the ones at distance 900 m and 2,000 m, which are located further north-east. Furthermore, altitude of each sampling point is indicated; b) grain size distribution of the seven samples collected between 2040 m asl and 2150 m a.s.l compared with those from other sites where EER events were observed and dust samples collected.

Estimate of the rock dust volume from field measurement of deposit thickness

The amount of rock dust in the deposit was estimated as follows. The thickness T of the dust deposit is integrated as a function of the distance r from the main impact point

$$V_{dust} \approx \int_0^{\infty} 2\pi r\, T(r) dr \tag{1}$$

Assuming an exponential decrease $T(r) \approx T_0 exp\,(-\eta\, r)$ where η is the inverse of the decay length, in accordance with the trend shown in Chapter 2a – Figure 6a, it follows that

$$V_{dust} \approx \frac{2\pi T_0}{\eta^2} \tag{2}$$

Chapter 2a – Figure 6a shows the exponential decay in dust thickness with the following fitting parameters: $T_0 \approx 6.41035\, cm$ and $\eta = \ 0.0852\, m^{-1}$. Applying equation (2), the dust volume is $V_{dust} \approx 55.49\, m^3$
This corresponds to an intact rock volume of about $44.4\, m^3$ computed by assuming a dust layer void ratio $e \ = \ 0.2$ by the equation $V_{rock} \approx (1-e)V_{dust}$. Hence, the dust cloud included only a rock volume equal to about 0.6% of the initial rockfall volume.

Grain size curves

The seven dust samples were analyzed via a Malvern Instruments Mastesizer 2000 particle size analyzer (laser granulometer capable of measuring materials in the range 0.02µm to 2000µm, based on Mie scattering principle) equipped with a Hydro 2000Mu large volume manual wet sample dispersion unit. Chapter 2a – Figure 6b shows the granulometric curves that are very similar to each other with a maximum difference between samples 1 and 7 represented by a shift in the grain size mode from 0.025 mm to 0.035 mm. The raw data tell us that 50% of the rock dust particles were finer than 0.025 mm, or 25 microns, and there was still an abundance of dust of size less than 10 microns. This indicates a very severe comminution, which is in line with other events recorded in the Alps (De Blasio et al., 2018). The data for Happy Isle Yosemite and the Gran Sasso (central Italy) rockfalls (Wieczorek et al., 2000; Bianchi Fasani et al., 2013; Viero et al., 2013) shown in Chapter 2a – Figure 6b indicate coarser grains suggesting a less intense fragmentation or local effects (e.g. rock texture, lithology, fall trajectory).

Rockfall simulation

The dynamics of the falling blocks was investigated by means of the HyStone rockfall simulator. HyStone is a 3D rockfall simulator code reproducing the block motion from the dynamics equations (Crosta et al. 2004; Frattini et al. 2012) and considering the topography of the region under study using the Digital Terrain Model (DTM). HyStone solves the equations of motion for a boulder travelling on the three-dimensional terrain by four basic processes: ballistic flight, bouncing along the flanks, sliding, and rolling. In the present case, the topography was described by means of a 0.5 m x 0.5 m DEM. Because of uncertainties regarding the initial block conditions and failure sequence, we ran the program for a different set of conditions including different initial velocities and positions.

In this section, we begin describing the HyStone rockfall simulation code. The aim of these simulations is the reproduction of the block trajectory and the computation of the impact points where a strong energy dissipation and block fragmentation is observed. In the successive section, the dust cloud motion is analyzed.

HyStone code

Two types of analysis are possible with the HyStone code: lumped mass approach in which the block geometry is completely neglected by modeling the block as a material point, and the hybrid description where the block geometry is taken into account. The detailed model equations solved by HyStone are reported in the supplementary materials. When the blocks impact on the soil the code computes the bouncing velocity starting from the impacting velocity and the chosen impact model. Four different types of impact models are implemented: (a) constant restitution approach, (b) restitution coefficient modified by impacting velocity, (c) restitution coefficient modified by the block mass and, finally, (d) the elasto-visco-plastic rheological model. In the supplementary materials a description of these equations is carried out. In the following HyStone analysis, for the sake of simplicity we use the first model. To reproduce the uncertainties due to the natural variabilities, HyStone allows stochastic numerical analysis to be performed via a series of parameters PDFs (Frattini et al. 2012). The code is able to reproduce the fragmentation splitting up a block in fragments moving, after their separation, independently from each other. The fragmentation onset occurs when the energy criterion proposed by Yashima et al. (1987) is satisfied, i.e. the block fragments when its kinetic energy at impact overcomes the fragmentation energy E_{fr} estimated by using the Weibull parameter m_w as follows

$$E_{fr} = 0.15\, B_f\, C_f \left(\frac{1-\nu^2}{E}\right)^{\frac{2}{3}} (2R_{bl})^{\frac{3m_w-5}{m_w}} \left[\sigma_0 V_0^{\frac{1}{m_w}}\right]^{\frac{5}{3}} \tag{3}$$

where E and ν are the Young's modulus and the Poisson's coefficient, respectively, σ_0 is the stress limit, V_0 is a representative volume. Finally, coefficients A_f, B_f and C_f are computed by means of the following expressions

$$A_f = \begin{cases} 0 & if\ m_w = 1 \\ \frac{5(m_w-1)}{3m_w} & otherwise \end{cases} \tag{4}$$

$$B_f = \begin{cases} 1.0 & if\ m_w = 1 \\ \pi^{A_f} & otherwise \end{cases} \tag{5}$$

$$C_f = 6^{\frac{5}{3m_w}} \tag{6}$$

Once the fragmentation criterion is satisfied, the block is split up in fragments; the fragmentation algorithm computes the number and the size of fragments according to a power law distribution

$$G(D) = \left(\frac{D}{D_m}\right)^n \tag{7}$$

where D is the fragment diameter, D_m is the maximum fragment diameter, n is a model parameter controlling the shape of particle size distribution, and $G(D)$ is the percentage of fragments finer than D. The maximum fragment diameter is proportional to the parent block diameter by means of a coefficient f_d. After the fragment generation, the velocity modulus of each fragment is computed under the hypothesis that the parent block translational kinetic energy is equally distributed to all fragments. Finally, the code imposes that the direction of the fragments velocity belongs to a cone whose apex coincides with the last impact point where the fragmentation took place. A fragmentation model parameter controls the apex angle of this cone. Experimental results have shown that fragmentation can affect the runout and the spatial distribution of velocities and heights of the rockfall (Matas et al., 2017; Lin et al.,2020).

Model settings

The regional DTM available for the Aosta Valley has a 0.5 m x 0.5 m resolution allowing for a detailed description of the topography. As noticeable in Chapter 2a - Figure 7, the propagation zone of the rockfall includes two main paths of which one characterized by a terminal 150-200 meters high cliff before reaching the talus deposit (see profile P1 in Chapter 2a – Figure 8). The rockfall source area extends for about 8,700 m^2 between 2,730 m and 2,905 m asl. To simplify the simulation and evaluate the different controls, the source area was split in two subparts (see Chapter 2a - Figure 7, upper and lower half), the number of launched blocks per cell was changed between 1 and 10, three block volumes were tested (i.e. 1, 3 or 10 m^3) and fragmentation was in some simulation allowed and in others enabled (see Table S1 in supplementary material for a list of the performed simulations). A hybrid modeling approach was adopted to include the effect of block geometry, with normal and tangential restitution coefficients and the friction coefficient determined by slope material characteristics (Chapter 2a – Table 1) and successively calibrated and a stochastic range was assumed for each of them. On the contrary, the block density (2700kg/m^3), launch translational and rotational velocities (1 m s^{-1}, 1 s^{-1}), and the launch angle (10°) were kept constant.

Chapter 2a - Table 1 Values of normal and tangential restitution coefficients and of the friction coefficient for the different slope materials used in the rockfall numerical simulations.

Material denomination	e_n **[-]**	e_t **[-]**	μ_s **[-]**
Glacial deposit	65	80	0.40
Slope debris	65	70	0.60
Bare slope debris	65	70	0.50
Alluvial deposit	55	60	0.40
Outcropping rock	85	85	0.30
Sub-outcropping rock	80	80	0.30

Rockfall simulation results

Two examples of the trajectories computed by neglecting blocks fragmentation in the calculations (SIM#01) or including fragmentation (SIM#13) are reported in **Errore. L'origine riferimento non è stata trovata.**. The final block positions are also reported in the same figures. The three main clusters of arrest points (D1, D2 and D3) are visible and fit well with the distribution observed in the field (Chapter 2a –Figure 8) with the D3 deposit area interested by a lower block frequency. To classify the arrest points and main impact points (i.e. the most energetic and possibly associated to fragmentation), the analysis domain was split up in six sectors as shown in Chapter 2a – Figure 8 where the stopping points are also reported.

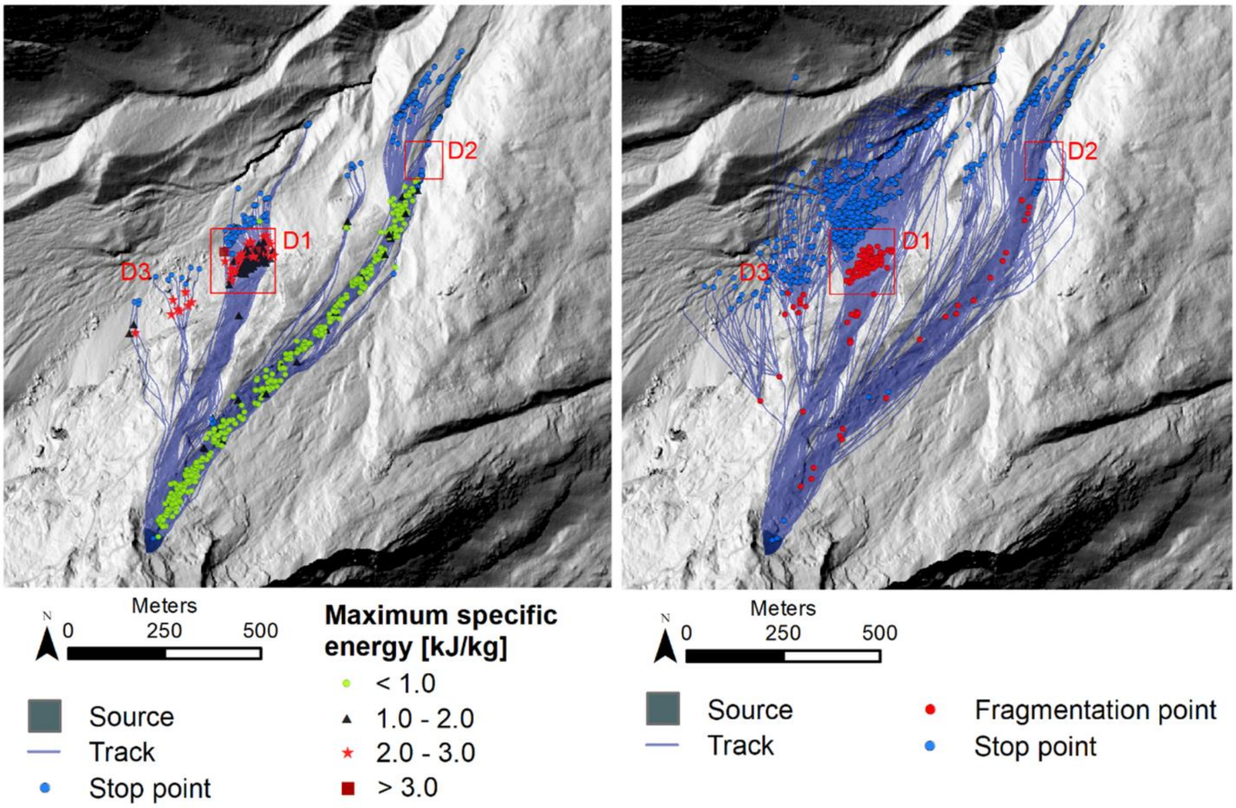

Chapter 2a - Figure 7 Simulated rockfall trajectories and arrest points for a) SIM01, with disabled fragmentation, showing the maximum specific energy in four energy intervals. Points and values refer to the maximum specific energy calculated by analyzing each impact of each simulated trajectory; b) SIM13 with fragmentation. The three main deposit areas D1, D2 and D3 are shown.

These zones were outlined according to in situ investigations, morphological features and the computed trajectories. The same figure shows the percentage of stopping blocks for each sector with respect to the total number of launched blocks. The majority of blocks belongs to sectors S1 (20.3%) and S2 (56.8%), while the remaining sectors account in total only for 22.9% of fallings blocks (Chapter 2a - Figure 8).

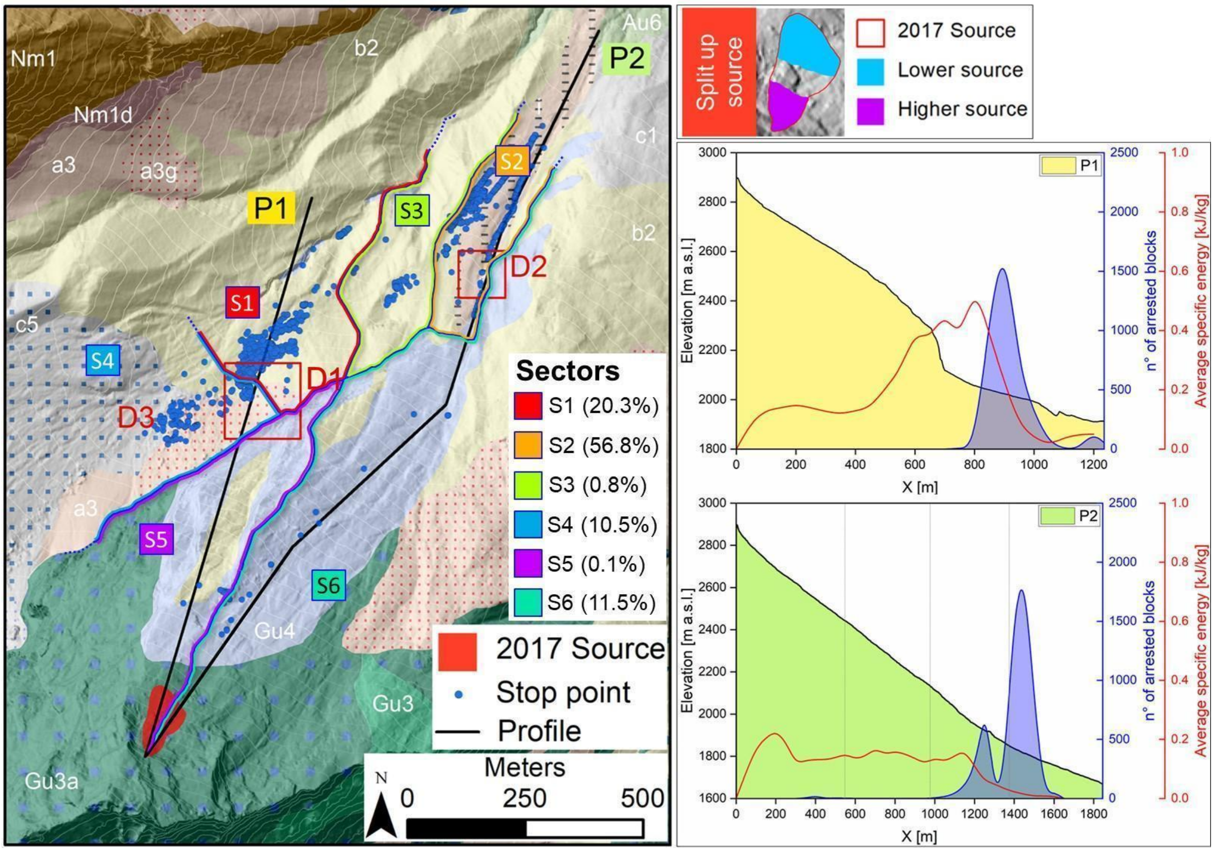

Chapter 2a - Figure 8 Numerical setting and altitude profiles of the preferential paths taken by blocks. In the right graphs, also the number of blocks come to rest and of average specific energy along the two profiles are reported. The location of the three main deposits D1, D2 and D3, and the arrest points of simulated blocks in simulation SIM09 and the subdivsions of the domain in six sectors are also indicated. For each sector, the percentage of final blocks with respect to the total number of blocks (50,707) is reported. The 1:10,000 geological map of the area is labelled: i) mixed origin deposit, c5) ablation till, a1) landslide deposit, b2) colluvium, a3g) large boulders deposit, c1) unsorted till, a3) landslide debris, Gu4) calc-schists, Gu3a) albitic amphibolites, Gu3) metabasites, Nm1) microcrystalline gneiss; Nm1d) quartz gneiss.

Since in the fragmentation process the main controlling parameter is the maximum specific energy (i.e. the block energy at impact divided by the block mass), we plotted this quantity in Chapter 2a – Figure 9. From the analysis of these impact points, two main macro-sectors were identified according to the different amount of energy dissipated. In coincidence with the deposit areas D1 and D3, the released energy (greater than 1.0 kJ/kg and up to more than 3.0 kJ/kg) is greater than within the deposit D2 area (lower than 1.0 kJ/kg). As shown in Chapter 2a - Figure 8, deposits D1 and D3 occur below a high terminal cliff (profile P1), whereas deposit D2 is located at the end of an even and gentler slope (P2). In the same figure, the number of final blocks and the average specific energy extracted along the profiles indicate a single main deposit for P1 whereas a more distributed deposit for P2, and an increase in the average specific energy at the main cliff jump for P1.

Chapter 2a – Figure 8 shows the analysis of the maximum specific energy collected for each sector for simulation SIM#01, assumed as representative of all our simulations. The dashed lines in the graphs identify the same energy classes (i.e. low, medium and high energy). The high-energy class (i.e. values greater than 3.0) is reached only in sectors S1 and S4 (with a relative frequency lower than 0.2) at deposit areas D1 and D3. The medium-energy class is reached in all the sectors, except in the very densely populated sector S2. Notice that the calculated specific energies in the sectors 1, 3 and 4 are the highest of all possible paths, including many blocks of energy larger than 2,000 J/kg. This corresponds to a free fall height of about 200 m. The energy threshold for fragmentation is shown in the same plot for three possible scenarios: a low, medium, and high energy threshold. These values are approximately indicated by in situ experiments with large boulders dropped from a certain height.

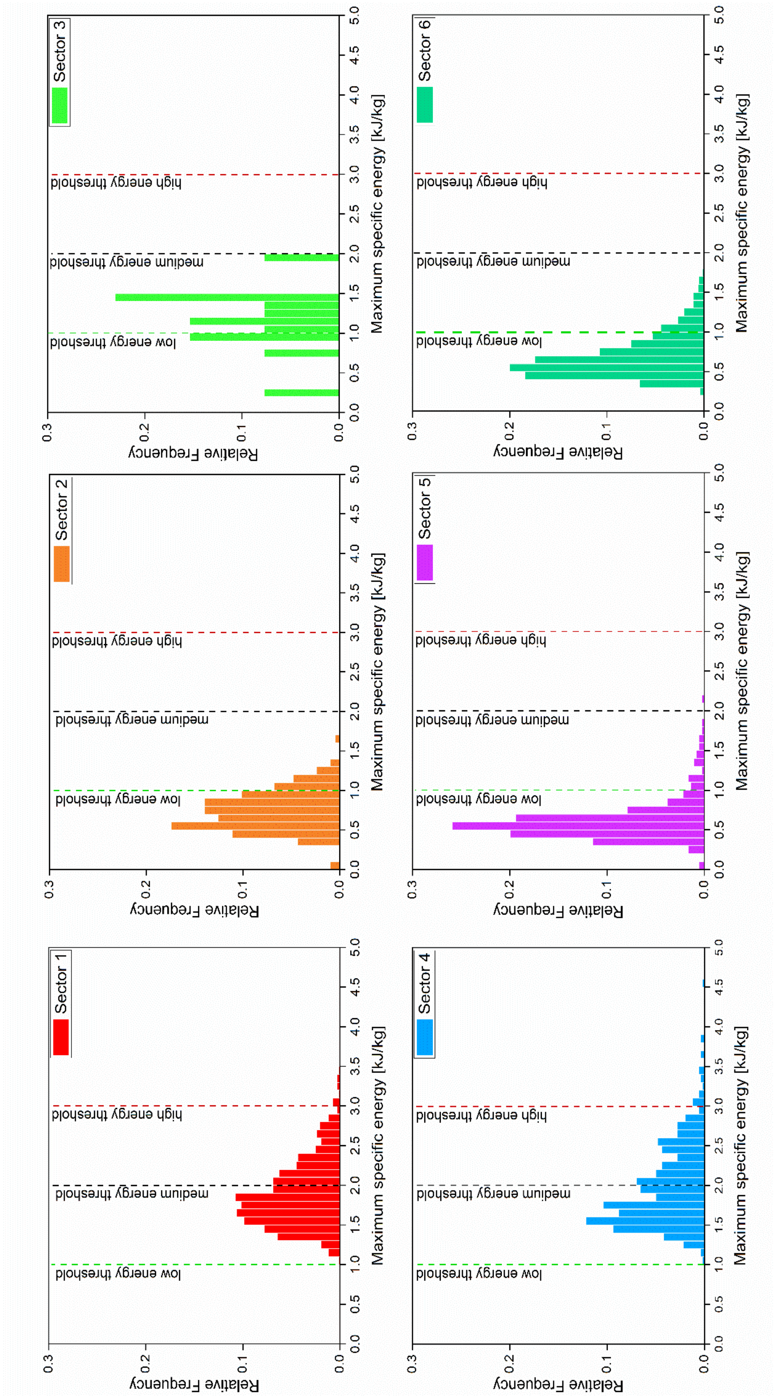

Chapter 2a - Figure 9 Histograms of maximum specific energy frequency distribution calculated for each one of the six sectors (see Chapter 2a –Figure 8, colours as in the figure) in simulation SIM01. Vertical dashed lines identify low, medium and high-energy threshold values.

Chapter 2a – Figure 10 shows the distance ranges between the impact point where the maximum dissipation occurs and the stopping point (box & whiskers plot) together with the maximum dissipation specific energy (histogram plots with dashed lines for distributions) for each sector. Apart sectors S5 and S6 where the blocks do not reach the terminal cliff, blocks experiencing the maximum values of dissipation energy (sectors S1 and S4) show the largest standard deviation and mean values. Specific energy dissipation values are greater for blocks belonging to sectors S1 and S4 confirming that these blocks can undergo fragmentation enhanced by presence of small precipice. In spite of this difference in energy dissipation, the blocks are capable of traveling a long distance but shorter than for those in sectors S2 and S3 where fragmentation was less severe.

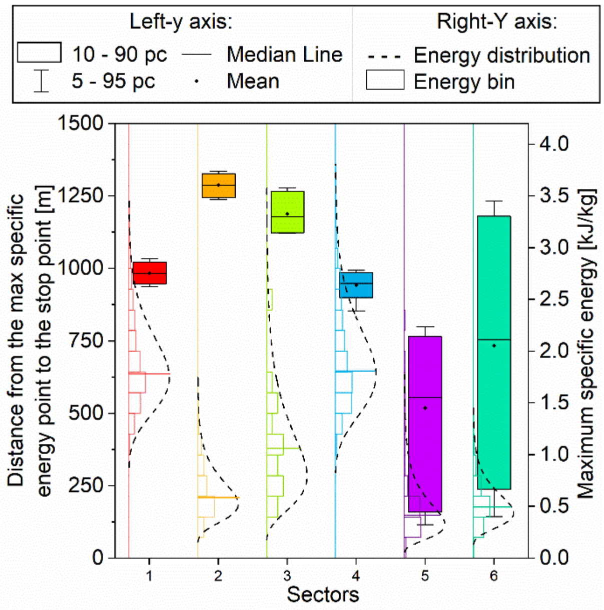

Chapter 2a - Figure 10 Box and whiskers plot of the distance between the impact point, where the maximum energy is dissipated, and the stopping point for the simulations SIM01; horizontal bar histograms refer to the maximum specific energy distribution. Data are analysed for each one of the six sectors delineated in Chapter 2a - Figure 7.

According to these observations, the D1 and D3 areas are the more likely sources for the fragmentation and consequently for the formation of the dust cloud. As a partial verification of the results obtained by HyStone for fragmentation, Fig. S 2 of the Supplementary material shows the characteristics of the deposits D1 and D2. In the D1 area the fragments are finer than in deposits D2, confirming the severity of fragmentation in D1 as from calculations. Another feature supporting this conclusion is represented by tree abrasion observed in the D1 and that is completely absent in the deposit D2. Furthermore, the blocks in D1 are covered and embedded in a greyish powder that is a residual of the dust cloud formation.

Dust cloud analysis

Fragmentation energy

A quantitative analysis of the various forms of energy dissipated by rockfall blocks at collapse was presented in De Blasio et al. (2018). The main energy dissipation processes are seismic waves, mass fragmentation, heat, kinetic energy of the fragments (responsible for the weak shock wave in the air), and acoustic energy. It was concluded that most of the initial EER energy goes into fragmentation of rock blocks and the kinetic energy of the fragments. In the following, the dust grain size data (Chapter 2a – figure 6) was used to estimate the fragmentation energy.

Using a series of functional forms to fit the granulometric curves, we found the best fit with the normalized Generalized Extreme Value (GEV), whose expression is

$$G(D) = \frac{(G_{Max} - G_{Min}) g(D) - G_{Min} g(D_{Max})}{g(D_{Max})} \tag{8}$$

being G_{Max}, G_{Min} the passing percentages for the maximum and minimum diameters D_{Min} and D_{Max}, respectively, whereas $g(D)$ is the following function

$$g(D) = exp\ exp\left\{-\left(1+\xi\,\frac{D-\mu}{\sigma}\right)^{-\frac{1}{\xi}}\right\} - exp\ exp\left\{-\left(1+\xi\,\frac{D_{Min}-\mu}{\sigma}\right)^{-\frac{1}{\xi}}\right\} \tag{9}$$

where ξ, μ and σ are three model parameters.

Assuming that the clasts have spherical shape, with diameter ranging between D_{Min} and D_{Max}, the newly generated area for all clasts (S) is

$$S_{sphere} = 6V_{dust} \int_{D_{Min}}^{D_{Max}} \frac{1}{D} \frac{dG}{dD} \, dD \tag{10}$$

In this equation the perfect sphericity of the particles is a strong approximation that causes an underestimation of the generated surface, and consequently of the energy absorbed by fragmentation. For this reason, De Blasio et al. (2018) suggested the use of the sphericity index, s, (i.e. the ratio between the surface area of a real particle and the area of a spherical particle of the same volume) for a better characterization of the grain surface and the quantification of the fragmentation energy. If the sphericity index remains constant (i.e. it is not a function of the particle size), then the surface produced is simply

$$S = \frac{6V_{dust}}{s} \int_{D_{Min}}^{D_{Max}} \frac{1}{D} \frac{dG}{dD} \, dD = \frac{S_{sphere}}{s} \tag{11}$$

Defining the fragmented fraction η_f, as the volume fraction of the initial rockfall volume that forms the dust cloud

$$\eta_f = \frac{V_{dust}}{V_b} \tag{12}$$

then the generated surface becomes

$$S = \frac{6\eta_f V_b}{s} \int_{D_{Min}}^{D_{Max}} \frac{1}{D} \frac{dG}{dD} \, dD. \tag{13}$$

The fragmentation energy, E_f, is given by the following expression

$$E_f = E_s S \tag{14}$$

where E_S is the fracture energy for unit surface, i.e., the energy cost to create a unit surface area.

The proposed approach to compute fragmentation energy is different from that normally employed in the comminution industry and its applications to rock avalanches. In the comminution industry, the Bond's law is used to estimate fragmentation energy as explained in Appendix A (see also Rhodes, 1998). Bond's law has been applied to estimate the energy sink of rock avalanches (Locat et al., 2006; Crosta et al., 2007; De Blasio and Crosta, 2014) but it may be unsuitable when dealing with very small particles, for which other comminution laws such as the von Rittinger's law (Rhodes, 1998) were suggested. In contrast, von Rittinger's equation is not suitable for larger clasts and, consequently, no expression in literature considers the whole particle clast distribution. For this reason, we introduced the clast size distribution in the energy computation.

To calculate the fragmentation energy, von Rittinger's law was initially used assuming that the total fragmentation energy needed to bring an initially intact block to powder of a size spectrum $G(D)$ is proportional to the surface created by fragmentation. In this equation, D is a size which is conveniently fixed as the sieve opening size or, for digital granulometers, as the "representative" radius of the clasts. Hence the energy absorbed by fragmentation is computed as

$$\Delta E = E_S \int_0^r G(r) S_c(r) dr \tag{15}$$

and $S_c(r)$ is the surface of the clast of radius r. This is an ill-defined quantity, since there is no univocal relationship between r and $S_c(r)$ as the clasts do not have all the same shape. In the following, we used the definition of the maximum particle diameter D_{Max}, as the maximum length possible for a given geometry. Thus, the maximum size for a spherical and a cubic grain is the diameter $S(r) = 4\pi r^2 = \pi D_{Max}^2$ and the diagonal $2D_{Max}^2$, respectively.

Because the von Rittinger's law was elaborated in the mining and comminution industry, it usually requires the starting size $D(m)_{initial}$ of the feed (i.e., initial grain size) and that of the final product $D(m)_{final}$. Since the original expression is strictly dependent on the adopted units, we modified it proposing the expression

$$E_f\left(\frac{J}{kg}\right) = \frac{1}{\rho\left(\frac{kg}{m^3}\right)} E_S\left(\frac{J}{m^2}\right)\left(\frac{1}{D(m)_{final}} - \frac{1}{D(m)_{initial}}\right) \tag{16}$$

where $D_{initial}$ and D_{final} are measured in meter, E_s is measured in $\frac{J}{m^2}$, ρ is measured in $\frac{kg}{m^3}$ and, finally, E_f is measured in $\frac{J}{kg}$. Our equation (14) is more complete than (16) as it uses the "real" area produced by insertion of the particle size distribution $G(D)$.

The fragmentation energy for unit surface of an ideal solid consisting of one atomic species is easily estimated. When a new atomic area S_a is created within the solid, about $N_a \approx \frac{S_a}{\pi a^2}$ atoms are separated, where a is the Wigner-Seitz radius (e.g., Kittel, 1996), which for the present order-of-magnitude estimate is approximately the lattice spacing. Hence, the energy cost is $E_{fa} = \frac{S_a \epsilon}{\pi a^2}$ where ϵ is the energy needed to separate two atoms apart. This energy is smaller than the cohesive energy per atom (which accounts for the energy of interaction with all the other ions in the lattice), but it is typically of the same order of magnitude and will suffice for the present estimate; thus

$$E_S \approx \frac{E_{fa}}{S_a} = \frac{\epsilon}{\pi a^2} \tag{17}$$

Cohesive energies are typically on the order of 1eV per atom for alkalis, and some eV for more bound solids (Poole, 1980). This amount would correspond to surface energies of $\approx 1J\,m^{-2}$ that is the order of magnitude of surface energy measured for different minerals. For example, $E_S = 1.27,\ 0.705$ o and $0.548\,J\,m^{-2}$ for graphite, quartz, and average feldspar, respectively (Brace and Walsh, 1962; Zhang and Ouchterlony, 2022). Valero et al. (2011) report a higher value of E_S ≈2-3 J m^{-2} for quartz showing some divergence among literature data. Similarly, higher values were reported for alkali feldspars by Brace and Walsh (1962) and Atkinson and Meredith (1987): $7.77\,J\,m^{-2}$ for orthoclase and 3.20 to $5.25\,J\,m^{-2}$ for microcline. However, a rock is a polycrystalline material with different mineral species. The energy needed to separate two different grains along pre-existing boundaries is less than the one necessary to break through a well-formed crystal. For example, for anorthite, the energy for unit of area necessary to produce an inter-granular crack is about 2.74 J m^{-2}, which dramatically reduces to $0.55\,J\,m^{-2}$ if the crack develops between two crystals (Tromans and Meech, 2002). A comparable reduction of the energy per unit area by a factor 4-5 was reported by Tromans and Meech (2002) from the case of crystal cracking to the one along crystal-crystal boundary). Furthermore, it can be expected that the fracture energy of rocks composed of more than one crystalline species will depend on the crystalline state (mono vs polycrystalline). Here, to be consistent with the few data available, we use a surface energy ranging between 0.1 to 0.5J m^{-2}. Note that in the comminution industry, it is known that only about 5% of the energy expended in dedicated apparatuses goes into fragmentation with the rest going into other energy sinks (e.g., noise, heat, Rhodes, 1988).

Table S 2 shows the parameter calibration of the lognormal particle size distribution (equation (16)) by means of the least square method together with the error of the estimation. To this purpose the granulometric curves obtained from the seven samples collected at different locations (Chapter 2a – Figure 5) were used. The curves fit very well the experimental data as suggested by the small error which reaches a maximum of 0.0019%.

Table S 3 shows the values of the generated particle surface area together with the fragmentation energy and the specific fragmentation energy (i.e. the fragmentation energy per unit volume). These computations are performed by considering the parameters of Table S 2 and considering the previously estimated V_{dust} value for $\eta_f = 0.00965$. The data reported in the first column of Table S 3 were calculated under the assumption that the whole failed mass of 8,000 m^3 had gone into the finest dust cloud component. Because only a fraction $\eta_f \approx 0.00965$ of the rock mass was so intensely comminuted to generate a dust cloud, the total energy gone into fragmentation for the formation of the dust cloud should be multiplied by η_f. The last column of Table S 3 shows the resulting values. Note that the fragmentation energy per unit mass calculated from the dust size analysis (about 10^4 J/kg except for one sample giving values one order of magnitude larger) even exceeds the kinetic energy per unit mass available (in any case, less than 4,000 J/kg as shown in Chapter 2a – Figure 9). This indicates that the energy was focused on a small portion of the mass, which were so profoundly fragmented, while the rest of the colliding block was spared such severe fragmentation. This indicates that the rocky dust was produced in the front of a sacrificial layer of the colliding blocks.

A final remark is due regarding the rock area generated by fragmentation. It may appear surprising that areas produced by fragmentation are so large as reported in Table S 3. This can be explained by a simple order of magnitude estimate. The breakage of a cubic block of side length L and volume V into N small cubical grains of side $l \ll L$ creates a total area ΔA increment due to the fragmentation on the order

$$\Delta A \approx 6Nl^2 \approx 6\left(\frac{L}{l}\right)^3 l^2 = \frac{6V}{l} \qquad (18)$$

Using $l \approx 10\,\mu\,m = 10^{-5} m$ and $V \approx 8000\,m^3$, it follows that $\Delta A \approx 4.8 \times 10^9\,m^2 = 4.8 \times 10^3\,km^2$, i.e., the same order of magnitude reported in our data. The maximum and minimum values obtained for the sample #1and sample #4, respectively, were of the same order of magnitude. Calculations, considering the shape of the clasts (Chapter 2a – Figure 2), show that a plausible value for s could be substantially lower than 0.806 corresponding to cubical clasts, and we used $s=0.5$.

Dust cloud propagation

The aim of this section is the estimation of maximum speed and run out of the dust cloud. Particulates clouds are initially set in motion by the momentum transmitted to the air by the exploding rock mass when hitting the ground at high speed (De Blasio et al. 2018). The subsequent acceleration is driven by the density difference between the suspension and ambient air. In the simple model suggested here, the cloud is already fully formed in its prismatic shape of dimensions H, W and L as in Chapter 2a – Figure 11. In our model, the density of the suspension is constant, while lateral flows are neglected. Furthermore, we assume that the cloud moves along a surface of constant slope β and the differences between the behavior of the cloud head and body (Simpson, 1982; Bridge and Demicco, 2008) are not considered. The cloud size and the forces acting on it are represented in Chapter 2a – Figure 11.

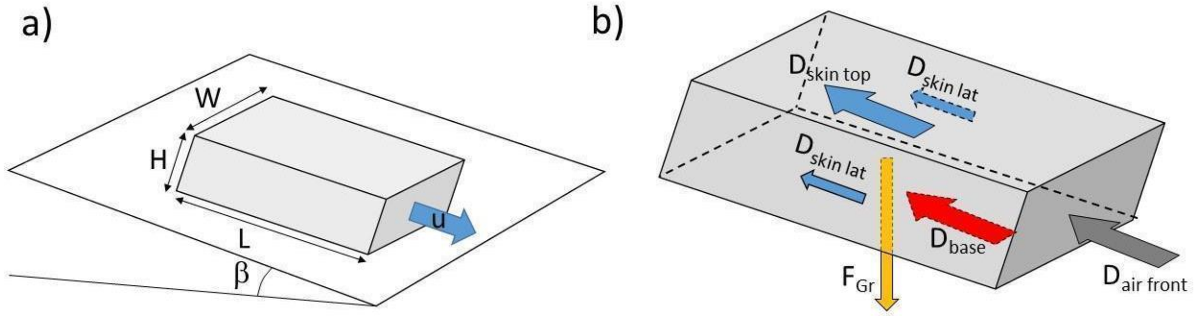

Chapter 2a - Figure 11 a) Dust cloud box used in the model with the cloud geometry and the ground surface sloping at an angle β; b) forces acting on the box of element a): the gravity force (FGr), the basal force slope-drag (DBase), the front air-drag (Dair front) and the skin-air force (Dskin top, Dskin lat) acts on the three lateral surfaces.

To estimate the velocity of the dust cloud, we write the Newton's equation for the centre of mass of the cloud

$$V\left(\rho_c + \frac{1}{2}\rho_a\right)\frac{du}{dt} = (\rho_c - \rho_a) g \sin\beta\, V - F_D \qquad (19)$$

where u is the velocity, ρ_c is the density of the dust cloud, ρ_a is the air density, g is the gravity acceleration, β is the slope angle and V is the dust volume. The dust density is given by the following expression

$$\rho_c = (1 - e)\rho_s + e\rho_a \qquad (20)$$

being ρ_s the particle material density, ρ_a air density under standard condition and e air fraction.

The drag force F_D is due to the interaction of the dust cloud with the air and the ground surface. The drag force is approximated as

$$F_D = \frac{1}{2}\rho_a\left(C_{cf}HW + C_{cb}WL + C_{cs}WL + 2C_{cs}HL\right)u^2 \tag{21}$$

where C_{cf} is the front drag coefficient, C_{cs} is the drag skin coefficient, while C_{cb} is the drag bottom coefficient accounting for the friction between the cloud and the ground surface. By introducing the following global drag coefficient

$$C = \frac{C_{cf}}{L} + \frac{C_{cs}}{W} + \frac{C_{cs}}{H} + \frac{C_{cb}}{H} \tag{22}$$

the drag force becomes:

$$F_D = \frac{1}{2}\rho_a C V u^2 \tag{23}$$

and the motion equation can be rewritten in the following form

$$\frac{du}{dt} = \frac{\rho_c - \rho_a}{\rho_c + \frac{1}{2}\rho_a} g \sin\beta - \frac{1}{2}\frac{\rho_a}{\rho_c + \frac{1}{2}\rho_a} C u^2 \tag{24}$$

Defining the two parameters k and λ as

$$k = 2\frac{\rho_c + \frac{1}{2}\rho_a}{\rho_a} \cdot \frac{1}{C} \tag{25}$$

$$\lambda = \sqrt{k\frac{\rho_c - \rho_a}{\rho_c + \frac{1}{2}\rho_a} g \sin\beta} = \sqrt{\frac{2}{C}\frac{\rho_c - \rho_a}{\rho_a} g \sin\beta} \tag{26}$$

the above differential equation becomes

$$\frac{du}{dt} = \frac{\lambda^2}{k} - \frac{1}{k}u^2 \tag{27}$$

and by using the method of variable separation, and after some algebra it becomes

$$\frac{\left(\frac{\lambda}{\sqrt{k}} + \frac{u}{\sqrt{k}}\right)}{\left(\frac{\lambda}{\sqrt{k}} - \frac{u}{\sqrt{k}}\right)} = e^{\frac{2\lambda t}{k}} \tag{28}$$

providing the solution as

$$u = \lambda\frac{\left(e^{\frac{2\lambda t}{k}} - 1\right)}{\left(e^{\frac{2\lambda t}{k}} + 1\right)} \tag{29}$$

This function is monotonically increasing from zero velocity to a finite maximum, called limit velocity u_l. By taking the limit for $t \to +\infty$, the limit velocity is λ.

The displacement of the cloud can be easily calculated by integrating the dust velocity as

$$d_c(t) = \int_0^t u(t')dt' = \lambda\int_0^t \frac{\left(e^{\frac{2\lambda t'}{k}} - 1\right)}{\left(e^{\frac{2\lambda t'}{k}} + 1\right)} dt = \lambda\int_0^t \tanh\left(\frac{\lambda t'}{k}\right) dt = k \ln\left[\cosh\left(\frac{\lambda t}{k}\right)\right] \tag{30}$$

Chapter 2a – Figure 12 shows the evolution of the velocity and displacement of the dust cloud considering both equations (29) and (30) using the parameters collected in the same figure and for three values of coefficient C_{cb}. For all curves the velocity increases with time reaching a limit value, which increases at reducing the coefficient C_{cb}. In particular for a coefficient $C_{cb} = 0.25$ the maximum cloud velocity is about $25\ m\ s^{-1}$ and the maximum dust cloud displacement is 1.5 km which approximate the direct observations at the site (see Chapter 2a – Figure 3).

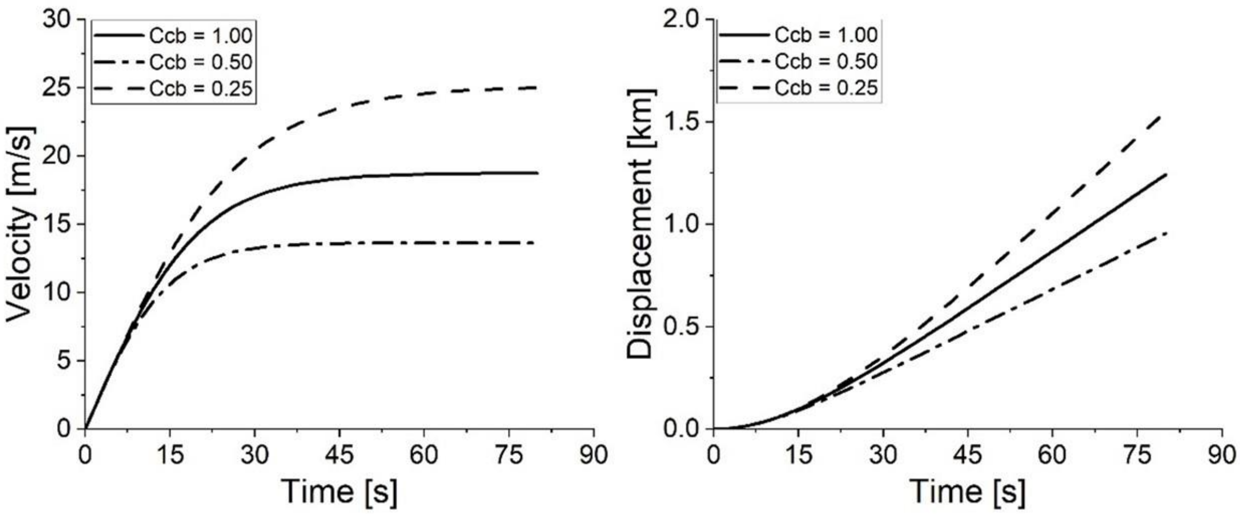

ρ_a	ρ_s	g	β	W	L	H	e	c_{cf}	c_{cs}
[kg m^{-3}]	[kg m^{-3}]	[m s^{-2}]	[°]	[m]	[m]	[m]	[-]	[-]	[-]
1.14	2700	9.81	20	200	1000	50	0.9975	1.0	0.01

Chapter 2a - Figure 12 Evolution of the cloud propagation a): displacement and b) velocity as a function of time calculated by equation (39). Three different values of the drag coefficients were considered. The values of the parameters employed in the computation are also reported.

Cloud settling

During the cloud motion, particles tend to move downward due to the gravity action, but this vertical fall is contrasted by turbulence. Hence, for the sake of simplicity, we assumed that the cloud settling is more relevant for low velocities of the dust cloud. We also neglected the particle-particle interactions and the hindered settling (i.e., the action of the upward air movement in response to the vertical particle displacement) and we assume spherical particles. Under these assumptions the particles are subject only to the gravity force and the air drag force which for small Reynolds number can be assumed to be Stokesian (Landau and Lifshitz, 2013) so that the motion equation has the following form

$$m_p \frac{du}{dt} = m_p g - 6\pi\eta R_p u \tag{31}$$

in which m_p is the particle mass, u is the vertical component of the particle velocity, η is the air viscosity and R_p the particle radius. By integrating the above differential equation, the following solution is obtained

$$u(t) = \frac{g}{\lambda}\left(1 - e^{-\lambda t}\right) \tag{32}$$

where λ is given by

$$\lambda = \frac{6\pi\eta R_p}{m_p} \tag{33}$$

and the particle displacement is obtained

$$d(t) = \frac{g}{\lambda}\left[t + \frac{1}{\lambda}\left(e^{-\lambda t} - 1\right)\right] \tag{34}$$

If H is the dust cloud thickness, then the settling time (i.e. the time required to the particle to reach the ground surface) is obtained by imposing

$$d(t_s) = H \tag{35}$$

and the particle velocity at the soil is called the maximum velocity (u_{max}) and is given by the velocity at $t = t_s$. The velocity function (eq.(32)) is an increasing monotonic function that tends for $t \to +\infty$ to the limit velocity u_l given by

$$u_l = \frac{m_p g}{6\pi\eta R_p} = \frac{2}{9}\frac{g\rho_s R_p^2}{\eta} \tag{36}$$

We define the limit settling time, t_{sl}, as the time required to the particle to settle starting its fall already at the limit velocity

$$t_{sl} = \frac{H}{u_l} = \frac{9}{2}\frac{\eta H}{g\rho_s R_p^2} \tag{37}$$

Using clean air dynamic viscosity value of $\eta = 1.8 \cdot 10^{-5} Pa \cdot s$, and a dust cloud height $H = 50m$ (i.e a value comparable with the one observed in the propagation along the upper tributary valley, see Chapter 2a – Figure 3), the evolution of the settling time and the limit settling time with particle diameter is represented in Chapter 2a – Figure 12a. This computation shows that the settling time and the limit settling time in still air decrease with increasing particle diameter and the dust suspension of micrometric particles will persist for many hours. Obviously, this analysis neglects air current, winds and the effect of air moisture that could contribute to clear the air in the area of interest. Furthermore, for small particles the limit settling time and the settling time are coincident since small particles reach the limit velocity in short time in comparison with the settling time and consequently it is possible to assume that these particles are at the beginning in the limit condition. The divergence between the settling time and the limit settling time increases with the particle diameters and for millimeter particles the difference can be about one order. The above considerations are also confirmed by the Chapter 2a - Figure 13b where the limit velocity and the maximum velocity are represented in terms of particle diameters. By increasing the particle diameter, the differences between the limit velocity and the maximum velocity increases.

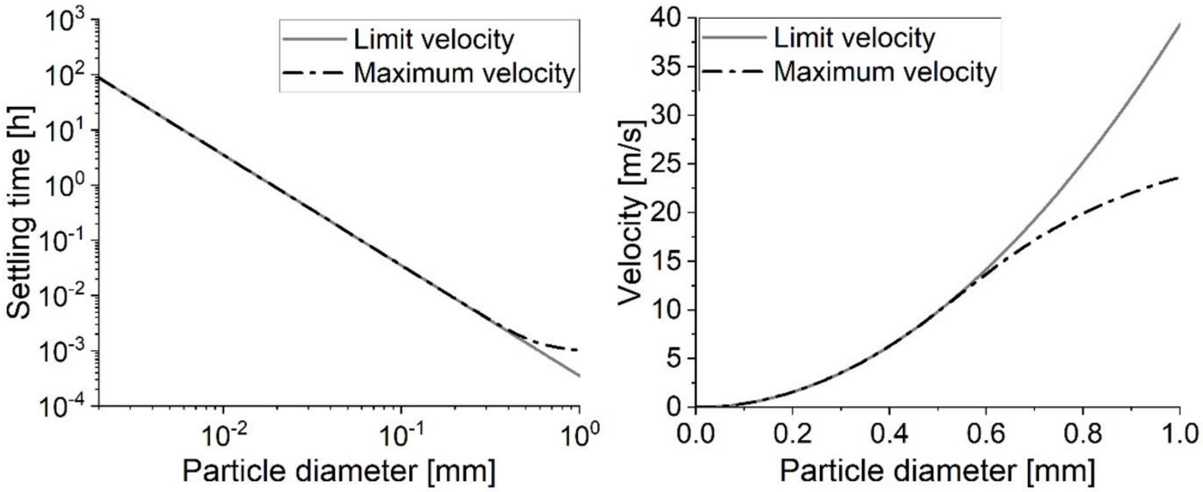

Chapter 2a - Figure 13 Settling time (a) and particle velocity (b) of the dust particles as a function of the particle diameter. The two curves are for a particle starting its fall at the limit velocity (continuous line) and for an accelerating particle (dash-dot line).

To study the effect of air viscosity we performed a parametric analysis in which we have considered other two values of air viscosities. The obtained results in terms of settling time and maximum velocity are reported in Chapter 2a – Figure 14. Independently from the air viscosity, an increment of particle diameter increases the maximum particle velocity and reduces the settling time. Note that an increment of the air viscosity increases the settling time and reduces the maximum particle velocity. Because the dust cloud is a mixture of particles with different class diameters (Chapter 2a - Chapter 2a – Figure 6), large particles settle first leaving a haze of clay-size particles which, as our calculations confirm, may persist for several hours.

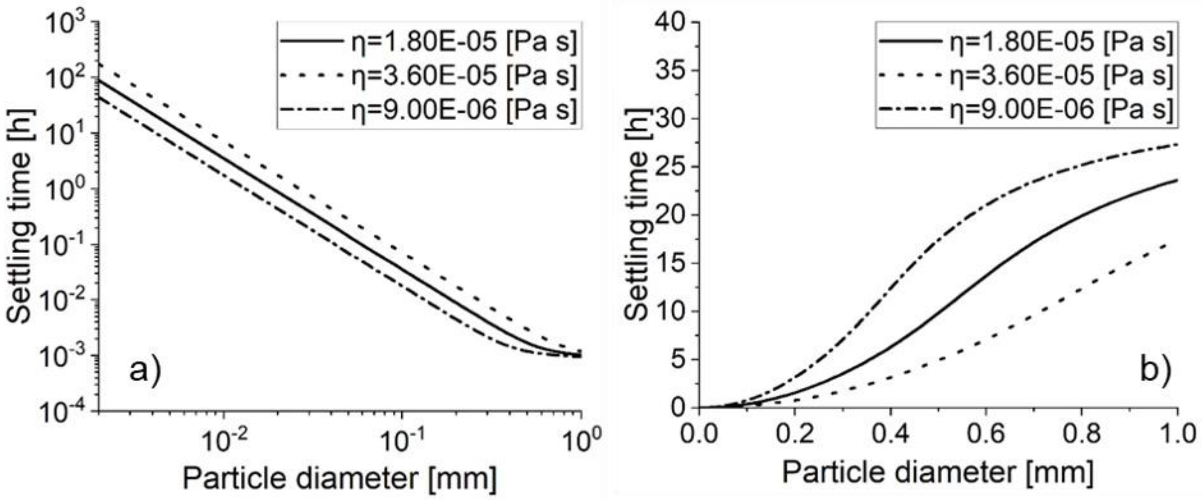

Chapter 2a - Figure 14 Parametric analysis of the air viscosity effect on the particle settling time and the velocity for different particle diameters.

Conclusions

Direct observations of the 2017 Pousset event and on site investigation of the source, transport and deposition areas allowed us to reconstruct the dynamic of event and to collect useful information for a more in depth analysis. Apart from the large blocks delivered at the base of the rocky cliff, most of the resulting clasts were found of millimeter-to decimeter size, and a fraction of the initial mass was comminuted to small particles of diameter between one micron to one tenth of a millimeter. This last part was converted into a dust cloud that traveled along the tributary valley down to the main valley. The thickness of the dust deposit was measured, and found to decrease from the impact area. The estimated fraction of rock volume that ended up in the dust deposit was found to be about 45 m^3, or 0.6% of the failed volume. Remarkably, the dust particles were found to be finer than in several EER events (or Extremely Energetic Rockfalls; De Blasio et al., 2018) which is surprising since EERs typically strike the ground with much higher energy per unit mass. It is possible that the impact energy was concentrated on a more localized area with the finest component of the dust produced by chipping of a sacrificial shell around the main failing block. The rest of the block enjoyed a buffering effect and was spared from such fine comminution. To verify such a condition, we simulated quantitatively the rock fall by the 3D HyStone code (Frattini et al., 2012; Crosta et al., 2015; Dattola et al., 2021) using a hybrid approach and including rock fragmentation. Simulations and direct observation both indicate that severe fragmentation occurred at two main impact points at the base of the cliff and these were the sources of the dust cloud. Fitting the particle size distribution, we found that the fragmentation energy per unit mass was about 10^4-10^5 J/Kg, that is a small fraction of the available potential energy (about 10^7 J/Kg) was required to fragment 0.6% of the initial rock fall volume. In other words, relatively little energy went into the fragmentation of the rock mass. This is, however, the result of buffering by the sacrificial layer where a large amount of energy was used up in comminution.

The Pousset rock fall represents a controlled case to analyze since the different processes (rockfall, rolling, fragmentation, dust cloud propagation, dust cloud settling) can be examined one at a time. Still, many problems were addressed in a partial or approximated way, and should be more thoroughly considered in a future analysis of similar rock fall events. Firstly, the rockfall trajectories are based on some assumptions concerning the initial block size distribution and the fragmentation model (following Yashima et al., 1987). Secondly, the dynamics of fragmentation should be understood in a more complete theory based on physical analysis of crack propagation in the crystalline rock. In the present work, the fragmentation energy is simply proportional to the area created during fragmentation. Although this approach is expected to provide the correct order of magnitude, it nevertheless neglects the possibility of non-linear effects in fragmentation. It also overlooks the polycrystalline nature of rocks and the composition of different mineralogical species. Also, the microscopic dust has been treated as composed of particles with a definite shape. The deviation from sphericity (which gives a larger area for the given volume, and thus a larger fragmentation energy) is treated by introducing a sphericity parameter equal for all particles. More realistically, particles have complex shapes, and moreover the ruggedness of their surface indicates a larger area of fragmentation and greater fragmentation energy. Thirdly, the dynamics of the dust cloud is treated with a simple mathematical model. In spite of its basic assumptions, the calculated velocities and the space traveled by the cloud are compatible with the observations as documented in the two videos of the Mount Pousset rock fall. We estimated a time needed for the dust cloud particles to settle ranging from some minutes to several hours for particles of different size. As we documented, the rock dust particles span two-three orders of magnitude in size (i.e., six-nine in volume), which implies a differential settling. In addition, air properties like turbulent viscosity, air engulfment and hindered settling should be properly introduced.

In the paper, we presented an analysis of the dust cloud deposit focused on the spatial thickness and granulometric distribution. Some potentially interesting features that for brevity were not reported require further investigations. In particular, the role of humidity could have played a role in the deposition and permanence of thick dust layers deposited on tree trunks that we found as hard as mortar. High velocity and compaction was relevant but also some moisture from water in the talus or from the scarred vegetation or from the air could be important. As a general outlook, it can be expected that during the occurrence of large rock falls and rock avalanches, significant amounts of dust must have been produced. If a rapid deposition buried patches of the consequent dust layers during large prehistoric rock falls and avalanches in the Alps, these could be still identifiable in some cases (Reznichenko et al., 2012). Hence, the investigation of these dust cloud layers for recent events may represent a valuable additional piece of information in the investigation of the dynamics of rock falls and avalanches.

Acknowledgements

Videos of the Pousset rockfall are available at https://www.youtube.com/watch?v=JnLsJBL1Uzs and https://www.youtube.com/watch?v=DqEIdmRLzbs&t=6s (last accessed on February 2022).

The work was supported by:

- CARIPLO 2016-0756 —@RockHoRiZon—Advanced Tools for Rockfall Hazard and Risk zonation at the Regional Scale
- The Ministry of University and Research is thanked for funding Project PRIN MIUR Urgent – Urban geology and geohazards: Engineering geology for safer, resilient and smart cities, 2017 HPJLPW

References

Atkinson, B.K., Meredith, P.G., (1987) Theory of subcritical crack growth with applications to minerals and rocks : In: Fracture Mechanics of Rock, edited by B. K. Atkinson, Publ London: Academic Press, 111–166.

Bergomi, M. A., Dal Piaz, G. V., Malusà, M. G., Monopoli, B., & Tunesi, A. (2017). The Grand St Bernard-Briançonnais nappe system and the Paleozoic inheritance of the Western Alps unraveled by zircon U-Pb dating. Tectonics, 36(12), 2950-2972.

Bianchi-Fasani, G., Esposito, C., Lenti, L., Martino, S., Pecci, M., and Scarascia-Mugnozza, G. (2013). Seismic analysis of the Gran Sasso catastrophic rockfall (Central Italy). In: C. Margottini et al. (eds). Landslide Science and Practice, Vol. 6, DOI 10.1007/978-3-642-31319-6_36. Springer Verlag Berlin Heidelberg.

Boeckli, L., Brenning, A., Gruber, S. & Noetzli J. (2012): Permafrost distribution in the European Alps: calculation and evaluation of an index map and summary statistics, The Cryosphere, 6, 807–820, doi:10.5194/tc-6-807-2012.

Brace, W. F., Walsh, J. B. (1962). Some direct measurements of the surface energy of quartz and orthoclase. American Mineralogist, 47 (9-10), 1111–1122.

Bridge, J., Demicco, R. (2008). Earth surface processes, landforms and sediment deposits. Cambridge University Press.

Crosta, G.B., Agliardi, F., Frattini, P., Imposimato, S. (2004) a Three Dimensional Hybrid Numerical Model for Rockfall Simulation. In: Geophys. Res. Abstr. p 7962

Crosta, G. B., Frattini, P., Fusi, N. (2007). Fragmentation in the Val Pola rock avalanche, Italian Alps. Journal of Geophysical Research: Earth Surface, 112(F1).

Crosta, G. B., Agliardi, F., Frattini, P., & Lari, S. (2015). Key issues in rock fall modeling, hazard and risk assessment for rockfall protection. In Engineering geology for society and territory-volume 2 (pp. 43-58). Springer, Cham.

Dattola, G., Crosta, G. B., di Prisco, C. (2021). Investigating the influence of block rotation and shape on the impact process. International Journal of Rock Mechanics and Mining Sciences, 147, 104867.

De Blasio, F. V., & Crosta, G. B. (2014). Simple physical model for the fragmentation of rock avalanches. Acta Mechanica, 225(1), 243-252.

De Blasio, F.V., Dattola, G., Crosta G.B. (2018) Extremely Energetic Rockfalls. J Geophys Res Earth Surf 123:2392–2421. https://doi.org/10.1029/2017JF004327

Di Prisco, C., Vecchiotti, M., (2006) A rheological model for the description of boulder impacts on granular strata. Géotechnique 56:469–482. https://doi.org/10.1680/geot.56.7.469

Frattini, P., Crosta, G.B., Agliardi, F., (2012) Chapter 22- Rockfall characterization and modeling. Landslides types, Mech Model 267

Geertsema, M., Clague, J. J., Schwab, J. W., Evans, S. G. (2006). An overview of recent large catastrophic landslides in northern British Columbia, Canada. Engineering Geology, 83(1), 120– 143. https://doi.org/10.1016/j.enggeo.2005.06.028

Gruber, S., Hoelzle, M., Haeberli, W. (2004). Permafrost thaw and destabilization of Alpine rock walls in the hot summer of 2003. Geophysical Research Letters, 31, L13504.

Gruber, S., Haeberli, W. (2007). Permafrost in steep bedrock slopes and its temperature-related destabilization following climate change. Journal of Geophysical Research, 112, F02S18.

King, R. P. (2001), Modeling and simulation of mineral processing systems. Butterworth Heinemann, Boston.

Kittel, C., (1996) Introduction to solid state physics. 7th ed. (Wiley, New York).

Landau, L. D., Lifshitz, E. M. (2013). Fluid Mechanics: Landau and Lifshitz: Course of Theoretical Physics, Volume 6 (Vol. 6). Elsevier.

Locat, P., Couture, R., Leroueil, S., Locat, J., Jaboyedoff, M. 2006. Fragmentation energy in rock avalanches. Can. Geotech. J. 43, 830-851.

Lin, Q., Cheng, Q., Li, K., Xie, Y., & Wang, Y. (2020). Contributions of rock mass structure to the emplacement of fragmenting rockfalls and rockslides: insights from laboratory experiments. Journal of Geophysical Research: Solid Earth, 125(4), e2019JB019296.

Malusà, M., Polino, R., and Martin, S. (2005), Alpine-tectono-metamorphic evolution of the Gran San Bernardo nappe (Western Alps): constraints from the Grand Nomenon unit of the Zona Interna. Bull. Soc. Géol. France 176, 417-431.

Malusà, M. G., Polino, R., & Zattin, M. (2009). Strain partitioning in the axial NW Alps since the Oligocene. Tectonics, 28(3).

Malusà, M. G., Faccenna, C., Baldwin, S. L., Fitzgerald, P. G., Rossetti, F., Balestrieri, M. L., ... & Piromallo, C. (2015). Contrasting styles of (U) HP rock exhumation along the Cenozoic Adria-Europe plate boundary (Western Alps, Calabria, Corsica). Geochemistry, Geophysics, Geosystems, 16(6), 1786-1824.

Matas,G., Lantada, N., Coromina J., Gili J.A., Ruiz-Carulla R., Prades A. “RockGIS: a GIS-based model for the analysis of fragmentation in rockfalls” Landslide (2017).

Morrissey, M.M., Savage, W.Z., Wieczorek, G.F. (1999). Analysis of the 1996 Happy Isles event in Yosemite National Park. Journal of Geophysical Research 104(B10): 23189–23198.

Paranunzio, R., Laio, F., Chiarle, M., Nigrelli, G., Guzzetti, F. (2016) Climate anomalies associated with the occurrence of rockfalls at high-elevation in the Italian Alps. Nat. Hazards Earth. Syst. Sci.16(9):2085-2106. https://doi.org/10.5194/nhess-16-2085-2016

Pfeiffer, T.J, Bowen TD (1989) Computer simulation of rockfalls. Bull. - Assoc. Eng. Geol. 26:135–146

Phillips, M., Wolter, A., Lüthi, R., Amann, F., Kenner, R., & Bühler, Y. (2017). Rock slope failure in a recently deglaciated permafrost rock wall at Piz Kesch (Eastern Swiss Alps), February 2014. Earth Surface Processes and Landforms, 42(3), 426-438.

Polino, R., F. Bonetto, F. Carraro, Franco Gianotti, Y. Gouffon, M. G. Malusà, S. Martin, P. Perello, and A. Schiavo (2015). Note illustrative CARG "Foglio 090 Aosta della Carta Geologica d'Italia.", 1-144.

Poole, R. T. (1980). Cohesive energy of the alkali metals. American Journal of Physics, 48(7), 536-538. doi:10.1119/1.12056

Ravanel, L., Allignol, F., Deline, P., Gruber, S., Ravello, M. 2010. Rock falls in the Mont Blanc Massif in 2007 and 2008. Landslides7: 493–501.DOI:10.1007/s10346-010-0206-z

Ravanel, L., Magnin, F., & Deline, P. (2017). Impacts of the 2003 and 2015 summer heatwaves on permafrost-affected rock-walls in the Mont Blanc massif. The Science of the Total Environment, 609, 132– 143. https://doi.org/10.1016/j.scitotenv.2017.07.055

Reznichenko, N. V., Davies, T. R., Shulmeister, J., & Larsen, S. H. (2012). A new technique for identifying rock avalanche–sourced sediment in moraines and some paleoclimatic implications. Geology, 40(4), 319-322.

Rhodes, M. (1998), Introduction to particle technology. Wiley, Chichester.

Simpson, J. E. (1982). Gravity currents in the laboratory, atmosphere, and ocean. Annual Review of Fluid Mechanics, 14(1), 213-234. doi.org/10.1146/annurev.fl.14.010182.001241

Tromans, D. and Meech, J.A. (2002) Fracture Toughness and Surface Energies of Minerals: Theoretical Estimates for Oxides, Sulphides, Silicates and Halides. Minerals Engineering, 15, 1027-1041, 10.1016/S0892-6875(02)00213-3

Valero, A., Valero, Al., and Cortés, C. (2011). Exergy of Comminution and the Crepuscular Planet. In Proceedings of the 6th Dubrovnik Conference on Sustainable Development of Energy Water and Environmental Systems, Dubrovnik, Croatia, September, 25-29.

Viero, A., Furlanis, S., Squarzoni, C., Teza, G., Galgaro, A., Gianolla, P. (2013). Dynamics and mass balance of the 2007 Cima Una rockfall (Eastern Alps, Italy). Landslides 10: 393-408.

Walter, F., Amann, F., Kos, A., Kenner, R., Phillips, M., de Preux, A., et al. (2020). Direct observations of a three million cubic meter rock-slope collapse with almost immediate initiation of ensuing debris flows. Geomorphology, 351, 106933.

Wieczorek, G.F. (2002), Catastrophic rockfalls and rockslides in the Sierra Nevada, USA. In: Catastrophic landslides: Effects, Occurrence, and Mechanisms. The Geological Society of America, S.G. Evans and J.V DeGraff (eds.), pp. 165-190.

Wieczorek, G.F., Snyder, J.B., Borchers, J.W., and Reichenbach, P. (2007), Staircase Falls Rockfall on December 26, 2003, and Geologic Hazards at Curry Village, Yosemite National Park, California: U.S. Geological Survey Open-File Report 2007-1378, available @ http://pubs.usgs.gov/of/2007/1378/. Paper presented at the 1st North American Landslide Conference, Vail, Colorado June 3-8, 2007.

Wieczorek, G.F., Snyder, J.B., Waitt, R.B., Morissey, M.M., Uhrhammer, R.A., Harp, E.L., Norris, R.D., Bursik, M.I., Finewood, L.G. (2000). Unusual July 10, 1996, rock fall at Happy Isles, Yosemite National Park, California. GSA Bulletin, 112, 75-85.

Yashima, S., Kanda, Y., Sano, S. (1987) Relationships between particle size and fracture energy or impact velocity required to fracture as estimated from single particle crushing. Powder Technol 51:277–282

Zhang, ZX., Ouchterlony, F. (2022) Energy Requirement for Rock Breakage in Laboratory Experiments and Engineering Operations: A Review. Rock Mech Rock Eng 55, 629–667. https://doi.org/10.1007/s00603-021-02687-6

Supplementary materials

HyStone motion equations

The HyStone code computes the block trajectories by splitting them in a succession of elementary motions: free fly, rolling, sliding and impacts/bouncing. Hereafter we illustrate the equation regarding these types of motions. Under the free fly condition the following ordinary differential equation is imposed:

$$m_{bl}\ddot{u} = m_{bl}g \tag{38}$$

where the m_{bl} is the block mass, u is the centre of mass position vector, and g is the gravity field. For sliding condition the block velocity is obtained by imposing

$$\ddot{u} = g - f\hat{t} \tag{39}$$

where f is the friction coefficient and $\hat{t}$ is the unit vector obtained normalizing the projection of block the velocity onto the sliding plane. The rolling motion is obtained by integrating the following equations

$$\{I_{bl}\ddot{\theta}_{y,me} = TR_{bl} - Nb\ N = -m_{bl}\ g_{z,me}\ \ T = m_{bl}g_{x,me} - m_{bl}\ddot{x}_{me} \tag{40}$$

where $\ddot{\theta}_{y,me}$ is the y-component of block angular velocity, N and T are the normal and tangential force components acting at the contact point, respectively. R_{bl} and I_{bl} are the block radius and its inertia moment, respectively, b is the tangential arm of the normal force which is used to introduce the rolling resistance, $g_{x,me}$ and $g_{z,me}$ are the x- and z- components of the gravity field components, and $\ddot{x}_{me}$ is the x-component of the centre of mass acceleration. All the vector components in the previous equations refer to the mechanical reference system, i.e. a reference system tangent to the slope with x-axis aligned to the motion direction.

When the impact process is concerned, HyStone has many different models comprising the constant and not-constant restitution coefficients (Pfeiffer and Bowen 1989) and the evolution of the elasto-visco-plasticelast-visco-plastic model initially proposed by di Prisco and Vecchiotti (2006) and extended to prismatic and blocks (Dattola et al., 2021). In this work, the hybrid approach was used with normal and tangential restitution coefficients depending on the normal velocity at impact. In particular, the normal velocity component is given by the following expression

$$\dot{u}_{za,me} = \ -\frac{e_n}{1+\left(\frac{\dot{u}_{zb,me}}{D}\right)^2}\dot{u}_{zb,me} \tag{41}$$

where $\dot{u}_{zb,me}$ is the z-component (normal direction in the mechanical reference system) of the block velocity before the impact, $\dot{u}_z^{a,me}$ is the same but after the impact. D is a model parameter and e_n is the normal restitution coefficient depending only on the material properties. For tangential direction along y-axis the velocity components are null before and after since in the mechanical reference system y-axis is perpendicular to the block motion. Finally, the velocity components along x-axis are computed by means of the following expressions:

$$\dot{u}_{xa,me}\sqrt{\frac{T_1}{m_{bl}(R_{bl})^2+I_{bl}}} \tag{42}$$

where $\dot{u}_{xa,me}$ is the x-component of the block velocity after the impact, and T_1 is computed as

$$T_1 = (R_{bl})^2\left[I_{bl}\left(\dot{\theta}_{yb,me}\right)^2 + m_{bl}\left(\dot{u}_{xb,me}\ \right)^2\right]S_fF_f \tag{43}$$

where $\dot{u}_{xb,me}$ is the velocity x-component of centre of mass before the impact, $\dot{\theta}_{yb,me}$ is the y-component of the angular velocity before the impact. Coefficients S_f and F_f are assessed by means of the expressions

$$S_f = \frac{e_t}{1+\left(\frac{\dot{u}_{zb,me}}{Ce_n}\right)^2} \tag{44}$$

and

$$F_f = e_t + \frac{1-e_t}{B+\left(\dot{u}_{xb,me} - \frac{R_{bl}}{A}\dot{\theta}_{yb,me}\right)} \tag{45}$$

in which A, B and C are three model parameters, e_t is the tangential restitution coefficients depending on the material properties.

Bond's law for fragmentation energy

Bond's law, is employed to calculate the energy consumption in comminution apparatuses, industrial mills and crushers (Rhodes 1998, King). It has also been applied to rock avalanches (De Blasio, 2005; Locat et al., 2006). The Bond work index W is defined as the energy necessary to disintegrate a unit mass of material from the top size D (that can be considered as infinite in our problem) down to a particle size d. To account for he non-uniform distribution of particle size, the work index is conventionally set to the size diameter d_{80}, i.e., the particle diameter at which 80% of the particles have a diameter smaller than d_{80}. If d_{80} is measured in microns, the energy consumption per unit mass due to disintegration E_{DIS} is then (Rhodes 1998)

$$\frac{E_{DIS}}{M} = \frac{10\,W}{\sqrt{d_{80}(\mu n)}} \tag{46}$$

being M the parent block mass.

Using the grain distribution of the disintegrated rock in the aftermath of the Yosemite (Wieczorek et al., 2000), d80(µm) is about 2,500 (or 2.5 mm), and with *W=60,000 J/Kg* for granitoid rock, it follows that $E_{DIS}/\,M = 1.2\ 104\ J/Kg$. The fact that this is comparable or even higher than the energy per unit mass available shows that Bond's law is not useful when the particle size is much smaller than the typical final product of comminution machines, for which this formula is designed.

Figure S 1 Superimposition of the tracks obtained from simulation SIM01 with a frame taken from a video of the event.

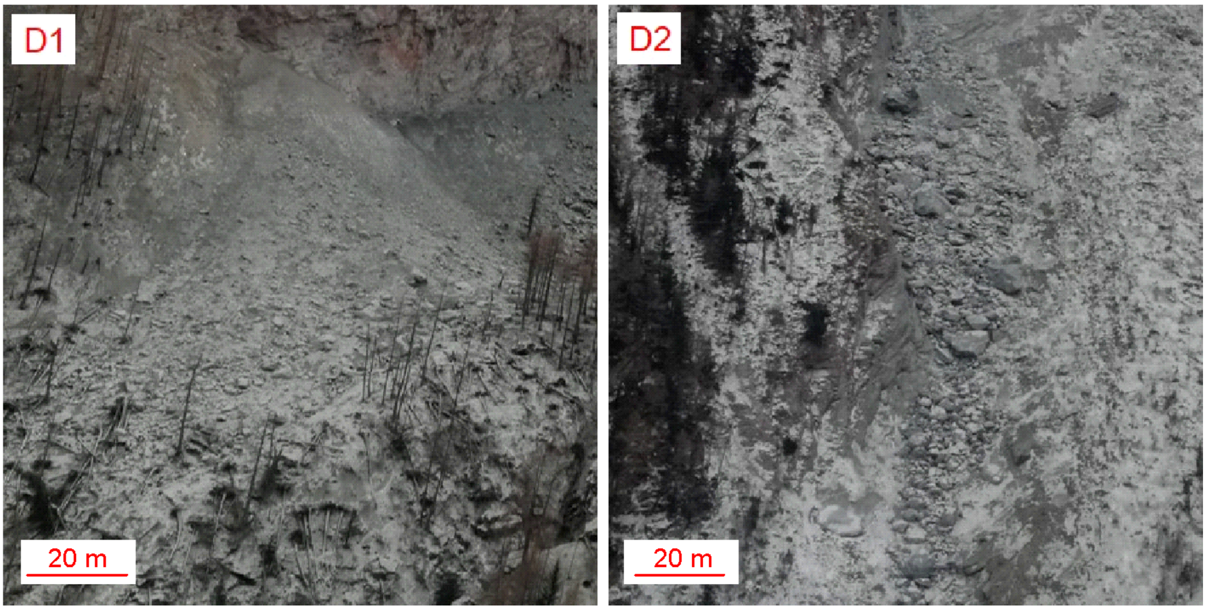

Figure S 2 The two deposits shown in Figure 3. These pictures have been taken by helicopter in November 2017, just a few days after the event

Table S 1 Values of normal and tangential restitution coefficients and of the friction coefficient for the different slope materials used in the rockfall numerical simulations.

Material denomination	e_n **[-]**	e_t **[-]**	μ_s **[-]**
Glacial deposit	65	80	0.40
Slope debris	65	70	0.60
Bare slope debris	65	70	0.50
Alluvial deposit	55	60	0.40
Outcropping rock	85	85	0.30
Sub-outcropping rock	80	80	0.30

Table S 2 Parameter calibration of the log normal particle size distributions (equation 16) for the seven samples collected at different locations within the dust cloud deposit(Figure 6).

Sample ID	ξ $[-]$	σ $[-](10^{-5})$	μ $[-](10^{-5})$	**Error** [%]
1	0.091	3.00	-1.296	0.0011
2	0.418	2.80	1.497	0.0006
3	0.034	2.88	1.69	0.0004
4	0.384	3.10	1.88	0.0004
5	0.456	2.71	1.47	0.001
6	0.81	3.40	2.15	0.0016

7	0.102	2.62	1.67	0.0413

Table S 3 Calculation of the new generated area based on the grain size and the fragmentation energy with $E_S = 0.5\ \frac{J}{m^2}$ *and an initial block volume* $V_{bl} = 8{,}000\ m^3$*.*

Sample ID	S $[km^2]\ (10^3)$	$E_f\ \left(E_s = \frac{0.5J}{m^2}\right)$ $[GJ]$	$\frac{E_f}{\rho_s V_{dust}}\ \left(E_s = \frac{0.5J}{m^2}\right)$ $\left[\frac{GJ}{kg}\right] (\cdot 10^{-5})$
1	5.095	2.55	1.70
2	3.621	1.81	1.21
3	3.212	1.61	1.07
4	2.976	1.41	9.41
5	3.755	1.89	1.26
6	3.216	1.61	1.07
7	3.012	1.51	1.01

Table S 4 List of the numerical simulations together with source area information with the corresponding volumes.

ID	***Block volume [m³]***	***Total gun volume [m³]***	***Launched blocks per cell***	***Number of source cells***	***Source Location***	***Fragmentation activated***
SIM01	1	499	1	551	Upper	N
SIM02	3	1,683	1	551	Upper	N
SIM03	10	5,071	1	551	Upper	N
SIM04	1	962	1	1,063	Lower	N
SIM05	3	3,246	1	1,063	Lower	N
SIM06	10	9,783	1	1,063	Lower	N
SIM07	1	4,895	10	551	Upper	N
SIM08	3	16,822	10	551	Upper	N
SIM09	10	50,707	10	551	Upper	N
SIM10	1	9,617	10	1,063	Lower	N
SIM11	3	32,460	10	1,063	Lower	N
SIM12	10	97,807	10	1,063	Lower	N
SIM13	1	499	1	551	Upper	Y
SIM14	3	1,683	1	551	Upper	Y

SIM15	10	5,071	1	551	Upper	Y
SIM16	1	962	1	1,063	Lower	Y
SIM17	3	3,246	1	1,063	Lower	Y
SIM18	10	9,783	1	1,063	Lower	Y
SIM19	1	4,895	10	551	Upper	Y
SIM20	3	16,822	10	551	Upper	Y
SIM21	10	50,707	10	551	Upper	Y
SIM22	1	9,617	10	1,063	Lower	Y
SIM23	3	32,460	10	1,063	Lower	Y
SIM24	10	97,807	10	1,063	Lower	Y

Table S 5 Stochastic ranges of the changed variables in the numerical simulations performed with HyStone code.

	e_n	e_t	μ_s
Stochastic range [%]	75	75	30
min	0	0	0.3
max	1	1	1

Rockfall events during which the processes of fragmentation and impact with trees played a decisive role

The work presented above (about Pousset event in 2017) is a case study of propagation analyses, in which the utmost attention was paid to studying the starting and triggering conditions, the complexity of the geological history, and the dynamics of the event, but the focus was limited to modeling the rockfall events without hypothesizing potential future scenarios. This chapter also presents two new case studies in which this possibility was considered, and a hazard analysis was conducted, taking into account the frequencies associated with these hypothetical future events. Moreover, the characteristics of the slope, such as the presence of forests, and the type of rockfall, whether it is fragmental, are considered during modeling, contributing to the overall assessment of rockfall potential and hazard. Indeed, we performed rockfall simulations using Hy-Stone, incorporating both the presence of trees and fragmentation through specific algorithms implemented in the code. By comparing these simulations with a more classical approach that attempts to implicitly account for such phenomena in the model parameters (restitution coefficients and rolling friction), we were able to quantify the impact of these phenomena on the design of countermeasures and on hazard assessment. This paper demonstrates that hazard changes significantly when explicitly accounting for these phenomena, emphasizing the necessity of doing so when designing mitigation measures.

Research background

The restitution coefficients

As well described in Scioldo (2006), the rockfall problem is quite complex because the real behaviour of boulders, when rolling down a slope, depends on apparently insignificant geometric and mechanical details. The interaction between the shape of the boulders and the trajectory they follow does not adhere to a linear pattern; rather, it exhibits chaotic characteristics. Notably, there exists no proportional relationship between alterations in initial conditions and corresponding shifts in the trajectory of descent. Even minute perturbations in the initial conditions often give rise to substantial and, consequently, unpredictable changes in the final outcomes. This underscores the infeasibility of establishing a model's calibration through a limited number of simulations, thereby precluding the precise prediction of the path and ultimate resting point of individual boulders in real-world scenarios. The only reasonable solution is a statistical approach (Scioldo, 2006), treating stop points not as isolated occurrences but as components of a probability distribution. A stochastic approach also encompasses geomechanical parameters that influence the behavior of blocks and takes into account variations along the path that may yield different values. These variations are incorporated into the analysis as probability distributions. The geomechanical parameters used in the model are defined as normal and tangential energy coefficients of restitution, friction coefficients of the rolling boulders. These parameter sets should be calibrated for a small range of block sizes, as the same material can have an elastic or plastic behaviour as a function of the rock boulder size. Accurate modelling of the rebound of a block at impact necessitates the utilization of geological and geomorphological data collection to delineate regions where uniform sets of restitution and friction coefficients can be assigned, considering that both slope and block characteristics affect rebound. The slope characteristics which more influence the bouncing phenomenon are strength, stiffness, roughness and inclination, while the rock characteristics are strength, stiffness, weight, size and shape, their velocity (translational and rotational) and their incidence angle configuration at the impact (Labiouse and Descoeudres, 1999). The kinetic energy of the block at impact converts into rebound kinetic energy, energy diffusion, and energy dissipation within the slope. Elastic deformation of the slope material, though present, is often disregarded (Volkwein et al. 2011). Energy diffusion is linked to elastic wave propagation at the impact point (Bourrier et al. 2008; Giani 1992), while energy dissipation mostly arises from frictional (plastic) processes within the slope material (Bozzolo and Pamini 1986; Giani 1992; Bourrier et al. 2008) and the fragmentation of the block and/or soil particles (Azimi et al. 1982; Fornaro et al. 1990; Giani 1992). Energy dissipation depends on the ratio between the block size and slope particle size, slope characteristics (e.g., hardness, roughness, composition), block properties (shape, size, mass, hardness), kinematic characteristics, and the kinetic energy of the block before impact, which is related to its mass and impact velocity (Ansari et al. 2015; Asteriou et al. 2013a; Jones et al. 2000; Pfeiffer and Bowen 1989; Urciuoli 1996; Ushiro et al. 2000).

Most of the existing rockfall trajectory models use coefficients of restitution (normal and tangential) to describe assess the impact process, and numerous experimental investigations were carried out in the field (Ritchie, 1963; Broili, 1977; Kirkby and Statham, 1975; Lied, 1977; Bozzolo et al., 1988; Pfeiffer and Bowen, 1989; Fornaro et al., 1990; Kobayashi et al., 1990; Azzoni et al., 1992; Azzoni and De Freitas, 1995; Statham and Francis, 1986; Wu, 1985; Giani, 1992; Urciuoli, 1996; Evans and Hungr, 1993; Wyllie, 2014; Giacomini et al., 2009, 2010, 2012; Asteriou et al., 2012; Ferrari et al., 2013; Berger and Dorren, 2006; Spadari et al., 2012) and in the laboratory (Camponuovo, 1977; Azimi and Desvarreux, 1977; Statham, 1979; Chau et al., 1998a, 1998b; Ushiro et al., 2000; Kamijo et al., 2000; Wong et al., 1999, 2000; Kawahara and Muro, 1999; Buzzi et al., 2012; Heidenreich, 2004; Bourrier, 2008; Imre et al., 2008; Masuya et al., 2001; Ye et al., 2019; Ji et al., 2019; Azimi et al., 1982; Asteriou et al., 2012; Ansari et al., 2015; Asteriou and Tsiambaos, 2018) to investigate the mechanisms occurring during impact and assess them. However, it is a common challenge to determine which values to assign to the parameters when it is not possible to conduct in-situ tests. In the literature, there are some lists of reported values for coefficients of restitution. In particular, an overview of typical values considered for the coefficients of restitution can be found in Scioldo (2006), which compiles some of the most famous works in this regard (Hoek, 1987; Descoeudres et Zimmermann, 1987; Pfeiffer and Bowen, 1989; Hungr and Evans, 1988; Giani, 1992; Budetta et al., 1996).

This chapter analyzes the role of restitution and friction coefficients in cases where there is a significant impact of blocks against trees and dynamic block fragmentation. It quantifies the importance of an approach that explicitly considers the presence of forests and the occurrence of fragmentation when discussing risk mitigation. In cases involving forests and fragmentation, a common approach involves adjusting coefficients to account for the effects of the forest and fragmentation. These coefficients are calibrated based on the kinetic energies involved in the phenomenon. However, this coefficient modification does not consider block mass, and the dynamic of the events. Explicitly modeling the impacts with trees and the fragmentation process remains challenging both theoretically and practically, introducing additional uncertainties in the analysis of rockfall dynamics and risk, but we made an attempt through Hy-Stone fragmentation sub-models (more details in paragraph “Hy-Stone”, Chapter 2).

The distinction between hazard and risk in the assessment and management of landslide risk

In the field of landslides, the term "risk" refers to the probability of a landslide occurring in a specific location and during a certain period of time, as well as the consequences that such an event could have on human life, property, and the surrounding environment. On the other hand, the term "hazard" refers to the measure of the landslide event, in terms of its size and propagation velocity, and therefore its capacity to cause damage and put human life and the environment at risk. In summary, risk is related to the probability of the landslide event and the consequences that it may have, while hazard refers to the severity of the event itself. It is important to keep in mind that hazard and risk are related but distinct concepts, and that both must be considered in the assessment and management of landslide risk.

The definition of risk given by Fell et al. (2008) is: “A measure of the probability and severity of an adverse effect to health, property or the environment. Risk is often estimated by the product of probability of a phenomenon of a given magnitude times the consequences. However, a more general interpretation of risk involves a comparison of the probability and consequences in a non-product form. For Quantitative Risk Assessment the use of the landslide intensity is recommended.” In the case of rockfalls, the risk is often analyzed considering different volumes and energies, which have different probabilities (or frequencies).

There are different types of risk:

- Individual risk to life (or individual human risk): “The annual probability that a particular life will be lost”.
- Societal risk to life (or societal human risk): “The risk of multiple fatalities or injuries in society as a whole”, which can be expressed as the annual number of deaths.
- Non-human societal risk concerns “financial, environmental, and other losses”. The elements at risk can be “buildings and engineering works, economic activities, public services utilities, infrastructure and environmental features in the area potentially affected by landslides”.

The definition of hazard given by Fell et al. (2008) is “A condition with the potential for causing an undesirable consequence. The description of landslide hazard should include the location, volume (or area), classification and velocity of the potential landslides and any resultant detached material, and the probability of their occurrence within a given period of time.” The potential cause for an unfavorable outcome in rockfalls is the movement of rock material, while the crucial factors that dictate the outcome are the volume, trajectory, and velocity of the rock blocks. These elements are determined by the geometry and position of the rock compartments prone to falling and the characteristics of the propagation zone. So, we see that with respect to the definition of risk, in the definition of hazardousness by Fell et al. (2008), the concept of frequency is introduced, which plays a central role in its calculation. As outlined in Hantz et al. 2021, temporal frequency is the number of occurrences per unit of time, and it can be divided by an area or a length giving a spatial-temporal frequency. When the qualifiers “temporal” and “spatial–temporal” are not used, confusion is possible with the term “frequency” used in the statistical sense, which does not refer to time.

Different temporal (or spatial–temporal) frequencies can be used:

- Failure frequency or rockfall release frequency: the number of rock compartments that detach from a given source area, per unit of time (and per unit of area for the spatial–temporal frequency). The spatial–temporal release frequency allows to compare the activity of different cliff areas (Guerin et al., 2014, D’Amato et al., 2015).
- Fragment release frequency: the number of rock fragments that detach from a given source area, per unit of time (and per unit of area for the spatial–temporal frequency). Hantz et al., 2017 proposed a method to derive the fragment release frequency from the failure frequency.
- Event transit frequency: the number of rock fall events that pass through a given location, per unit of time (and per unit of length for the spatial–temporal frequency). In other words, it is the number of rock fall events, at least one fragment of which passes through the given location. The spatial–temporal passage frequency allows one to derive the passage frequency at any location according to its width, measured perpendicularly to the movement direction (Evans et al., 1993).
- Fragment transit frequency: the number of rock fragments that pass through a given area or location, per unit of time (and per unit of length for the spatial–temporal frequency).
- Fragment deposit or landing frequency (Evans et al., 1993, van Veen et al., 2018): the number of rock fragments that stop in a given area, per unit of time (and per unit of area for the spatial–temporal frequency).

To comprehensively describe the hazard of rockfalls in a specific area, it is essential to understand the different temporal frequencies and to incorporate the probabilities or frequencies of a rock block or fragment reaching a particular spot within a specific timeframe with a minimum volume, velocity, or energy, as well as height. Just as the disaggregation and fragmentation of blocks are important, the presence of elements along the slope such as trees, capable of modifying the trajectories of the blocks, interrupting them or in any case reducing their kinetic energy, is also important.

Assessing impact frequency of fragmental rockfalls

As highlighted in Corominas et al., 2003, the concept of hazard is space-time. It is defined as the probability of occurrence, within a specific period of time and within a given area, of a potentially damaging phenomenon (Varnes, 1984). According to this definition, landslide hazard assessment requires not only the identification of landslide-susceptible sites but also to determine the probability of slope failure, and, implictely, its frequency. Information on rock-fall frequency is critical in order to fully evaluate hazard (Varnes, 1984), but to assess the impact frequency of fragmental rockfalls, we rely on a combination of factors, including the onset of a rockfall and the propagation of individual blocks within the fallen compartment. As mentioned by Crosta & Agliardi (2003), Jaboyedoff et al. (2005), and Labiouse & Abbruzzese (2011), the assessment of this frequency can be approached in two ways: through a historical approach (Stock et al. 2014) or a mechanical approach.

The historical approach involves observing the blocks deposited over a given period, assuming that these blocks remain undisturbed (removed or mined). Traditional methods like tree-ring analysis have been used for dating rockfalls, as seen in works by Clague (2010) and Stoffel et al. (2010). Lichenometry has also been employed for this purpose, as demonstrated by research from Bull et al. (1994). For dating outlying boulders, Stock et al. (2014) utilized terrestrial cosmogenic beryllium-10 exposure dating. However, this historical approach has limitations, especially when historical data is scarce or when dealing with smaller rockfalls, it is limited by the relatively short historical time period and does not contain specific information about the recurrence of events that produce outlying boulders beyond the base of talus slopes (Stock et al., 2014). Moreover, it only provides information on the total volume of rockfalls, not the number or volumes of individual blocks required for propagation simulations.

The mechanical or physically based approach aims to determine the failure time of potentially unstable rock compartments, their fragmentation, and their propagation on the slope. While this approach is more comprehensive, predicting the exact failure time of these compartments is usually impossible in the present state of knowledge (except in some cases when the compartment is already moving and is monitored).

To bridge these gaps, a mixed method, combining historical data for onset frequency assessment and mechanical analysis for block propagation modeling, is commonly employed (Hungr et al, 1999; Guzzetti et al. 2003; Corominas et al, 2005; Fell et al, 2005; Jaboyedoff et al, 2005; Agliardi et al, 2009; Abbruzzese et al, 2009). As highlighted by Hantz et al. (2018), this approach allows for a more comprehensive evaluation of the impact frequency and it consists in: i) determining the mean annual total rockfall volume (volumetric retreat rate), using the volume-frequency relation for rockfalls, ii) determining the volume distribution of the individual blocks which will propagate on the slope, iii) simulating the trajectories of the blocks which fall from the cliff during a period of interest, using a probabilistic approach to take account of the variability of the parameters.

Historical rockfall data analysis has revealed a power-law relationship between rockfall volume and cumulative frequency. This relationship enables the calculation of temporal rockfall frequency based on the observation period's length, cliff area, and a parameter representing the cliff's rockfall activity. To determine the total volume of rockfalls per unit time, researchers integrate the volume-frequency relationship, encompassing rockfalls of varying sizes that occurred both within and beyond the observation period (Hantz et al., 2003). Modern techniques like terrestrial laser scanning and photogrammetry have enhanced the detection of smaller rockfalls, enabling shorter observation periods and more accurate volume-frequency relations, especially in uniform cliff areas (Rosser et al., 2005; Abellan et al., 2010; Dewez et al., 2013; Guerin et al., 2014).

Furthermore, to determine the impact frequency at specific points beneath the cliff, we need to understand the volume distribution of individual blocks that propagate down the slope. This distribution results from factors such as the initial structure of the rock mass and the fragmentation process. It can be determined through block inventories, which involve measuring the dimensions of blocks deposited by rockfalls. Research by Hantz et al. (2014) and Ruiz-Carulla et al. (2015) suggests that also block volume distribution typically follows a power-law pattern with a scaling exponent, describing the cumulative number of blocks larger than a specific volume. To calculate the total block volume, integration of the volume-frequency relation is necessary (Hantz et al., 2014). While this volume distribution may not fully represent initial propagation, considering potential fragmentation during early impacts, it serves as a reasonable approximation for most of the trajectory.

Finally, to simulate trajectories of falling blocks over a defined period, a 3D block propagation model is utilized. Models allow for the calculation of impact frequencies for different cells on the slope, taking into account the number of blocks reaching each cell and the length of the simulated period. By combining historical data, mechanical analysis, and simulation modeling, it is possible to comprehensively assess the impact frequencies associated with fragmental rockfalls (Hantz et al., 2018).

In the paper below, we adopted a methodology inspired by Hantz et al. (2018) to calibrate onset frequency parameters. This approach links the magnitude-frequency distribution of recorded rockfall events with the size-frequency distribution of blocks observed along the talus at the same site. By combining these two distributions, we calculated the onset frequency accurately, considering the natural comminution of large rockfall volumes upon impact with the slope. This methodology emphasizes the importance of the block size distribution in defining design volumes and ensures the correct determination of onset frequency, contributing to a comprehensive hazard assessment.

The strategies for mitigating rockfall hazards

Risk mitigation measures aim to decrease the probability of hazardous events occurring, such as rockfall, by implementing protective measures. Mitigating the danger associated with rockfall can be achieved through various strategies, including engineering or nature-based measures. Engineering measures, such as rockfall barriers, ditches, embankments, and catch fences, can provide protection by intercepting falling rocks and preventing them from reaching their target. Nature-based measures, such as safeguarding protective forests, reforestation, or the use of bioengineering techniques, can intercept and interrupt blocks and stabilize slopes, reducing the likelihood of rockfall. Implementing these mitigation strategies significantly reduces the risk of damage or loss of life from rockfall, making the area safer and more secure.

Rockfall protection structures in Italy and Europe are designed based on site-specific conditions and require the application of various geotechnical engineering methods and techniques. The design process involves an initial assessment of the rockfall risk in the affected area, considering factors such as terrain morphology, geology, topography, and vegetation. Based on this assessment, the appropriate technical protection solutions are identified, which can be passive or active. Passive protection structures prevent rocks from falling onto the road or affected area and consist of containment barriers such as walls or nets. These structures are designed to the size and energy of the rocks that are expected to fall. Active protection structures use techniques such as drainage, naturalization, terracing, or concrete walls to stabilize the slope and prevent rockfall when instability is the cause. The design process also includes evaluating the environmental impacts of the chosen protection solutions, selecting materials, and planning construction and maintenance activities, as well as cost and schedule estimates.

In Italy, the Department of Civil Protection has established guidelines for the design of rockfall protection structures, while in Europe, there are various national regulations and EU directives that provide guidance and requirements for the design and construction of these structures. Italy's guidelines for the design of rockfall protection structures established by the Department of Civil Protection provide a methodology for evaluating rockfall risk and indications for the design of protective structures. The guidelines define methods for risk assessment, identifying at-risk areas, selecting technical solutions, defining design criteria, cost and time estimates, and maintenance procedures. Additionally, Italy has established UNI standards (Italian National Unification Body) that govern the design and construction of rockfall protection structures, and the design of rockfall barriers is based on the use of the 95th percentiles of the blocks' height in flight and their kinetic energy, obtained from numerical models (UNI 11211).

To obtain the necessary input for the correct sizing and positioning of protective structures, rockfall hazard and risk assessment is necessary. The design of defensive works requires numerical modeling of rockfalls to assess the dynamics of the blocks (i.e., velocity, kinetic energy, and bouncing height) and the lateral and longitudinal spreading (Agliardi & Crosta 2003; Volkwein et al., 2009). In the paper presented in this chapter, the importance of creating a detailed modeling of rockfall events is discussed and quantified, including the processes that can lead to the interception, diversion, and dispersion of block trajectories, as well as the processes that can cause variations in the kinetic energy of the falling blocks.

Quantifying the contribution of fragmentation and tree impact on rockfall dynamics and hazard

When it comes to rockfall risk, it is important to take into account all the factors that contribute to determining it. In particular, the hazard associated with rockfalls is the potential for rocks or boulders to detach from a cliff, rock face, or hillside and fall onto people, property, or infrastructure below. This hazard is inherent in the physical characteristics of the rock and the geological and environmental conditions of the area. The risk associated with rockfall hazard depends on various factors, such as the location and frequency of rockfall events, the size and trajectory of falling rocks, and the vulnerability of people and property in the affected area. Therefore, it is crucial to carry out a hazard analysis and risk assessment for rockfalls to identify the areas where rockfall hazards exist, evaluate the potential consequences of rockfall events, and develop appropriate measures to manage and mitigate the risk. In this regard, it is essential to consider and simulate the fragmentation phenomenon, which can reduce the kinetic energy of the falling blocks and modify their trajectories. Similarly, the presence of vegetation on the slope capable of retaining or modifying the trajectories and kinetic energies of the blocks is also crucial.

The research question behind this chapter is therefore: *Is it possible to quantify the contribution of the two processes of fragmentation and impact on trees based on a comparison between numerical simulations that explicitly take them into account and simulations that only implicitly consider them?* This chapter presents the work of Lanfranconi et al. (2023) published in Natural Hazards and Earth System Sciences journal, which addresses this question and investigates the effects of trees and block fragmentation on rockfall dynamics and resulting hazard. The authors use two case studies of rockfall events in which the block fragmentation process and the block impact process on trees played a significant role in the event dynamics. They replicate the events using the 3D rockfall simulator Hy-Stone and, once the parameters of both models are calibrated, simulate potential future events. With the results obtained using and not using the specific fragmentation and tree impact algorithms, the authors compare the kinetic energies associated with the 95th percentile of the simulated distributions and discuss any differences in terms of designing defense works. Subsequently, the authors use a new probabilistic rockfall hazard analysis (PRHA) method to quantify the impact of those phenomena on hazard, building rockfall hazard curves starting from a set of block-volume scenario simulations. By using an onset frequency for five different volume classes obtained through the combination of the magnitude frequency relationship of rockfall events with the size frequency relationship of blocks along the talus, the authors propose hazard maps. One map was created using the fragmentation algorithm during the development process, one in which it was not used, one that utilized the tree impact algorithm, and one that did not.

I’m author of the paper below, for which I contributed to the conceptualisation of the project, I dealt with formal analysis, investigation, methodology, visualisation, writing of the original draft, and reviewing and editing of the text.
https://doi.org/10.5194/nhess-23-2349-2023

Background Bibliography

Abbruzzese, J. M., Sauthier, C., & Labiouse, V. (2009). Considerations on Swiss methodologies for rock fall hazard mapping based on trajectory modelling. Natural Hazards and Earth System Sciences, 9(4), 1095-1109.

Abellán, A., Calvet, J., Vilaplana, J. M., & Blanchard, J. (2010). Detection and spatial prediction of rockfalls by means of terrestrial laser scanner monitoring. Geomorphology, 119(3-4), 162-171.

Agliardi, F., Crosta, G. B., & Frattini, P. (2009). Integrating rockfall risk assessment and countermeasure design by 3D modelling techniques. Natural Hazards and Earth System Sciences, 9(4), 1059-1073.

Ansari MK, Ahmad M, Singh R, Singh TN. (2015). Correlation between Schmidt hardness and coefficient of restitution of rocks. Journal of African Earth Sciences 104:1-5. doi:https://doi.org/10.1016/j.jafrearsci.2015.01.005

Asteriou P, Saroglou H, Tsiambaos G. (2012). Geotechnical and kinematic parameters affecting the coefficients of restitution for rock fall analysis. International Journal of Rock Mechanics and Mining Sciences 54:103-113. doi:https://doi.org/10.1016/j.ijrmms.2012.05.029

Asteriou P, Saroglou H, Tsiambaos G. (2013). Rockfalls: influence of rock hardness on the trajectory of falling rock blocks. Bulletin of the Geological Society of Greece 47:1684. doi:https://doi.org/10.12681/bgsg.11033

Asteriou P, Tsiambaos G. (2018). Effect of impact velocity, block mass and hardness on the coefficients of restitution for rockfall analysis. International Journal of Rock Mechanics and Mining Sciences 106:41-50. doi:https://doi.org/10.1016/j.ijrmms.2018.04.001

Azimi C, Desvarreux P, Giraud A, Martin-Cocher J. (1982). Méthode de calcul de la dynamique des chutes de blocs - Application à l'étude du versant de la montagne de La Pale (Vercors). Bull de Liaison Labo P et Ch 122:93-102

Azimi C, Desvarreux P. (1977). Calcul de Chutes de Blocs et Vérification sur Modèle Réduit. Paper presented at the Association pour le développement des recherches sur les glissements de terrain, Grenoble

Azzoni A, De Freitas MH. (1995). Experimentally gained parameters, decisive for rock fall analysis. Rock Mechanics and Rock Engineering 28:111-124. doi:https://doi.org/10.1007/BF01020064

Azzoni A, Rossi PP, Drigo E, Giani GP, Zaninetti A. In situ observation of rockfall analysis parameters. In: Sixth International Symposium of Landslides, 1992. pp 307-314

Berger F, Dorren LKA. (2006). Objective comparison of rockfall models using real size experimental data. Disaster Mitigation of Debris Flows, Slope Failures and Landslides:245-252

Bourrier F, Nicot F, Darve F. (2008). Physical processes within a 2D granular layer during an impact. Granular Matter 10:415-437. doi:https://doi.org/10.1007/s10035-008-0108-0

Bozzolo D, Pamini R. (1986). Simulation of rock falls down a valley side. Acta Mechanica 63:113-130. doi:https://doi.org/10.1007/bf01182543

Broili L. Relations between scree slope morphometry and dynamics of accumulation processes. In: Meeting on Rockfall dynamics and protective works effectiveness, 1977. pp 11-23

Bull, W. B., King, J., Kong, F., Moutoux, T., & Phillips, W. M. (1994). Lichen dating of coseismic landslide hazards in alpine mountains. In Geomorphology and Natural Hazards (pp. 253-264). Elsevier.

Buzzi, O., Giacomini, A., & Spadari, M. (2012). Laboratory investigation on high values of restitution coefficients. Rock mechanics and rock engineering, 45, 35-43.

Camponuovo GF. (1977). ISMES experience on the model of St. Martino. Proc Meet Rockfall Dynamics Protective Works Effectiveness 90:25-38

Chau KT, Chan LCP, Wu JJ, Liu J, Wong RHC, Lee CF. (1998a). Experimental studies on rockfall and debris flow. Proc Seminar on Planning, Design and Implementation of Debris Flow and Rockfall Hazards Mitigation Measures:115-128

Chau KT, Wong RHC, Lee CF. (1998b). Rockfall problems in Hong Kong and some new experimental results for coefficients of restitution. International Journal of Rock Mechanics and Mining Sciences 35:662-663

Chau KT, Wong RHC, Wu JJ. (2002). Coefficient of restitution and rotational motions of rockfall impacts. International Journal of Rock Mechanics and Mining Sciences 39:69-77. doi:https://doi.org/10.1016/S1365-1609(02)00016-3

Chau KT, Wu JJ, Wong RH, Lee CF. (1999b). The coefficient of restitution for boulders falling onto soil slopes with various values of dry density and water content. Proc Int Symp on Slope Stability Engineering: Geotechnical and Geoenvironmental Aspects 2:1355-1360

Clague, J. J. (2010). Dating landslides with trees. Tree Rings and Natural Hazards: A State-of-Art, 81-89.

Corominas, J., Copons, R., Moya, J., Vilaplana, J. M., Altimir, J., & Amigó, J. (2005). Quantitative assessment of the residual risk in a rockfall protected area. Landslides, 2, 343-357.

Corominas, J., Copons, R., Vilaplana, J. M., Altimir, J., & Amigó, J. (2003). Integrated landslide susceptibility analysis and hazard assessment in the principality of Andorra. Natural Hazards, 30, 421-435.

Crosta, G. B., & Agliardi, F. (2003). A methodology for physically based rockfall hazard assessment. Natural Hazards and Earth System Sciences, 3(5), 407-422.

Crosta, G. B., & Agliardi, F. (2003). A methodology for physically based rockfall hazard assessment. Natural Hazards and Earth System Sciences, 3(5), 407-422.

D’Amato, J.; Guerin, A.; Hantz, D.; Rossetti, J.P.; Baillet, L.; Mariscal, A.; Jaboyedoff, M. Influence of Geological and Meteorological Factors on the Frequency of Rockfalls. In Proceedings of the ISRM Regional Symposium—EUROCK 2015, Salzburg, Austria, 7–10 October 2010; International Society for Rock Mechanics and Rock Engineering: Salzburg, Austria, 2015; p. 6.

Descoeudres F, Zimmermann TH (1987) Three-dimensional dynamics calculation of rock fall. Proceedings of the 6th International Congress on Rock Mechanics, Montreal, Vol. 1, pp 337–342

Dewez, T. J., Rohmer, J., Regard, V., & Cnudde, C. (2013). Probabilistic coastal cliff collapse hazard from repeated terrestrial laser surveys: case study from Mesnil Val (Normandy, northern France). Journal of Coastal Research, (65), 702-707.

Evans, S.G.; Hungr, O. The assessment of rockfall hazard at the base of talus slopes. Can. Geotech. J. 1993, 30, 620–636.

Fell, R., Ho, K. K., Lacasse, S., & Leroi, E. (2005). A framework for landslide risk assessment and management. Landslide risk management, 3-25.

Fell, R.; Corominas, J.; Bonnard, C.; Cascini, L.; Leroi, E.; Savage, W.Z. Guidelines for landslide susceptibility, hazard and risk zoning for land use planning. Eng. Geol. 2008, 102, 85–98.

Ferrari F, Giani G, Apuani T. (2013). Why can rockfall normal restitution coefficient be higher than one? Rendiconti Online Societa Geologica Italiana 24:122-124

Fornaro M, Peila D, Nebbia M. (1990). Block falls on rock slopes. Application of a numerical simulation program to some real cases. Proceedings of the 6th International Congress IAEG:2173

Giacomini A, Buzzi O, Renard B, Giani GP. (2009). Experimental studies on fragmentation of rock falls on impact with rock surfaces. International Journal of Rock Mechanics and Mining Sciences 46:708-715. doi:http://dx.doi.org/10.1016/j.ijrmms.2008.09.007

Giacomini A, Spadari M, Buzzi O, Fityus SG, Giani GP. Rockfall motion characteristics on natural slopes of eastern australia. In: Rock Mechanics in Civil and Environmental Engineering - Proceedings of the European Rock Mechanics Symposium, EUROCK 2010, 2010. pp 621-624

Giacomini A, Thoeni K, Lambert C, Booth S, Sloan SW. (2012). Experimental study on rockfall drapery systems for open pit highwalls. International Journal of Rock Mechanics and Mining Sciences 56:171-181. doi:https://doi.org/10.1016/j.ijrmms.2012.07.030

Giani GP, Giacomini A, Migliazza M, Segalini A. (2004). Experimental and Theoretical Studies to Improve Rock Fall Analysis and Protection Work Design. Rock Mechanics and Rock Engineering 37:369-389. doi:https://doi.org/10.1007/s00603-004-0027-2

Giani GP. (1992). Rock slope stability analysis. CRC Press, Balkera

Guerin, A.; D’amato, J.; Hantz, D.; Rossetti, J.-P.; Jaboyedoff, M. Investigating rockfall frequency using Terrestrial Laser Scanner. In Proceedings of the Vertical Geology Conference 2014, Lausanne, Switzerland, 6–7 February 2014; University of Lausanne, Switzerland: Lausanne, Switzerland, 2014.

Guzzetti F, Reichenbach P, Wieczorek GF (2003) Rockfall hazard and risk assessment in the Yosemite Valley, California, USA. Nat Hazards Earth Syst Sci 3:491–503

Hantz D, Rossetti JP, Servant F, D’Amato J (2014) Etude de la distribution des blocs dans un éboulement pour l’évaluation de l’aléa. Proceedings of Rock Slope Stability 2014, Marrakesh, p 10

Hantz, D., Corominas, J., Crosta, G. B., & Jaboyedoff, M. (2021). Definitions and concepts for quantitative rockfall hazard and risk analysis. Geosciences, 11(4), 158.

Hantz, D.; Rossetti, J.-P.; Valette, D.; Bourrier, F. Quantitative rockfall hazard assessment at the Mont Saint-Eynard (French Alps). In Proceedings of the 6th Interdisciplinary Workshop on Rockfall Protection, Barcelona, Spain, 22–24 May 2017.

Heidenreich, B. (2004). Small-and half-scale experimental studies of rockfall impacts on sandy slopes (No. THESIS). EPFL.

Hoek E (1987) RockFall—a program for the analysis of rockfall from slopes. Dept. Civil Engineering, Univ. Toronto, Ontario

Hungr O, Evans SG. (1988). Engineering evaluation of fragmental rockfall hazards. Landslides Proc 5th symposium, Lausanne, 1988 Vol 1:685-690

Hungr, O., Evans, S. G., & Hazzard, J. (1999). Magnitude and frequency of rock falls and rock slides along the main transportation corridors of southwestern British Columbia. Canadian Geotechnical Journal, 36(2), 224-238.

Imre B, Räbsamen S, Springman SM. (2008). A coefficient of restitution of rock materials. Computers & Geosciences 34:339-350. doi:https://doi.org/10.1016/j.cageo.2007.04.004

Jaboyedoff M, Dudt JP, Labiouse V. (2005). An attempt to refine rockfall hazard zoning based on the kinetic energy, frequency and fragmentation degree. Natural Hazards and Earth System Sciences 5:621-632

Ji Z-M, Chen Z-J, Niu Q-H, Wang T-J, Song H, Wang T-H. (2019). Laboratory study on the influencing factors and their control for the coefficient of restitution during rockfall impacts. Landslides 16:1939-1963. doi:https://doi.org/10.1007/s10346-019-01183-x

Jones CL, Higgins JD, Andrew RD. (2000). Colorado Rockfall Simulation Program Users Manual for Version 4.0. Denver: Colorado Department of Transportation. Colorado Rockfall Simulation Program Version 40

Kamijo A, Onda S, Masuya H, Tanaka Y. (2000). Fundamental test on restitution coefficient and frictional coefficient of rock fall. 5th Symposium on Impact Problems in Civil Engineering:83-86

Kawahara S, Muro T. (1999). Effect of soil slope gradient on motion of rockfall. International Symposium on Slope Stability Engineering 2:1343-1348

Kirkby MJ, Statham I. (1975). Surface stone movement and scree formation. Journal of Geology 83:349-362

Kobayashi Y, Harp EL, Kagawa T. (1990). Simulation of rockfalls triggered by earthquakes. Rock Mechanics and Rock Engineering 23:1-20. doi:https://doi.org/10.1007/BF01020418

Labiouse V, Abbruzzese JM (2011) Rockfall hazard zoning for land use planning. In: Stéphane Lambert, François Nicot (eds) Rockfall engineering. Wiley/ISTE ltd, New York/London

Labiouse V, Descoeudres F. Possibilities and difficulties in predicting rockfall trajectories. In: Proc. of the Joint Japan-Swiss Scientific Seminar on Impact Load by Rock Falls and Design of Protection Structures, Kanazawa, Japan, 1999. pp 29-36

Lanfranconi, C., Frattini, P., Sala, G., Bertolo, D., Sun, J., & Crosta, G. B. (2023). Accounting for the effect of forest and fragmentation in probabilistic rockfall hazard. EGUsphere, 1-27.

Lied K. (1977). Rockfall problems in Norway. Rockfall Dynamics and Protective Work Effectiveness 90:51-53

Masuya H, Ihara T, Onda S, Kamijo A. (2001). Experimental study on some parameters for simulation of rock fall on slope. Fourth Asia-Pacific Conf on Shock and Impact Loads on Structures:63-69

Pfeiffer TJ, Bowen TD. (1989). Computer simulation of rockfalls. Bulletin - Association of Engineering Geologists 26:135-146

Ritchie AM. (1963). Evaluation of rockfall and its control. Highway Research Record 17:13-28

Rosser, N. J., Petley, D. N., Lim, M., Dunning, S. A., & Allison, R. J. (2005). Terrestrial laser scanning for monitoring the process of hard rock coastal cliff erosion. Quarterly Journal of Engineering Geology and Hydrogeology, 38(4), 363-375.

Ruiz-Carulla R, Corominas J, Mavrouli O. (2015). A methodology to obtain the block size distribution of fragmental rockfall deposits. Landslides 12:815-825. doi:https://doi.org/10.1007/s10346-015-0600-7

Scioldo G. (2006). User guide ISOMAP & ROTOMAP-3D surface modelling and rockfall analysis. http://www.geoandsoft.com/manuali/english/rotomap.pdf.

Spadari M, Giacomini A, Buzzi O, Fityus S, Giani GP. (2012). In situ rockfall testing in New South Wales, Australia. International Journal of Rock Mechanics and Mining Sciences 49:84-93. doi:https://doi.org/10.1016/j.ijrmms.2011.11.013

Statham I, Francis S. (1986). Hillslope processes. Influence of Scree Accumulation and Weathering on the Development of Steep Mountain Slopes

Statham I. (1979). A simple dynamic model of rockfall: Some theoretical principles and field experiments. International Colloquium on Physical and Geomechanical Models:237-258

Stock, G. M., Luco, N., Collins, B. D., Harp, E. L., Reichenbach, P., & Frankel, K. L. (2014). Quantitative rock-fall hazard and risk assessment for Yosemite Valley, Yosemite National Park, California (p. 52citation_URL). US Department of the Interior, US Geological Survey.

Stoffel, M., Bollschweiler, M., Butler, D. R., & Luckman, B. H. (Eds.). (2010). Tree rings and natural hazards: a state-of-art (Vol. 41). Springer Science & Business Media.

Urciuoli G. (1996). Giornata di Studio Su la Protezione Contro la Caduta Massi Dai Versanti Rocciosi. Torino, Italy

Ushiro T, Shinohara S, Tanida K, Yagi N. (2000). A study on the motion of rockfalls on slopes. Proceedings of the 5th Symposium on Impact Problems in Civil Engineering:91-96

van Veen, M.; Hutchinson, D.J.; Bonneau, D.A.; Sala, Z.; Ondercin, M.; Lato, M. Combining temporal 3-D remote sensing data with spatial rockfall simulations for improved understanding of hazardous slopes within rail corridors. Nat. Hazards Earth Syst. Sci. 2018, 18, 2295–2308.

Volkwein, A., Roth, A., Gerber, W., & Vogel, A. (2009). Flexible rockfall barriers subjected to extreme loads. Structural engineering international, 19(3), 327-332.

Volkwein, A., Schellenberg, K., Labiouse, V., Agliardi, F., Berger, F., Bourrier, F., ... & Jaboyedoff, M. (2011). Rockfall characterisation and structural protection–a review. Natural Hazards and Earth System Sciences, 11(9), 2617-2651.

Wong RH, Ho K, Chau KT. (1999). Experimental study for rockfall simulation. Construction Challenges into the Next Century:92-97

Wong RHC, Ho KW, Chau KT. Shape and mechanical properties of slope material effects on the coefficient of restitution of rockfall study. In: 4th North American Rock Mechanics Symposium, 2000. American Rock Mechanics Association,Wu 1985

Wyllie DC. (2014). Calibration of rock fall modeling parameters. International Journal of Rock Mechanics and Mining Sciences 67:170-180. doi:https://doi.org/10.1016/j.ijrmms.2013.10.002

Ye Y, Thoeni K, Zeng Y, Buzzi O, Giacomini A. (2019). Numerical Investigation of the Fragmentation Process in Marble Spheres Upon Dynamic Impact. Rock Mechanics and Rock Engineering. doi:https://doi.org/10.1007/s00603-019-01972-9

Accounting for the effect of forest and fragmentation in probabilistic rockfall hazard

Camilla Lanfranconi[1], Paolo Frattini[1], Gianluca Sala[1], Giuseppe Dattola[1], Davide Bertolo[2], Juanjuan Sun[3], and Giovanni Battista Crosta[1]

[1] Department of Earth and Environmental Sciences, – DISAT, Università degli studi di Milano – Bicocca, Milan 20126, Italy
[2]Struttura attività geologiche, Regione autonoma Valle d’Aosta, Quart 11020, Italy
[3]Key Laboratory of Shale Gas and Geoengineering, Institute of Geology and Geophysics, Chinese Academy of Sciences, Beijing 100029, China

Abstract

The presence of trees along the slope and block fragmentation at impact strongly affect rockfall dynamics and hazard as a consequence. However, these phenomena are rarely simulated explicitly in rockfall studies. We performed rockfall simulations by using the 3D rockfall simulator Hy- Stone, modeling both the presence of trees and fragmenta- tion through specific algorithms implemented in the code. By comparing these simulations with a more classical approach that attempts to account implicitly for such phenomena in the model parameters and by using a new probabilistic rockfall hazard analysis (PRHA) method, we were able to quantify the impact of these phenomena on the design of countermea- sures and on hazard.

We demonstrated that hazard changes significantly when accounting explicitly for these phenomena and that a classi- cal implicit approach usually overestimates both the hazard level and the 95th percentile of kinetic energy, leading to an oversizing of mitigation measures.

Introduction

Rockfalls are widespread in mountain ranges, coastal cliffs, volcanos, riverbanks, and slope cuts, and threat people, structures and infrastructures, and lifelines (Crosta et al., 2015). Although rockfalls generally have a limited size, they are extremely rapid processes that exhibit high kinetic energies, long runout and damaging capability (Corominas et al., 2017). Rockfall hazard and risk assessment (Corominas et al., 2005; Agliardi et al, 2009; Lari et al, 2014; Wang et al., 2014; De Biagi et al, 2017; Farvacque et al, 2019, 2021; Hantz et al., 2021) and the design of defensive works (Volkwein et al., 2009) require numerical modelling of rockfalls to assess the dynamics of the blocks (i.e., velocity, kinetic energy and bouncing height) and the lateral and longitudinal spreading (Agliardi & Crosta 2003). In Italy, for example, the design of rockfall barriers is based on the use of the 95th percentiles of the blocks' height in flight and their kinetic energy, obtained from numerical models (UNI 11211; Volkwein et al., 2011). Since rockfall dynamics depends on block geometry, slope topography, surficial geology, vegetation, and some peculiar rockfall behaviours (e.g. dynamic fragmentation), the reliability of analyses and the efficiency of rockfall protections depend on the correct account for all these variables (Crosta et al., 2015). Both the characteristics of the slope (e.g. topography, material properties and presence of forests) and the type of rockfall (e.g. whether it is fragmental) must be taken into account during modelling, because they contribute to the overall extent of rockfall potential and hazard zonation in mountain areas (Frattini et al, 2012). Both these characteristics can modify the trajectories, the extent and the dynamics of the rockfall events, the frequency, and the probability of impact.

Forests provide important protection against rockfall in steep mountain terrain, defending structures and infrastructures (Berger et al. 2002; Dorren et al. 2004a; Perret et al. 2004). Thanks to this nature-based solution, maintenance and installation costs of technical protection measures, such as embankments or nets, are financially bearable or can even be avoided at many places due to the reduction of rockfall rebound heights and impact energies by previous impacts on trees (Grêt-Regamey et al., 2008; Häyhä et al., 2015; Getzner et al., 2017; Moos & Dorren, 2021). Although this protective effect is evident in hazard assessment processes because it supports decisions on risk prevention measures, it is often accounted only in implicit terms, by adopting a set of modified restitution coefficients (Pfeiffer and Bowen 1989; Azzoni et al, 1995). Less frequently, the presence of trees is simulated explicitely by using numerical modelling approaches (Dorren et al. 2006; Stoffel et al. 2006; Berger and Dorren 2007; Bigot et al. 2009; Jancke et al. 2009; Rammer et al. 2010; Leine et al. 2014; Radtke et al. 2014; Kajdiž et al. 2015; Dupire et al. 2016; Moos et al. 2017; Toe et al. 2018).

When stiff and strong rock blocks hit a hard impact substratum or other blocks of comparable size like a talus deposit, they may fragment and explode (Crosta et al., 2015). The rockfall fragmentation process is defined as the separation of the initial rock mass into smaller pieces generally upon the first impact on the ground (Evans & Hungr, 1993), and the resultant fragments propagate downslope following trajectories and new dynamics (especially in terms of kinetic energy and height) compared to the source block. This definition covers both the disaggregation of the block fragments delimited by pre-existing discontinuities in the initial mass and the generation of new fragments due to the breakage of intact rock (Corominas et al. 2012; Ruiz-Carulla, 2018). Block fragmentation is generally at the origin of extreme behaviors, major damages and accidents, and can interact strongly with protection structures (Nocilla et al., 2009; Wang et al., 2010; Corominas et al., 2019). Even if fragmentation during rockfall is recognized as fundamental in risk analysis (Corominas et al. 2012), a complete understanding of the process during rockfall has not been achieved so far, remaining a phenomenon largely neglected during numerical modelling. Only a few numerical codes allow modelling propagation that explicitly takes into account fragmentation (Crosta et al., 2003; Frattini et al, 2012; Matas et al., 2017; Ruiz-Carulla, 2018). When missing an explicit algorithm, the modeling of rockfalls with fragmentation can be done with two alternative approaches: either the model is calibrated to replicate the spreading of the event, including the most distal fragments, or the model is calibrated to replicate only the main deposit, neglecting the most distal blocks. The first approach leads to hazard overestimation, the second to hazard underestimation.

The aim of this paper is to quantify rockfall hazard when accounting for the presence of trees and fragmentation with an explicit simulation approach (i.e. using specific model), and to evaluate the differences with a classical approach that does not simulate explicitly such phenomena. The simulator Hy-Stone (Crosta et al. 2003; Crosta et al. 2004), which allows to model both the presence of forest and fragmentation, and a new revised Probabilistic Rockfall Hazard Analysis (PRHA) are adopted to quantify the impact of these phenomena on the design of countermeasures and on hazard.

Methods

Rockfall analysis

Hy-Stone (HS)

The analysis of rockfall propagation was performed by means of Hy-Stone, a 3D rockfall simulator that reproduces the block motion from the dynamics equations (Crosta et al. 2004; Frattini et al. 2012; Dattola et al., 2021) using a triangulated vector topography derived from Digital Terrain Models (DTMs). The model allows to simulate blocks with the shape of spheres, cylinders, ellipsoids, and discs. The stochastic nature of rockfall processes is accommodated by slope morphology and roughness, and by the random sampling of most parameters from different probability density distributions (e.g. uniform, normal, exponential). The block trajectories are computed by splitting them in a succession of elementary motions: free fly, rolling, sliding and impacts/bouncing. When the impact process is concerned, Hy-Stone has many different models comprising the constant and not-constant restitution coefficients (Pfeiffer and Bowen 1989) and the elasto-visco-plastic model initially formulated by di Prisco and Vecchiotti (2006) and subsequently extended by introducing rotation and prismatic blocks (Dattola et al., 2021). Specific sub-model explicitly account for the interactions between blocks and countermeasures or structures, between blocks and trees, and fragmentation (Frattini et al. 2012).

Tree-impact sub-model

The block-forest interaction is modeled through a stochastic tree-impact sub-model. Tree height, trunk diameter, absorbable energy, and density (as number of trees per 10 square meters) are used as input to calculate at each cell a probability of impact, that depends on the tree density, tree size and block size, and, in case of impact of impact, a loss of block kinetic energy and a lateral deviation of the trajectories (Frattini et al., 2012) are computed. The block kinetic energy lost by impact on tree stems is greatest for central impacts, and decreases according to a Gaussian distribution away from the stem axis, while the angular deflection of the block on impact is assumed to vary according to the type of impact (central, lateral, scour) (Dorren et al 2004b).

Fragmentation sub-model

Hy-Stone can simulate the splitting up of a block in fragments moving independently from each other. The fragmentation occurs at impact when the kinetic energy of a block exceeds a limit energy defined by Yashima et al, (1987) based on the Weibull distribution. The Yashima expression is:

$$E_{k,lim} = 0.15\, B_f\, C_f \left(\frac{1-\nu^2}{E}\right)^{\frac{2}{3}} \left(2R^{bl}\right)^{\frac{3m_w-5}{m_w}} \left[\sigma_0 V_0^{1/m_w}\right]^{5/3} \tag{47}$$

where $E_{k,lim}$ is the limit energy, ν is the Poisson's coefficient, E is the Young's modulus, R^{bl} is the radius of the parent block, V_0 is a reference volume, σ_0 is the strength at the reference volume and m_w is the Weibull distribution parameter. Coefficients B_f and C_f are computed according to the following expression:

$$B_f = \begin{cases} 1.0\ if\ m_w = 1 \\ \frac{\pi}{A_f} otherwise \end{cases} \tag{48}$$

and

$$C_f = 6^{\frac{5}{3m_w}} \tag{49}$$

Coefficient A_f is the result of the following expression:

$$A_f = \begin{cases} 0 & if\ m_w = 1 \\ \frac{5(m_w-1)}{3m_w} & otherwise \end{cases} \tag{50}$$

Therefore, the threshold fragmentation energy depends on the geomechanical properties of the block and its volume (the larger the block, the lower the fragmentation energy). Once the fragmentation criterion is satisfied, a distribution of fragments is generated according to a power-law distribution:

$$R(D) = \left(\frac{D}{D_m}\right)^n \tag{51}$$

where $R(D)$ is the fragment size distribution, D is the fragment diameter, D_m is the maximum fragment diameter and n is a model parameter. The maximum fragment size is a fixed fraction of the parent block size. The number of fragments is computed according to the mass conservation (the total fragments mass must be about the mass of the parent block) and the above distribution, and the energy of each fragment is calculated by means of the following expression:

$$E_{f,i}^{k,tr} = \beta\left(m_{fi}\right)^{\alpha_f} \tag{52}$$

in which m_{fi} is fragment mass, $E_{f,i}^{k,tr}$ is the translational kinetic energy of the fragment and α_f is a model parameter. β is computed by imposing the translational energy conservation. Once the kinetic energy of fragment is known the inverse formula gives the fragment ejection velocity modulus. Fragment ejection velocity direction is computed stochastically within a cone whose aperture is a model parameter. Frattini et al. (2012) showed that block fragmentation has an effect on the runout extent and on the spatial distribution of velocities and heights of the flying rocks. The largest fragments, however, display a behaviour that is more similar to that of the parent blocks.

Rockfall hazard assessment

To assess rockfall hazard, we propose a new revised PRHA (Probabilistic Rockfall Hazard Analysis), based on Lari et al. (2014), to build rockfall hazard curves starting from a set of block-volume scenario simulations. This methodology owes its idea on Cornell's (1968) probabilistic seismic hazard analysis (PSHA), which considers all possible earthquake scenarios to provide the exceedance probability of a certain level of ground motion at a site within a defined time frame. For each block-volume scenario, s, the probability of exceeding a certain value of intensity (i.e. the reach of a specific value of kinetic energy), for each position along the slope (z) is:

$$P_s(E_k > \bar{E}_k) = \int_{I_c}^{\infty} p_s(E_k)\,dE_k \tag{53}$$

where $p_s(E_k)$ is the probability density function of kinetic energy at the position z for the scenario s. Multiplying the exceedance probability by the annual frequency of occurrence (f_s), we obtain the annual rate at which *i* is exceeded, $F_s(E_k > \bar{E}_k)$ as:

$$F_s(E_k > \bar{E}_k) = f_s \cdot P_s(E_k > \bar{E}_k) \tag{54}$$

The annual frequency of occurrence (f_s) of each scenario combines the onset frequency (f_o) and the transit frequency ($f_{t,s}$) at a certain position and for the specific scenario:

$$f_s = f_{0,s} \cdot f_{t,s} \tag{55}$$

The onset frequency ($f_{o,s}$) of blocks with a certain volume, V_s, can be expressed in terms of magnitude-frequency relationships (Hungr et al. 1999; Dussauge et al. 2003; Rosser et al., 2007).

$$f_{0,s} = N(V_s) = aV_s^{-b} \tag{56}$$

where $N(V_s)$ is the cumulative number of individual blocks with volume larger than V_s for the scenarios s; parameter a depends on both the area extent and the overall susceptibility of the cliff, whereas the power law exponent, b, mainly depends on lithology and geological structure (Hungr et al., 1999). To properly account for the frequency of individual blocks that propagate on the slope, it is necessary to combine the volume frequency relationship of rockfall events with the volume frequency relationship of blocks (Hantz et al., 2018; Hantz et al., 2020). The first relationship can be developed from surveyed historical events (e.g. Dussauge-Peisser et al. 2002; Chau et al., 2003; Guzzetti et al., 2003; Guthrie and Evans, 2004; Malamud et al., 2004) and provides annual frequencies of released rockfall volumes. However, these volumes should not be used for hazard analysis because single rockfall events disaggregate or fragment (Ruiz-Carulla et al., 2017) soon after the detachment and during propagation into a distribution of smaller individual blocks. On the other hand, the volume frequency relationship of blocks can be derived from the rock mass fracture network or directly from already stopped blocks, both in the talus (Ruiz-Carulla et al., 2017), along roads (Hungr et al. 1999), and caught by rockfall nets within a certain range of time (Matasci et al., 2015; Moos et al., 2018). However, these distributions usually lack the temporal frame that allows to correctly estimate the annual frequency. The combination of the two distributions can be achieved by calculating the total volume of the event (integrating the first distribution) and by calculating the a parameter of the second distribution by assuming the total volume to be equal to the first one (Hantz et al., 2018).

The transit relative frequency (f_t) can be calculated for the rockfall simulation and corresponds to the ratio between the number of potential paths passing through a position (t_s) and the total number of simulated paths from the rockfall trajectories, (t_{tot}):

$$f_{t,s} = \left(\frac{t_s}{t_{tot}}\right) \tag{57}$$

For rockfall scenarios with different magnitude that occur in a certain position along the slope, the total annual rate at which i is exceeded, $F_{tot}(E_k > \bar{E}_k)$, derives from the sum of these scenarios, s:

$$F_{tot}(E_k > \bar{E}_k) = \sum_{\mathrm{s}=1}^{\mathrm{N}} F_s(E_k > \bar{E}_k) = \sum_{s=1}^{N} f_s P_s(E_k > \bar{E}_k) \tag{58}$$

By assuming a homogeneous, stationary Poisson process for the occurrence of the events (Crovelli, 2000), the probability of exceeding each intensity i in the next T years from this annual rate, P_{poiss}, is:

$$P_{poiss}(E_k > \bar{E}_k i, T) = 1 - e^{-F_{tot}\,T} \tag{59}$$

This represents the hazard curve at each position along the slope.

With respect to Lari et al. (2014), the revised PRHA method adopts a more flexible non-parametric approach for the kinetic energy probability distribution. Moreover, the new PRHA implements the approach proposed by Hantz et al (2016, 2019) for the calculation of the onset frequency (f_o), using the frequency-size distribution of the blocks observed along the talus to downscale the magnitude-frequency distribution of larger study areas.

Demonstration case studies

The application of potential rockfall scenarios was performed at the two representative sites that were recently affected by rockfall events in the Aosta Valley Region (Western Italian Alps) showing a significant role of forest and fragmentation at Saint Oyen and Roisan (Chapter 2b - Figure 1), respectively. During both the events, the rockfalls impacted roads and buildings, thus requiring a practical implementation of hazard assessment (for zonation) and the design of protection barriers (for mitigation).

Saint Oyen and Roisan are located in the Western Alps, within the Austroalpine-Pennidic collisional prism, consisting of overburden layers formed by continental crust and fragments of oceanic lithosphere, strongly reworked by the Alpine tectono-metamorphic processes (Dal Piaz et al., 2016).

In the Saint Oyen case study (45°48'59.0"N 7°12'21.0"E), about 17,500 m^3 of Ruitor micascists detached in March 2020, and reached a service road and the playing field in the lower part of the slope, passing through a mature fir forest. The presence of the forest significantly influenced the blocks distribution along the slope, increasing the lateral dispersion of trajectories and reducing their mobility. The case study is well documented by UAV flights conducted by the Regional Authority soon after the events, allowing for a detailed mapping of arrested blocks on the slope. We adopted this case study to investigate the role of forest, which has been fundamental for the rockfall dynamic, as observed in the field. Although minor fragmentation may have occurred during the event, we neglected it during the simulation to focus on tree-impact only.

Less than 10 km far, at Roisan (45°47'49.3"N 7°18'49.0"E), about 1,050 m^3 of Arolla gneiss toppled in October 2019 and impacted after 20 m of free fall (Polino et al., 2015) against a bench. While the main body of the rockfall stopped in a relatively flat area close to the source area, two blocks reached the foot of the slope causing the interruption of a municipal road. The event is documented by a post-event UAV flight, and by a detailed field survey of the blocks. For this case study, the presence of forest was minor due to the size and age of the trees and it has been neglected in order to reveal better the role of fragmentation.

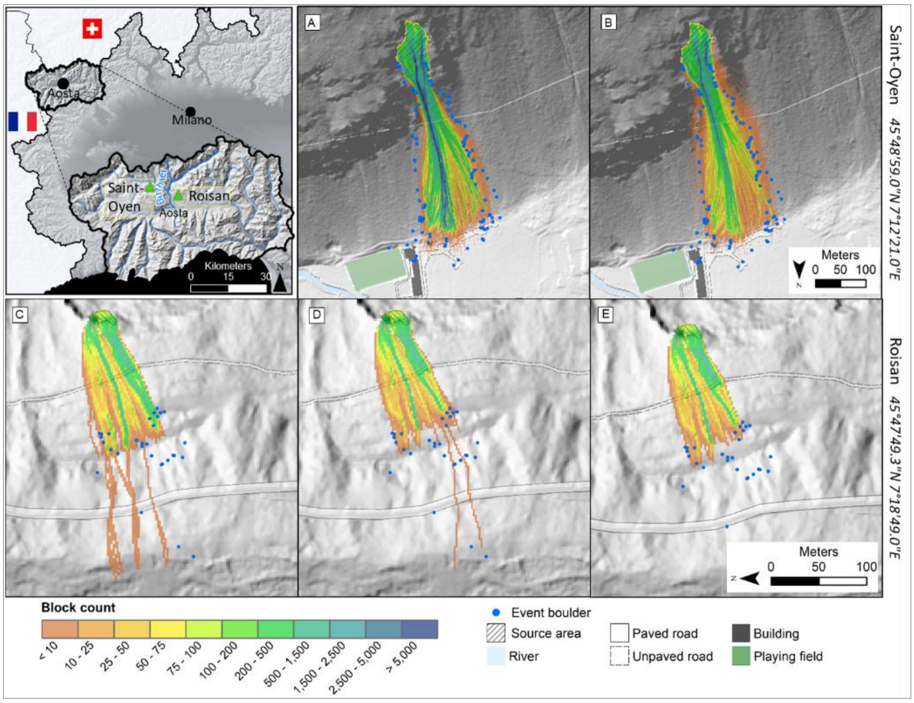

Chapter 2b - Figure 1 A) Location of the two case studies in Aosta Valley region. The other panels show the back calibration of the rockfall events: A) and B) simulation of Saint-Oyen rockfall (A) with parameters modified to account for the forest (SO_HS) and (B) by adopting the Hy-Stone tree-impact algorithm (SO_HStree); C) and D) simulation of Roisan rockfall (C) with parameters modified to implicitly account for the possibility of fragmentation (R_HS) and (D) by adopting the Hy-Stone fragmentation algorithm (R_HSfrag). Panel E) shows the calibration R_HSshort, obtained by neglecting the most distal blocks: this approach simulates only the blocks that stopped in the main deposit, without crossing the paved road.

Analysis and results

For both case studies, we firstly back-calibrated the model parameters on the rockfall events in order to simulate several volume scenarios from local-scale rockfall source areas (with and without the use of specific algorithms for tree-impact and fragmentation) to quantify the differences in terms of dynamics, spreading and rockfall hazard. We simulated all the scenarios by using spherical blocks and a 3D topography derived from the available 1 x 1 m Lidar DTM of Aosta Valley Region. The characteristics of each simulation, the number of simulated blocks, and the parameters adopted when using the two algorithms are reported in supplementary Table S1, 2 and 3.

Calibration by back-analysis

The calibration of model parameters was obtained by fitting the longitudinal and lateral extent of rockfall trajectories and deposits by using the Hy-Stone model with and without tree-impact and fragmentation. In particular, we simulated the following scenarios (Chapter 2b - Figure 1):

- SO_HS (Saint-Oyen tree impact implicit): the values of parameters are set to account for the forest, e.g. increasing rolling friction and reducing the tangential restitution coefficient. This is the most classical approach adopted in the practice to “simulate” the effect of forest with an implicit approach.
- SO_HS$_{tree}$ (Saint-Oyen tree impact explicit): the values of parameters are calibrated by adopting the Hy-Stone tree-impact algorithm that explicitly simulates the effect of forest; in this case, the motion parameters used in the simulation do not account for the forest.
- R_HS (Roisan Fragmentation Implicit): the values of parameters are set to allow the model to replicate the spreading of the event, including the most distal blocks, implicitly accounting for the possibility of fragmentation.
- R_HS$_{frag}$ (Roisan Fragmentation Explicit): the values of parameters are calibrated by adopting the Hy-Stone fragmentation algorithm that explicitly simulates the distal blocks as fragments.

For Roisan, we experimented a different calibration strategy that replicates the spreading of the main deposit only (R_HS$_{short}$), neglecting most distal blocks (Chapter 2b - Figure 1E). Although this strategy is physically correct to simulate non-fragmenting blocks, it provides an overall spreading that strongly underestimate the possible reach distance of fragments and the hazard level, accordingly.

For Saint-Oyen, both the simulations (SO_HS, SO_HS$_{tree}$) provide a good match with the main deposit of the 2020 event (Chapter 2b - Figure 1 A and B), with a slightly larger spreading when using the tree-impact algorithm, consistently with the fact that the impact with trees adds a component of lateral dispersion to the trajectories.

For Roisan, we can observe a good match between the longitudinal and lateral extent of the main deposit from the 2019 event and the simulations (R_HS, R_HS$_{frag}$) but we observe an overestimation of the blocks reaching the paved road (18 blocks modelled, while just 2 blocks during the event) when the fragmentation algorithm is not used (Chapter 2b - Figure 1C). The comparison with simulated stopping points shows that the model without fragmentation is able to reach the maximum distance, but not in the right location, since trajectories are strongly controlled by topography. This does not happen with the fragmentation algorithm, which is able to replicate the right position of the distal blocks in the meadow (Chapter 2b - Figure 1D).

In addition, the volume distribution is also considered. To this purpose the In-situ Block Size Distribution (IBSD) at the cliff considered in the previous numerical simulations was obtained previously by the Geological survey of Valle d’Aosta by means of a terrestrial laser scanner survey. In the Figure S1 a comparison of the Rock Block Size Distribution (RBSD) obtained with the ortophotos at the toe of the slope, and the distributions obtained with the scenario R_HS, R_HS$_{frag}$ is shown. The comparison reveals a good agreement since the curves are parallel each other although the Hy-Stone distributions overestimate the in situ one.

Chapter 2b – Table 1 and Chapter 2b – Table 2 report the values of normal and tangential restitution coefficients and of the friction coefficient for the different slope materials used in the rockfall numerical simulations in the cases of SO_HS and R_HS. Supplementary Table S1 and Table S2 report the parameters of tree-impact and fragmentation algorithms used in the cases of SO_HS$_{tree}$ and R_HS$_{frag}$.

Chapter 2b - Table 1 Values of normal (e_n) and tangential restitution (e_t) coefficients and of the friction coefficient (μ_s) for the different slope materials used in the rockfall numerical simulations for the Saint-Oyen case study.

Material	e_n **[-]**	e_t **[-]**	μ_s **[-]**
Outcropping rock	85	85	0.3
Coarse bare debris	65	70	0.55
Fine bare debris	55	65	0.45
Slope debris + damaged forest$^{(1)}$	64	71	0.5
Slope debris + undamaged forest$^{(1)}$	75	80	0.4
Alluvial deposit	55	74	0.4
Paved road	70	77	0.3
Unpaved road	60	70	0.3
Buildings	20	10	1

$^{(1)}$ *Only for the explicit approach (HS$_{tree}$)*

Chapter 2b - Table 2 Values of normal (e_n) and tangential restitution (e_t) coefficients and of the friction coefficient (μ_s) for the different slope materials used in the rockfall numerical simulations for the Roisan case study.

Material	e_n **[-]**	e_t **[-]**	μ_s **[-]**

	HS	HS	HS
Outcropping rock	75	85	0.2
Sub-cropping rock	60	70	0.3
Slope debris in HS model	60	65	0.4
Slope debris in HS_{frag} model	50	60	0.5
Paved road	75	85	0.2
Unpaved road	55	65	0.3
Alluvial deposit	40	50	0.35

Chapter 2b - Table 3 Volume scenarios for hazard analysis.

Scenario	**Range of volume [m^3]**	**Roisan –** **onset frequency f_o**	**Saint-Oyen –** **onset frequency f_o**
S1	0.001 – 0.01	9	67
S2	0.01 – 0.1	0.6	4.0
S3	0.1 - 1	0.03	0.24
S4	01-10	0.002	0.015
S5	10 -100	0.0001	0.0009

Effect of tree-impact and fragmentation sub-models on kinetic energy

To quantify the effect of explicitly simulating tree-impact and fragmentation in rockfall modelling, we performed simulations for five scenarios in which the released volumes are changed (Chapter 2b - Table 3), using the modelling parameters that were back-calibrated from the events as previously described. The volume scenarios range from 0.001 m^3 to 100 m^3 to encompass the block sizes surveyed on the field at the two sites. For the spatial analysis, we divided the slope into a 10 x 10 meters square lattice and we calculated statistics of kinetic energy within each square.

Effect of tree-impact sub-model

Figure 2 shows the 95th percentile of the blocks kinetic energy in each 10 m square considering the first and fifth scenario with and without the forest sub-model. This statistic variable has been chosen since it is frequently used for designing defensive works (UNI 11211; Maciotta et al., 2015; Lambert et al., 2021). In the case of small volume blocks, the simulation without tree-impact sub-model (Chapter 2b - Figure 2A) shows a central sector characterized by the highest kinetic energies (from 2,500 kJ up to over 10,000 kJ for the 95th percentile), and a distal zone characterized by lower values. Trajectories are able to reach the base of the slope, the unpaved road, buildings, and playing field, and overpass the location of the outermost blocks of the 2020 event. When using the tree-impact sub-model (Chapter 2b - Figure 2B) the number of trajectories passing through the central sector of the slope decreases dramatically. The trajectories that reach the base of the slope are concentrated in the area affected by the 2020 event where the forest is damaged. These trajectories reach only the unpaved road, with associated 95th percentile kinetic energy values of less than 2,500 J. For large blocks (fifth scenario), the kinetic energy is high enough to nullify the effect of forest, and the two analysis without and with tree-impact sub-models become similar (Chapter 2b - Figure 2 C and D).

From these results, it is evident that the use of the tree impact sub-model is relevant in the case of small volume blocks, for which the simulated trees are able to interrupt most of the computed trajectories, and in any case to decrease the kinetic energies. On the contrary, tree-impact analysis is almost irrelevant for large-volume blocks.

Analysing the distribution of kinetic energies along the road and the blocks number at the foot of the slope without (HS) and with (HS_{tree}) the tree impact sub-model, we systematically observe lower values of energy for the HS analyses (Chapter 2b – Figure 3). Indeed, in these models, the effect of the forest is simulated by reducing the restitution coefficients and increasing friction coefficient, calibrated on the range of kinetic energies of the event. However, this coefficients modification is independent of the block mass of the simulated blocks, and, therefore, it is not possible to observe the scale effect revealed in the HS_{tree} analyses.

When the kinetic energies are lower both than the calibrated kinetic energies and the kinetic absorption energies of the trees (scenarios S1 and S2), the classical HS approach overestimates the runout (see the large number of blocks intersecting the road after crossing the forest in Chapter 2b - Figure 2 A). Instead, the HS_{tree} algorithm intercepts, slows, and stops the least energetic blocks, allowing only the most energetic to reach the lower part of the slope. As a result, few transits are obtained, but with much higher kinetic energies due to the filtering effect of the forest (Chapter 2b – Figure 3).

In contrast, when the kinetic energies grow beyond the calibration range (scenarios S4 and S5), the classical HS approach continues to apply the forest effect (through the modified parameters) even though the kinetic energies are well above the tree absorption energies, underestimating the runout (the number of blocks intercepting the road remains about the same as in the low energy scenarios) and the kinetic energies (Chapter 2b – Figure 3). For the HS_{tree} analyses in these scenarios S4 through S5, show higher kinetic energies and a high number of transits (compared to the lower-volume scenarios) because the effect of the trees becomes negligible, as it should be.

In the intermediate S3 scenario, greater congruence between the two approaches HS and HS_{tree} is observed (Chapter 2b – Figure 3) because the simulated volumes are similar to the calibration range (between 0.001 m^3 and 34 m^3).

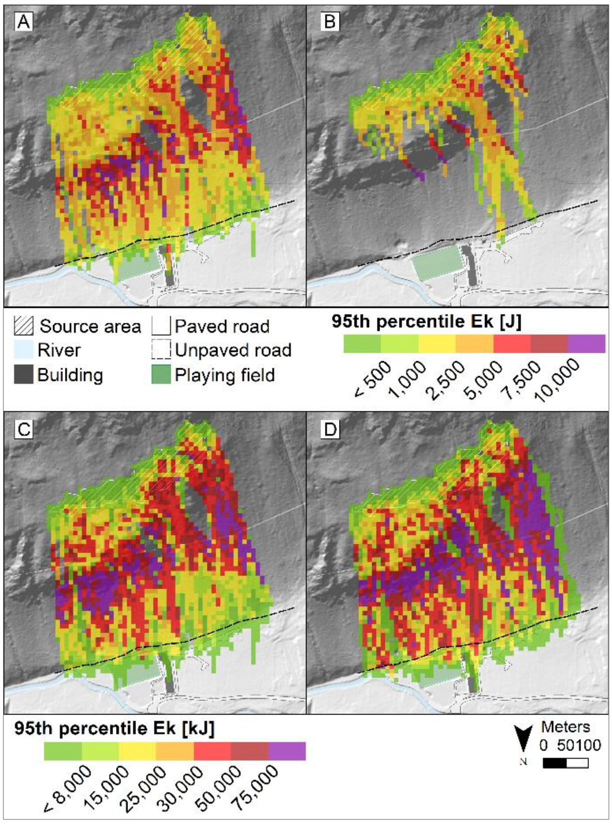

Chapter 2b - Figure 2 Distribution of kinetic energies of blocks along the slope in Saint-Oyen case study. The value of each cell corresponds to the 95th percentile of the kinetic energy of the blocks passing through that cell. Box A) scenario S1 (small blocks) HS, B) scenario S1 (small blocks) HStree, C) scenario S5 (large blocks) HS, D) scenario S5 HStree (large blocks).

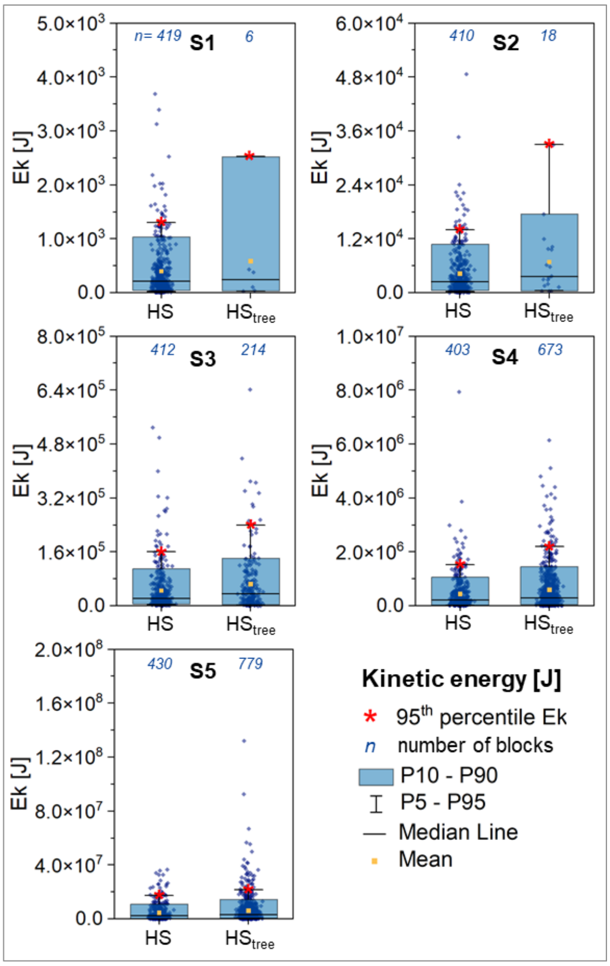

Chapter 2b - Figure 3 Boxplots of kinetic energy values recorded for each scenario (S1 to S5) at the foot of the slope in Saint-Oyen case study. The associated 95th percentile value is highlighted by the red star. The total number of simulated blocks for each scenario is 995.

Effect of fragmentation sub-model

Chapter 2b – Figure 4 shows the 95th percentile of the blocks kinetic energy in each 10 m square grid with and without the adoption of the fragmentation sub-model considering the first and fifth scenarios. The behaviour of the analyses with small or large block volumes is extremely different. In the case of small volume blocks, the adoption of fragmentation algorithm is almost negligible, because blocks are too small to undergo fragmentation. In Chapter 2b – Figure 4A the highest 95th percentile values of kinetic energy for the first scenario and without fragmentation are concentrated in the area located just below the modelled source and at the highest escarpment, and only four trajectories characterized by values up to 3 kJ reach and cross the paved road. In Chapter 2b – Figure 4B we observe that the highest 95th percentile values considering the fragmentation are concentrated in the area close to the cliff, but only one trajectory passes the road, characterized by 95th percentile of kinetic energy much lower (up to 1.5 kJ).

For larger blocks (S5 scenario), the difference with and without fragmentation is much more significant because more blocks are fragmented (612 out of 2646, 23%). In Chapter 2b - Figure 4C without fragmentation the runout achieved by blocks does not exceed that of Chapter 2b - Figure 4A, but with much larger values associated with the 95th percentile of kinetic energy reached all over the slope. The area located just below the modelled source and in the highest escarpment is characterized by kinetic energy values greater than 50,000 kJ at the intersection with the unpaved road. Values remain high also at the intersection with the paved road. In Chapter 2b - Figure 4D in which the fragmentation is considered there is an increase in the number of blocks crossing the roads, a consequent spread of trajectories with longer runouts (more than those actually achieved during the event) and a decrease in kinetic energy due to block fragmentation. On the unpaved road, the values associated with the 95th percentile drop to 50,000 kJ, and where the event boulder stopped it decreases to 8,000 kJ. At the intersection with the paved road, percentile values are more frequently lower than 15,000 kJ except in an isolated section where they reach 50,000 kJ and over.

Analysing the distribution of kinetic energies along the paved road at the foot of the slope without (HS) and with (HS_{frag}) the fragmentation sub-model, we systematically observe higher values of energy for the HS analyses (Chapter 2b - Figure 5). Although during the event very few blocks crossed the paved road and only two of them reached the meadow at the foot of the slope, the calibration of the model without fragmentation was accomplished by adjusting the parameters in order to reach the maximum runout. This causes a strong overestimation of the number of blocks crossing the paved road, a general overestimation of the landslide runout, and therefore also an overestimation of the kinetic energies at the element at risk. As already said for the Saint-Oyen case study, the runout in the HS models is almost independent from the block mass. Therefore, the number of transits is roughly constant in all five scenarios.

Instead, in the HS_{frag} approach, the kinetic energy at the element at risk is systematically lower because the model is calibrated in order to allow only ejected fragments (characterized by much lower volumes with respect to original blocks) to reach and cross the paved road as occurred during the event. The number of fragments reaching the road increases significantly through different volumes scenarios (from S1 to S5). This depends on the relationship between block size and fracture energy (Yashima et al., 1987); according to this relationship, the fracture energy scales with the radius of the block by an exponent that depends on the Weibull's coefficient of uniformity, and is always lower than 3, which is the scaling of the kinetic energy with radius. Hence, the larger the block, the higher is the probability of fracturing for a certain velocity.

The two approaches HS and HS_{frag} provide similar results in the S4 scenario (characterized by simulated volumes that are similar to the calibration range, between 0.5 m^3 and 23 m^3) both in terms of number of blocks intersecting the road and in terms of kinetic energies: compared to all other scenarios, less than an order of magnitude separates the two 95th percentile values of kinetic energy.

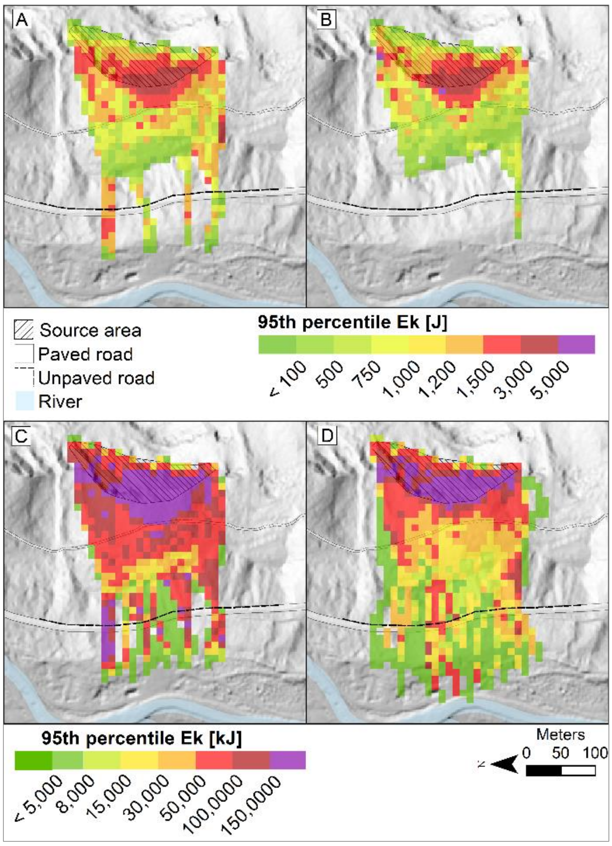

Chapter 2b - Figure 4 Distribution of kinetic energy of blocks along the slope in Roisan case study. The value of each cell corresponds to the 95th percentile of the kinetic energy of the blocks passing through that cell. Box A) scenario S1 (small blocks) HS, B) scenario S1 (small blocks) HSfrag, C) scenario S5 (large blocks) HS, D) scenario S5 (large blocks) HSfrag.

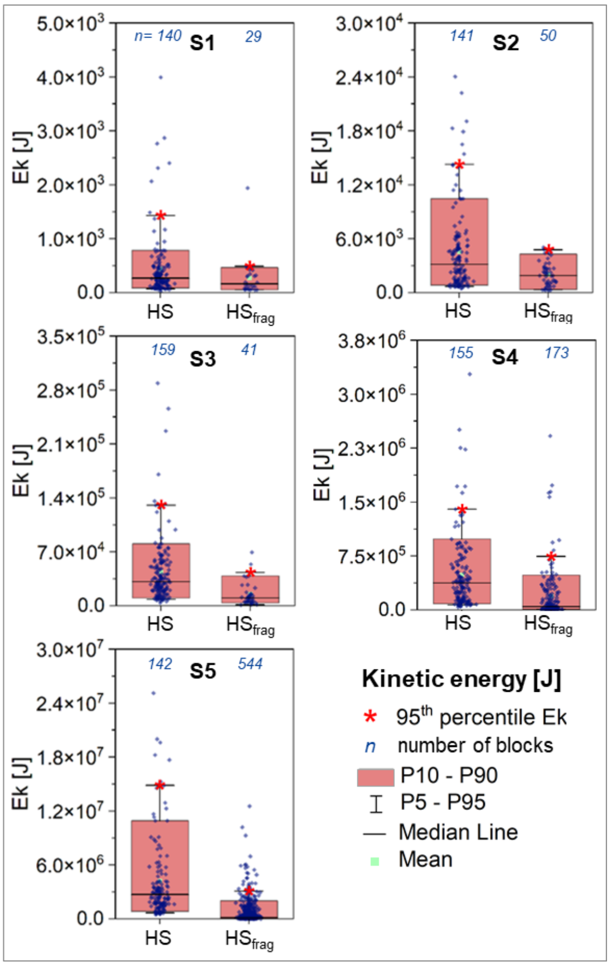

Chapter 2b - Figure 5 Boxplots of kinetic energy values recorded along the road at the foot of the slope in Roisan case study. The associated 95th percentile value is highlighted by the red star. The total number of simulated blocks is 2646.

Rockfall Hazard

As explained in the metholody section, the assessment of rockfall hazard requires the onset frequencies $f_{0,s}$ for each magnitude scenario, the transit frequency, $f_{t,s}$ and the distribution of kinetic energy in each position along the slope. For the calibration of onset frequency parameters (eq. 56), we adopted the methodology of Hantz et al (2018) who related the magnitude-frequency relationship of all rockfall events within a fixed site with the size-frequency relationship of blocks along the talus for a specific event in the same site.

We obtained magnitude-frequency relationship by analysing the available rockfall database of the Valle d'Aosta region, which includes 306 events with volume information (Chapter 2b – Figure 6). Among them, only 25 belongs to the same catchment of the case studies (Buthier catchment, Chapter 2b – Figure 7). Since this subsample appears to be insufficient to characterize the magnitude-frequency curve, especially for smaller volumes that are not recorded, we therefore adopted the entire inventory that we fitted with a maximum likelihood approach, obtaining a good power-law fitting ($R^2 = 0.99$) for rockfalls larger than 10 m^3, with a scaling exponent of 0.56. We believe that this parameter value is reliable also for the Buthier catchment, since the fitting curve has the same slope of larger rockfalls volumes (with a volume greater than 500 m^3) within the subsample. Therefore, this parameter b is adopted for the two cases studies.

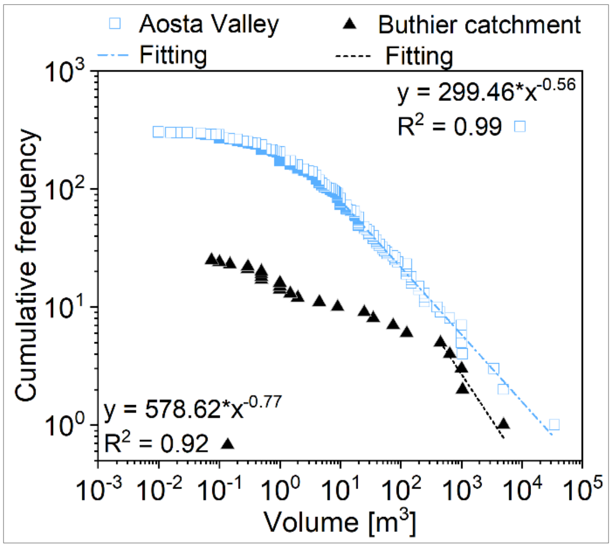

Chapter 2b - Figure 6 The two magnitude frequency relationships of 306 rockfall events collected in the Aosta Valley region (blue empty squares) and the 25 events from the Buthier catchment (black triangles).

For the parameter a, we used the size-frequency relationship of blocks along the talus obtained by image analysis. Chapter 2b - Figure 7 shows an excellent power-law fitting ($R^2 = 0.99$) for blocks larger than 0.2 m^3, with a scaling exponent b equals to 1.22. Eventually, by relating the magnitude-frequency size-frequency and accounting for the potential unstable area of both case studies, we obtained an a value of 0.0072 and of 0.0021 for Saint-Oyen and Roisan, respectively. The resulting onset frequencies for the different volume scenarios are reported in Chapter 2b - Table 3 for both case studies.

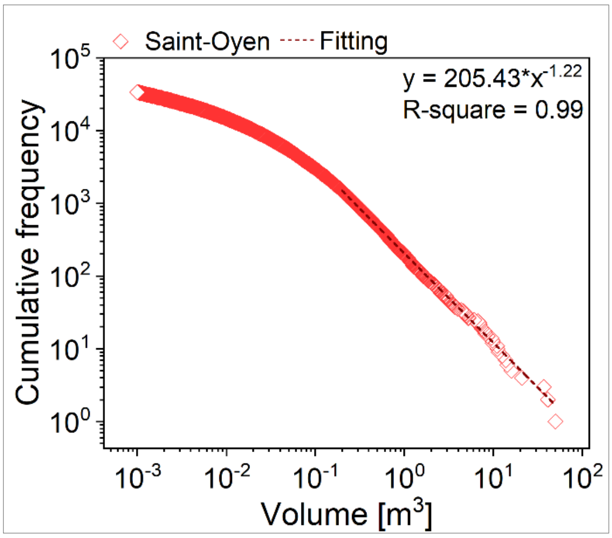

Chapter 2b - Figure 7 The size frequency relationship of blocks along the talus obtained by image analysis for the Saint-Oyen event.

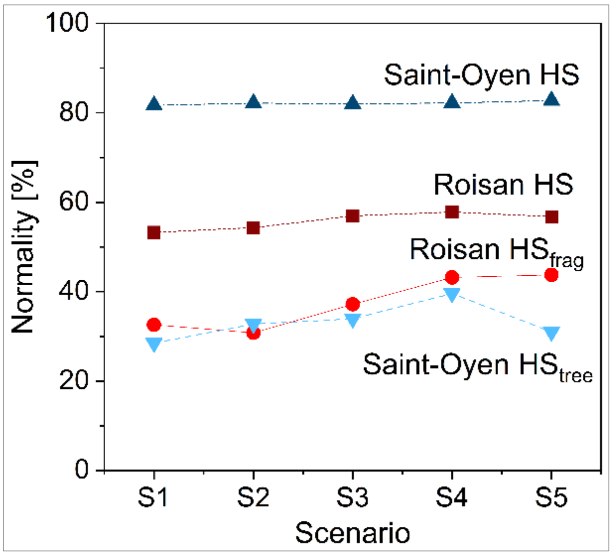

Chapter 2b - Figure 8 Test of the normality of log-kinetic energy distribution within 10x10 m cells for all the volume scenarios. The y-axis shows the percentage of cells where the normality is not rejected by the Kolmogorov-Smirnov test.

Both transit frequency ($f_{t,s}$) and the distribution of the kinetic energy come from the rockfall simulation trajectories sampled within 10x10 m cells. In order to characterize the kinetic energy distribution, we tested the hypothesis adopted by Lari et al, (2014), who assumed the logarithm of the kinetic energy to be normally distributed, and obtained the kinetic energy probability density $p_s(E_k)$ by using the mean and standard deviation statistics. The Kolmogorov-Smirnov's test (Chapter 2b – Figure 8) shows that the normality is not rejected for more than 50% of the 10x10 m cells when using Hy-Stone without additional algorithms. However, this percentage is lower when using the tree-impact and fragmentation algorithms, suggesting that a non-parametric approach should be adopted when the level of complexity increases.

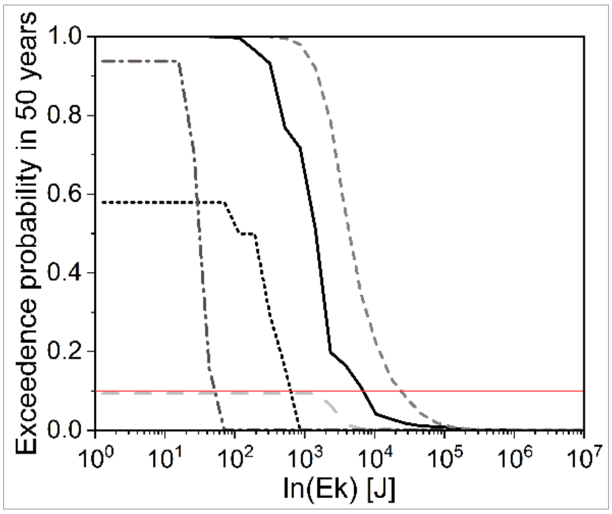

Chapter 2b - Figure 9 Example of hazard curves characterized by a non-logarithmic trend, calculated in five cells of R_HS model.

By combining the various scenarios and taking into account their associated probabilities (Equation 58), we constructed the hazard curves (by equation 59), which show the probability of exceeding a certain level of intensity in 50 years. Chapter 2b – Figure 9 shows hazard curves only for some representative cells. We can assert that they do not always have a logarithmic distribution, and that some curves (not here reported) do not reach the exceedance probability of 0.1 due to a very low transit frequency. Subsequently, for each location along the slope and for each model analyses (SO_HS, SO_HS_{tree}, R_HS, and R_HS_{frag}), we computed from each hazard curve, fixing the exceedance probability in 50 years at 10% as done by Lari et al (2014), the corresponding kinetic energy which is used to represent the hazard through a hazard map (Chapter 2b – Figure 10).

Compared to the SO_HS model (Chapter 2b – Figure 10A), in SO_HS_{tree} (Chapter 2b – Figure 10B) the hazard decreases because kinetic energy is significantly lowered, except in correspondence of the two sectors most affected by the event, where it remains similar (Chapter 2b – Figure 10A and B). The total area involved remains about the same, although with slightly lower runout. However, if only the areas with $Ek > 1kJ$ are considered, hazard decreases significantly along the road at the foot of the slope.

For the Roisan case study, compared to the R_HS model, in R_HS_{frag} the hazard decreases because the kinetic energy is significantly lowered, but note that the area involved increases (Chapter 2b - Figure 10C and D). Analysing the distribution of the hazard values (Chapter 2b – Figure 11) at the foot of the slope obtained by the different approaches without and with the tree impact and fragmentation algorithms, we observe an overestimation of the potential hazard in both case studies. In the Roisan case study, the overestimation is particularly high because the chance to fragment the blocks into smaller fragments greatly reduces the kinetic energy of those. Moreover, the distribution is less sparse because the only blocks with an energy value higher than the minimum energy value (1 kJ) that are able to reach the foot of the slope are few and localized in a 10-meter corridor.

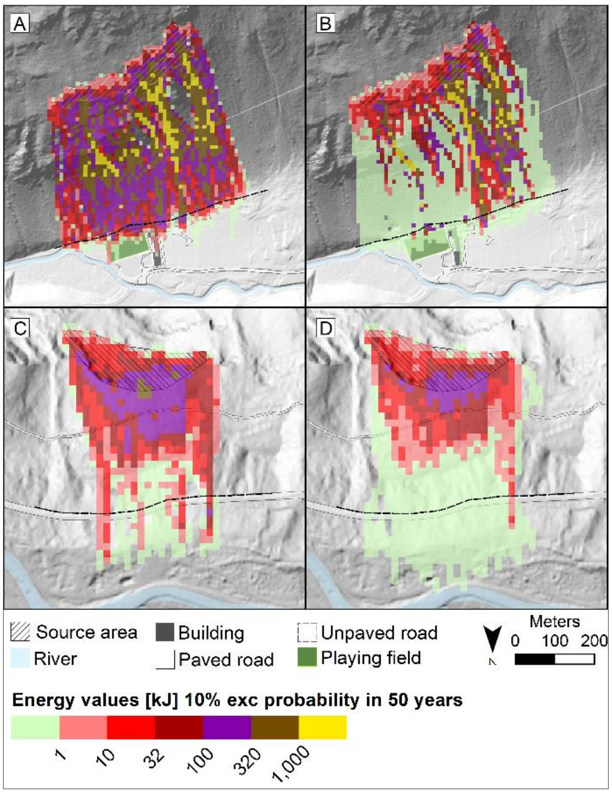

Chapter 2b - Figure 10 Hazard map for: A) Saint-Oyen SO_HS model, B) Saint-Oyen SO_HStree model, C) Roisan R_HS model, and D) Roisan R_HSfrag model. The hazard is quantified as the kinetic energy associated to a 10% probability in 50 years.

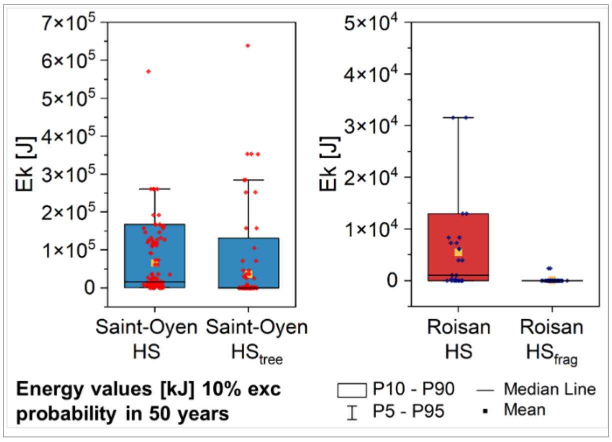

Chapter 2b - Figure 11 Boxplot of the kinetic energy associated to a 10% probability in 50 years for Saint-Oyen (blue boxplots on the left) and Roisan (red boxplots on the right) case studies, recorded along the road at the foot of the slope (dashed line in Figure 10).

Discussion

When hazard and risk need to be assessed, it is required to have a repeatable procedure and possibly a unique result. This study demonstrates that different modelling approach can influence both the hazard analysis and the design of countermeasures, but also points out the problems involved in advanced modelling, leading to necessary discussions on the topic.

Tree impact

The classical approach for modelling rockfall propagating along forested slopes is based on the modification of restitution and friction coefficients, calibrated on the extent of block propagation. This study shows that the adoption of this set of modified restitution coefficients provides a correct replication of the maximum lateral spreading and longitudinal runout, but inaccurate energy of blocks. In fact, the modification of the restitution coefficients is independent on the size of the blocks and can slow down even those blocks that are large enough to be actually unaffected by the presence of the forest. This leads to an overestimation of rockfall runout and of the number of blocks reaching the elements at risk. When the protective role played by the forest is explicitly simulated (HS_{tree}), the hazard decreases due to the forest protection, but the high-percentiles of kinetic energy become higher. This occurs because the trees stop the blocks with lower kinetic energy, generating a *filtering effect* of the larger blocks, leading to the risk of considering, paradoxically, the presence of the forest as more dangerous. These considerations open an important discussion on the opportunity to design the defensive works only based on percentiles of the kinetic energy.

Fragmentation

In case of rockfalls charcaterized by fragmentation, the classical approach for calibrating the model with this events is based on a conservative adjustment of the parameters in order to reach the maximum runout of single fragments. We demonstrate that this approach leads to a strong overestimation of the number of transits (Chapter 2b – Figure 4), the overall landslide runout, the kinetic energy of blocks impacting the elements at risk (Chapter 2b – Figure 5), and the hazard (Chapter 2b – Figure 10). On the other side, the alternative approach to replicate only the main deposit, neglecting the most distal blocks would result in an underestimation of all these quantities (supplementary Figure S5). Therefore, regardless of whether deciding to simulate only the blocks that have stopped in the main deposit (Chapter 2b – Figure 1E) or to extend the trajectories to the maximum fragment extent (Chapter 2b – Figure 1C), this study demonstrates that the result is fundamentally incorrect, especially for the design of defensive works. On the other side, the explicit modelling of fragmentation is still challenging from both a theoretical point of view (Ruiz-Carulla et al., 2017; Shen et al., 2017; Guccione et al., 2022) and a practical point of view, due to the difficulty to calibrate the geotechnical parameters that control fragmentation. This adds further uncertainty in the analysis of rockfall dynamics and hazard.

The results of hazard computation when using the fragmentation show a decrease of the hazard. However, as in case of forest, this results from the fact that more importance is given to the kinetic energy of the blocks and not the frequency. Is it correct to infer that the hazard decreases, mostly due to the decrease of kinetic energy, even if the frequency increases and the trajectories are much more dispersed? Our belief is that this inference is not entirely accurate since the area affected by rockfalls is larger, even if blocks are smaller. This discussion leaves room for future new studies.

Probabilistic rockfall hazard

The PRHA approach allows to quantify rockfall hazard in terms of hazard curves, thus describing the probability of exceeding a certain level of hazard. For each magnitude scenario, the approach overcomes the need of selecting a statistic of the kinetic energy at a certain positon along the slope (Agliardi et al, 2009; Farvacque et al, 2021), and allows to consider the full energy distribution within a certain grid cell. With respect to Lari et al. (2014), the revised PRHA method presents two improvements: (i) the adoption a more flexible non-parametric approach for the kinetic energy probability distribution, instead of assuming a log-normal distribution, that we demonstrate in this paper to be frequently violated if tree impacts and fragmentation subsist (Chapter 2b – Figure 8); (ii) the implementation of the approach proposed by Hantz et al (2016, 2019) for the calculation of the onset frequency ($f_{o,s}$). This approach allows to relate the onset frequency estimated from historical catalogues with the frequency-size distribution of blocks along the slope. In fact, the large volumes recorded in the catalogues typically disaggregate into a population of blocks, as soon as they impact on the slope. This disaggregation occurs due to the presence of pre-existing joints and fractures of a jointed rock mass (Ruiz-Carulla et al., 2017) and does not correspond to a fragmentation. The adoption of the Hantz et al (2016, 2019) approach place emphasis on the block size distribution along the slope, both to define the design volumes (Melzner et al, 2020), and to support the correct definition of the onset frequency.

Conclusions

The insight drawn from this study leads us to the conclusions that:

- If we do not explicitly simulate forest, we underestimate the protective role of trees and we consequently overestimate the hazard. On the other hand, the 95th percentile of the simulated kinetic energy of the blocks is higher when adopting the tree-impact algorithm because of the filtering effect performed by trees.
- If we do not explicitly simulate the fragmentation phenomenon, we overestimate the hazard in terms of energy values, but we underestimate the spreading of blocks during the events. The 95th percentile of kinetic energy along the element at risk is significantly lower when adopting the fragmentation algorithm.

- We obtained non-log-normal distributions of the kinetic energy values, so we adopted a non-parametric approach that we demonstrate being suitable for the hazard analysis. We highlight how PRHA fits different methodological models, and we quantify how much explicitly simulating both the interaction with forest and the fragmentation process lead to more accurate hazard mapping.
- As already mentioned in the discussion, we pointed the need to simulate a distribution of blocks that is representative of what already occurred as the so far most likely, because the dimensioning of the mitigation works is centered on the expected and simulated kinetic energies of the blocks. We also used the frequency-size distribution of the blocks along the talus to downscale the magnitude-frequency distribution of the study area, as proposed by Hantz et al (2018), to simulate different volume class scenarios.
- This study highlights the strong dependency of the 95th percentile of kinetic energy on the adopted modelling approach, showing the fluctuations of this value and thus the uncertainty related to the use of this parameter for hazard analysis.

Acknowledgments

The authors would like to acknowledge the support of the Geological Survey of the Aosta Valley Region, and also Serena Lari for useful discussions.

References

Agliardi, F., Crosta, G. B., & Frattini, P. (2009). Integrating rockfall risk assessment and countermeasure design by 3D modelling techniques. Natural Hazards and Earth System Sciences, 9(4), 1059-1073.

Azzoni, A., La Barbera, G., & Zaninetti, A. (1995, October). Analysis and prediction of rockfalls using a mathematical model. In International journal of rock mechanics and mining sciences & geomechanics abstracts (Vol. 32, No. 7, pp. 709-724). Pergamon.

Berger, F. and Dorren, L. K.: Principles of the tool Rockfor.net for quantifying the rockfall hazard below a protection forest, Schweizerische Zeitschrift fur Forstwesen, 158, 157–165, doi:10.3188/szf.2007.0157, 2007

Berger, F., Quetel, C., & Dorren, L. K. (2002). Forest: a natural protection mean against rockfalls, but with which efficiency. In International congress INTERPRAEVENT (Vol. 2, pp. 815-826).

Bigot, C., Dorren, L. K., & Berger, F. (2009). Quantifying the protective function of a forest against rockfall for past, present and future scenarios using two modelling approaches. Natural hazards, 49(1), 99-111.

Chau, K. T., Wong, R. H. C., Liu, J., & Lee, C. F. (2003). Rockfall hazard analysis for Hong Kong based on rockfall inventory. Rock Mechanics and Rock Engineering, 36(5), 383-408.

Corominas J, Mavrouli O, Santana D, Moya J (2012) Simplified approach for obtaining the block volume distribution of fragmental rockfalls. In: Eberhardt E, Froese C, Turner AK, Leroueil S (eds) Landslides and engineered slopes, 2, pp 1159–1164.

Corominas, J., Copons, R., Moya, J., Vilaplana, J. M., Altimir, J., & Amigó, J. (2005). Quantitative assessment of the residual risk in a rockfall protected area. Landslides, 2(4), 343-357.

Corominas, J., Matas, G., & Ruiz-Carulla, R. (2019). Quantitative analysis of risk from fragmental rockfalls. Landslides, 16(1), 5-21.

Crosta, G. B., & Agliardi, F. (2003). A methodology for physically based rockfall hazard assessment. Natural Hazards and Earth System Sciences, 3(5), 407-422.

Crosta, G. B., & Agliardi, F. (2004). Parametric evaluation of 3D dispersion of rockfall trajectories. Natural Hazards and Earth System Sciences, 4(4), 583-598.

Crosta, G.B.; Agliardi, F.; Frattini, P.; Lari, S. Key Issues in Rock Fall Modeling, Hazard and Risk Assessment for Rockfall Protection. In Engineering Geology for Society and Territory—Volume 2; 2015

Crovelli, R. A. (2000). Probability models for estimation of number and costs of landslides. foot (ft), 25, 0-3048.

Dal Piaz, G. V., Bistacchi, A., Gianotti, F., Monopoli, B., Passeri, L., & Schiavo, A. (2016). Note illustrative del F. 070 Monte Cervino della Carta Geologica d'Italia alla scala 1: 50.000.

Dattola, G., Crosta, G. B., & di Prisco, C. (2021). Investigating the influence of block rotation and shape on the impact process. International Journal of Rock Mechanics and Mining Sciences, 147, 104867.

Dorren, L. K. A., Berger, F., & Putters, U. S. (2006). Real-size experiments and 3-D simulation of rockfall on forested and non-forested slopes. Natural hazards and earth system sciences, 6(1), 145-153.

Dorren, L.K.A., Berger, F., Imeson, A.C., Maier, B. & Rey, F. 2004a. Integrity, stability and management of protection forests in the European Alps. Forest Ecology and Management 195: 165-176.

Dorren, L.K.A., Maier, B., Putters, U.S. & Seijmonsbergen, A.C. 2004b. Combining field and modelling techniques to assess rockfall dynamics on a protection forest hillslope in the European Alps. Geomorphology 57: 151-167.

Dupire, S., Bourrier, F., Monnet, J. M., Bigot, S., Borgniet, L., Berger, F., & Curt, T. (2016). Novel quantitative indicators to characterize the protective effect of mountain forests against rockfall. Ecological Indicators, 67, 98-107.

Dussauge-Peisser, C., Helmstetter, A., Grasso, J. R., Hantz, D., Desvarreux, P., Jeannin, M., & Giraud, A. (2002). Probabilistic approach to rock fall hazard assessment: potential of historical data analysis. Natural hazards and earth system sciences, 2(1/2), 15-26.

Evans, S. G., & Hungr, O. (1993). The assessment of rockfall hazard at the base of talus slopes. Canadian geotechnical journal, 30(4), 620-636.

Farvacque, M., Eckert, N., Bourrier, F., Corona, C., Lopez-Saez, J., & Toe, D. (2021). Quantile-based individual risk measures for rockfall-prone areas. International Journal of Disaster Risk Reduction, 53, 101932.

Farvacque, M., Lopez-Saez, J., Corona, C., Toe, D., Bourrier, F., & Eckert, N. (2019). Quantitative risk assessment in a rockfall-prone area: the case study of the Crolles municipality (Massif de la Chartreuse, French Alps). Géomorphologie: relief, processus, environnement, 25(1), 7-19.

Frattini, P., Crosta, G. B., Agliardi, F., Clague, J. J., & Stead, D. (2012). 22 Rockfall characterization and modeling. Landslides: types, mechanisms and modeling, 267.

Getzner M, Gutheil-KnoppKirchwald G, Kreimer E, Kirchmeir H, Huber M. Gravitational natural hazards: Valuing the protective function of alpine forests. Forest Policy and Economics, 2017;80: 150-159.

Grêt-Regamey A, Bebi P, Bishop, ID, Smid WA. Linking GIS-based models to value ecosystem services in an alpine region. Journal of Environmental Management, 2008. 89(3);197-208.

Guccione, D. E., Giacomini, A., Thoeni, K., Fityus, S., & Buzzi, O. (2022). On the Dynamic Fragmentation of Rock-Like Spheres: Insights into Fragment Distribution and Energy Partition. Rock Mechanics and Rock Engineering, 1-27.

Guthrie, R. H., & Evans, S. G. (2004). Magnitude and frequency of landslides triggered by a storm event, Loughborough Inlet, British Columbia. Natural Hazards and Earth System Sciences, 4(3), 475-483.

Guzzetti, F., Reichenbach, P., & Wieczorek, G. F. (2003). Rockfall hazard and risk assessment in the Yosemite Valley, California, USA. Natural Hazards and Earth System Sciences, 3(6), 491-503.

Hantz, D., Colas, B., Dewez, T., Lévy, C., Rossetti, J. P., Guerin, A., & Jaboyedoff, M. (2020). Caractérisation quantitative des aléas rocheux de départ diffus. Revue Française de Géotechnique, (163), 2.

Hantz, D., Corominas, J., Crosta, G. B., & Jaboyedoff, M. (2021). Definitions and concepts for quantitative rockfall hazard and risk analysis. Geosciences, 11(4), 158.

Hantz, D., Ventroux, Q., Rossetti, J. P., & Berger, F. (2018). A new approach of diffuse rockfall hazard. In Landslides and Engineered Slopes. Experience, Theory and Practice (pp. 1063-1067). CRC Press.

Häyhä T, Franzese P. P, Paletto A, Fath B.D. Assessing, valuing, and mapping ecosystem services in alpine forests. Ecosystem Services, 2015;14:12-24.

Hungr, O., Evans, S. G., & Hazzard, J. (1999). Magnitude and frequency of rock falls and rock slides along the main transportation corridors of southwestern British Columbia. Canadian Geotechnical Journal, 36(2), 224-238.

Jancke, O., Dorren, L. K., Berger, F., Fuhr, M., & Köhl, M. (2009). Implications of coppice stand characteristics on the rockfall protection function. Forest ecology and management, 259(1), 124-131.

Kajdiž, P., Diaci, J., & Rebernik, J. (2015). Modelling facilitates silvicultural decision-making for improving the mitigating effect of beech (Fagus sylvatica L.) dominated alpine forest against rockfall. Forests, 6(6), 2178-2198.

Lambert, S., Toe, D., Mentani, A., & Bourrier, F. (2021). A meta-model-based procedure for quantifying the on-site efficiency of rockfall barriers. Rock Mechanics and Rock Engineering, 54(2), 487-500.

Lari, S., Frattini, P., & Crosta, G. B. (2014). A probabilistic approach for landslide hazard analysis. Engineering geology, 182, 3-14.

Leine, R. I., Schweizer, A., Christen, M., Glover, J., Bartelt, P., & Gerber, W. (2014). Simulation of rockfall trajectories with consideration of rock shape. Multibody System Dynamics, 32(2), 241-271.

Macciotta, R., Martin, C. D., & Cruden, D. M. (2015). Probabilistic estimation of rockfall height and kinetic energy based on a three-dimensional trajectory model and Monte Carlo simulation. Landslides, 12(4), 757-772.

Malamud, B. D., Turcotte, D. L., Guzzetti, F., & Reichenbach, P. (2004). Landslide inventories and their statistical properties. Earth Surface Processes and Landforms, 29(6), 687-711.

Matas, G.; Lantada, N.; Corominas, J.; Gili, J. A.; Ruiz-Carulla, R.; Prades, A., RockGIS: a GIS-based model for the analysis of fragmentation in rockfalls. Landslides 2017, 14 (5), 1565-1578.

Matasci, B., Jaboyedoff, M., Loye, A., Pedrazzini, A., Derron, M. H., & Pedrozzi, G. (2015). Impacts of fracturing patterns on the rockfall susceptibility and erosion rate of stratified limestone. Geomorphology, 241, 83-97.

Melzner, S., Rossi, M., & Guzzetti, F. (2020). Impact of mapping strategies on rockfall frequency-size distributions. Engineering Geology, 272, 105639.

Moos C, Bebi P, Schwarz M, Stoffel M, Sudmeier-Rieux K, Dorren L. Ecosystem-based disaster risk reduction in mountains. Earth-Science Reviews, 2018;177: 497-513.

Moos, C. A., & Dorren, L. (2021). Cost-benefit analysis as a basis for risk-based rockfall protection forest management.

Moos, C., Fehlmann, M., Trappmann, D., Stoffel, M., & Dorren, L. (2018). Integrating the mitigating effect of forests into quantitative rockfall risk analysis–Two case studies in Switzerland. International journal of disaster risk reduction, 32, 55-74.

Nocilla, N., Evangelista, A., & Di Santolo, A. S. (2009). Fragmentation during rock falls: two Italian case studies of hard and soft rocks. Rock mechanics and rock engineering, 42(5), 815.

Perret, S., Dolf, F., & Kienholz, H. (2004). Rockfalls into forests: analysis and simulation of rockfall trajectories—considerations with respect to mountainous forests in Switzerland. Landslides, 1(2), 123-130.

Pfeiffer, T.J., and Bowen, T.D., "Computer Simulation of Rockfalls." Bulletin of Association of Engineering Geologists. Vol. 26, No. 1. 1989. pp135-146

Polino, R., Bonetto, F., Carraro, F., Gianotti, F., Gouffon, Y., Malusà, M. G., ... & Schiavo, A. (2015). Foglio 090 Aosta della Carta Geologica d'Italia.

Radtke, A., Toe, D., Berger, F., Zerbe, S., & Bourrier, F. (2014). Managing coppice forests for rockfall protection: lessons from modeling. Annals of Forest Science, 71(4), 485-494.

Rammer, W., Brauner, M., Dorren, L. K. A., Berger, F., & Lexer, M. J. (2010). Evaluation of a 3-D rockfall module within a forest patch model. Natural Hazards and Earth System Sciences, 10(4), 699-711.

Rosser, N., Lim, M., Petley, D., Dunning, S., & Allison, R. (2007). Patterns of precursory rockfall prior to slope failure. Journal of geophysical research: earth surface, 112(F4).

Ruiz Carulla, R. (2018). Rockfall analysis: failure, fragmentation and propagation characterization: a fractal fragmentation of rockfalls.

Ruiz-Carulla, R., Corominas, J., & Mavrouli, O. (2017). A fractal fragmentation model for rockfalls. Landslides, 14(3), 875-889.

Shen, W. G., Zhao, T., Crosta, G. B., & Dai, F. (2017). Analysis of impact-induced rock fragmentation using a discrete element approach. International Journal of Rock Mechanics and Mining Sciences, 98, 33-38.

Stoffel, M., Wehrli, A., Kühne, R., Dorren, L. K., Perret, S., & Kienholz, H. (2006). Assessing the protective effect of mountain forests against rockfall using a 3D simulation model. Forest Ecology and Management, 225(1-3), 113-122.

Toe, D., Bourrier, F., Dorren, L., & Berger, F. (2018). A novel DEM approach to simulate block propagation on forested slopes. Rock Mechanics and Rock Engineering, 51(3), 811-825.

UNI (2012) UNI 112111-4: 2012 rockfall protective measures – Part 4: definitive and executive design. Ente Nazionale Italiano di Unificazione, Milano Italia (in Italian). http://www.uni.com

Volkwein, A., Roth, A., Gerber, W., & Vogel, A. (2009). Flexible rockfall barriers subjected to extreme loads. Structural engineering international, 19(3), 327-332.

Volkwein, A., Schellenberg, K., Labiouse, V., Agliardi, F., Berger, F., Bourrier, F., ... & Jaboyedoff, M. (2011). Rockfall characterisation and structural protection–a review. Natural Hazards and Earth System Sciences, 11(9), 2617-2651.

Yashima S, Kanda Y, Sano S. Relationships between particle size and fracture energy or impact velocity required to fracture as estimated from single particle crushing. Powder Technol. 1987;51: 277–282

Wang, Y., Tonon, F., Crosta, G. B., Agliardi, F., & Zavodni, Z. M. (2010, January). Rock Fragmentation Module in 3-D Rock-fall Analysis. In 44th US Rock Mechanics Symposium and 5th US-Canada Rock Mechanics Symposium. American Rock Mechanics Association

Chapter 3: Fragmentation tests

As already mentioned, fragmentation during rockfall events represents a complex phenomenon, the full understanding of which remains a subject of ongoing research and inquiry, particularly on the governing laws. Numerous numerical tests have been conducted in recent years, as well as physical tests under controlled conditions, both in small-scale laboratory settings, and at a full-scale quarry.

This chapter is componed by two studies on experiments at various scales, organized in the style of scientific papers to maintain consistency with the rest of the thesis, although they gather preliminary results and they are still in preparation. The investigations focused on two intriguing aspects such as rockfall dispersion, deposition, mobility, and the influence of discontinuities on the fragmentation process, particularly:

- whether the ground distribution of fragments exhibits any coherence with field observations presented in Chapter 1;
- how the presence of planes of weakness within the samples influences the fragmentation phenomenon.

The initial ambitious goal of this thesis was to gain insights into the fundamental principles governing fragmentation, with the aim of enhancing existing models, particularly Hy-Stone. The plan involved achieving this through tracking the trajectories and velocities of the blocks and fragments after impact using high-speed video cameras. Given the intricate nature of the process and the setbacks caused by the pandemic and a landslide that affected the designated quarry for experiments, the tests were conducted during the last year of the thesis. In the following parts, we have put forward new hypotheses and affirmed some empirical observations.

Fragmentation tests | in-situ and laboratory experiments

This first part of the chapter delves into two primary aspects of fragmentation testing: in-situ observations within a natural environment and controlled laboratory experiments designed to replicate and investigate fragmentation phenomena. The methodologies employed enable the calculation of ground fragment volumes and spatial distribution analysis, supported by a simplified image analysis approach for laboratory test frames. The chapter summarizes preliminary findings from these tests and underscores their significance in validating earlier ground evidence. Despite certain limitations, these results indicate that similar outcomes are observed in both quarry and laboratory environments, particularly concerning the travel distances of smaller fragments and the possible correlation with mass and exit angles. Moreover, the study generates valuable hypotheses, particularly regarding the chaotic fragmentation process within the population of fragments.

In-situ testing occurred at a serizzo-quarry in Foppiano (Italy), while laboratory experiments took place at the University of Milano-Bicocca, utilizing a mixture material with the potential for fragmentation from modest release heights.

Research Background

Numerical studies on fragmentation upon impact

Numerical models provide a valuable alternative to the challenging, time-consuming, and costly experimental research. In recent years, there has been notable progress in applying advanced numerical tools to analyze rockfall fragmentation. Several researchers have explored this area, employing both 2D and 3D models. The increasing prominence of three-dimensional studies has exposed the constraints of two-dimensional modeling in representing the formation of meridional cracks, a critical component of the primary breakage mechanism.

Several authors delved into the numerical investigation of rockfall impact and fragmentation using advanced discrete element modeling (DEM). Notable contributions include Behera et al. (2005), Liu et al. (2010), Moreno et al. (2003), Paluszny et al. (2016), Reddish et al. (2005), Sator and Hietala (2010), Thornton et al. (1996), Wang and Tonon (2011), Wittel et al. (2008), Ye et al. (2019a), and Zhao et al. (2017).

Of particular interest is the work by Wang and Tonon (2011), who investigated rock fragmentation upon impact, considering factors like impact velocity, ground conditions, and fracture properties. Their 3D DEM model showed that the number of fragments increased with impact velocity, incidence angle, and ground stiffness. The study also demonstrated that softer ground extended the duration of impact and produced lower impact stresses, resulting in less fragmentation. Wittel et al. (2008) and Paluszny et al. (2016) used 3D DEM to reproduce experimental results of brittle fragmentation of spheres, providing realistic representations of fragmentation processes, fragment shape, and mass distribution. However, they did not account for factors such as discontinuities, material heterogeneities, size effects, and impact conditions that can affect fragmentation. Lisjak et al. (2010) proposed a hybrid finite-discrete element approach for modeling rockfall fragmentation, calibrated with in situ tests and material data, successfully reproducing field observations for blocks breaking and fragments accumulating along the slope in a 2D space. Liu et al. (2010) investigated the breakage of agglomerates of different shapes impacting a target wall using DEM. They found that spherical impacts caused more damage compared to impacts on cuboidal edges, cylindrical rims, and cuboidal corners. Ye et al. (2019) employed a 3D clumped particle method to study the fragmentation process of marble spheres upon impact. They introduced a new calibration procedure to account for both quasi-static and dynamic material behavior, successfully replicating the evolution of fragmentation patterns as a function of impact velocity. Their results revealed that some small fragments could have significantly higher translational velocities than the impact velocity due to high-tensile stress waves near the contact area. Furthermore, they found no correlation between fragment mass and kinetic energy.

Fragmentation modelling and real-scale tests

Understanding and modeling the fragmentation process in rockfall events is essential for improving the reliability of predictions and assessments related to the spread, impact, and potential damage caused by such events. Indeed, fracturing often involves the opening of pre-existing or latent defects, resulting in the subdivision of the initial rock block into smaller fragments. These fragments tend to exhibit behavior closely resembling that of the original block during their descent (Giacomini et al., 2009; Prades-Valls et al., 2022). In more extreme cases, such as explosive fragmentation scenarios (Wang and Tonon, 2011; Frattini et al., 2012), rockfall events can lead to the rapid generation of high-speed, long-reaching fly-rocks and the formation of large, dense dust clouds that can quickly spread and cause extensive damage across relatively wide areas (Wieczorek et al., 2000; Wieczorek, 2002; De Blasio et al., 2018; Crosta et al., 2023). This exceptional behavior challenges the effectiveness of many conventional rockfall simulation tools, necessitating a more integrated modeling approach (Wang & Tonon, 2011; Crosta et al., 2015; Shen et al., 2017; Zhao et al., 2017; Zhao et al., 2018; Yang et al., 2022). Simultaneously, the design of effective countermeasures in rockfall-prone areas requires the consideration of these phenomena to obtain reliable estimates of block size, velocity, energy, and trajectory (Frattini et al., 2012). Until now, few models have addressed the issue of fragmentation in the field of rockfall engineering. In 2009, Wang introduced an impact fragmentation model that allowed for examining how rock blocks fragment upon impact and the subsequent formation of fragments. It employed either an interpolation method or a neural network model, leveraging an extensive database of DEM simulations. Despite being refined through laboratory tests, this model faced challenges in replicating the observed distribution of fragment sizes in real-world cases.

The 3D rockfall simulator proposed by Crosta et al. (2003) Hy-Stone replicates the motion of rock blocks using dynamic equations and utilizes a triangulated vector topography derived from Digital Terrain Models (DTM). Its submodule dedicated to fragmentation simulates how a rock block shatters into independently moving fragments upon impact. Fragmentation occurs when the block's kinetic energy exceeds a predefined threshold, determined by the Weibull distribution and linked to the block's geomechanical properties and volume. After satisfying fragmentation criteria, Hy-Stone generates a distribution of fragments based on a power-law distribution. The number and energy of fragments are computed while adhering to mass conservation principles. The ejection velocity of each fragment is determined considering translational and kinetic energy conservation, with stochastic direction within a cone.

In subsequent years, Corominas and his colleagues introduced the "Rockfall Fractal Fragmentation Method" (RFFM) to deduce the distribution of rockfall block sizes (RBSD) from the in situ block size distribution (IBSD) (Ruiz-Carulla et al. 2017; Ruiz-Carulla and Corominas 2020; Ruiz-Carulla et al. 2020). Additionally, they developed RockGIS, a GIS-based software, for the stochastic simulation of rockfall fragmentation (Matas et al. 2017; Matas 2020; Matas et al. 2020). The RFFM is versatile, adapting to various fragmentation scenarios based on the initial block's characteristics: disaggregation, pure breakage, or a combination of both. It is based on Perfect's (1997) generic fractal fragmentation model, employing three key parameters: probability of failure (which indicate the degree of breakage of the instable identified block), survival rate (which expresses the percentage of blocks in a rock mass that will survive at impact), and scaling factor b (which expresses the size ratio between the block and its fragments). These parameters can be applied iteratively to generate progressively smaller fragments. In contrast, RockGIS simulates block propagation using a lumped mass approach within the spatial constraints of a DTM and determines rebound through restitution factors based on the slope material's properties. Fragmentation is triggered by pre-existing discontinuities, and the initial mass distribution is stochastically generated, following a power-law distribution. Both models have been recently updated to enhance accuracy, incorporating block kinematics (Ruiz-Carulla and Corominas 2020; Matas et al. 2020).

While these models represent important steps in the effort to understand and model rockfall fragmentation, it is crucial to emphasize that all these models should undergo validation through real-scale fragmentation experiments. These experiments are essential to ensure the accuracy and reliability of these models in practical applications. Gaining physical evidence and validation from real-scale experiments is a critical next step in advancing our understanding of rockfall fragmentation processes and improving the precision of predictive models. Only through this combination of modeling and empirical data can we achieve a more comprehensive and accurate approach to rockfall hazard analysis and mitigation. In-situ tests have been widely performed (Ritchie 1963; Chau et al. 2002; Dorren et al. 2006; Bourrier et al. 2009; Labiouse and Heidenreich 2009; Giacomini et al. 2009; Dewez et al. 2010; Giacomini et al. 2010; Spadari et al. 2012; Volkwein and Klette 2014; Gili et al. 2016; Ruiz-Carulla et al. 2016; Matas et al. 2020; Prades-Valls et al. 2022), but their high cost and, most importantly, the significant logistical challenges involved in their execution make it very difficult to effectively use them in the context of quantitative numerical modeling.

The research question behind the following paper is: *Do laboratory and in situ fragmentation tests provide consistent results with respect to the enhanced travel of smaller fragments observed in the field?*

I’m author of the paper below (still in preparation), for which I contributed to the conceptualisation of the project, I dealt with analysis, investigation, methodology, visualisation, and writing of this draft. I was assisted in this work by the thesis student Giorgio Misasi, whom I would like to thank for his contribution.

Background Bibliography

Behera B, Kun F, McNamara S, Herrmann HJ. (2005). Fragmentation of a circular disc by impact on a frictionless plate. Journal of Physics: Condensed Matter 17:S2439

Bourrier F, Dorren L, Nicot F, Berger F, Darve F. (2009). Toward objective rockfall trajectory simulation using a stochastic impact model. Geomorphology 110:68-79. doi:https://doi.org/10.1016/j.geomorph.2009.03.017

Chau KT, Wong RHC, Wu JJ. (2002). Coefficient of restitution and rotational motions of rockfall impacts. International Journal of Rock Mechanics and Mining Sciences 39:69-77. doi:https://doi.org/10.1016/S1365-1609(02)00016-3

Agliardi, F., & Crosta, G. B. (2003). High resolution three-dimensional numerical modelling of rockfalls. International Journal of Rock Mechanics and Mining Sciences, 40(4), 455-471.

Crosta, G. B., Dattola, G., Lanfranconi, C., De Blasio, F. V., Malusà, M., & Bertolo, D. (2023). Rockfalls, fragmentation, and dust clouds: analysis of the 2017 Pousset event (Northern Italy). Landslides, 1-18.

De Blasio, F. V., Dattola, G., & Crosta, G. B. (2018). Extremely energetic rockfalls. Journal of Geophysical Research: Earth Surface, 123(10), 2392-2421.

Dewez T et al. (2010). OFAI: 3D block tracking in a real-size rockfall experiment on a weathered volcanic rocks slope of Tahiti, French Polynesia. Rock Slope Stability

Dorren LKA, Berger F, Putters US. (2006). Real-size experiments and 3-D simulation of rockfall on forested and non-forested slopes. Natural Hazards and Earth System Sciences 6:145-153. doi:https://doi.org/10.5194/nhess-6-145-2006

Frattini, P., Crosta, G.B., Agliardi, F., (2012) Chapter 22- Rockfall characterization and modeling. Landslides types, Mech Model 267

Giacomini A, Buzzi O, Renard B, Giani GP. (2009). Experimental studies on fragmentation of rock falls on impact with rock surfaces. International Journal of Rock Mechanics and Mining Sciences 46:708-715. doi:http://dx.doi.org/10.1016/j.ijrmms.2008.09.007

Giacomini A, Spadari M, Buzzi O, Fityus SG, Giani GP. Rockfall motion characteristics on natural slopes of eastern australia. In: Rock Mechanics in Civil and Environmental Engineering - Proceedings of the European Rock Mechanics Symposium, EUROCK 2010, 2010. pp 621-624

Gili JA et al. Experimental study on rockfall fragmentation: In situ test design and first results. In: Landslides and Engineered Slopes. Experience, Theory and Practice, 2016. pp 983-990

Labiouse V, Heidenreich B. (2009). Half-scale experimental study of rockfall impacts on sandy slopes. Natural Hazards and Earth System Sciences 9:1981-1993. doi:https://doi.org/10.5194/nhess-9-1981-2009

Lisjak A, Spadari M, Giacomini A, Grasselli G. (2010). Numerical modelling of rock falls using a combined finite-discrete element approach. Paper presented at the In Proceedings of the symposium rock slope stability, Paris, France

Liu L, Kafui KD, Thornton C. (2010). Impact breakage of spherical, cuboidal and cylindrical agglomerates. Powder Technology 199:189-196. doi:https://doi.org/10.1016/j.powtec.2010.01.007

Matas G, Lantada N, Corominas J, Gili J, Ruiz-Carulla R, Prades A. (2020). Simulation of Full-Scale Rockfall Tests with a Fragmentation Model. Geosciences 10:168

Moreno R, Ghadiri M, Antony SJ. (2003). Effect of the impact angle on the breakage of agglomerates: a numerical study using DEM. Powder Technology 130:132-137. doi:https://doi.org/10.1016/S0032-5910(02)00256-5

Paluszny A, Tang X, Nejati M, Zimmerman RW. (2016). A direct fragmentation method with Weibull function distribution of sizes based on finite- and discrete element simulations. International Journal of Solids and Structures 80:38-51. doi:https://doi.org/10.1016/j.ijsolstr.2015.10.019

Perfect E. (1997). Fractal models for the fragmentation of rocks and soils: a review. Engineering Geology 48:185-198. doi:http://dx.doi.org/10.1016/S0013-7952(97)00040-9

Prades-Valls, A., Corominas, J., Lantada, N., Matas, G., & Núñez-Andrés, M. A. (2022). Capturing rockfall kinematic and fragmentation parameters using high-speed camera system. Engineering Geology, 302, 106629.

Reddish, D. J., Stace, L. R., Vanichkobchinda, P., & Whittles, D. N. (2005). Numerical simulation of the dynamic impact breakage testing of rock. International Journal of Rock Mechanics and Mining Sciences, 42(2), 167-176.

Ritchie AM. (1963). Evaluation of rockfall and its control. Highway Research Record 17:13-28

Ruiz-Carulla R, Corominas J. (2020). Analysis of Rockfalls by Means of a Fractal Fragmentation Model. Rock Mechanics and Rock Engineering 53:1433-1455. doi:https://doi.org/10.1007/s00603-019-01987-2

Ruiz-Carulla R, Corominas J, Mavrouli O. (2017). A fractal fragmentation model for rockfalls. Landslides 14:875-889. doi:https://doi.org/10.1007/s10346-016-0773-8

Ruiz-Carulla R, Corominas J. (2020). Analysis of Rockfalls by Means of a Fractal Fragmentation Model. Rock Mechanics and Rock Engineering 53:1433-1455. doi:https://doi.org/10.1007/s00603-019-01987-2

Sator N, Hietala H. (2010). Damage in impact fragmentation. International Journal of Fracture 163:101-108. doi:https://doi.org/10.1007/s10704-009-9406-8

Spadari M, Giacomini A, Buzzi O, Fityus S, Giani GP. (2012). In situ rockfall testing in New South Wales, Australia. International Journal of Rock Mechanics and Mining Sciences 49:84-93. doi:https://doi.org/10.1016/j.ijrmms.2011.11.013

Thornton C, Yin KK, Adams MJ. (1996). Numerical simulation of the impact fracture and fragmentation of agglomerates. Journal of Physics D: Applied Physics 29:424

Volkwein A, Klette J. (2014). Semi-Automatic Determination of Rockfall Trajectories. Sensors 14:18187-18210

Wang Y, Tonon F. (2011). Discrete Element Modeling of Rock Fragmentation upon Impact in Rock Fall Analysis. Rock Mechanics and Rock Engineering 44:23-35. doi:https://doi.org/10.1007/s00603-010-0110-9

Wieczorek, G. F., Snyder, J. B., Waitt, R. B., Morrissey, M. M., Uhrhammer, R. A., Harp, E. L., ... & Finewood, L. G. (2000). Unusual July 10, 1996, rock fall at Happy Isles, Yosemite National Park, California. Geological Society of America Bulletin, 112(1), 75-85.

Wieczorek, G. F. (2002). Catastrophic rockfalls and rockslides in the Sierra Nevada, USA.

Wittel FK, Carmona HA, Kun F, Herrmann HJ. (2008). Mechanisms in impact fragmentation. International Journal of Fracture 154:105-117. doi:https://doi.org/10.1007/s10704-008-9267-6

Ye Y, Thoeni K, Zeng Y, Buzzi O, Giacomini A. (2019). Numerical Investigation of the Fragmentation Process in Marble Spheres Upon Dynamic Impact. Rock Mechanics and Rock Engineering. doi:https://doi.org/10.1007/s00603-019-01972-9

Zhao T, Crosta GB, Utili S, De Blasio FV. (2017). Investigation of rock fragmentation during rockfalls and rock avalanches via 3-D discrete element analyses. Journal of Geophysical Research: Earth Surface 122:678-695.

Investigating fragmentation patterns in rockfall events: a comparative analysis of in-situ and laboratory experiments

Camilla Lanfranconi[1], Giorgio Misasi[1], Stefano Basiricò[1], Paolo Frattini[1], Giuseppe Dattola[1], Fabio De Blasio[1], and Giovanni Battista Crosta[1]

[1] Department of Earth and Environmental Sciences, – DISAT, Università degli studi di Milano – Bicocca, Milan 20126, Italy

Introduction

The Rock Block Size Distribution (RBSD) parameter plays a crucial role in assessing the risk associated with rockfall events. Block size significantly influences detachment frequency and kinetic energy (Hungr et al., 1999; Lari et al., 2014; Wang et al., 2014). Additionally, the volume of rockfall blocks has implications for mitigation measures and the efficiency of forest protection (Lanfranconi et al., 2020). Understanding RBSD is essential for designing protective structures such as barriers and containment nets, which must be appropriately sized to withstand falls of varying block sizes (Brunetti et al., 2009; Corominas et al., 2017a, 2017b; Crosta et al., 2015; De Biagi et al., 2017; Dussauge et al., 2003; Dussauge-Peisser et al., 2002; Lambert and Bourrier, 2013; Lari et al., 2014; Malamud et al., 2004).

In the forthcoming article presented in Chapter 1 (Lanfranconi et al. in preparation - *Field evidence and indicators of rockfall fragmentation and implications for mobility*), it has been demonstrated that RBSD can serve as an indicator of fragmentation. In cases where significant fragmentation is absent, there is a trend of increasing block size with distance from the impact point or source area. Conversely, for energetic rockfall events characterized by intense fragmentation, small fragments exhibit longer travel distances compared to larger ones. Differentiating between blocks resulting primarily from the disaggregation process and those resulting from dynamic fragmentation is highly relevant for mitigation and the design of protective measures (Lanfranconi et al., 2023). The dynamic fragmentation of blocks leads to varying flight heights, velocities, and energies compared to non-fragmented blocks. Quantifying these differences experimentally is challenging due to significant anisotropies and weak structural components of rocks. In real rockfall scenarios, multiple impacts may simultaneously occur on the block's edges or face, and the outcomes vary depending on the impact direction relative to joint sets or anisotropic weakness planes, adding complexity to the phenomenon. While some real-scale tests have observed a connection between the number of anisotropies and the block's shape with the likelihood of receiving an effective impact direction (Giacomini et al., 2009; Gili et al., 2016; Ruiz-Carulla et al., 2016), there have been no studies focusing on the deposit patterns generated, as explored in the forthcoming article presented in Chapter 1 (Lanfranconi et al. in preparation - *Field evidence and indicators of rockfall fragmentation and implications for mobility*). In addition, some experiments conducted in rock quarries have contributed valuable insights into this phenomenon, with the most prominent ones being those by Spadari et al., 2012, Matas et al., 2020, and Prades-Valls et al., 2022.

On the other hand, some laboratory tests have been conducted (Guccione et al., 2021; Sun et al., 2019; Xing et al., 2022; Chau et al., 2000; Matas et al., 2021; Wu et al., 2004; Yang et al., 2022; Ye et al., 2020; Haug et al., 2014). However, these studies have primarily examined the dynamics of the impact process rather than the ground deposition.

Therefore, this study concentrates on performing real-scale tests in quarry and replicating the fragmentation process in the laboratory to investigate fragmentation-derived deposits and determine whether the results align with field observations, particularly regarding the travel distances of smaller fragments. A simplified image processing attempt was conducted, which allowed us to initiate a discussion about the hypotheses underlying this ground evidence.

Methods

In-Situ Test

In-situ tests took place at a quarry in Foppiano (Formazza, Verbano-Cusio-Ossola, Italian Central Alps). The site belongs to the Lower-Penninic Antigorio orthogneissic nappe, and the rock type is a granitic to granodioritic orthogneiss (Bigioggero et al., 1977) with medium grain size, generally marked planar foliation and augen texture (Cavallo et al, 2004). In particular, the quarry exploit a stone commercialized as Serizzo Formazza, showing uniform grain size, with a mineralogical composition including quartz, small porphyroclasts of potassic feldspar, plagioclase, biotite, and muscovite (Chapter 3a – Table 1). The physical-mechanical properties of Serizzo Formazza are reported in Chapter 3a – Table 2.

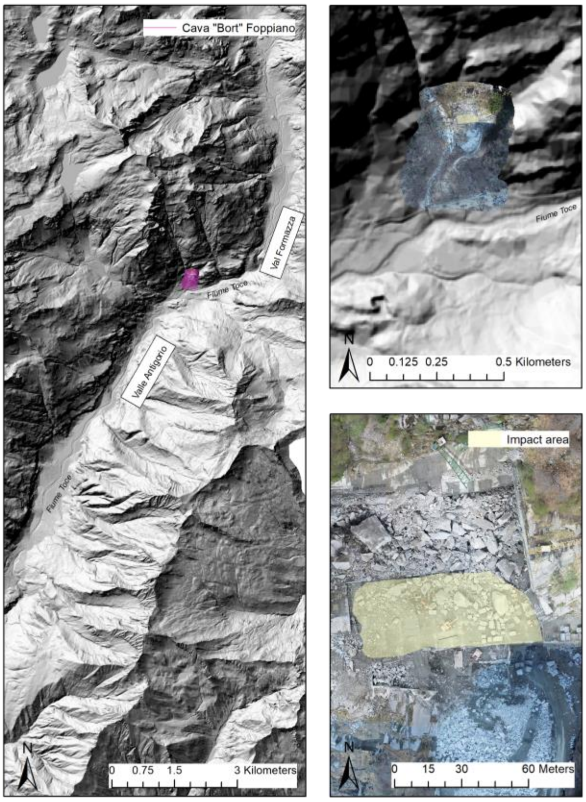

Chapter 3a - Figure 1 Study area in Cava Bort Foppiano quarry.

Experimental Setup and Data Collection Procedures

During the test, six blocks with a similar cubic shape but varying in size from 230 kg to 800 kg, have been released from heights of 30, 40, and 50 meters, and impacted on a horizontal plane made of the same rock of the blocks. The rock blocks were lifted using a crane and then released through a remote-controlled hook. Data collection during the test involved four video cameras, including one high-speed camera (Phantom v9.1, 700 fps, 1632 x 1200 pixels) and three GoPro Hero 8 cameras (240 fps, 1920 x 1080 pixels), and a Trimble X73D laser scanner.

The test surface was partially obstructed by large pre-existing blocks on the north side, while the southern side is limited by the main scarp of the quarry. Therefore, part of the small blocks generated by fragmentation have been lost down the scarp.

Before and after each test, a Trimble X7 3D laser scanner was used to generate point clouds of the quarry surface to characterize the Rock Block Surface Deposit (RBSD) and the distribution of blocks with distance. The laser scanner's features include an automated calibration system and self-leveling capabilities, enhancing accuracy on uneven terrain. Before each test, the quarry yard was cleared of remnants from previous impacts. The point clouds obtained using the 3D laser scanner was processed with Autodesk ReCap software to clean the cloud and to generate a 3D model. The volumes of ground fragments were calculated using two different methods: GeoMagic Wrap and ArcGIS. GeoMagic Wrap provides a 3D reconstruction of the volumes by converting the point clouds into 3D objects using a polygonal mesh, while ArcGIS provides a 2.5D reconstruction of the volumes by converting the point clouds into raster files with a resolution of 0.015 m x 0.015 m, and calculating the volumes by Difference of Dem (DoD) approach.

Chapter 3a - Table 1 Modal composition analysis of Serizzo Formazza

Mineralogical composition % by volume of the component minerals of the rock	
Quartz	30
Plagioclase	30
Feldspars	25
Biotite	10
Muscovite	3
Accessories	2

Chapter 3a - Table 2 Physical-mechanical characteristics of Serizzo Formazza

Serizzo Formazza parameters		
Compression breaking load (MPa)		150
Compression breaking load after freezing (MPa)		138
Imbibition coefficient (by weight) (°/°°)		3.05
Ultimate tensile strength (MPa)		15
Impact resistance: minimum fall height (cm)		98
Thermal linear expansion coefficient (10^{-6}/°C)		11.25
Frictional wear test: relative		0.76
Weight per unit of volume (kN/m^3)		26.9
Elasticity modulus (MPa)	tg Et	36880
	sec Es	23886
Knoop microhardness (MPa)		4729
Coefficient de Poisson		0.273
Speed waves ultrasonic (m/s)		2508

Chapter 3a - Table 3 Characteristics of the tested blocks

Test n	Block n	L_1 [m]	L_2 [m]	L_3 [m]	Volume [m^3]	Mass [kg]	Height of drop [m]
1	1	0.45	0.45	0.4	0.081	226.8	50
2	6	0.5	0.5	0.4	0.1	280	50
3	5	0.8	0.7	0.4	0.224	627.2	50
4	11	0.55	0.5	0.4	0.11	308	40
5	4	0.5	0.5	0.4	0.1	280	30
6	8	0.8	0.7	0.5	0.28	784	30

Laboratory Test

Experiments were conducted at the laboratories of the University of Milano – Bicocca by using a material that was sufficiently brittle to fragment even when released from relatively low heights (5 m and 6.1 m).

Following Haug et al., 2014, the samples were made of sand, potato starch, and water, at different concentration (Chapter 3a – Table 4). The sample preparation process involved several steps: i) the specified amounts of sand and starch were dry-mixed to create a homogeneous mixture; ii) a predetermined quantity of water was added and thoroughly mixed to form a uniform mass; iii) the resulting material was then placed in a spherical mold of 100 mm diameter, and compacted using a hammer; iv) the material underwent microwave treatment at 900 W for 15 minutes to yield solid samples. Chapter 3a – Table 4 provides an overview of the different starch concentrations, from 0.30% to 0.40%.

Chapter 3a - Table 4 Spherical samples and their mixture parameters

Sphere n.	**Potato starch [%]**	**Water [%]**	**Potato starch [g]**	**Water [g]**	**Volume [cm^3]**	**Dry weight [g]**	**γ_{dry} [g/cm^3]**
1	0.30	10	2.10	70	432.95	648.17	1.62
2	0.30	10	2.10	70	432.95	665.83	1.62

3	0.30	10	2.10	70	432.95	654.35	1.62
4	0.35	10	2.80	70	432.95	662.0	1.62
5	0.40	10	2.45	70	432.95	666.12	1.62
6	0.35	10	2.80	70	432.95	663.08	1.62
7	0.40	10	2.45	70	432.95	658.60	1.62

The compressive strength of the different mixtures have been characterized by uniaxial compressive tests on cylindrical samples prepared within silicone moulds with an inner diameter of 5 cm and a height of 10 cm. Based on the starch concentration, the resulting UCS varies between 0.6 and 0.25 MPa (Chapter 3a –Table 5).

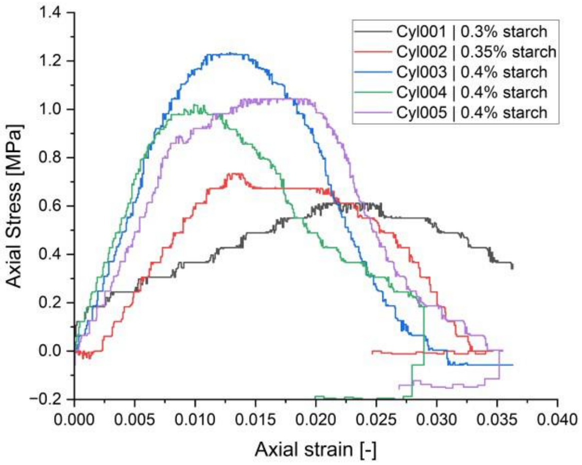

Chapter 3a - Figure 2 Uniaxial compressive test of starch-mixture samples

Experimental Setup and Data Collection Procedures

The experimental tests were conducted within a laboratory at the University of Milano - Bicocca (see Chapter 3a - Figure 3), releasing the spheres from 5.00 m and 6.10 m that impacted on the horizontal floor of the laboratory, on which a green plastic tarpaulin was placed, with a numbered grid impressed on it.

Three Chronos 1.4 High-Speed Cameras (500 fps, 1280 x 1024 pixels) mounting NIKON lenses 200 mm, f/ 1.8 have been used to record the impact. The cameras were placed 120 degrees apart from each other to cover a 360-degree view field. The cameras were synchronized via cables, with a manual triggering to define the start and end times.

Before initiating recordings, a calibration element (Chapter 3a - Figure 4) was placed as a reference volume to enable the absolute positions of fragments to be reconstructed. This calibration element was removed before each release. LED spotlights were used to illuminate the impact zone, and they were designed to provide continuous illumination, free from flickering, owing to their direct current power source.

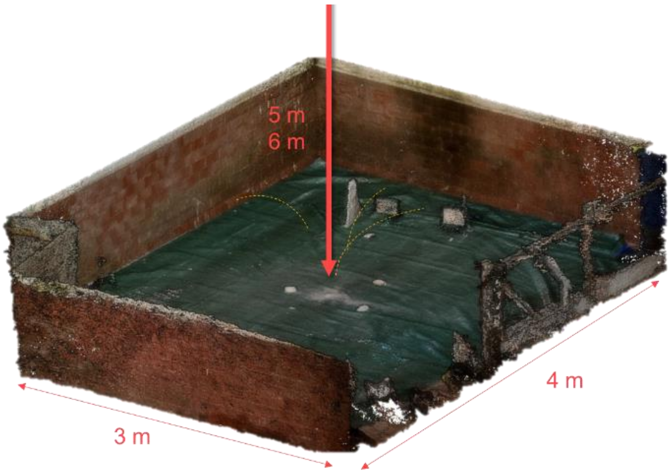

Chapter 3a - Figure 3 3D photogrammetric reconstruction of the laboratory test site at the University of Milano - Bicocca

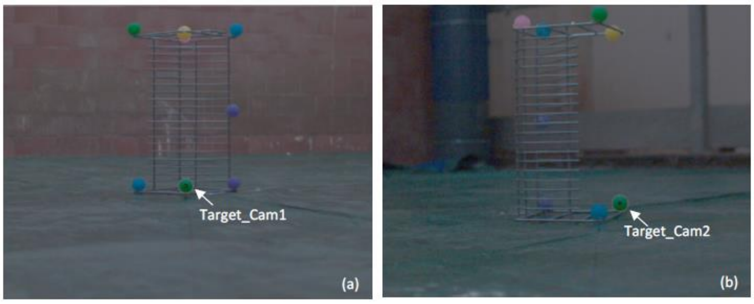

Chapter 3a - Figure 4 Calibration element and target points' relative positions from Camera 1 (a) and Camera 2 (b) during the recordings of Test 1, used for the calculations of fragments absolute positions in the space.

Simplified fragment tracking

Most of automatic particle-tracking software exhibit limitations that became apparent during this test. Notably, they struggle with delineating fragments when they overlap with one another or are very small. Therefore, a simplified semi-automatic approach aimed at calculating fragment velocities and post-impact exit angles has been adopted for this research. In each test, we selected a few fragments suitable for the analysis, including those with substantial mass and size, as well as smaller, more representative fragments that closely mimicked the motion of the projectile. Considering one frame out of four between the impact and the moment of maximum height, the algorithm allowed to calculate the center of gravity of the selected fragments in the x and z coordinates, portraying the fragment positions in each frame (Chapter 3a - Figure 5a). The approach involves several phases: i) Calculation of fragments' absolute positions, ii) Formulation of the view direction equation with respect to the i-th camera, iii) Determination of the absolute position of a point by knowing the position and orientation of two cameras and the corresponding relative coordinates, iv) Assignment of camera orientations and target points, allowing the determination of camera positions, v) Solving the problem arising from the singular matrix. Formulas are reported in the Supplementary Material chapter.

This approach enabled the determination of the absolute positions of objects in space, relying solely on the relative positions of the target fragments and a recognizable stationary point in space, which were obtained from just two cameras (Chapter 3a - Figure 5b). Starting from this, the absolute positions of the target fragments, including their azimuth and zenith angles, was obtained.

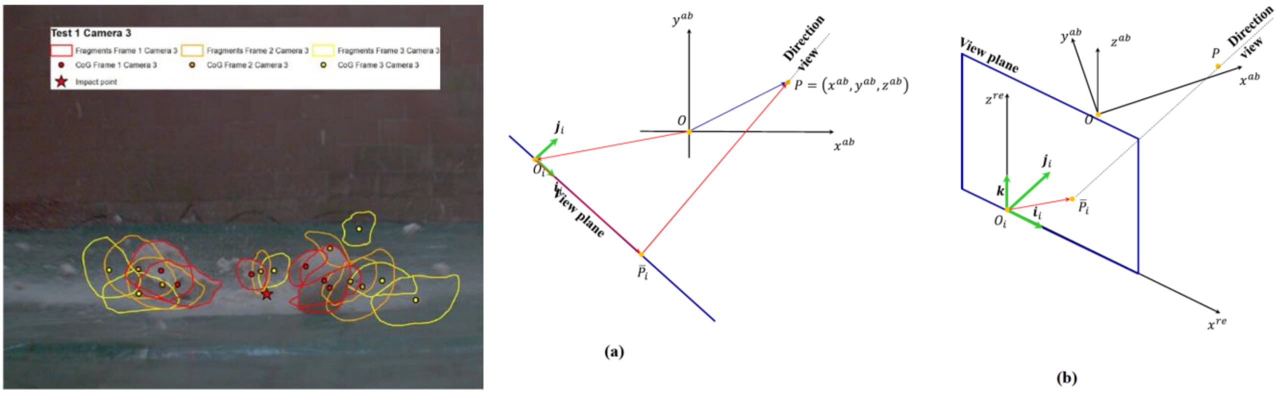

Chapter 3a - Figure 5 a) ArcGIS fragments analysis (Camera 3, Test 1); Representation of a camera view and the absolute reference system to which all cameras refer.

Statistical analysis of block shape and size

To characterize the fragment-size distribution, we adopted two approaches. First, we calculated the non-cumulative probability density of volume or mass classes, calculated as the number of fragments for each class dN, divided by the total number of fragments (N) and by the size of the class, dx (Malamud et al, 2004):

$$p(x) = \frac{1}{N}\frac{dN}{dx}$$

The distribution of the probability density as a function of volume or mass follows a power-law distribution, such as:

$$p(x) = ax^{-(b+1)}$$

Where b is the scaling exponent.

Then, we analyzed the fractal dimension, D_f, which describes the degree of comminution of the blocks during fragmentation. The fractal dimension was calculated from the number-size approach by using the scaling exponent (Turcotte, 1986):

$$D_f = 3b$$

Analysis and results

In-situ quarry test

Upon impact, due to the conditions in the quarry, a cloud of dust and debris would rise with each impact (Chapter 3a - Figure 7). This cloud was comprised of new fragments generated by the impact as well as material already lying on the quarry surface. This hampered a reliable image analysis aimed at tracking the fragment trajectories.

Fragmented volume calculation

The fragmented volume on the ground was computed from the in-situ point cloud data. Two distinct methodologies were employed for volume calculations, allowing for a comparative analysis between them and with respect to the initial volume measured prior to block testing. The 3D reconstruction made by GeoMagic Wrap revealed a notable reduction of over 40% in the initial volumes (Chapter 3a –Figure 8), while the 2.5D reconstruction made by ArcGIS showed a smaller reduction, occasionally resulting in volumes exceeding the initial volume (Chapter 3a - Figure 8), due to the approximations introduced by 2.5D reconstruction. For this reason, the first methodology is considered more reliable in volume calculations. The reduction in volume compared to the initial volume is mostly due to the loss of fragments down the scarp that limits the southern part of the impact surface.

Chapter 3a - Figure 6 First in-situ test (images from Phantom High-Speed camera)

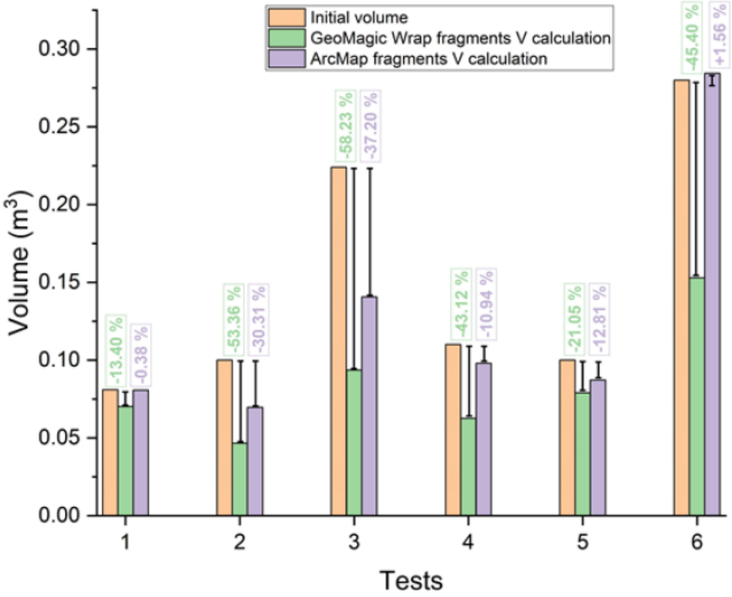

Chapter 3a - Figure 7 volume reconstructions showing the initial block volume with respect to the volume of fragments reconstructed with a 3D (Geomagic Wrap) and 2.5D (ArcMap) approaches.

The size-probability density distribution of the fragments shows a power-law distribution with a roll-over for some tests, and different values of the scaling exponent b (Chapter 3a – Figure 8). The fractal dimensions obtained from these scaling exponents range between 1.26 (test 1) and 3.06 (test 3). The relationship of the fractal dimension and the volumes show a clear positive correlation: the larger the block, the higher the fractal dimension. (Chapter 3a – Figure 9). This suggests that fragmentation is more efficient as the size of the blocks becomes higher. Regarding the release height, the correlation with fractal dimension is unclear.

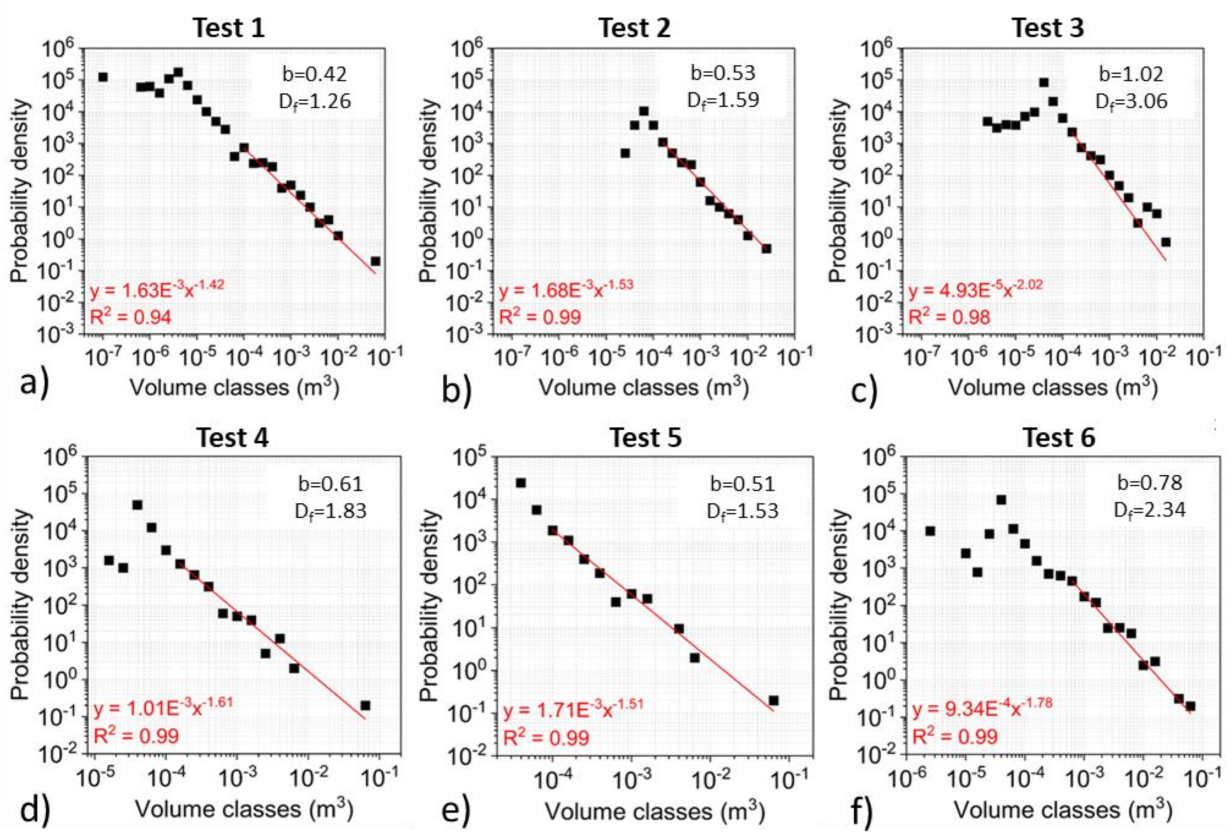

Chapter 3a - Figure 8 Probability density of volume for the fragments generated during the quarry field tests. The power-law fitting is shown red.

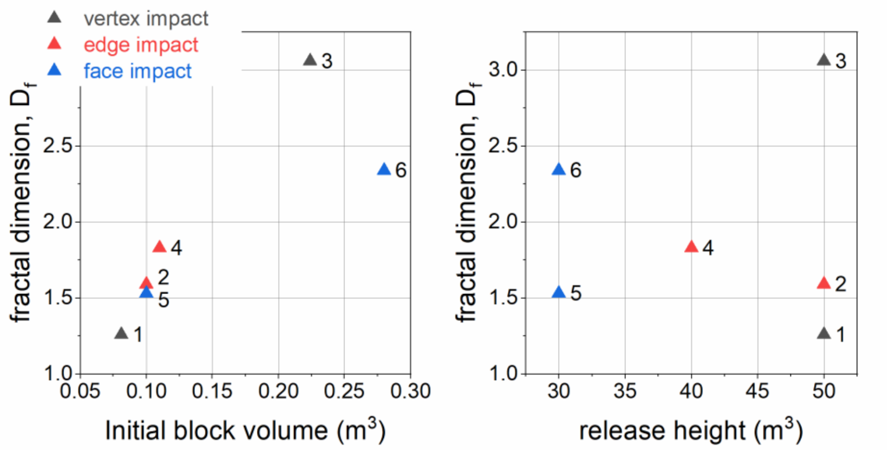

Chapter 3a - Figure 9 Summary results of power law exponent as a function of the initial block volume (left) and the fall height of the test (right).

Furthermore, it appears that the efficiency of fragmentation depends on the point of impact. In the six launches, two blocks impacted a face, two struck a vertex, and two landed on an edge. When the block impacts a vertex, the fragment distribution exhibits a distinct peak characterized by numerous smaller fragments (Chapter 3a – Figure 10). Conversely, when the impact occurs on an edge, the distribution appears flatter, with fragments dispersed across multiple volumetric classes, resembling the pattern observed when the impact transpires on a face.

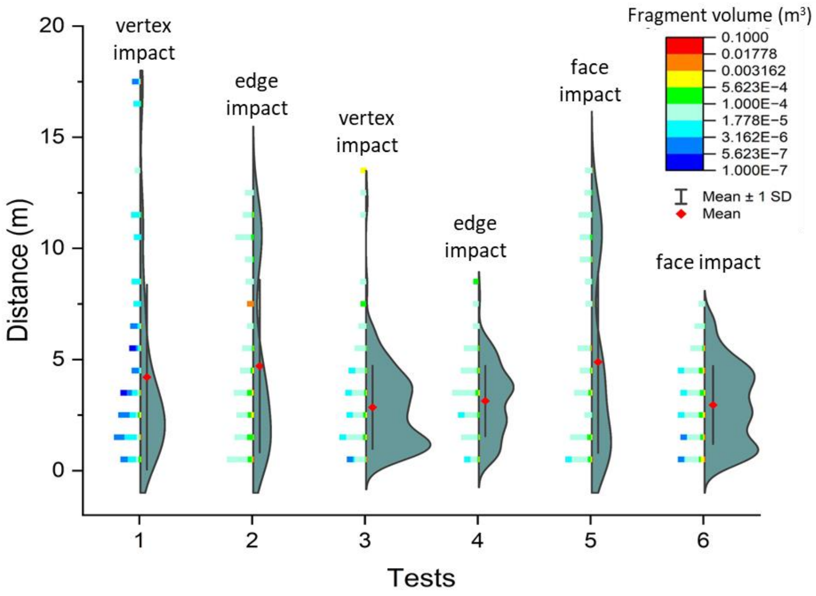

Chapter 3a - Figure 10 Fragments number distribution with distance (polygon) and size class of fragments (colored columns).

Ground Dispersion of Fragments Resulting from Impacts

The spatial distribution of fragments on the ground reveals that fragments of different size are diffusely mixed, especially at smaller distances, apparently with a random behavior. However, when analyzing in terms of block frequency (see Chapter 3a - Figure 11), it is possible to observe that the results align with the field evidence observed in the case studies presented in Chapter 1: i.e., that smaller blocks tend to reach greater distances.

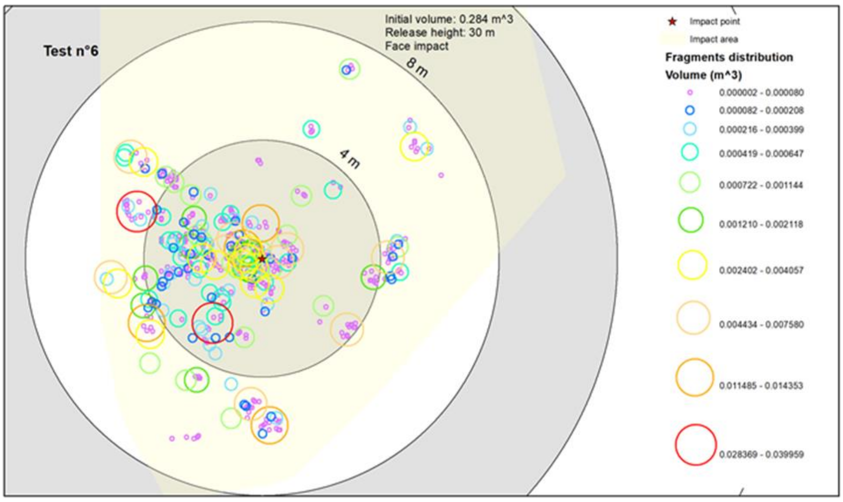

Chapter 3a - Figure 11 spatial distribution of fragments with respect to the impact point. Each fragments is represented by a circle with size and color classified according to fragmant volume.

In particular, Chapter 3a - Figure 11 shows the fragment-size distribution expressed in terms of cumulative relative frequency. By increasing the distance from the impact point, the total number of fragments decreases, and also the size decreases significantly, as shown by a shift of the distribution toward left. This demonstrates that fragments at higher distances are smaller with respect to fragments closer to the impact point.

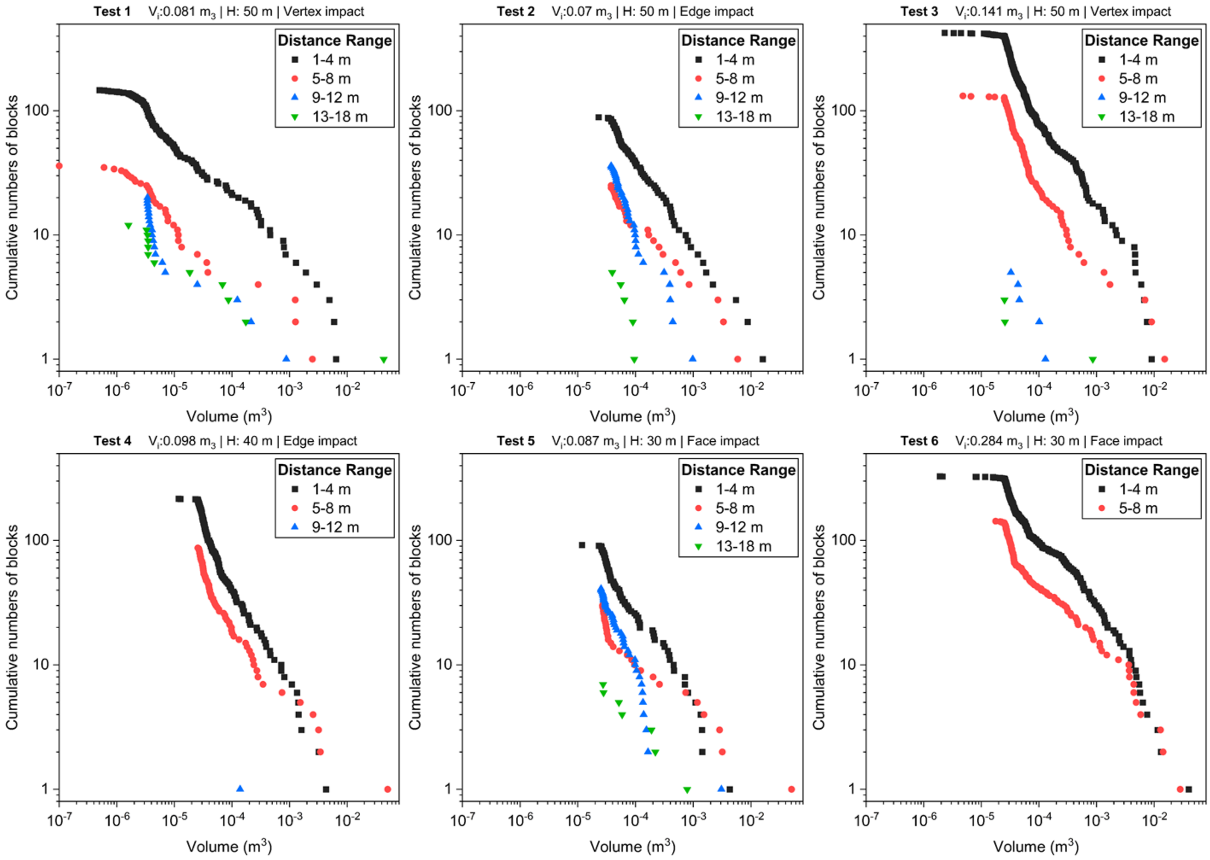

Chapter 3a - Figure 12 Cumulative number of blocks obtained from each fragmentation test performed. Colors mean the distance range where blocks and fragments stopped.

The evidence that smaller blocks tends to reach greater distances becomes even more apparent when analyzing the 99th percentile of block volume associated with specific distances (Chapter 3a - Figure 12). This analysis reveals a clear trend of reduced fragment volume as distances increase. This trend is either exponential or power-law, but the goodness-of-fit values are very small, due to the large scatter of the values.

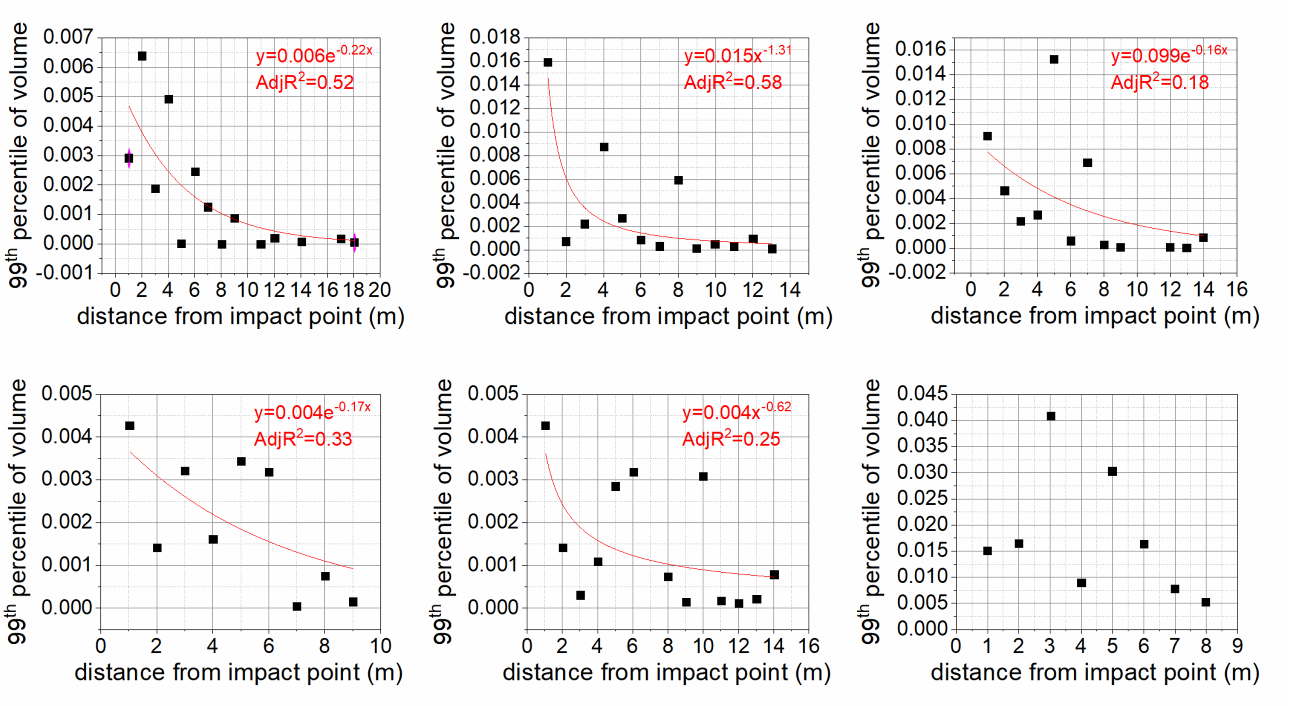

Chapter 3a - Figure 13 99th percetile of te fraent volume as a function of the distance from the impact point. The fitting functions should be intendend purely as indicative of the size-distance trend

Laboratory test

Fragmentation Intensity and Correlations

Since the mixture of sand, starch and water is very weak, the fragments collected after impact often broke before they could be analyzed for volume, the size of the single particles was analyzed based on their weight. The probability density of fragments size follows a power law almost for the entire range of size, except the smallest fragments where undersampling may have occurred (Chapter 3a – Figure 14).

As observed in the in-situ tests, the results reveal that the samples with greater weight exhibit higher fractal dimension. The exponent shows a slight negative correlation with the fall height and a slight positive correlation with the percentage of starch, which can be considered as a proxy of compressive strength (Chapter 3a – Figure 15c,d).

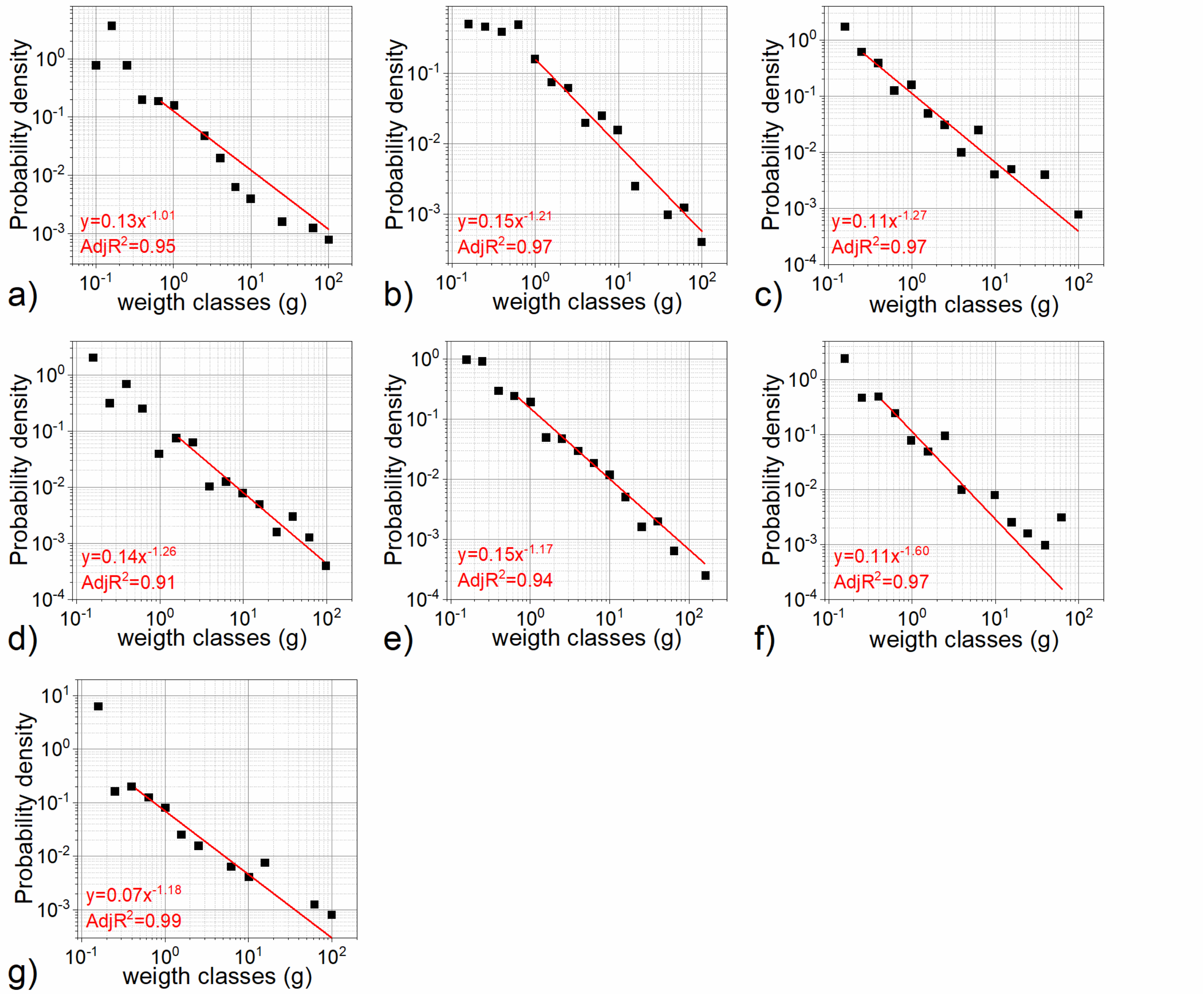

Chapter 3a - Figure 14 Probability density of volume for the fragments generated during the laboratory tests. The power-law fitting is shown in red.

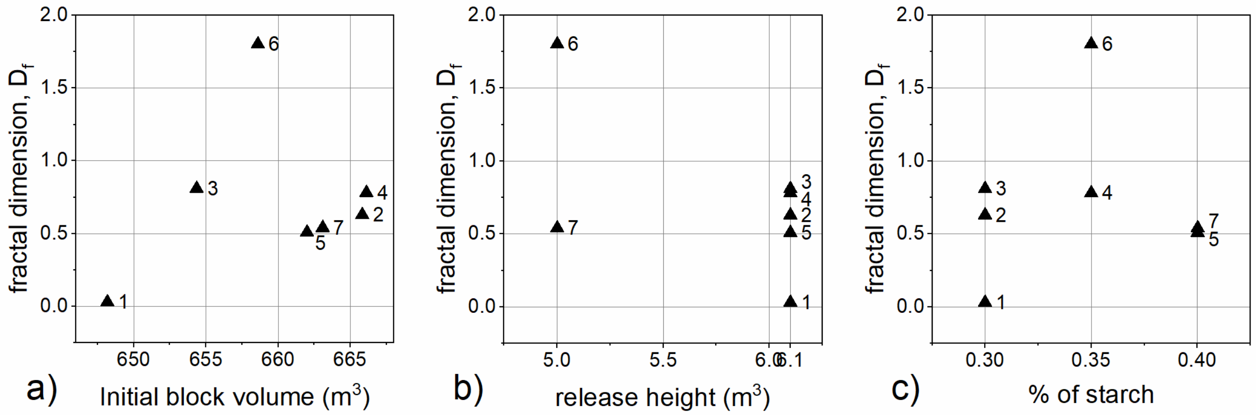

Chapter 3a - Figure 15 Summary results of power law exponent as a function of the initial weight (a), the fall height (b), and the percentage of starch in the mixture (c).

Ground Dispersion of Fragments Resulting from Impacts

We measured the ground dispersion of the fragments after impact, cataloging them based on their position within the grid and collected their weights. Chapter 3a – Figure 16 illustrates an example of this spatial distribution of fragments from test 1 (see Supplementary materials for the other tests). The results can be challenging to interpret due to the well-distributed spatial arrangement of fragments. However, by analyzing the 99th percentile (Chapter 3a - Figure 17) it is possible to recognize a clear trend in the spatial distribution of fragments with different size, with smaller fragments exhibiting a tendency to travel greater distances following fragmentation.

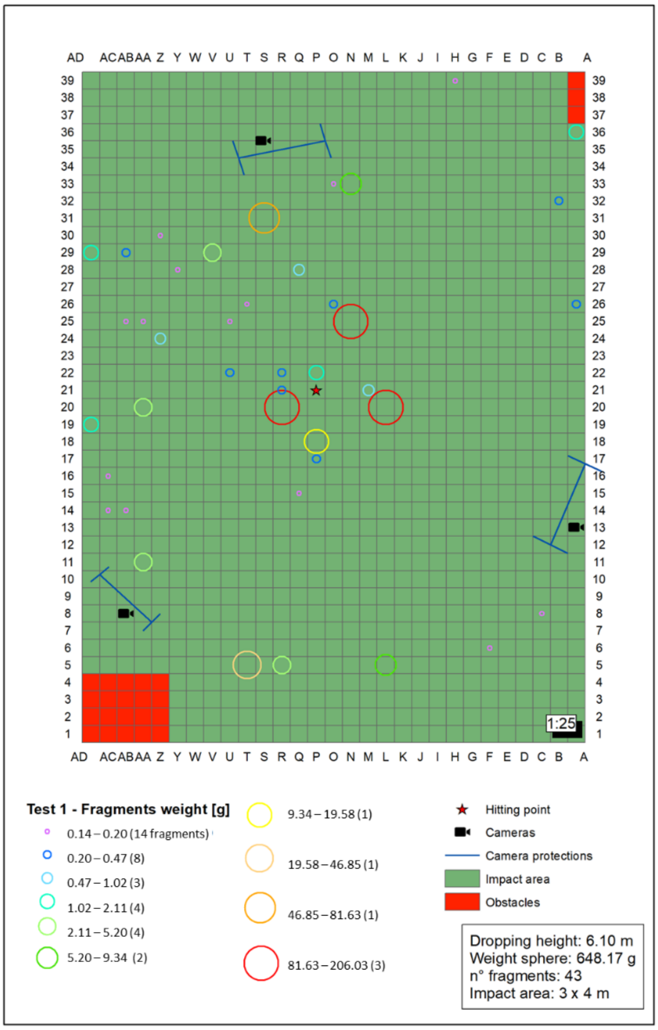

Chapter 3a - Figure 16 fragments dispersion after impact of sample Sph003

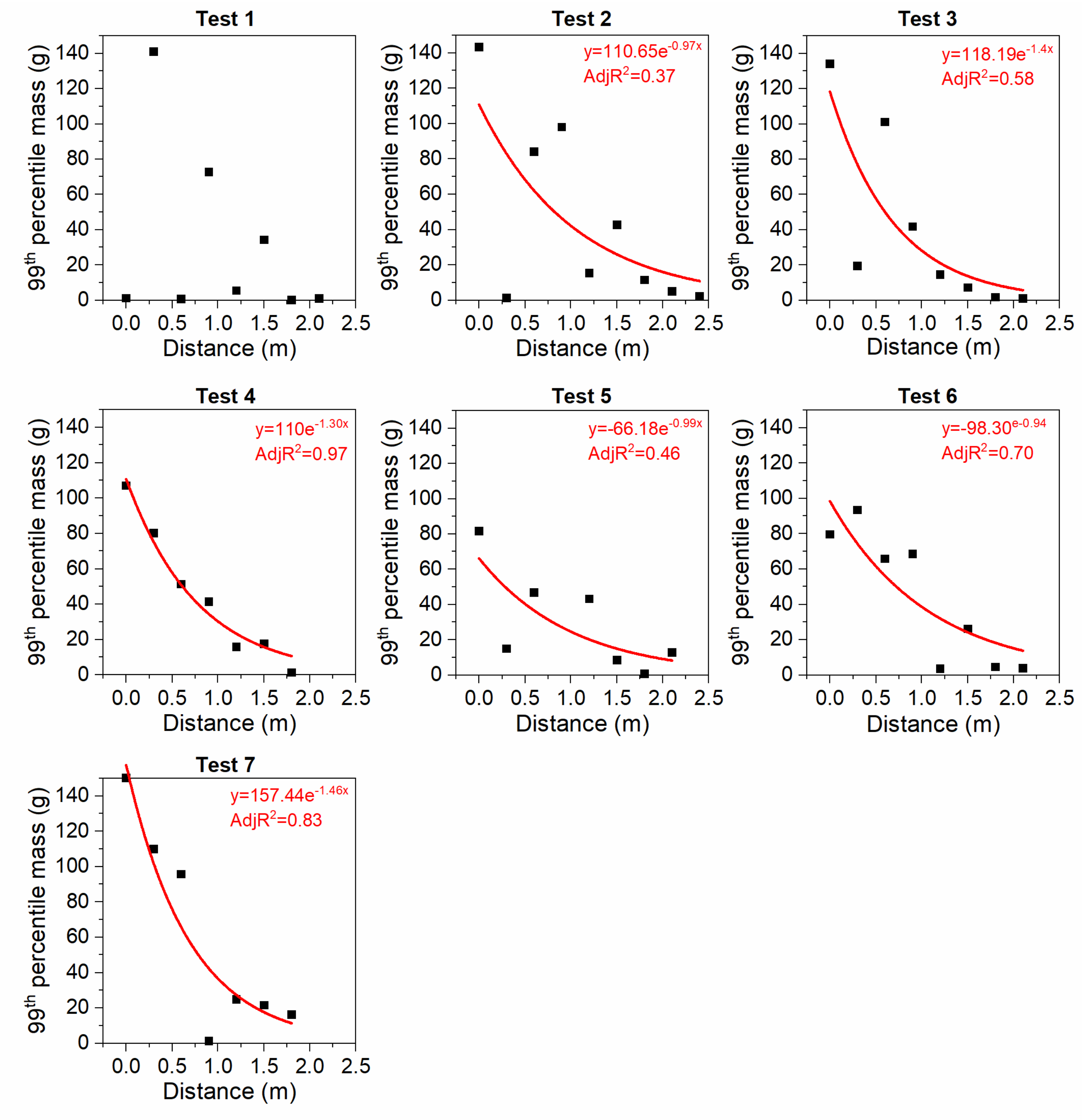

Chapter 3a - Figure 17 Distances reached by fragments based on their 99th percentile of mass

Exit angles

By using the simplified tracking approach, we reconstructed the absolute position of the target fragments in time, from which we could calculate the exit zenith angles and the velocity of the fragments moving from the impact zone. In Chapter 3a – Figure 18 it is possible to recognize a weak trend of velocity as a function of the zenith angle (the larger the angle, the higher the velocity), whereas the weight of the fragments seems not correlated with either the angle or the velocity.

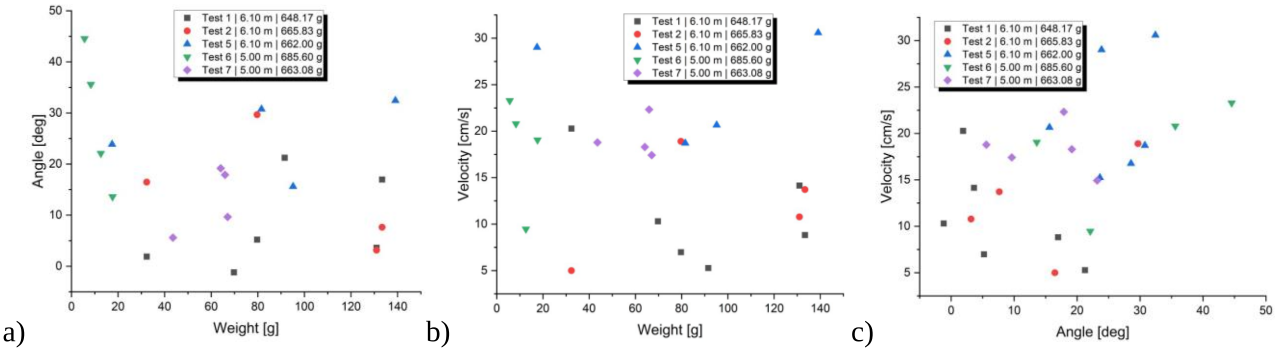

Chapter 3a - Figure 18 Results of fragment tracking: a) zenith angle vs weight; b) velocity vs weight, c) velocity vs zenith angle.

Discussion

Fragmentation is a complex process that can be influenced by various factors, so that the study of this phenomenon presents several challenges, whether the test is performed in the field or under controlled laboratory conditions. In this research, two main topics have been addressed: i) the size frequency distribution resulting from fragmentation, which has been analyzed with respect to the size of the blocks and the release height; ii) the spatial distribution of fragments in relationship with the fragments size.

The size distribution resulting from fragmentation follows a power-law for all tests, confirming the fragmentation process to be fractal in nature (Turcotte, 1986). In the quarry test, a rollover was observed, probably due to the difficulties in the analysis of the smallest fragments from the point cloud of the laser scanner on a relatively irregular (natural) impact surface. The analysis of the fractal dimension, Df, show that the values are larger for the quarry test (from 1.26 to 3.06) with respect to the laboratory test (from 0.51 to 1.8, excluding the D_f of test 1). This may be related to the different energy available in the quarry, with respect to the laboratory, due to the different release height. Both in the quarry and in the laboratory tests, the fractal dimension is a function of the size of the block: the larger the block, the higher the degree of comminution. On the other hand, the release height, that one may expect to affect the degree of comminution, does not show any clear relationship with the fractal dimension. However, we should consider that the degree of comminution is likely affected by a combination of factors, such as the release height, the position of the impact, the orientation of schistosity (in case of the orthogneiss), and the mass. Unfortunately, the limited number of tests did not allow to fully investigate the role of these factors. Moreover, the testing site was laterally constrained by large preexisting boulders on the northern side and by the scarp on the southern side, hindering a complete mapping of fragment distribution and a total recover of the volume.

The spatial distribution of fragments in relationship with the fragments size shows a consistent trend of smaller fragments to travel further with respect to larger ones. This trend was clearly recognized, both in the quarry tests and in the laboratory tests, by analyzing the 99th percentiles of the volumes of weight, similarly to what has been done for rockfall events (Chapter 1). The underlying reasons for this phenomenon prompt the formulation of three main hypotheses:

1. Mass and Velocity: A potential relationship between fragment mass and exit velocity may exist.
2. Mass and Exit Angles: There could be a connection between fragment mass and the angles at which fragments exit the impact point.
3. Effect of Sampling Size in the Longitudinal Distribution of Blocks: Smaller blocks, characterized by a larger population, might have a higher probability of appearing in the tail of the longitudinal distribution compared to larger blocks with a smaller population.

From prior research conducted by Guccione et al., 2023 it appears that the first hypothesis may not hold true, as there is no discernible trend between fragment velocity (normalized by the impact velocity of the sphere) and fragment mass. In other words, small fragments do not seem to consistently possess higher or lower velocities than larger ones. In this study, the investigation of the dynamics of fragments through the semi-automatic analysis of particle tracking from the high-speed videos was impossible for the quarry test because of the non-uniform background and the similarity of background color with fragments color. In addition, dust generated during impacts further complicated the image analysis. In the laboratory test it was possible to apply particle tracking by using a simplified algorithm, but the procedure was extremely time-consuming, and not feasible for a mass analysis of the fragment dynamics (Chapter 3a – Figure 5). Hence, the sample of fragments was limited. Notwithstanding, it was possible to recognize a relationship of velocity with the zenith angle (Chapter 3a – Figure 18c), suggesting the horizontal fragments to travel faster than the vertical ones, but no relationships have been recognized with the fragment mass (Chapter 3a – Figure 18b), confirming the findings of Guccione et al, 2023. Heowever, both Guccione at al (2023) and this study do not account for the smallest fragments, leaving room for further conclusions. The second hypothesis (mass and exit angle) was tested with the particle tracking of laboratory tests. The results do not show any appreciable trend (Chapter 3a - Figure 18a). However, the number of fragments is limited, and the smallest fragments were not analyzed, hence the results are far from being conclusive. The third hypothesis (effect of sampling) holds merit. While the first two physical explanations remain undemonstrated, a statistical explanation, grounded in statistical mechanics, may be more suitable. In this context, assuming a random distribution of momentum to the fragments, regardless of the size, a chaotic fragmentation process where overall momentum is conserved would arise, leading to a random spatial distribution of blocks. However, given the larger population of smaller fragments compared to larger ones, it becomes more probable to observe smaller blocks in the tail of the spatial distribution, giving rise to an apparent sorting of the fragment size with distance.

Conclusions

This article summarizes the findings obtained from on-site and laboratory fragmentation tests. As for the size frequency distribution, a power-law behavior was observed in both the in-situ and laboratory tests, confirming the fragmentation process to be fractal in nature. The fractal dimensions are significantly larger in the in-situ test with respect to the laboratory tests, probably due to the higher energy at impact, leading to a greater comminution. In all tests, the larger the blocks, the higher the degree of comminution. Despite the limitations experienced in both tests, the results obtained are significant as they validate the previously described ground evidence in Chapter 1, regarding smaller fragments traveling longer distances. Furthermore, these tests have provided valuable insights to elaborate hypotheses that may explain this behavior. Specifically, while the physical explanations remains inconclusive, a statistical explanation may be more plausible. This hypothesis suggests that the random distribution of momentum among the fragments, regardless of the size, would lead to a chaotic fragmentation process, resulting in a random distribution of fragments in space. Given the larger population of smaller fragments, it becomes more likely to observe smaller blocks in the tail of the spatial distribution.

References

Brunetti, M. T., Guzzetti, F., & Rossi, M. J. N. P. I. G. (2009). Probability distributions of landslide volumes. Nonlinear Processes in Geophysics, 16(2), 179-188.

Chau, K. T., Wei, X. X., Wong, R. H. C., & Yu, T. X. (2000). Fragmentation of brittle spheres under static and dynamic compressions: experiments and analyses. Mechanics of materials, 32(9), 543-554.

Corominas J, Lantada N, Gili J, Ruiz R, Matas G, Mavrouli O, Núñez-Andrés MA, Moya J, Buill F, Abellán A, Puig-Polo C, Prades A, Martinez-Bofill J, Salo L (2017b) The RockRisk project: rockfall risk quantification and prevention. Proceedings of ROCEXS 2017, 6th Interdisciplinary Workshop on Rockfall Protection, May 2017, Barcelona (Spain). pp 39–42.

Corominas J, Mavrouli O, Ruiz-Carulla R (2017a) Rockfall occurrence and fragmentation. In: Sassa K, Mikoš M, Yin Y (Eds): Advancing Culture of Living with Landslides. World Landslide Forum, WLF 2017, Ljubljana. Springer, Cham. pp 75–97. https://doi.org/10.1007/978-3-319-59469-9_4

Crosta, G. B., Agliardi, F., Frattini, P., & Lari, S. (2015). Key issues in rock fall modeling, hazard and risk assessment for rockfall protection. In Engineering geology for society and territory-volume 2 (pp. 43-58). Springer, Cham.

De Biagi, V., Napoli, M. L., & Barbero, M. (2017). A quantitative approach for the evaluation of rockfall risk on buildings. Natural hazards, 88, 1059-1086.

Dussauge, C., Grasso, J. R., & Helmstetter, A. (2003). Statistical analysis of rockfall volume distributions: Implications for rockfall dynamics. Journal of Geophysical Research: Solid Earth, 108(B6).

Dussauge-Peisser, C., Helmstetter, A., Grasso, J. R., Hantz, D., Desvarreux, P., Jeannin, M., & Giraud, A. (2002). Probabilistic approach to rock fall hazard assessment: potential of historical data analysis. Natural hazards and earth system sciences, 2(1/2), 15-26.

GIACOMINI, A., et al. Experimental studies on fragmentation of rock falls on impact with rock surfaces. International Journal of Rock Mechanics and Mining Sciences, 2009, 46.4: 708-715.

GILI, J. A., et al. Experimental study on rockfall fragmentation: in situ test design and firsts results. Landslides and engineered slopes, 2016, 2: 983-990.

Guccione, D. E., Buzzi, O., Thoeni, K., Fityus, S., & Giacomini, A. (2021). Predicting the fragmentation survival probability of brittle spheres upon impact from statistical distribution of material properties. International Journal of Rock Mechanics and Mining Sciences, 142, 104768.

Guccione, D. E., Giacomini, A., Thoeni, K., Fityus, S., & Buzzi, O. (2023). On the Dynamic Fragmentation of Rock-Like Spheres: Insights into Fragment Distribution and Energy Partition. Rock Mechanics and Rock Engineering, 56(2), 847-873.

Haug, Ø. T., Rosenau, M., Leever, K., & Oncken, O. (2014). Modelling fragmentation in rock avalanches. In Landslide Science for a Safer Geoenvironment: Volume 2: Methods of Landslide Studies (pp. 93-100). Springer International Publishing.

Hungr, O., Evans, S. G., & Hazzard, J. (1999). Magnitude and frequency of rock falls and rock slides along the main transportation corridors of southwestern British Columbia. Canadian Geotechnical Journal, 36(2), 224-238.

Lambert, S., & Bourrier, F. (2013). Design of rockfall protection embankments: a review. Engineering geology, 154, 77-88.

Lanfranconi et al. – Field evidence and indicators of rockfall fragmentation and implications for mobility ------in preparation

Lanfranconi, C., Frattini, P., Sala, G., Dattola, G., Bertolo, D., Sun, J., & Crosta, G. B. (2023). Accounting for the effect of forest and fragmentation in probabilistic rockfall hazard. Natural Hazards and Earth System Sciences, 23(6), 2349-2363.

Lanfranconi, C., Sala, G., Frattini, P., Crosta, G. B., & Valagussa, A. (2020). Assessing the rockfall protection efficiency of forests at the regional scale. Landslides, 17, 2703-2721.

Lari, S., Frattini, P., & Crosta, G. B. (2014). A probabilistic approach for landslide hazard analysis. Engineering geology, 182, 3-14

Malamud, B. D., Turcotte, D. L., Guzzetti, F., & Reichenbach, P. (2004). Landslide inventories and their statistical properties. Earth Surface Processes and Landforms, 29(6), 687-711.

Matas, G., Lantada, N., Corominas, J., Gili, J., Ruiz-Carulla, R., & Prades, A. (2020). Simulation of full-scale rockfall tests with a fragmentation model. Geosciences, 10(5), 168.

Matas, G., Parras, E., Lantada, N., Gili, J., Ruiz-Carulla, R., Corominas, J., ... & Puig, C. (2021, February). Laboratory test to study the effect of comminution in rockfalls. In Proceedings of the XIII International Symposium on Landslides, Cartagena de Indias, Cartagena, Colombia (pp. 22-26).

Ruiz Carulla, R., Matas Casado, G., Prades Valls, A., Gili Ripoll, J. A., Corominas Dulcet, J., Lantada, N., ... & Moya Sánchez, J. (2016). Analysis of rock block fragmentation by means of real-scale tests. In International Symposium Rock Slope Stability 2016: proceedings (pp. 107-108). Sage.

RUIZ-CARULLA, Roger; COROMINAS, Jordi; MAVROULI, Olga. A fractal fragmentation model for rockfalls. Landslides, 2017, 14.3: 875-889.

Spadari, M., Giacomini, A., Buzzi, O., Fityus, S., & Giani, G. P. (2012). In situ rockfall testing in new south wales, australia. International Journal of Rock Mechanics and Mining Sciences, 49, 84-93.

Sun, H., Zeng, Y., Ren, S., Ye, Y., & Chen, X. (2019). Breakage probability of marble spheres under normal, repeated impacts. International Journal of Impact Engineering, 130, 68-78.

Wang, X., Frattini, P., Crosta, G. B., Zhang, L., Agliardi, F., Lari, S., & Yang, Z. (2014). Uncertainty assessment in quantitative rockfall risk assessment. Landslides, 11, 711-722.

Wu, S. Z., Chau, K. T., & Yu, T. X. (2004). Crushing and fragmentation of brittle spheres under double impact test. Powder Technology, 143, 41-55.

Xing, H., Wang, M., Ju, M., Li, J., & Li, X. (2022). Measurement of ejection velocity of rock fragments under dynamic compression and insight into energy partitioning. International Journal of Rock Mechanics and Mining Sciences, 149, 104992.

Yang, T., Ma, H., Weng, L., Liu, Y., Chu, Z., Zhang, P., ... & Chang, W. (2022). Fragmentation analyses of rocks under high-velocity impacts using the combined finite-discrete element simulation. Frontiers in Earth Science, 10, 998521.

Ye, Y., Thoeni, K., Zeng, Y., Buzzi, O., & Giacomini, A. (2020). Numerical investigation of the fragmentation process in marble spheres upon dynamic impact. Rock Mechanics and Rock Engineering, 53, 1287-1304.

Supplementary materials

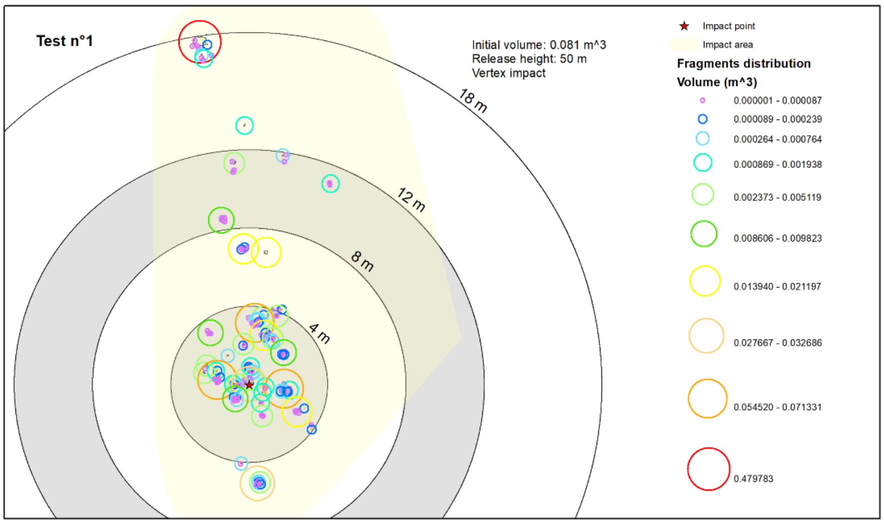

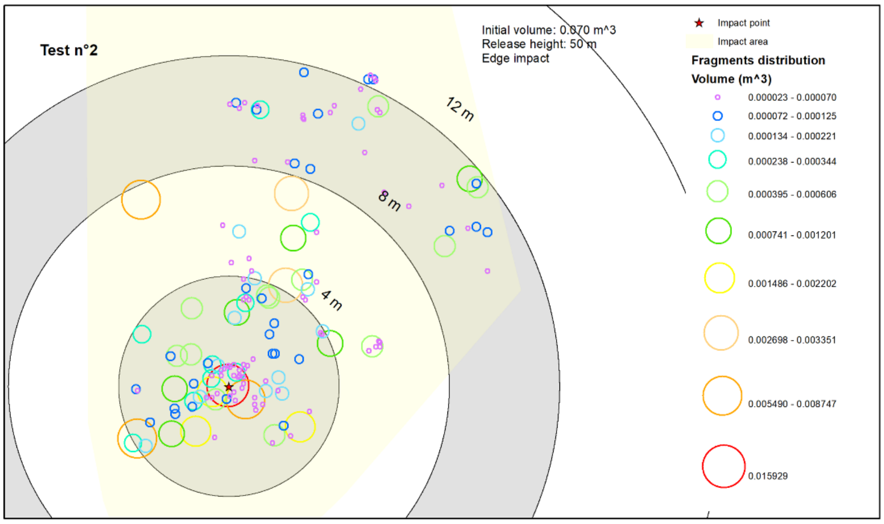

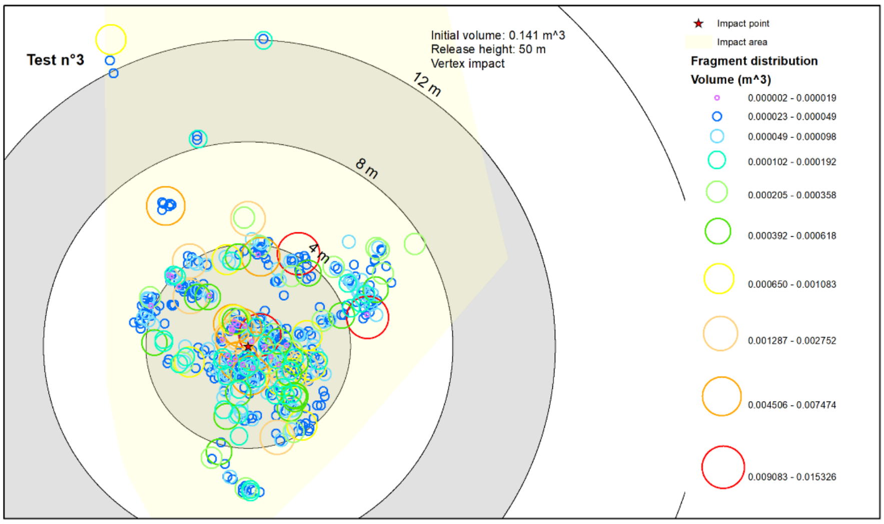

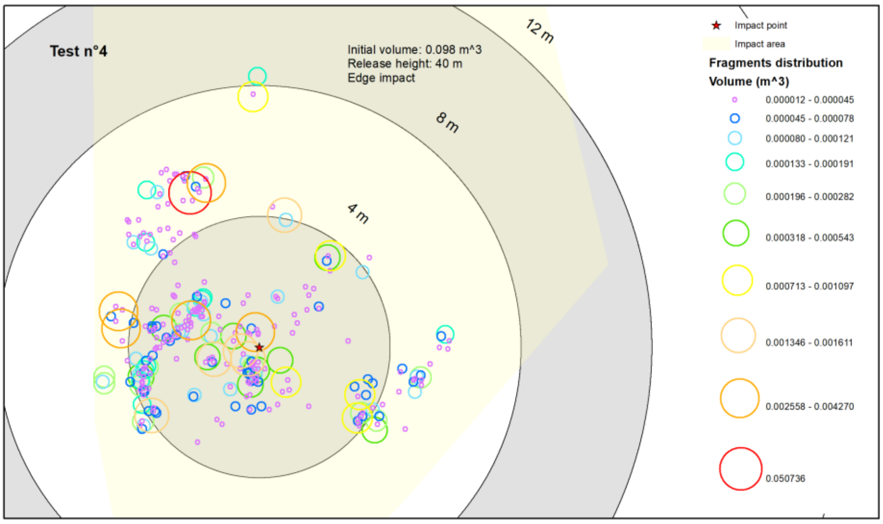
Test n°4
Initial volume: 0.098 m^3
Release height: 40 m
Edge impact
12 m
8 m
4 m
★ Impact point
Impact area
Fragments distribution
Volume (m^3)
0.000012 - 0.000045
0.000045 - 0.000078
0.000080 - 0.000121
0.000133 - 0.000191
0.000196 - 0.000282
0.000318 - 0.000543
0.000713 - 0.001097
0.001346 - 0.001611
0.002558 - 0.004270
0.050736

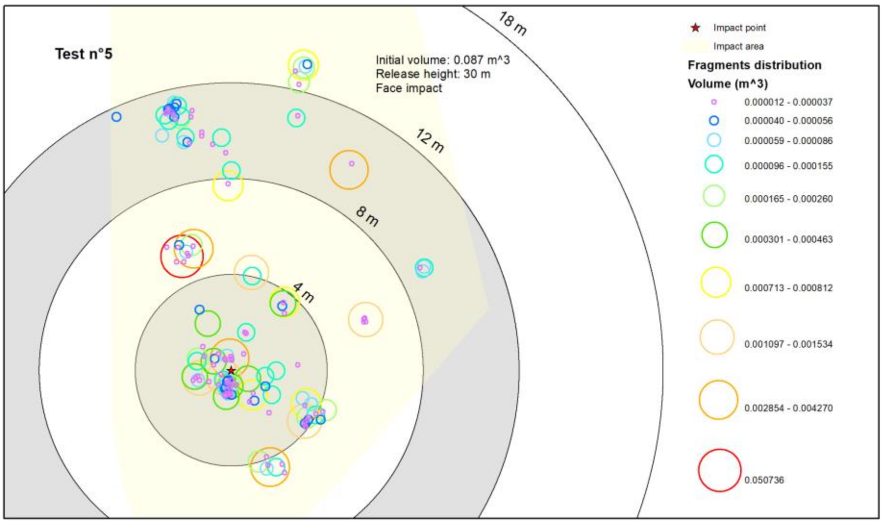
Test n°5
Initial volume: 0.087 m^3
Release height: 30 m
Face impact
18 m
12 m
8 m
4 m
★ Impact point
Impact area
Fragments distribution
Volume (m^3)
0.000012 - 0.000037
0.000040 - 0.000056
0.000059 - 0.000086
0.000096 - 0.000155
0.000165 - 0.000260
0.000301 - 0.000463
0.000713 - 0.000812
0.001097 - 0.001534
0.002854 - 0.004270
0.050736

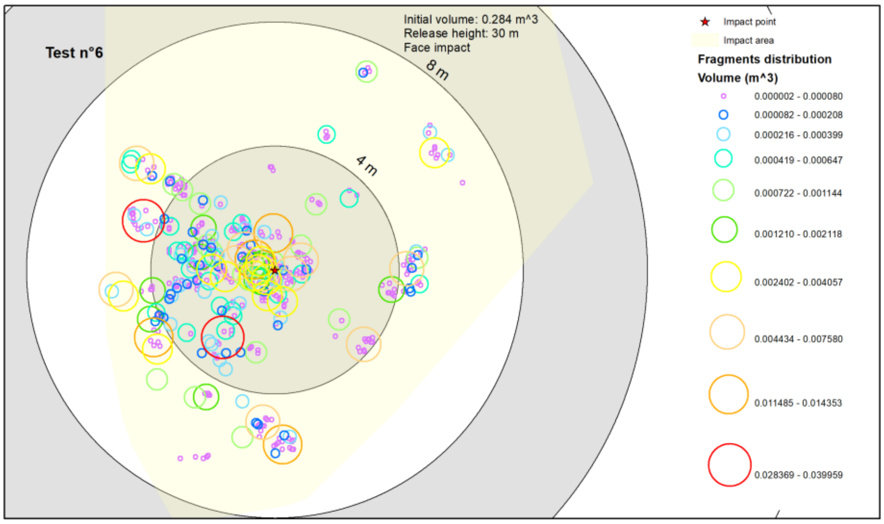
Test n°6
Initial volume: 0.284 m^3
Release height: 30 m
Face impact
8 m
4 m
★ Impact point
Impact area
Fragments distribution
Volume (m^3)
0.000002 - 0.000080
0.000082 - 0.000208
0.000216 - 0.000399
0.000419 - 0.000647
0.000722 - 0.001144
0.001210 - 0.002118
0.002402 - 0.004057
0.004434 - 0.007580
0.011485 - 0.014353
0.028369 - 0.039959

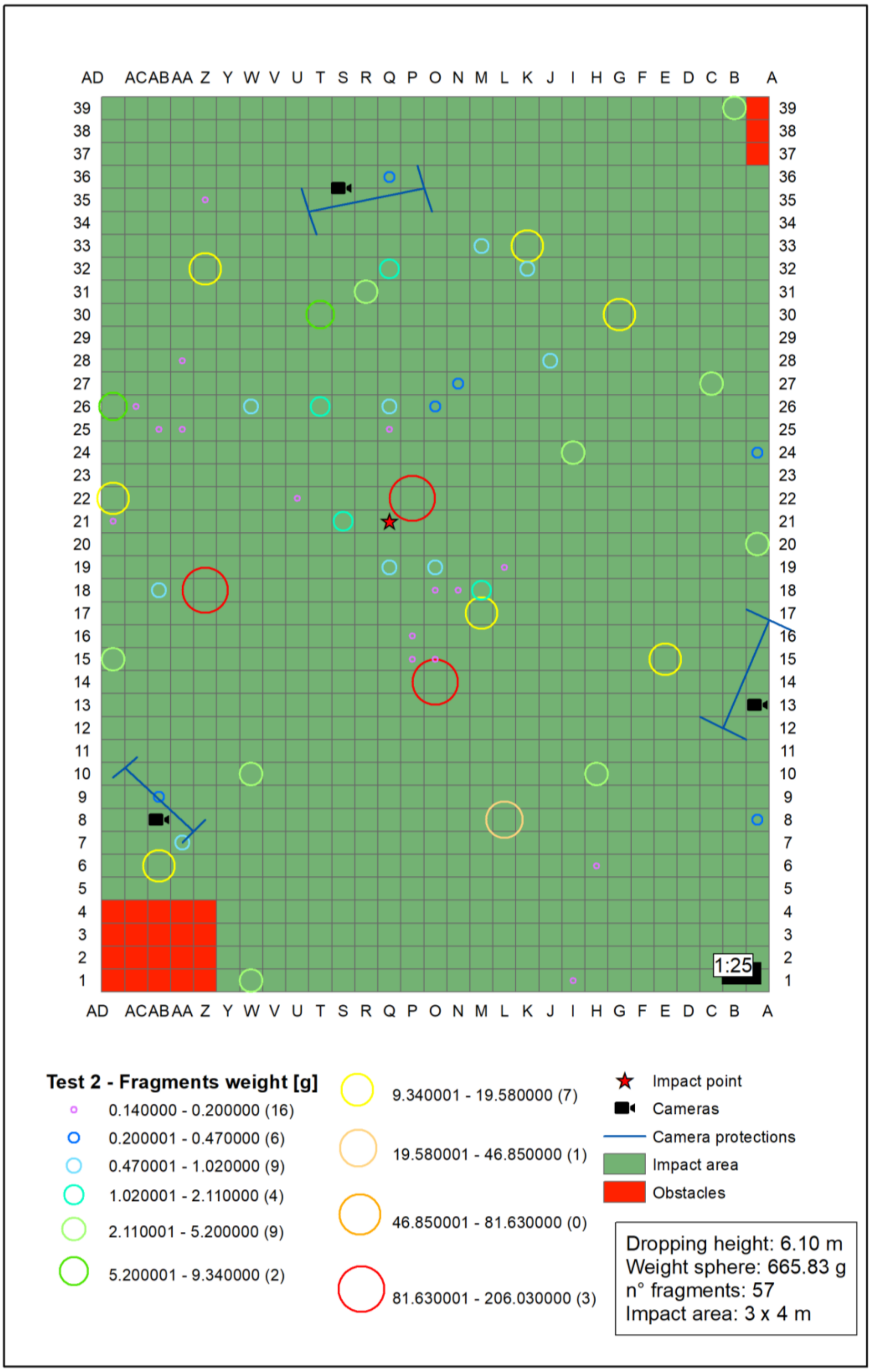

S Figure 1 Test 2: fragments dispersion after impact of sample Sph004

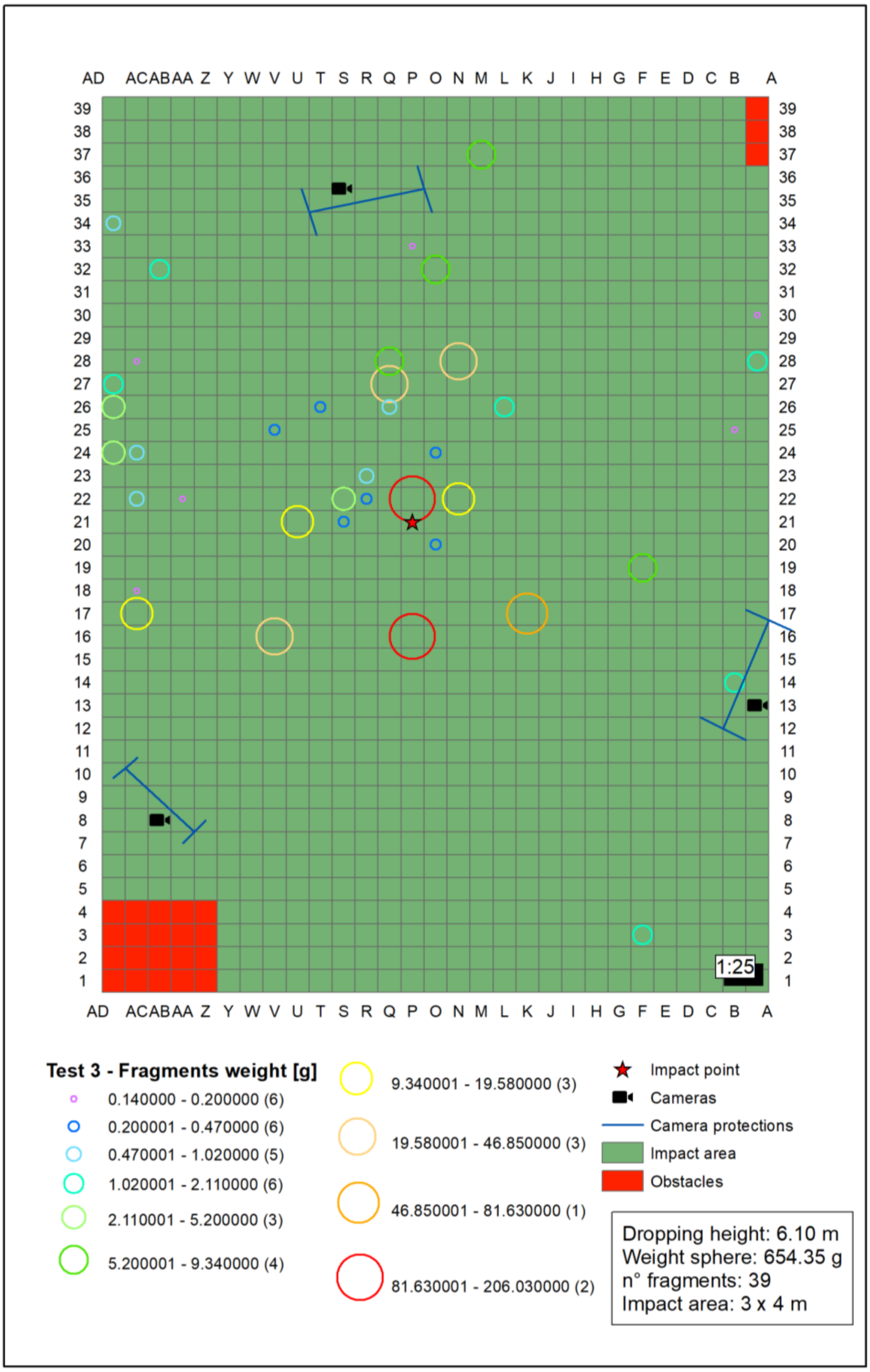

S Figure 2 Test 3: fragments dispersion after impact of sample Sph005

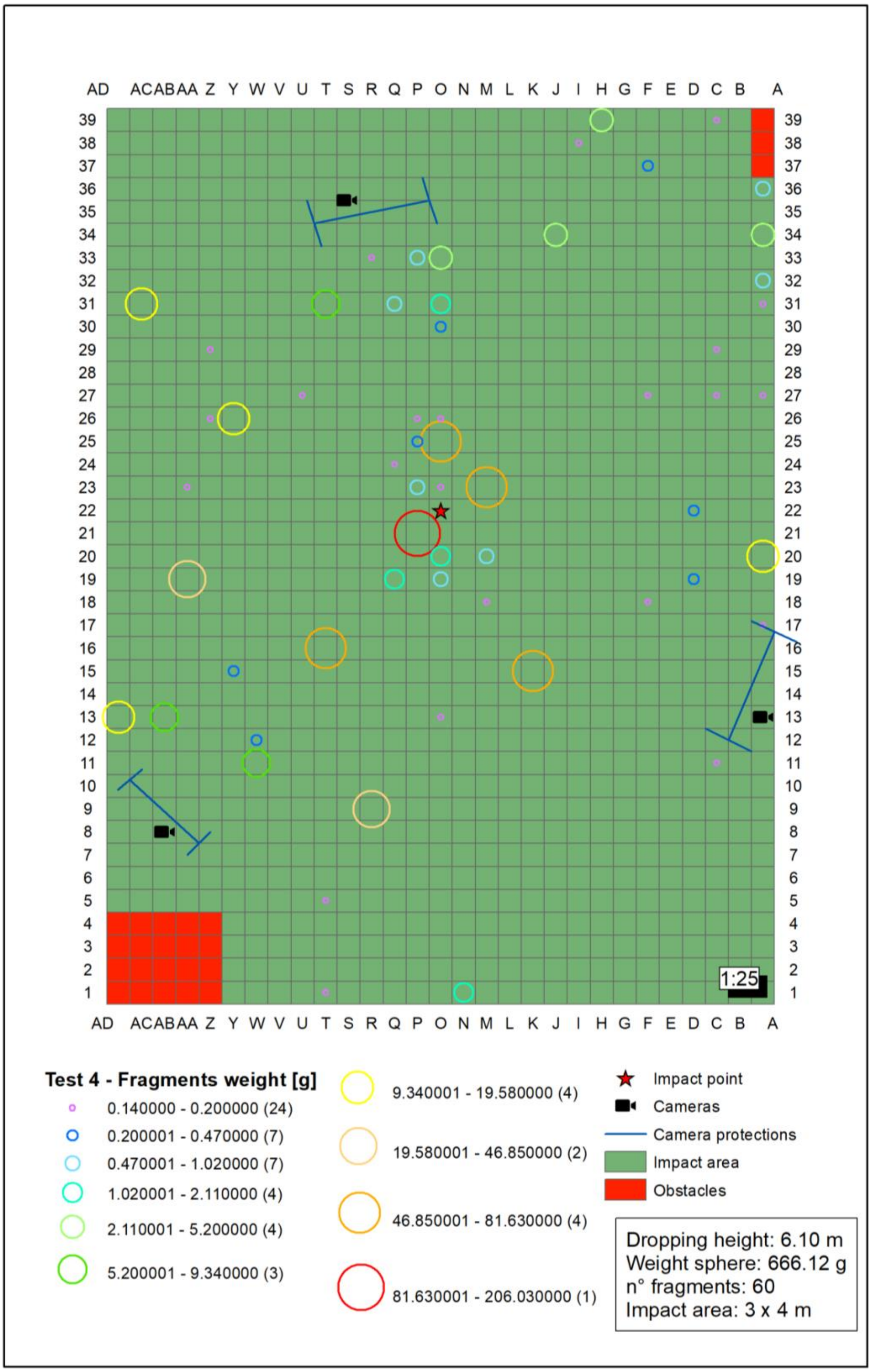

S Figure 3 Test 4: fragments dispersion after impact of sample Sph006

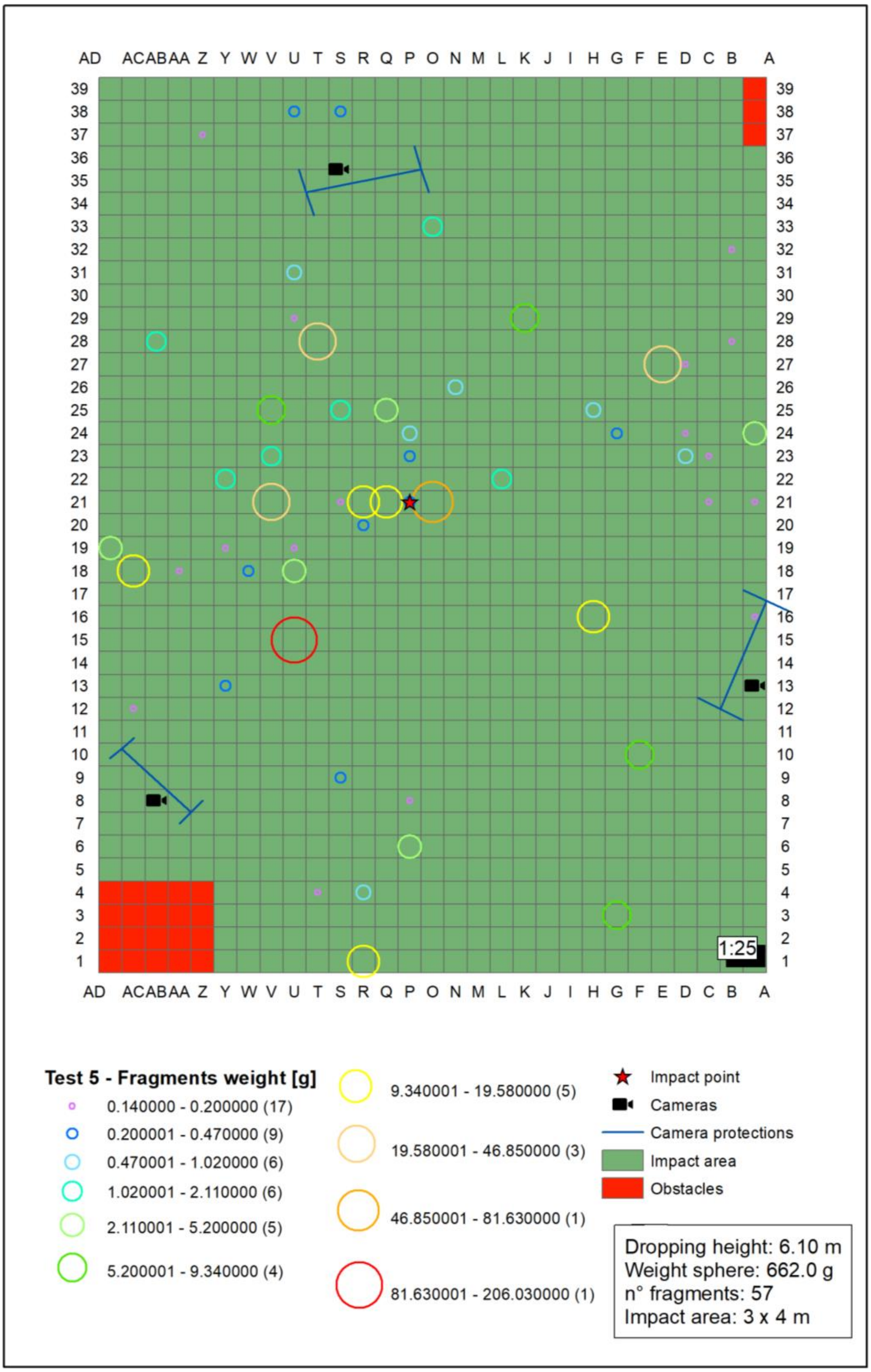

S Figure 4 Test 5: fragments dispersion after impact of sample Sph007

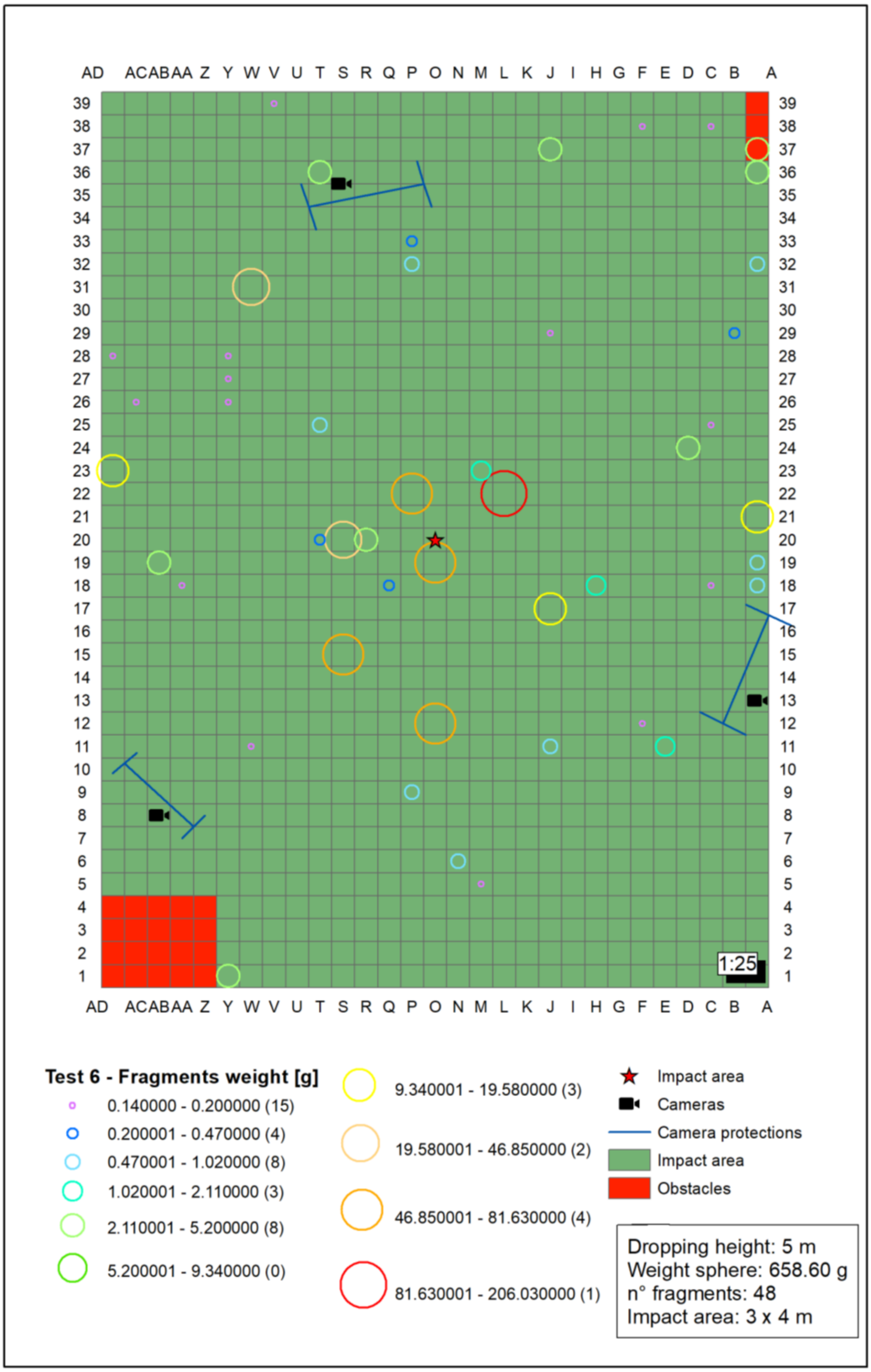

S Figure 5 Test 6: fragments dispersion after impact of sample Sph008

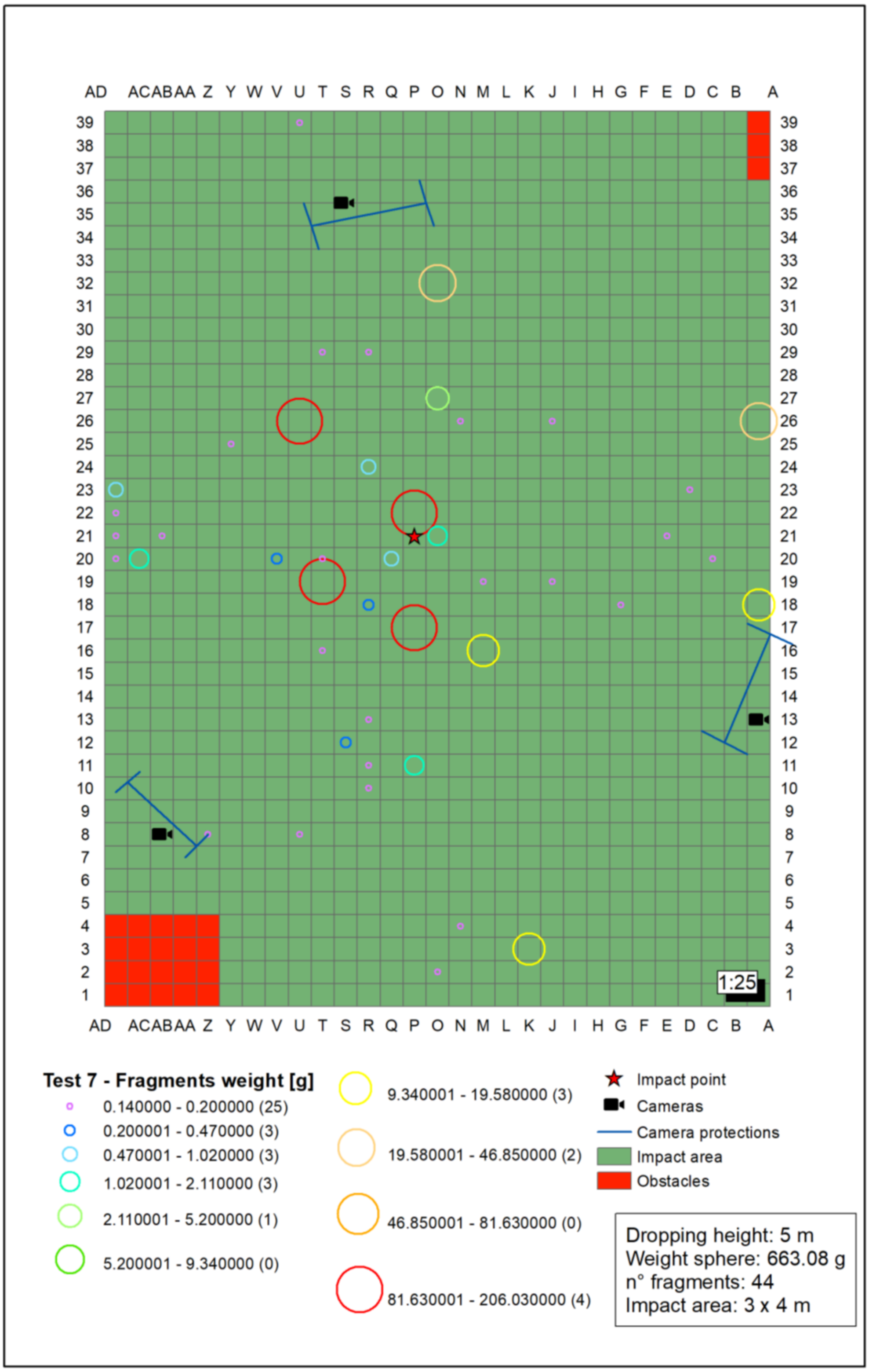

Dropping height: 5 m
Weight sphere: 663.08 g
n° fragments: 44
Impact area: 3 x 4 m

S Figure 6 Test 7: fragments dispersion after impact of sample Sph009

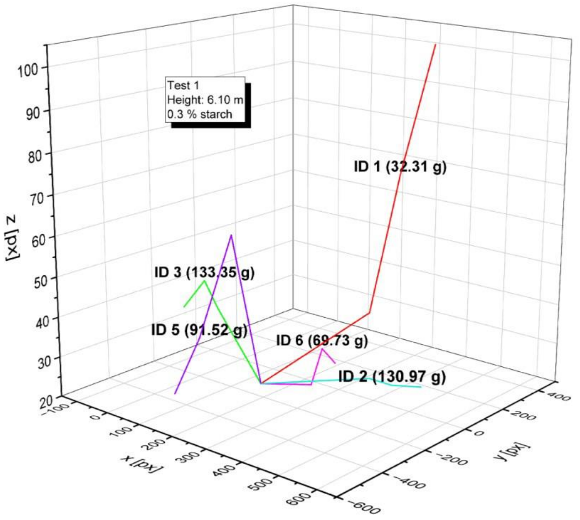
Test 1
Height: 6.10 m
0.3 % starch
ID 1 (32.31 g)
ID 3 (133.35 g)
ID 5 (91.52 g)
ID 6 (69.73 g)
ID 2 (130.97 g)
z [px]
100
90
80
70
60
50
40
30
20
x [px]
−100
0
100
200
300
400
500
600
y [px]
400
200
0
−200
−400
−600

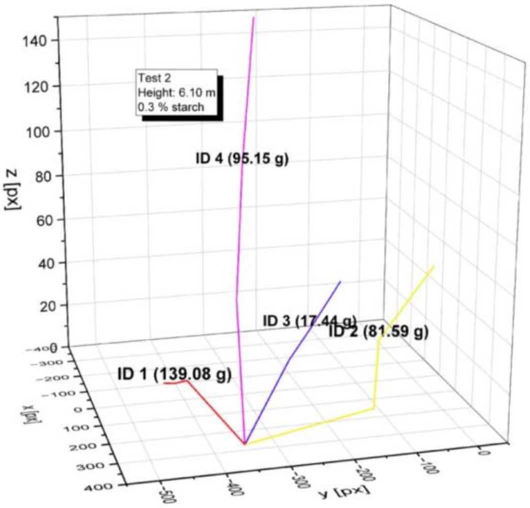
Test 2
Height: 6.10 m
0.3 % starch
ID 4 (95.15 g)
ID 3 (17.44 g)
ID 2 (81.59 g)
ID 1 (139.08 g)
z [px]
140
120
100
80
60
40
20
0
x [px]
−400
−300
−200
−100
0
100
200
300
400
y [px]
−500
−400
−300
−200
−100
0

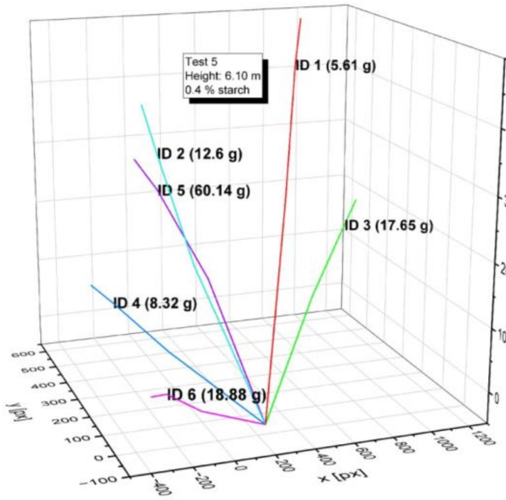
Test 5
Height: 6.10 m
0.4 % starch
ID 1 (5.61 g)
ID 2 (12.6 g)
ID 5 (60.14 g)
ID 3 (17.65 g)
ID 4 (8.32 g)
ID 6 (18.88 g)
z [px]
500
400
300
200
100
0
y [px]
600
500
400
300
200
100
0
−100
x [px]
−400
−200
0
200
400
600
800
1000
1200

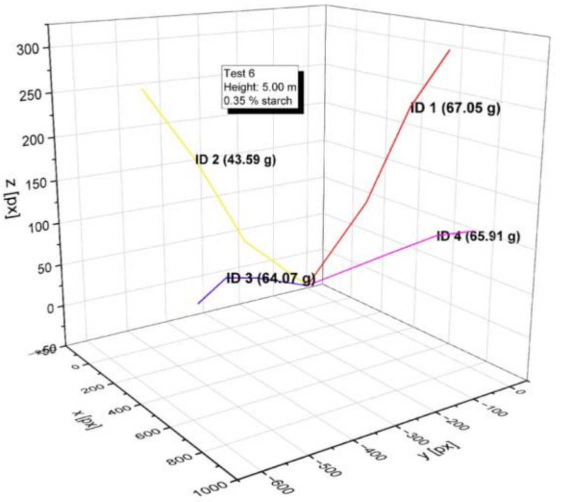
Test 6
Height: 5.00 m
0.35 % starch
ID 1 (67.05 g)
ID 2 (43.59 g)
ID 4 (65.91 g)
ID 3 (64.07 g)
z [px]
300
250
200
150
100
50
0
−50
x [px]
0
200
400
600
800
1000
y [px]
−600
−500
−400
−300
−200
−100
0

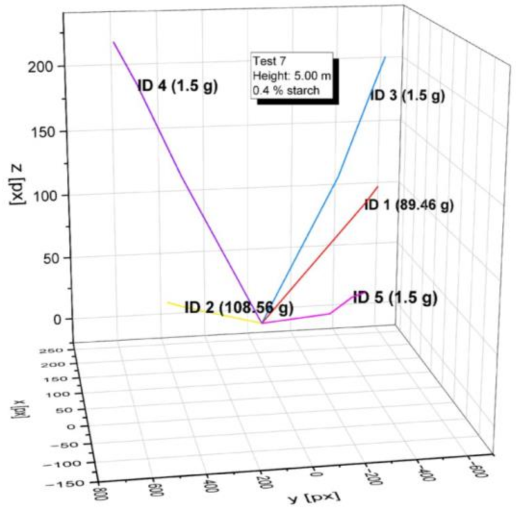
Test 7
Height: 5.00 m
0.4 % starch
ID 4 (1.5 g)
ID 3 (1.5 g)
ID 1 (89.46 g)
ID 2 (108.56 g)
ID 5 (1.5 g)
z [px]
200
150
100
50
0
x [px]
250
200
150
100
50
0
−50
−100
−150
y [px]
800
600
400
200
0
−200
−400
−600

Simplified fragment tracking results and Exit angles calculation

The following formulas provide a procedure for determining the position of a generic point in space in the absolute reference system (hereafter referred to by superscripts ab) from the position of that point in the plane of view of the single camera. The camera represents any point in space as its projection in its plane of view. This projection is identified in the local reference system below by re followed by a subscript to indicate the camera. The position of the cameras is identified in space by the position of the origin of the local reference system as well as between three mutually perpendicular $\boldsymbol{i}_i$ $\boldsymbol{j}_i$ e $\boldsymbol{k}_i$ verses called orientation verses. The coordinates in the local reference system are two-dimensional.

This is achieved in the following steps:

- formulation of the equation representing the direction of view.
- finding the position in space of a generic point once the relative coordinates with respect to two different viewpoints are known.
- search for the position of the individual viewpoint once the absolute coordinates of predetermined points, hereafter called target points, are known.

Formulation of the view direction equation with respect to the i-th camera

The following formulation is based on the following assumptions:

i. camera vision is not altered by optical effects such as aberrations.
ii. the distances of a generic point from the plane of view are small enough to consider perspective effects negligible.

It follows from the second assumption that all directions of view are parallel to each other. The position vector of the generic point P in space is obtained by means of the following vector sum.

$$\boldsymbol{OP} = \boldsymbol{OO_i} + \boldsymbol{O_i\overline{P}_i} + \boldsymbol{\overline{P}_iP} \tag{60}$$

Below we explain the individual vectors that are present in expression (1). The vector joining the origin of the absolute reference system with the origin of the relative reference system is given by:

$$\boldsymbol{OO}_{\mathrm{i}} = \begin{pmatrix} x_{O\mathrm{i}}^{ab} \\ y_{O\mathrm{i}}^{ab} \\ z_{O\mathrm{i}}^{ab} \end{pmatrix} \tag{61}$$

where $x_{O\mathrm{i}}^{ab}$, $y_{O\mathrm{i}}^{ab}$ e $z_{O\mathrm{i}}^{ab}$ are the coordinates of the origin of the relative reference system in the absolute reference system.

$$\boldsymbol{O}_i\boldsymbol{\overline{P}}_i = x_i^{re}\boldsymbol{i}_i + z_i^{re}\boldsymbol{k}_i \tag{62}$$

where x_i^{re} e z_i^{re} are the coordinates of the projection of the generic point in space in the plane of view of the i-th camera in the relative reference system. Using the components of the orientation verses in the absolute reference system:

$$\boldsymbol{O}_i\boldsymbol{\overline{P}}_i = x_i^{re}\begin{pmatrix} i_{ix}^{ab} \\ i_{iy}^{ab} \\ i_{iz}^{ab} \end{pmatrix} + z_i^{re}\begin{pmatrix} k_{ix}^{ab} \\ k_{iy}^{ab} \\ k_{iz}^{ab} \end{pmatrix} = \begin{pmatrix} x_i^{re} i_{ix}^{ab} + z_i^{re} k_{ix}^{ab} \\ x_i^{re} i_{iy}^{ab} + z_i^{re} k_{iy}^{ab} \\ x_i^{re} i_{iz}^{ab} + z_i^{re} k_{iz}^{ab} \end{pmatrix} \tag{63}$$

Finally, the third vector in formula (1) is given by:

$$\boldsymbol{\overline{P}_iP} = d_i\boldsymbol{j_i} = \begin{pmatrix} d_i j_{ix}^{ab} \\ d_i j_{iy}^{ab} \\ d_i j_{iz}^{ab} \end{pmatrix} \tag{64}$$

In which d_i is the distance of the point with respect to the plane of view of the i-th camera. Therefore, by substituting in expression (1) all the vectors of its sum we obtain:

$$\begin{pmatrix} x^{ab} \\ y^{ab} \\ z^{ab} \end{pmatrix} = \begin{pmatrix} x_{O\mathrm{i}}^{ab} \\ y_{O\mathrm{i}}^{ab} \\ z_{O\mathrm{i}}^{ab} \end{pmatrix} + \begin{pmatrix} x_i^{re} i_{ix}^{ab} + z_i^{re} k_{ix}^{ab} \\ x_i^{re} i_{iy}^{ab} + z_i^{re} k_{iy}^{ab} \\ x_i^{re} i_{iz}^{ab} + z_i^{re} k_{iz}^{ab} \end{pmatrix} + \begin{pmatrix} d_i j_{ix}^{ab} \\ d_i j_{iy}^{ab} \\ d_i j_{iz}^{ab} \end{pmatrix} \tag{65}$$

Which can be rewritten as:

$$\begin{pmatrix} x^{ab} \\ y^{ab} \\ z^{ab} \end{pmatrix} = \begin{pmatrix} x_{O\mathrm{i}}^{ab} + x_i^{re} i_{ix}^{ab} + z_i^{re} k_{ix}^{ab} + d_i j_{ix}^{ab} \\ y_{O\mathrm{i}}^{ab} + x_i^{re} i_{iy}^{ab} + z_i^{re} k_{iy}^{ab} + d_i j_{iy}^{ab} \\ z_{O\mathrm{i}}^{ab} + x_i^{re} i_{iz}^{ab} + z_i^{re} k_{iz}^{ab} + d_i j_{iz}^{ab} \end{pmatrix} \tag{66}$$

Note that once the position of the camera and its orientation in space are known, equation (7) only provides the absolute position of the point if its distance to the plane of view and its relative coordinates are known. While the relative co-ordinates are determined from the frames, the distance remains an unknown and can only be determined using two cameras. It follows that only one camera is not sufficient to determine the position in space of a generic point. This problem will be addressed in the following section.

How to determine the absolute position of a point by knowing the position and orientation of two cameras and the corresponding relative coordinates

The following discussion is based on both the assumptions of the previous paragraph and the fact that the two cameras are not oriented in parallel.

Geometrically speaking, the point in space is determined as the intersection of two directions of view of two different cameras. Such cameras are the i-th and j-th. As seen above, we can write equation (7) of the direction of view for both the i-th and j-th cameras, obtaining:

$$\begin{pmatrix} x^{ab} \\ y^{ab} \\ z^{ab} \end{pmatrix} = \begin{pmatrix} x_{O\mathrm{i}}^{ab} + x_i^{re} i_{ix}^{ab} + z_i^{re} k_{ix}^{ab} + d_i j_{ix}^{ab} \\ y_{O\mathrm{i}}^{ab} + x_i^{re} i_{iy}^{ab} + z_i^{re} k_{iy}^{ab} + d_i j_{iy}^{ab} \\ z_{O\mathrm{i}}^{ab} + x_i^{re} i_{iz}^{ab} + z_i^{re} k_{iz}^{ab} + d_i j_{iz}^{ab} \end{pmatrix} \tag{67}$$

and

$$\begin{pmatrix} x^{ab} \\ y^{ab} \\ z^{ab} \end{pmatrix} = \begin{pmatrix} x_{O\mathrm{j}}^{ab} + x_j^{re} i_{jx}^{ab} + z_j^{re} k_{jx}^{ab} + d_j j_{jx}^{ab} \\ y_{O\mathrm{j}}^{ab} + x_j^{re} i_{jy}^{ab} + z_j^{re} k_{jy}^{ab} + d_j j_{jy}^{ab} \\ z_{O\mathrm{j}}^{ab} + x_j^{re} i_{jz}^{ab} + z_j^{re} k_{jz}^{ab} + d_j j_{jz}^{ab} \end{pmatrix} \tag{68}$$

Since the point in space is the intersection of these two lines, I derive this position by equating the two position vectors:

$$\begin{pmatrix} x_{O\mathrm{i}}^{ab} + x_i^{re} i_{ix}^{ab} + z_i^{re} k_{ix}^{ab} + d_i j_{ix}^{ab} \\ y_{O\mathrm{i}}^{ab} + x_i^{re} i_{iy}^{ab} + z_i^{re} k_{iy}^{ab} + d_i j_{iy}^{ab} \\ z_{O\mathrm{i}}^{ab} + x_i^{re} i_{iz}^{ab} + z_i^{re} k_{iz}^{ab} + d_i j_{iz}^{ab} \end{pmatrix} = \begin{pmatrix} x_{O\mathrm{j}}^{ab} + x_j^{re} i_{jx}^{ab} + z_j^{re} k_{jx}^{ab} + d_j j_{jx}^{ab} \\ y_{O\mathrm{j}}^{ab} + x_j^{re} i_{jy}^{ab} + z_j^{re} k_{jy}^{ab} + d_j j_{jy}^{ab} \\ z_{O\mathrm{j}}^{ab} + x_j^{re} i_{jz}^{ab} + z_j^{re} k_{jz}^{ab} + d_j j_{jz}^{ab} \end{pmatrix} \tag{69}$$

Obtaining a system of three equations in two unknowns d_i and d_j. To write the system more conveniently, coefficients containing known terms are introduced:

$$c_{ix} = x_{O\mathrm{i}}^{ab} + x_i^{re} i_{ix}^{ab} + z_i^{re} k_{ix}^{ab} \tag{70}$$

$$c_{iy} = y_{O\mathrm{i}}^{ab} + x_i^{re} i_{iy}^{ab} + z_i^{re} k_{iy}^{ab} \tag{71}$$

$$c_{iz} = z_{O\mathrm{i}}^{ab} + x_i^{re} i_{iz}^{ab} + z_i^{re} k_{iz}^{ab} \tag{72}$$

$$c_{jx} = x_{Oj}^{ab} + x_j^{re} i_{jx}^{ab} + z_j^{re} k_{jx}^{ab} \tag{73}$$

$$c_{jy} = y_{O\mathrm{j}}^{ab} + x_j^{re} i_{jy}^{ab} + z_j^{re} k_{jy}^{ab} \tag{74}$$

$$c_{jz} = z_{O\mathrm{j}}^{ab} + x_j^{re} i_{jz}^{ab} + z_j^{re} k_{jz}^{ab} \tag{75}$$

$$\begin{pmatrix} \mathrm{c_{ix}} + d_i j_{ix}^{ab} \\ \mathrm{c_{iy}} + d_i j_{iy}^{ab} \\ \mathrm{c_{iz}} + d_i j_{iz}^{ab} \end{pmatrix} = \begin{pmatrix} \mathrm{c_{jx}} + d_j j_{jx}^{ab} \\ \mathrm{c_{jy}} + d_j j_{jy}^{ab} \\ \mathrm{c_{jz}} + d_j j_{jz}^{ab} \end{pmatrix} \tag{76}$$

Equalizing the components gives the following system:

$$\begin{cases} \mathrm{c_{ix}} + d_i j_{ix}^{ab} = \mathrm{c_{jx}} + d_j j_{jx}^{ab} \\ \mathrm{c_{iy}} + d_i j_{iy}^{ab} = \mathrm{c_{jy}} + d_j j_{jy}^{ab} \\ \mathrm{c_{iz}} + d_i j_{iz}^{ab} = \mathrm{c_{jz}} + d_j j_{jz}^{ab} \end{cases} \tag{77}$$

Taking the unknowns to the first member and the known terms to the second member, we have:

$$\begin{cases} j_{ix}^{ab} d_i - j_{jx}^{ab} d_j = \mathrm{c_{jx}} - \mathrm{c_{ix}} \\ j_{iy}^{ab} d_i - j_{jy}^{ab} d_j = \mathrm{c_{jy}} - \mathrm{c_{iy}} \\ j_{iz}^{ab} d_i - j_{jz}^{ab} d_j = \mathrm{c_{jz}} - \mathrm{c_{iz}} \end{cases} \tag{78}$$

We have thus obtained a system of three equations in two unknowns. I solve the system by considering only the first two equations and theoretically verifying whether the solution found also satisfies the third. If the cameras are arranged horizontally, the third equation is always verified regardless of the solution found in the first two. To solve the system, we use the Cramer rule:

$$\boldsymbol{d_i} = \frac{(\mathbf{c_{jx}}-\mathbf{c_{ix}})(-\boldsymbol{j_{jy}^{ab}})-(-\boldsymbol{j_{jx}^{ab}})(\mathbf{c_{jy}}-\mathbf{c_{iy}})}{\boldsymbol{j_{ix}^{ab}}\left(-\boldsymbol{j_{jy}^{ab}}\right)-\left(-\boldsymbol{j_{jx}^{ab}}\right)\boldsymbol{j_{iy}^{ab}}} = \frac{\boldsymbol{j_{jx}^{ab}}(\mathbf{c_{jy}}-\mathbf{c_{iy}})-\boldsymbol{j_{jy}^{ab}}(\mathbf{c_{jx}}-\mathbf{c_{ix}})}{\boldsymbol{j_{jx}^{ab}}\boldsymbol{j_{iy}^{ab}}-\boldsymbol{j_{ix}^{ab}}\boldsymbol{j_{jy}^{ab}}} \tag{79}$$

$$\boldsymbol{d_j} = \frac{\boldsymbol{j_{ix}^{ab}}(\mathbf{c_{jy}}-\mathbf{c_{iy}})-(\mathbf{c_{jx}}-\mathbf{c_{ix}})\boldsymbol{j_{iy}^{ab}}}{\boldsymbol{j_{jx}^{ab}}\boldsymbol{j_{iy}^{ab}}-\boldsymbol{j_{ix}^{ab}}\boldsymbol{j_{jy}^{ab}}} \tag{80}$$

Once the distances are known, we can know the co-ordinates of the point in space by substituting in the equations for the directions of view.

Assign the orientation of the cameras, and target points, determine the position of the cameras

The target points are denoted by A and B . Once the i-th camera is fixed, the equation of the direction of view for the two target points are:

$$\begin{pmatrix} x_A^{ab} \\ y_A^{ab} \\ z_A^{ab} \end{pmatrix} = \begin{pmatrix} x_{O\mathrm{i}}^{ab} + x_{Ai}^{re} i_{ix}^{ab} + z_{Ai}^{re} k_{ix}^{ab} + d_{iA} j_{ix}^{ab} \\ y_{O\mathrm{i}}^{ab} + x_{Ai}^{re} i_{iy}^{ab} + z_{Ai}^{re} k_{iy}^{ab} + d_{iA} j_{iy}^{ab} \\ z_{O\mathrm{i}}^{ab} + x_{Ai}^{re} i_{iz}^{ab} + z_{Ai}^{re} k_{iz}^{ab} + d_{iA} j_{iz}^{ab} \end{pmatrix} \tag{81}$$

and

$$\begin{pmatrix} x_B^{ab} \\ y_B^{ab} \\ z_B^{ab} \end{pmatrix} = \begin{pmatrix} x_{O\mathrm{i}}^{ab} + x_{Bi}^{re} i_{ix}^{ab} + z_{Bi}^{re} k_{ix}^{ab} + d_{iB} j_{ix}^{ab} \\ y_{O\mathrm{i}}^{ab} + x_{Bi}^{re} i_{iy}^{ab} + z_{Bi}^{re} k_{iy}^{ab} + d_{iB} j_{iy}^{ab} \\ z_{O\mathrm{i}}^{ab} + x_{Bi}^{re} i_{iz}^{ab} + z_{Bi}^{re} k_{iz}^{ab} + d_{iB} j_{iz}^{ab} \end{pmatrix} \tag{82}$$

We can then write a system of five unknowns in six equations:

$$\begin{cases} x_{O\mathrm{i}}^{ab} + x_{Ai}^{re} i_{ix}^{ab} + z_{Ai}^{re} k_{ix}^{ab} + d_{iA} j_{ix}^{ab} = x_A^{ab} \\ y_{O\mathrm{i}}^{ab} + x_{Ai}^{re} i_{iy}^{ab} + z_{Ai}^{re} k_{iy}^{ab} + d_{iA} j_{iy}^{ab} = y_A^{ab} \\ z_{O\mathrm{i}}^{ab} + x_{Ai}^{re} i_{iz}^{ab} + z_{Ai}^{re} k_{iz}^{ab} + d_{iA} j_{iz}^{ab} = z_A^{ab} \\ x_{O\mathrm{i}}^{ab} + x_{Bi}^{re} i_{ix}^{ab} + z_{Bi}^{re} k_{ix}^{ab} + d_{iB} j_{ix}^{ab} = x_B^{ab} \\ y_{O\mathrm{i}}^{ab} + x_{Bi}^{re} i_{iy}^{ab} + z_{Bi}^{re} k_{iy}^{ab} + d_{iB} j_{iy}^{ab} = y_B^{ab} \\ z_{O\mathrm{i}}^{ab} + x_{Bi}^{re} i_{iz}^{ab} + z_{Bi}^{re} k_{iz}^{ab} + d_{iB} j_{iz}^{ab} = z_B^{ab} \end{cases} \tag{83}$$

For horizontal cameras with a vertical plane of view, we can write:

$$i_{iz}^{ab} = 0$$

$$j_{iz}^{ab} = 0$$

$$k^{ab}{}_{ix} = 0$$

$$k_{iy}^{ab} = 0$$

$$k_{iz}^{ab} = 1$$

Substituting these conditions gives:

$$\begin{cases} x_{O\mathrm{i}}^{ab} + x_{Ai}^{re} i_{ix}^{ab} + d_{iA} j_{ix}^{ab} = x_A^{ab} \\ y_{O\mathrm{i}}^{ab} + x_{Ai}^{re} i_{iy}^{ab} + d_{iA} j_{iy}^{ab} = y_A^{ab} \\ z_{O\mathrm{i}}^{ab} + z_{Ai}^{re} = z_A^{ab} \\ x_{O\mathrm{i}}^{ab} + x_{Bi}^{re} i_{ix}^{ab} + d_{iB} j_{ix}^{ab} = x_B^{ab} \\ y_{O\mathrm{i}}^{ab} + x_{Bi}^{re} i_{iy}^{ab} + d_{iB} j_{iy}^{ab} = y_B^{ab} \\ z_{O\mathrm{i}}^{ab} + z_{Bi}^{re} = z_B^{ab} \end{cases} \tag{84}$$

We can therefore consider the sub-system:

$$\begin{cases} x_{O\mathrm{i}}^{ab} + d_{iA} j_{ix}^{ab} = x_A^{ab} - x_{Ai}^{re} i_{ix}^{ab} \\ y_{O\mathrm{i}}^{ab} + d_{iA} j_{iy}^{ab} = y_A^{ab} - x_{Ai}^{re} i_{iy}^{ab} \\ x_{O\mathrm{i}}^{ab} + d_{iB} j_{ix}^{ab} = x_B^{ab} - x_{Bi}^{re} i_{ix}^{ab} \\ y_{O\mathrm{i}}^{ab} + d_{iB} j_{iy}^{ab} = y_B^{ab} - x_{Bi}^{re} i_{iy}^{ab} \end{cases} \tag{85}$$

We wrote then a system of four equations in four unknowns. We can write this system in matrix form:

$$\begin{pmatrix} 1 & 0 & j_{ix}^{ab} & 0 \\ 0 & 1 & j_{iy}^{ab} & 0 \\ 1 & 0 & 0 & j_{ix}^{ab} \\ 0 & 1 & 0 & j_{iy}^{ab} \end{pmatrix} \begin{pmatrix} x_{O\mathrm{i}}^{ab} \\ y_{O\mathrm{i}}^{ab} \\ d_{iA} \\ d_{iB} \end{pmatrix} = \begin{pmatrix} x_A^{ab} - x_{Ai}^{re} i_{ix}^{ab} \\ y_A^{ab} - x_{Ai}^{re} i_{iy}^{ab} \\ x_B^{ab} - x_{Bi}^{re} i_{ix}^{ab} \\ y_B^{ab} - x_{Bi}^{re} i_{iy}^{ab} \end{pmatrix} \tag{86}$$

i.e.

$$AX = D \tag{87}$$

When $\det A \neq 0$ then the matrix is invertible and thus:

$$X = A^{-1} D \tag{88}$$

We solved the system and thus solved the problem.

Solving the problem form the singular matrix

Following the application of the calculations performed above, it can be deduced that the matrix A obtained in the previous paragraph is singular. This implies that there is a free variable, and the linear system admits infinite solutions.

We therefore proceed as follows:

$$\begin{cases} x_{O\mathrm{i}}^{ab} + x_{Ai}^{re} i_{ix}^{ab} + d_{iA} j_{ix}^{ab} = x_A^{ab} \\ y_{O\mathrm{i}}^{ab} + x_{Ai}^{re} i_{iy}^{ab} + d_{iA} j_{iy}^{ab} = y_A^{ab} \\ z_{O\mathrm{i}}^{ab} + z_{Ai}^{re} = z_A^{ab} \end{cases} \tag{89}$$

In this case we take a variable and make it free d_{iA}

$$\begin{cases} x_{O\mathrm{i}}^{ab} = x_A^{ab} - x_{Ai}^{re} i_{ix}^{ab} - d_{iA} j_{ix}^{ab} \\ y_{O\mathrm{i}}^{ab} = y_A^{ab} - x_{Ai}^{re} i_{iy}^{ab} - d_{iA} j_{iy}^{ab} \\ z_{O\mathrm{i}}^{ab} = z_A^{ab} - z_{Ai}^{re} \end{cases} \tag{90}$$

Repeating the same reasoning on the second cameras we have:

$$\begin{cases} x_{O\mathrm{j}}^{ab} = x_A^{ab} - x_{Aj}^{re} i_{jx}^{ab} - d_{jA} j_{jx}^{ab} \\ y_{O\mathrm{j}}^{ab} = y_A^{ab} - x_{Aj}^{re} i_{jy}^{ab} - d_{jA} j_{jy}^{ab} \\ z_{O\mathrm{j}}^{ab} = z_A^{ab} - z_{Aj}^{re} \end{cases} \tag{91}$$

Calculating

$$c_{ix} = x_{O\mathrm{i}}^{ab} + x_i^{re} i_{ix}^{ab} \tag{92}$$

$$c_{iy} = y_{O\mathrm{i}}^{ab} + x_i^{re} i_{iy}^{ab} + \tag{93}$$

$$c_{jx} = x_{Oj}^{ab} + x_j^{re} i_{jx}^{ab} + \tag{94}$$

$$c_{jy} = y_{O\mathrm{j}}^{ab} + x_j^{re} i_{jy}^{ab} + \tag{95}$$

$$c_{ix} = x_A^{ab} - x_{Ai}^{re} i_{ix}^{ab} - d_{iA} j_{ix}^{ab} + x_i^{re} i_{ix}^{ab} \tag{96}$$

$$c_{iy} = y_A^{ab} - x_{Ai}^{re} i_{iy}^{ab} - d_{iA} j_{iy}^{ab} + x_i^{re} i_{iy}^{ab} \tag{97}$$

$$c_{jx} = x_A^{ab} - x_{Aj}^{re} i_{jx}^{ab} - d_{jA} j_{jx}^{ab} + x_j^{re} i_{jx}^{ab} \tag{98}$$

$$c_{jy} = y_A^{ab} - x_{Aj}^{re} i_{jy}^{ab} - d_{jA} j_{jy}^{ab} + x_j^{re} i_{jy}^{ab} \tag{99}$$

$$c_{jy} - c_{iy} = \left(y_A^{ab} - x_{Aj}^{re} i_{jy}^{ab} - d_{jA} j_{jy}^{ab} + x_j^{re} i_{jy}^{ab}\right) - \left(y_A^{ab} - x_{Ai}^{re} i_{iy}^{ab} - d_{iA} j_{iy}^{ab} + x_i^{re} i_{iy}^{ab}\right)$$

$$c_{jy} - c_{iy} = y_A^{ab} - x_{Aj}^{re} i_{jy}^{ab} - d_{jA} j_{jy}^{ab} + x_j^{re} i_{jy}^{ab} - y_A^{ab} + x_{Ai}^{re} i_{iy}^{ab} + d_{iA} j_{iy}^{ab} - x_i^{re} i_{iy}^{ab}$$

$$\alpha_y = y_A^{ab} - x_{Aj}^{re} i_{jy}^{ab} + x_j^{re} i_{jy}^{ab} - y_A^{ab} + x_{Ai}^{re} i_{iy}^{ab} - x_i^{re} i_{iy}^{ab}$$

$$\boldsymbol{\alpha_y = x_{Ai}^{re} i_{iy}^{ab} - x_{Aj}^{re} i_{jy}^{ab} - x_i^{re} i_{iy}^{ab} + x_j^{re} i_{jy}^{ab}}$$

$$c_{jy} - c_{iy} = \alpha_y - d_{jA} j_{jy}^{ab} + d_{iA} j_{iy}^{ab}$$

$$\mathrm{c_{jx}} - \mathrm{c_{ix}} = \left(x_A^{ab} - x_{Aj}^{re} i_{jx}^{ab} - d_{jA} j_{jx}^{ab} + x_j^{re} i_{jx}^{ab}\right) - \left(x_A^{ab} - x_{Ai}^{re} i_{ix}^{ab} - d_{iA} j_{ix}^{ab} + x_i^{re} i_{ix}^{ab}\right)$$

$$\mathrm{c_{jx}} - \mathrm{c_{ix}} = x_A^{ab} - x_{Aj}^{re} i_{jx}^{ab} - d_{jA} j_{jx}^{ab} + x_j^{re} i_{jx}^{ab} - x_A^{ab} + x_{Ai}^{re} i_{ix}^{ab} + d_{iA} j_{ix}^{ab} - x_i^{re} i_{ix}^{ab}$$

$$\alpha_x = x_A^{ab} - x_{Aj}^{re} i_{jx}^{ab} + x_j^{re} i_{jx}^{ab} - x_A^{ab} + x_{Ai}^{re} i_{ix}^{ab} - x_i^{re} i_{ix}^{ab}$$

$$\boldsymbol{\alpha_x = +x_{Ai}^{re} i_{ix}^{ab} - x_i^{re} i_{ix}^{ab} - x_{Aj}^{re} i_{jx}^{ab} + x_j^{re} i_{jx}^{ab}}$$

$$\mathrm{c_{jx}} - \mathrm{c_{ix}} = \alpha_x - d_{jA} j_{jx}^{ab} + d_{iA} j_{ix}^{ab} \tag{100}$$

$$d_i = \frac{j_{jx}^{ab}(\mathrm{c_{jy}}-\mathrm{c_{iy}}) - j_{jy}^{ab}(\mathrm{c_{jx}}-\mathrm{c_{ix}})}{j_{jx}^{ab} j_{iy}^{ab} - j_{ix}^{ab} j_{jy}^{ab}} \tag{101}$$

(102)

$$d_i = \frac{\left(\alpha_y j_{jx}^{ab} - d_{jA} j_{jx}^{ab} j_{jy}^{ab} + d_{iA} j_{jx}^{ab} j_{iy}^{ab}\right) - \left(j_{jy}^{ab} \alpha_x - d_{jA} j_{jy}^{ab} j_{jx}^{ab} + d_{iA} j_{jy}^{ab} j_{ix}^{ab}\right)}{j_{jx}^{ab} j_{iy}^{ab} - j_{ix}^{ab} j_{jy}^{ab}} \tag{103}$$

$$d_i = \frac{\alpha_y j_{jx}^{ab} - d_{jA} j_{jx}^{ab} j_{jy}^{ab} + d_{iA} j_{jx}^{ab} j_{iy}^{ab} - j_{jy}^{ab} \alpha_x + d_{jA} j_{jy}^{ab} j_{jx}^{ab} - d_{iA} j_{jy}^{ab} j_{ix}^{ab}}{j_{jx}^{ab} j_{iy}^{ab} - j_{ix}^{ab} j_{jy}^{ab}} \tag{104}$$

$$d_i = \frac{\alpha_y j_{jx}^{ab} + d_{iA}\left(j_{jx}^{ab} j_{iy}^{ab} - j_{ix}^{ab} j_{jy}^{ab}\right) - j_{jy}^{ab} \alpha_x + d_{jA}\left(j_{jy}^{ab} j_{jx}^{ab} - j_{jx}^{ab} j_{jy}^{ab}\right)}{j_{jx}^{ab} j_{iy}^{ab} - j_{ix}^{ab} j_{jy}^{ab}} \tag{105}$$

$$d_i = \frac{\alpha_y j_{jx}^{ab} - j_{jy}^{ab} \alpha_x + d_{jA}\left(j_{jy}^{ab} j_{jx}^{ab} - j_{jx}^{ab} j_{jy}^{ab}\right)}{j_{jx}^{ab} j_{iy}^{ab} - j_{ix}^{ab} j_{jy}^{ab}} + d_{iA} \tag{106}$$

$$d_i = \frac{\alpha_y j_{jx}^{ab} - j_{jy}^{ab} \alpha_x + d_{jA}\left(j_{jx}^{ab} j_{jy}^{ab} - j_{jx}^{ab} j_{jy}^{ab}\right)}{j_{jx}^{ab} j_{iy}^{ab} - j_{ix}^{ab} j_{jy}^{ab}} + d_{iA} \tag{107}$$

$$d_i = \frac{\alpha_y j_{jx}^{ab} - j_{jy}^{ab} \alpha_x}{j_{jx}^{ab} j_{iy}^{ab} - j_{ix}^{ab} j_{jy}^{ab}} + d_{iA} \tag{108}$$

For the 2nd camera:

$$d_j = \frac{j_{ix}^{ab}(\mathrm{c_{jy}}-\mathrm{c_{iy}}) - (\mathrm{c_{jx}}-\mathrm{c_{ix}}) j_{iy}^{ab}}{j_{jx}^{ab} j_{iy}^{ab} - j_{ix}^{ab} j_{jy}^{ab}} \tag{109}$$

$$d_j = \frac{j_{ix}^{ab}\left(\alpha_y - d_{jA} j_{jy}^{ab} + d_{iA} j_{iy}^{ab}\right) - \left(\alpha_x - d_{jA} j_{jx}^{ab} + d_{iA} j_{ix}^{ab}\right) j_{iy}^{ab}}{j_{jx}^{ab} j_{iy}^{ab} - j_{ix}^{ab} j_{jy}^{ab}} \tag{110}$$

$$d_j = \frac{\left(j_{ix}^{ab} \alpha_y - d_{jA} j_{ix}^{ab} j_{jy}^{ab} + d_{iA} j_{ix}^{ab} j_{iy}^{ab}\right) - \left(\alpha_x j_{iy}^{ab} - d_{jA} j_{iy}^{ab} j_{jx}^{ab} + d_{iA} j_{iy}^{ab} j_{ix}^{ab}\right)}{j_{jx}^{ab} j_{iy}^{ab} - j_{ix}^{ab} j_{jy}^{ab}} \tag{111}$$

$$d_j = \frac{j_{ix}^{ab} \alpha_y - d_{jA} j_{ix}^{ab} j_{jy}^{ab} + d_{iA} j_{ix}^{ab} j_{iy}^{ab} - \alpha_x j_{iy}^{ab} + d_{jA} j_{iy}^{ab} j_{jx}^{ab} - d_{iA} j_{iy}^{ab} j_{ix}^{ab}}{j_{jx}^{ab} j_{iy}^{ab} - j_{ix}^{ab} j_{jy}^{ab}} \tag{112}$$

$$d_j = \frac{j_{ix}^{ab} \alpha_y + d_{iA}\left(j_{ix}^{ab} j_{iy}^{ab} - j_{ix}^{ab} j_{iy}^{ab}\right) - \alpha_x j_{iy}^{ab}}{j_{jx}^{ab} j_{iy}^{ab} - j_{ix}^{ab} j_{jy}^{ab}} + d_{jA} \tag{113}$$

$$d_j = \frac{j_{ix}^{ab} \alpha_y - \alpha_x j_{iy}^{ab}}{j_{jx}^{ab} j_{iy}^{ab} - j_{ix}^{ab} j_{jy}^{ab}} + d_{jA} \tag{114}$$

Using the direction equation, we have for the first camera:

$$\begin{cases} x^{ab} = x_{O\mathrm{i}}^{ab} + x_i^{re} i_{ix}^{ab} + d_i j_{ix}^{ab} \\ y^{ab} = y_{O\mathrm{i}}^{ab} + x_i^{re} i_{iy}^{ab} + d_i j_{iy}^{ab} \\ x^{ab} = x_{O\mathrm{j}}^{ab} + x_j^{re} i_{jx}^{ab} + d_j j_{jx}^{ab} \\ y^{ab} = y_{O\mathrm{j}}^{ab} + x_j^{re} i_{jy}^{ab} + d_j j_{jy}^{ab} \end{cases}$$

Substituting we have:

$$\begin{cases} x^{ab} = x_A^{ab} - x_{Ai}^{re} i_{ix}^{ab} - d_{iA} j_{ix}^{ab} + x_i^{re} i_{ix}^{ab} + j_{ix}^{ab} \left[\dfrac{\alpha_y j_{jx}^{ab} - j_{jy}^{ab} \alpha_x}{j_{jx}^{ab} j_{iy}^{ab} - j_{ix}^{ab} j_{jy}^{ab}} + d_{iA} \right] \\ y^{ab} = y_A^{ab} - x_{Ai}^{re} i_{iy}^{ab} - d_{iA} j_{iy}^{ab} + x_i^{re} i_{iy}^{ab} + j_{iy}^{ab} \left[\dfrac{\alpha_y j_{jx}^{ab} - j_{jy}^{ab} \alpha_x}{j_{jx}^{ab} j_{iy}^{ab} - j_{ix}^{ab} j_{jy}^{ab}} + d_{iA} \right] \\ x^{ab} = x_A^{ab} - x_{Aj}^{re} i_{jx}^{ab} - d_{jA} j_{jx}^{ab} + x_j^{re} i_{jx}^{ab} + j_{jx}^{ab} \left[\dfrac{j_{ix}^{ab} \alpha_y - \alpha_x j_{iy}^{ab}}{j_{jx}^{ab} j_{iy}^{ab} - j_{ix}^{ab} j_{jy}^{ab}} + d_{jA} \right] \\ y^{ab} = y_A^{ab} - x_{Aj}^{re} i_{jy}^{ab} - d_{jA} j_{jy}^{ab} + x_j^{re} i_{jy}^{ab} + j_{jy}^{ab} \left[\dfrac{j_{ix}^{ab} \alpha_y - \alpha_x j_{iy}^{ab}}{j_{jx}^{ab} j_{iy}^{ab} - j_{ix}^{ab} j_{jy}^{ab}} + d_{jA} \right] \end{cases}$$

$$\begin{cases} x^{ab} = x_A^{ab} + (x_i^{re} - x_{Ai}^{re}) i_{ix}^{ab} + j_{ix}^{ab} \left[\dfrac{\alpha_y j_{jx}^{ab} - j_{jy}^{ab} \alpha_x}{j_{jx}^{ab} j_{iy}^{ab} - j_{ix}^{ab} j_{jy}^{ab}} \right] \\ y^{ab} = y_A^{ab} + (x_i^{re} - x_{Ai}^{re}) i_{iy}^{ab} + j_{iy}^{ab} \left[\dfrac{\alpha_y j_{jx}^{ab} - j_{jy}^{ab} \alpha_x}{j_{jx}^{ab} j_{iy}^{ab} - j_{ix}^{ab} j_{jy}^{ab}} \right] \\ x^{ab} = x_A^{ab} + \left(x_j^{re} - x_{Aj}^{re}\right) i_{jx}^{ab} + j_{jx}^{ab} \left[\dfrac{j_{ix}^{ab} \alpha_y - \alpha_x j_{iy}^{ab}}{j_{jx}^{ab} j_{iy}^{ab} - j_{ix}^{ab} j_{jy}^{ab}} \right] \\ y^{ab} = y_A^{ab} + \left(x_j^{re} - x_{Aj}^{re}\right) i_{jy}^{ab} + j_{jy}^{ab} \left[\dfrac{j_{ix}^{ab} \alpha_y - \alpha_x j_{iy}^{ab}}{j_{jx}^{ab} j_{iy}^{ab} - j_{ix}^{ab} j_{jy}^{ab}} \right] \end{cases}$$

The last system obtained allows us to calculate the absolute positions of objects in space, using only the relative positions of the fragment in interest and a target point (recognizable stationary point in space, from calibration element) obtained from only two cameras.

Fragmentation tests | in-situ and laboratory experiments

This second part of the chapter explores the study of the significance of the presence of discontinuities during the fragmentation process, in terms of their quantity, strength, and orientation at the time of impact.
The following data, analysis and results have been collected between January and May 2023, during which I had the opportunity to spend time abroad working at the Newcastle University in Australia, in the civil engineering group of Giacomini, Guccione, Buzzi and Spadari.

Research Background

Impact loading behavior and fragmentation patterns

Significant advancements in the understanding of sphere failure under impact loads have been achieved through a series of theoretical and experimental studies, which enhance our understanding of material behavior under impact loading, allowing for the development of safer and higher-performing materials, advanced computational methods, and applications in geology and engineering fields. Notable contributions to this topic have come from various researchers, including Dean et al. (1952), Arbiter et al. (1969), Gan-Mor and Galili (1987), Shipway and Hutchings (1993b), and Schönert (2004), particularly for single impact scenarios. Additionally, behaviors under double impact conditions were explored in works by Arbiter et al. (1969), Schönert (2004), and Wu and Chau (2006).
It is noteworthy that quasi-static loading and low-velocity dynamic loading, whether in compression or single impact, induce similar stress fields, fracture patterns, and fragment shapes upon impact. This observation was made by Arbiter et al. (1969) and Schönert (2004). However, dynamic tests generally require a higher energy input to fracture a sphere compared to quasi-static conditions. In this context, Chau et al. (2000) proposed an empirical correlation between the energy required to break a sphere under static compression and double impact loading conditions. Wu and Chau (2006) introduced an innovative analytical solution for an elastic sphere subjected to a double impact load. Their approach addressed two auxiliary problems: a static solution of the applied loading, solved using the Hiramatsu and Oka (1966) model, and the free vibration of the sphere following an initial deformation induced by the applied load, modeled using a Heaviside step function of time along the sphere's diameter. This solution was validated through experimental observations and proved to be a valuable tool for explaining fracture initiation and patterns observed in the crushing of brittle spheres or particles under double impact. Schönert (2004) conducted comprehensive experimental and theoretical investigations involving the dynamic impact of polymethylmethacrylate and glass spheres. These studies established a strong correlation between stress distribution and deformation within the contact area. Notably, the research revealed maximum tensile stresses around the meridional plane, resulting from pure elastic deformation, and a non-symmetrical stress field relative to the equatorial plane due to crack development. This led to the formation of a cone-shaped fragment at the top of the sphere. High stress concentrations caused by inelastic deformation resulted in stress distributions perpendicular to the meridional planes, enhancing sphere fracture into orange slice-shaped fragments. The combination of elastic and inelastic deformations was found to determine the coexistence of two distinct fracture patterns, with their likelihood increasing with rising impact energies. Guccione et al. (2020, 2021, 2022, 2023) contributions involve the development of a novel model for predicting the survival probability of brittle spheres during impact. This model relies on statistical distributions of material properties and employs shape and scale parameters to describe the probability of survival upon impact. The approach they followed connects the impact survival probability with survival probabilities derived from material characterization tests using techniques such as the Weibull function or linear functions. The significance of this work lies in understanding how brittle spheres fragment upon impact, the magnitude of which is quantified by work.
Chapter 3b - Figure 1, provides a comprehensive illustration of the various fragmentation patterns observed in the literature. These patterns account for different fragment geometries.

In double impact scenarios (Chapter 3b - Figure 1a, b, and c), the fragmentation pattern exhibits distinct characteristics. Figure 2-13a depicts two cones near the contact points, which initiate the splitting of the sphere in tensile mode along one or more meridian fracture planes. With an increase in impact energy, secondary cracks emerge (as shown in Chapter 3b - Figure 1b), eventually leading to the generation of several small fragments. This intense fragmentation is commonly referred to as "crushing" (Chapter 3b - Figure 1c), a phenomenon explored by Chau et al. (2000), Schönert (2004), Wu and Chau (2006), and Wu et al. (2004).

In single impact cases, the fragmentation pattern resembles that of double impacts, but there is a notable difference. At lower impact energies, the top cone is not always present, primarily due to the absence of impact force on the top of the sphere. However, as observed by Arbiter et al. (1969), Shipway and Hutchings (1993a), Tomas et al. (1999), Gorham et al. (2003), Salman et al. (2004), Schönert (2004), and Gorham and Salman (2005), a remaining cone can appear at the top of the sphere as the impact energy increases (as shown in Chapter 3b - Figure 1Chapter 3b - Figure 1d, e, and f). This phenomenon highlights the dynamic nature of fragmentation patterns and their sensitivity to impact conditions.

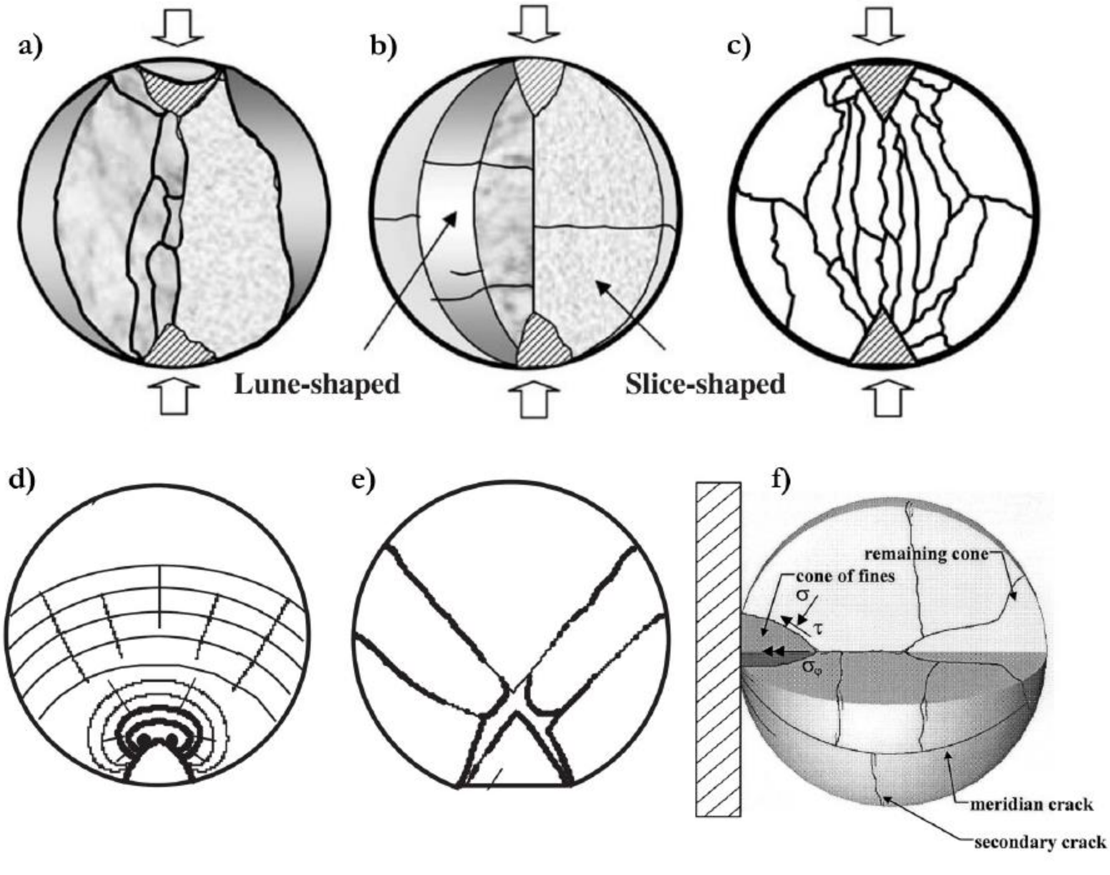

Chapter 3b - Figure 1 Sketches of the main form of failure from Guccione (2020), for double (a, b and c) and single impact test (d, e and f): a) double cone with meridian cracks; b) double cone with meridian cracks and secondary cracks; c) cross section of a crushed sphere (Wu et al., 2004); d) single cone with meridian crack; e) single cone with oblique fractures forming a remaining (top) cone (Gorham et al., 2003); f) single cone with meridian, secondary cracks and remaining (top) cone (Tomas et al., 1999).

Guccione et al. (2022) focuses in this sensitivity observing three main fragmentation patterns across a range of normalized impact velocities:

- Meridian crack: spheres split along a meridian fracture,
- Three orange slices: spheres split in tensile mode along two meridian fractures, and the created fragments look like orange slices,
- Orange slices with cone: this pattern involves the creation of a cone fragment at the point of impact due to stress concentration. Meridian tension cracks then divide the sphere into three or four parts.

Increasing the normalized impact velocity introduced various fragmentation patterns. Initially, a top cone of variable size emerged due to enhanced crack propagation. As the velocity increase, the number of slices increases and the top cone typically split into two parts. At even higher velocities, a distinct fragmentation pattern emerged, with the top cone splitting into three to five primary fragments and generating up to 12 slices. Moreover, their work shows that as impact velocity (or energy) increases, both the number of fragments and the total fracture area also increase. A power-law relationship has been proposed for estimating the total fracture area based on the number of fragments and the diameter of the impacting sphere.

The research question behind the following paper is: *How do discontinuities within spheres impact the fragmentation behavior during controlled vertical drop tests?*

I'm author of the paper below (still in preparation), for which I contributed to the conceptualisation of the project, I dealt with analysis, investigation, visualisation, and writing of this draft.

Background Bibliography

Arbiter N, Harris CC, Stramboltzis GA. (1969). Single fracture of brittle spheres. Transaction of AIME 244:118-133

Chau KT, Wei XX, Wong RHC, Yu TX. (2000). Fragmentation of brittle spheres under static and dynamic compressions: experiments and analyses. Mechanics of Materials 32:543-554. doi:https://doi.org/10.1016/S0167-6636(00)00026-0

Dean WR, Sneddon IM, Parsons HW. (1952). Distribution of stress in a deccelerating elastic sphere. Selected Government Research Reports: Strength and Testing of Materials: Part II: Testing Methods and Test Results:212-234

Gan-Mor S, Galili N. (1987). Model for failure and plastic-flow in dynamic loading of spheres. Transactions of the ASAE 30:1506-1511

Gorham DA, Salman AD. (2005). The failure of spherical particles under impact. Wear 258:580-587. doi:https://doi.org/10.1016/j.wear.2004.09.012

Gorham DA, Salman AD, Pitt MJ. (2003). Static and dynamic failure of PMMA spheres. Powder Technology 138:229-238. doi:https://doi.org/10.1016/j.powtec.2003.09.008

Guccione, D. E. (2020). An experimental investigation of fragmentation occurrence and outcome in the context of rockfall (Doctoral dissertation, University of Newcastle).

Hiramatsu Y, Oka Y. (1966). Determination of the tensile strength of rock by a compression test of an irregular test piece. International Journal of Rock Mechanics and Mining Sciences & Geomechanics Abstracts 3:89-90. doi:https://doi.org/10.1016/0148-9062(66)90002-7

Salman AD et al. (2004). Descriptive classification of the impact failure modes of spherical particles. Powder Technology 143-144:19-30.

Shipway PH, Hutchings IM. (1993). Attrition of brittle spheres by fracture under compression and impact loading. Powder Technology 76:23-30. doi:https://doi.org/10.1016/0032-5910(93)80037-B

Tomas J, Schreier M, Gröger T, Ehlers S. (1999). Impact crushing of concrete for liberation and recycling. Powder Technology 105:39-51. doi:https://doi.org/10.1016/S0032-5910(99)00116-3

Wu SZ, Chau KT. (2006). Dynamic response of an elastic sphere under diametral impacts. Mechanics of Materials 38:1039-1060. doi:https://doi.org/10.1016/j.mechmat.2005.08.005

Wu SZ, Chau KT, Yu TX. (2004). Crushing and fragmentation of brittle spheres under double impact test. Powder Technology 143-144:41-55. doi:https://doi.org/10.1016/j.powtec.2004.04.028

Investigating the influence of discontinuities on fragmentation: experimental insights

Camilla Lanfranconi[1], Paolo Frattini[1], Giuseppe Dattola[1], Fabio De Blasio[1], Giovanni Battista Crosta[1], Davide Ettore Guccione[2], Olivier Buzzi[2], and Anna Giacomini[2]

[1] Department of Earth and Environmental Sciences, – DISAT, Università degli studi di Milano – Bicocca, Milan 20126, Italy

[2]Priority Research Centre for Geotechnical Science and Engineering, The University of Newcastle, Callaghan, NSW 2308, Australia

Abstract

Understanding how discontinuities influence fragmentation is crucial for enhancing safety in mining industries where impact events are common and for providing substance and validation to numerical models aiming to simulate block fragmentation during rockfall events. This study delves into the response of spheres undergoing controlled vertical drop tests and subsequent impact analysis. The experimental configuration, consists of a hexagonal fragmentation cell and high-speed cameras for impact monitoring. We tested spheres made of plaster-water mixtures, spanning solid spheres and spheres housing discontinuities. The preliminary results point toward a marked influence of both the number and strength of discontinuities on the fracture patterns. A new anvil-type fracture pattern was observed, particularly when spheres feature three discontinuities. This pattern signifies a significant dissipation of energy during the fracture process, resulting in reduced fragment heights and a more pronounced horizontal movement.

Introduction

The examination of fragmentation within the context of rockfall events is of significant importance, encompassing several key aspects. An overview of fragmentation in rockfall events reveals that as rocks or debris descend during such events, the occurrence of fragmentation leads to the dissipation of a substantial amount of energy upon impact. This phenomenon results in a consequential reduction in the final energy that protective structures must be designed to withstand, thereby affecting their capacity. Moreover, the influence of fragmentation on the trajectories of falling blocks is a significant and intricate facet, and the control of falling block trajectories is needed for ensuring the safety of structures and individuals in the affected areas. However, the advent of fragmentation introduces complexities into this scenario. Indeed, fragments can pursue divergent paths compared to intact blocks, thereby posing the risk of smaller fragments bypassing intended safeguards. This divergence adds an element of uncertainty regarding the distribution of energy among post-fragmentation fragments.

However, an understanding of the energy dissipated with fragmentation and the behavior of trajectories still need an understanding of the mechanisms that occur when the blocks fragment, studying the interplay of fracture modes, comprising tensile, in-plane shear, and anti-plane shear (Atkinson 1987), and other factors that may affect these processes. The main fragmentation patterns known in the literature depends on the type of impact. In double impact scenarios, specific features such as the presence of two cones initiating sphere splitting along meridian fracture planes are well recognized. As impact energy increases, secondary cracks form, leading to the creation of multiple small fragments, a phenomenon known as "crushing" (Chau et al., 2000; Schönert, 2004; Wu and Chau, 2006; Wu et al., 2004).

In single impact cases (Arbiter et al., 1969; Shipway and Hutchings, 1993; Tomas et al., 1999; Gorham et al., 2003; Salman et al., 2004; Schönert, 2004; Gorham and Salman, 2005), the fragmentation pattern shares similarities with double impacts, albeit with a critical distinction. At lower impact energies, the top cone might be absent due to the lack of impact force on the sphere's top. However, as impact energy increases, a remaining cone can appear at the sphere's top, underscoring the dynamic nature and sensitivity of fragmentation patterns to impact conditions. Guccione et al. (2023) identified three primary fragmentation patterns across a range of normalized impact velocities: i) meridian crack, ii) three orange slices, and iii) orange slices with cone.

Moreover, as normalized impact velocity increases, various fragmentation patterns emerge. Initially, a variable-sized top cone appears due to enhanced crack propagation. With continued velocity increase, the number of slices and the splitting of the top cone increase too.

Among the factors influencing fragmentation, the presence and number of discontinuities, their orientation at impact and the strength along these discontinuities are poorly studies in the literature (Giacomini et al., 2009; Einstein & Hirschfeld, 1973), even if they may be a major control on the fragmentation mechanisms.

The focus of this study is on conducting tests involving spheres with discontinuities, paying particular attention to the distinctive fracture patterns in stratified materials, weak planes, and isotropic materials. This approach provides a more in-depth understanding of how fragmentation occurs in these diverse material scenarios. Additionally, this study lays the groundwork for further research aimed at enhancing the numerical modeling algorithms of existing codes like Hy-Stone, RockGIS, and Rocscience by means of validation through real-scale and laboratory experiments.

Methodology

Experimental setup

The experimental setup was tailored for controlled vertical drop tests and the measurement of impact. To read the detailed description of the setup, please refers to Guccione et al. (2021). Just the key components of the setup are reported below.

Hexagonal Fragmentation Cell:

- Developed to enable secure and controlled drop tests while closely observing brittle materials
- Comprises alternating panels of polycarbonate and plywood, with a hexagonal shape
- A door on one plywood panel allows entry
- Cameras placed outside the cell with clear panels facilitate high-speed recording of the impact at its center, with painted plywood panels serving as a background
- Cell dimensions are 2.3 m in height and 1.2 m for each side
- The impact zone features a 1.1 m x 1.1 m x 0.2 m fibre-reinforced concrete slab of 60 MPa compressive strength
- A vacuum tube or pulley system lifts and releases test blocks from the structure, with a maximum drop height of 5.1 m
- Steel plates (10 mm thick) are integrated beneath the slab to prevent localized concrete damage where it contacts the load cells

Motion Capture:

- Four high-speed cameras capture the impact from various positions
- Cameras are equipped with different lenses based on their location
- Cameras are synchronized through a custom-built synchronization box
- We conducted the fragmentation tests with a frame rate of 500 frames per second
-

Lighting:

Adequate lighting is essential to achieve high shutter speed and minimize object blur, so these lights are installed:

- White LED flex ribbon strips are installed on clear panels, and LED spotlights are mounted on each side of the cell.
- 53-Watt LED panels are attached to plywood panels opposite specific cameras to ensure appropriate contrast for images.
- And a black-painted slab enhances contrast for top views.

Materials

To choose the most suitable materials for simulating intact rock and discontinuities, different plasters have been tested: a dental plaster (abbreviated as D) and two construction plasters referred to as B, and O. The first analysis carried out was the study of plaster curing. 115 cylindrical specimens were made for each type of mixture and were tested with UCS tests three times a day for a month. Performing UCS (Unconfined Compressive Strength) tests on plaster samples provided several parameters, including compressive strength and modulus of elasticity. We performed unconfined compression tests on cylinders (diameter around 54 mm and height 135 mm) according to standard ISRM 1979 (Bieniawski and Bernede 1979), carried out at a velocity of 0.5 millimeters per minute.

Different mixtures of plaster and water were tested, out of which one was chosen to represent the intact rock, and two others were selected as fillings for discontinuities. Each mixture was identified by a combination of a letter representing the type of plaster (B, O) and a number indicating the percentage of water in weight (75, 45, 60%). To evaluate the curing process, UCS tests were conducted simultaneously on three samples for approximately a month. By monitoring the maximum stress over time, we gained insights into the curing behavior of the mixtures. The results are presented in Chapter 3b – Figure 2 and the corresponding data in Chapter 3b – Table 1. Each data point on the graph represents the average of three samples tested in UCS at a speed of 2.5 mm/min.

Chapter 3b - Figure 2 shows the results obtained for the different mixtures. As shown, the most resistant mixture is D45, followed by O60, and the less resistant is B75. To meet the fragmentation needs in the previously described hexagonal cell and the usable heights, the D45 mixture was chosen as the material to simulate intact rock, and the B75 and O60 mixtures were chosen as filling mixtures, respectively 25% and 75% resistant compared to D45 (Glue 1 and Glue 2, respectively), respectively.

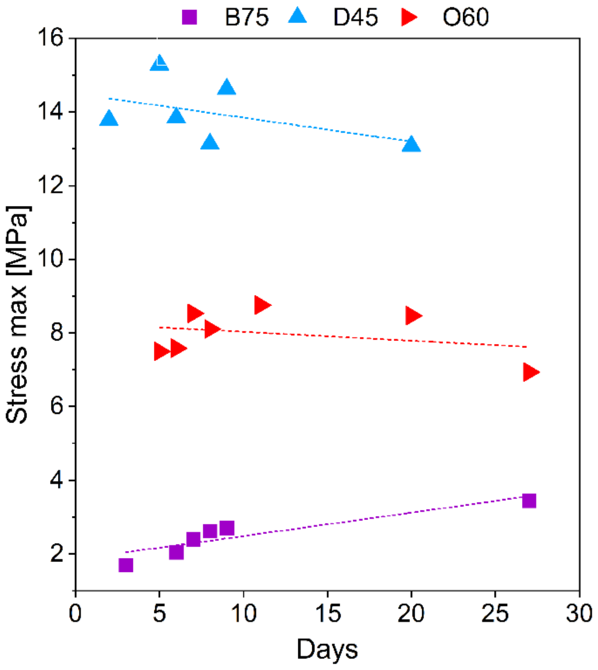

Chapter 3b - Figure 2 "Curing" of the selected mixtures.

Chapter 3b - Table 1 Characterization of strength during one-month "curing".

B75		D45		O60	
days	max stress [MPa]	days	max stress [MPa]	days	max stress [MPa]
3	1.7	2	13.8	5	7.5
6	2.1	5	15.3	6	7.6

	7	2.4	6	13.8	7	8.5
	8	2.6	8	13.1	8	8.1
	9	2.7	9	14.6	11	8.8
	27	3.5	20	13.1	20	8.5
					27	6.9
Stress max at the end of the curing time	3.5		13.1		6.9	
Average stress max	2.5		14.0		8.0	

Procedures for preparing dental plaster mixtures

Owing to the rapid solidification properties of dental plaster, the utilization of a large mixer for material amalgamation is precluded. Instead, the procedure involves employing four glass bowls: two containing 1200 g of dental plaster each and two containing 540 ml of water each. Commencing the preparation, the initial step entails transferring the contents of the first water bowl into the first dental plaster bowl. This mixture is stirred using a spoon, ensuring the removal of any surplus material accumulating at the periphery. Subsequently, the compact kitchen mixer is activated, and the amalgamation process is initiated. After a lapse of 30 seconds, the contents of the second water bowl are introduced along with the material from the second dental plaster bowl. The blending process is continued using the compact kitchen mixer until a homogenous consistency, devoid of any lumps, is attained.

Preparation of the spheres

To prepare and assemble the spheres we used 3D printed molds of half-spheres with a diameter of 100 mm, discs thick 2 mm and a placer hereafter called “spider” that, with a weight placed on top of it, prevents the lower disc from tilting during the pouring of the upper layer (Chapter 3b - Figure 3). The two discs simulates the discontinuities and are placed in the middle of the sphere and at ¼ of the height. The discs have holes that allow the excess mixture to escape.

Procedure for intact spheres

The process of preparing whole spheres involves six steps. First, the semi-spherical molds are greased with oil. Next, the spherical molds are assembled. The dental plaster mixture chose as intact rock, referred to as D45, is prepared with a water content of 45% by weight. The mixture is then poured into cylinders for UCS testing using a scoop, as well as into discs for Brazilian testing, also using a scoop. Finally, the mixture is poured into the spherical molds. Following this procedure, enough material is prepared to fill three spheres, one cylinder, and one disk.

Procedure for spheres with 1 discontinuity

The process of preparing spheres with one discontinuity involves six steps. First, the semi-spherical molds are greased with oil. Next, the D45 mixture is prepared. The mixture is then poured into cylinders for UCS testing using a scoop, as well as into discs for Brazilian testing, also using a scoop. After that, the mixture is poured into the semi-spherical molds. Finally, a 100 mm diameter disc (2 mm thick) is inserted to close the molds. By following this procedure and preparing the appropriate amount of material, it is possible to fill six semi-spheres, one cylinder, and one disk.

Procedure for spheres with 3 discontinuities

The preparation of spheres with three discontinuities involves eight steps, which includes two additional steps compared to the preparation of spheres with one discontinuity. These extra steps are necessary because the pouring into the molds occurs in two stages. The steps for preparing the spheres are as follows:

First, the semi-spherical molds are greased with oil. Then, the D45 mixture is prepared. The mixture is poured into the cylinders for UCS testing using a scoop, and also into the discs for Brazilian testing using a scoop. When pouring the mixture into the semi-spherical molds, it is filled until reaching half the height of the mold.

At this point, a smaller diameter disc is inserted to close the first layer of material, and a "spider" with weight is placed on top to prevent any movement during the pouring of additional materials (Chapter 3b –Figure 3). Next, the mixture is poured into the semi-spherical molds to completely fill them. The "spider" and its weight are then gently removed. Finally, a 100 mm diameter disc is inserted to close the molds.

By following this procedure and preparing the necessary amount of material, it is possible to fill six semi-spheres, one cylinder, and one disc.

Since following this procedure it is possible to fill 2 molds of 6 half-spheres at a time (for a total of 3 spheres) and we had 6 molds in the laboratory, 3 batches are prepared each time, denominated A, B, and C (Chapter 3b - Figure 4).

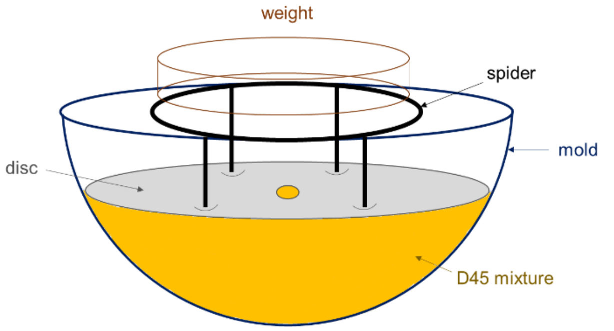

Chapter 3b - Figure 3 Sketch of step #6: Insert of the disc with the smaller diameter to close the first layer of material D45, and put the plastic "spider" with the weight on top of it, to avoid any movements of the smaller disc when pouring other materials on it (step #7).

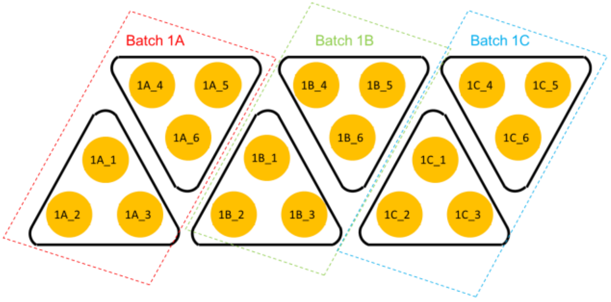

Chapter 3b - Figure 4 Configuration of the semi-spheres and their naming. With one batch it's possible to fill 6 semi-spheres, and their names will be the Batch ID and a progressive number from 1 to 6 (for example: 1A_1, 1A_2, 1A_3, 1A_4, 1A_5 and 1A_6).

As previously specified in each section dedicated to the preparation of the spheres, the batch of prepared material was sufficient to fill not only the spheres but also cylinders for unconfined compression tests (diameter 54 mm, height 135 mm) conducted in accordance with the ISRM 1979 standard (Bieniawski and Bernede 1979) and discs for indirect tension tests (also known as Brazilian tests) on mortar discs (diameter 54 mm, thickness 27 mm) conducted in accordance with the ISRM 1978 standard (ISRM 1978).

All of these characterization tests were carried out under quasi-static loading conditions, with loading rates ranging from 2 to 2.4 mm/min. The number of tests conducted for each mixture (more than 110) is detailed in Table 2. These tests were performed for every set of prepared spheres to consistently monitor the mechanical characteristics of the spheres that were subsequently tested.

Procedure for gluing the spheres

To glue the spheres together using the filling mixtures (B75 or O60), follow these steps:

First, check if the three cylinders/spacers formed at the median discontinuity are not higher than 2 mm. If they are, use a spatula to file them away. Next, prepare the 3D printed cages, as well as the three cylinders and three disks that will be filled. Group the spheres on the table according to their letter (A, B, C). Start by filling the first cylinder and the first disk of sphere A. Then, position the first section of sphere A in the cage. Using a spoon if necessary, add the filling mixture to the cage. Alternate the filling mixture with the other sections of sphere A. Close the cage and repeat the process for all spheres in group A. Next, move on to filling the first cylinder and the first disk of sphere B. Position the first section of sphere B in the cage and add the filling mixture, again alternating with the other sections of sphere B. Close the cage and repeat the process for all spheres in group B. Repeat the same steps for sphere C, filling its cylinder and disk, positioning its first section in the cage, and alternating with the filling mixture for the remaining sections. Close the cage for each sphere in group C. Finally, use a spatula to fill any holes in the discontinuities and remove any excess material. The result is shown in Chapter 3b – Figure 5. Following this procedure and preparing the necessary amount of material allows to glue together nine spheres, three cylinders, and three disks.

Chapter 3b - Figure 5 Examples of spheres with 1 and 3 discontinuities.

With the initial batch of spheres ready, preliminary fragmentation tests were conducted, which resulted in deformation rather than fracture. Consequently, a decision was made to place the samples in an oven at 60°C overnight and repeat the test. Upon observation, it was noted that this time the samples did fragment. As a result, we decided to modify the initial experimental program for drop tests, wherein all samples would be placed in the oven for one night before being utilized for material characterization and drop tests.

Material Characterization through UCS, Brazilian, and Shear Tests

On all the disks and cylinders obtained from the sphere preparation processes (intact spheres, with one, and with three discontinuities), as well as from the gluing process, UCS (Uniaxial Compressive Strength) tests, Indirect Tension tests (also known as Brazilian tests), and Shear tests were conducted. These tests were aimed at characterizing the materials and quantifying their variability.

The UCS tests enable the characterization of material strength and the assessment of its response to compressive loading conditions. In this test, cylindrical specimens with uniform cross-sectional dimensions are subjected to progressively increasing axial loads until failure occurs. The axial load and axial strain data collected during the test are used to determine the UCS, which represents the maximum compressive stress the material can endure before failing.

The UCS tests were performed on mortar cylinders with a diameter of approximately 54 mm and a height of 135 mm. The tests followed the standard ISRM 1979 (Bieniawski and Bernede 1979) and were conducted at varying velocities based on the material type:

- Dental plaster,
- Glue 1,
- Glue 2.

The Brazilian tests assess the tensile strength of brittle materials. The test involves placing a disc-shaped specimen between two loading platens and applying compressive forces to the specimen's peripheral edge. The induced tensile stress at the center of the disc causes a radial crack to propagate across the specimen, creating two halves. This test configuration transforms the tensile forces into a compressive state on the specimen's lateral surface, thereby evaluating its tensile strength.

Brazilian tests, were carried out on mortar discs with a diameter of 54 mm and a thickness of 27 mm, using two flat plates. These tests followed the standard ISRM 1978 (ISRM 1978) and were conducted under quasi-static conditions. Brazilian tests evaluate the tensile strength of materials under compressive loading and are utilized to understand their brittleness and fracture behavior.

Shear tests, on the other hand, serve to evaluate the shear strength of materials and were conducted to assess their response to shear forces acting parallel to the contact interface between the dental plaster and the two glue materials.

These tests provide insights into how materials react when subjected to lateral forces and are valuable for understanding their structural behavior, particularly in scenarios involving shear loading.

The fragmentation tests

The fragmentation tests were conducted at the Civil Engineering laboratory of the University of Newcastle in Australia, and the setup details of the fragmentation cell, where the tests took place, are described in the works of Guccione et al. 201. The tests were carried out at two different heights, capturing the impact of a sphere by using high-speed cameras, positioned at a 120° angle from each other, that recorded the impact footage. Both solid spheres and spheres with discontinuities were used. Spheres with one or three discontinuities, filled with glue 1 (B75) or glue 2 (O60), were tested at five different impact angles (Chapter 3b - Figure 6). The average mass of the spheres is 790 g and the impact velocity is 9.7 m/s.

Following each test, we collected and weight each single fragment heavier than 0.2 g in order to obtain the cumulative number of fragments per weight class.

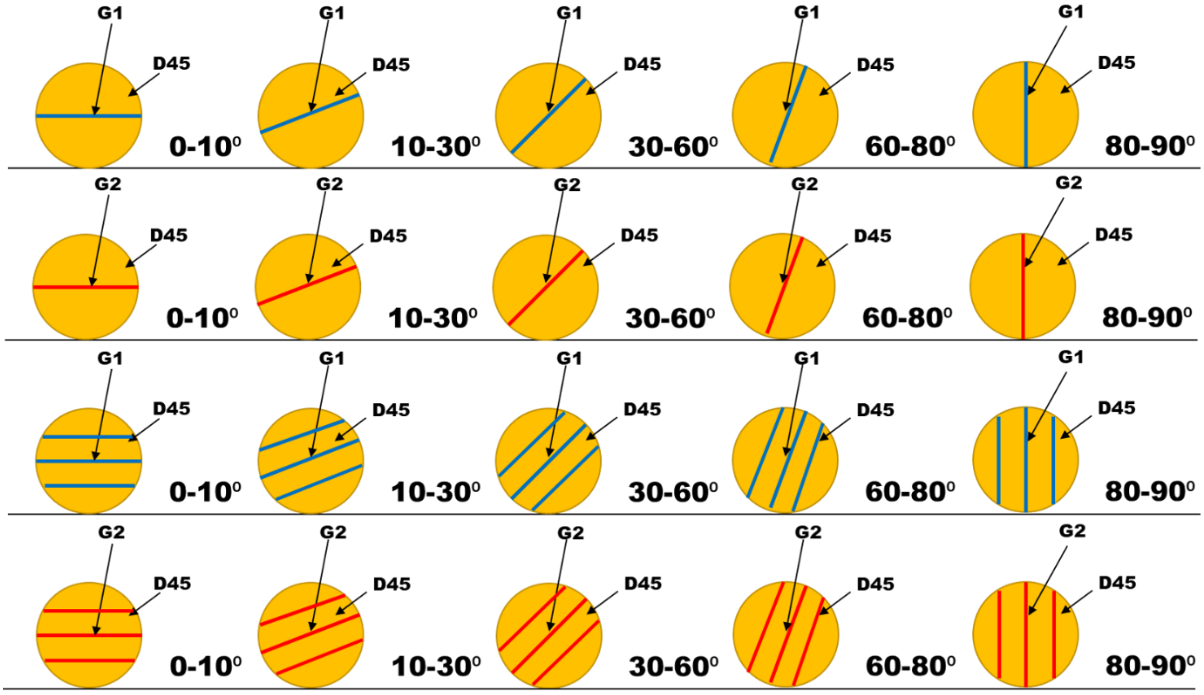

Chapter 3b - Figure 6 Modes of impact for spheres with one and three discontinuities.

Analysis and results

Qualitative analysis of sphere fracture modes and fragment characteristics

The analysis of images captured during the test enabled the observation of fracture patterns, fragment distribution, and the overall mode of failure. Such visual observations provided qualitative insights into the fragmentation mechanisms and fracture propagation within the spheres.

We conducted two types of analyses:

1. Classification of fracture mechanisms in spheres based on impact type
2. Characterization of vertical bouncing of large fragments.

By analyzing the same frame for each test (i.e., the tenth frame, 0.02 s after impact), we were able to classify each test according to a few characteristic fragmentation behaviours, namely: deformation (D), chipping (C), hemisphere-meridian (M), orange-slicing (O), parallel splitting (S), anvil (A) (Chapter 3b – Figure 7). The term “anvil” has been chosen because the behavior of sphere resembles that of being struck by a hammer.

This qualitative analysis also shows that spheres undergo various fracture modes, including compression, tension, and sometimes even shear. The last scenario is particularly clear for the parallel splitting with vertical orientation of the discontinuities (Chapter 3b - 7S), where the two external slices slide along the discontinuities towards the slab while the central part has already made contact.

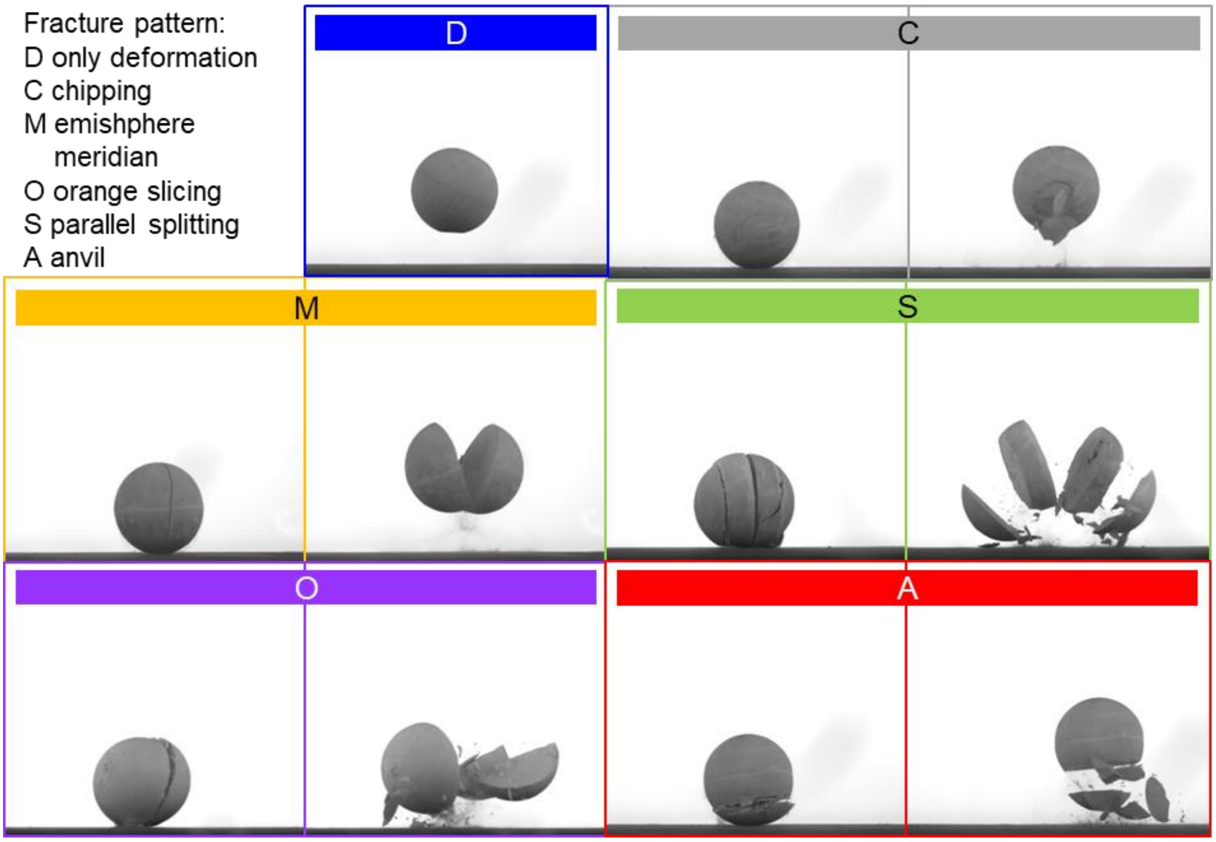

Chapter 3b - Figure 7 Typical fracture patterns recognized in the fragmentation tests. The images refer to the same frame, 0.02 s after impact.

From the results presented in Chapter 3b - Table 2, it is evident that the number of discontinuities (D0, D1, or D3) controls the fragmentation mechanism more than the strength of the glue (G1 being weaker than G2). Spheres without any discontinuity (D0) mostly remain unbroken, or they fracture in a hemisphere-meridian pattern (Chapter 3b – Table 2). In the first case, the deformed area observed in the impact zone of the sphere covers approximately 4 cm, nearly double that of the mortar tested by Guccione et al. in 2023. The impact energy is dissipated through elastoplastic deformation of the sphere.

Chapter 3b - Table 2 Fracture patterns for spheres with different discontinuity configurations and glue strengths

	D	**C**	**M**	**O**	**S**	**A**
D0	60%	0%	40%	0%	0%	0%
D1_G1	20%	5%	25%	45%	5%	0%
D1_G2	22%	0%	28%	50%	0%	0%
D3_G1	0%	0%	6%	0%	44%	50%
D3_G2	0%	0%	6%	13%	56%	25%

When there is only one discontinuity (D1), regardless of the strength of the glue, the spheres mostly fracture following the orange slicing pattern or the meridian pattern. About 20% of cases shows only deformation.

Finally, when there are three discontinuities, the spheres invariably fragment, and the role of glue strength becomes more pronounced. With weaker glue (G1), half of the spheres follows the anvil type, and the parallel slicing in over 40% of cases. With stronger glue (G2), the spheres predominantly fracture in a parallel slicing pattern, with occasional occurrences of anvil and, to a lesser extent, orange slicing and hemisphere-meridian patterns.

The anvil pattern mostly occurs when the discontinuities are horizontal or sub-horizontal. Moreover, when the glue is weaker (G1) the fractures tend to be constrained within the first discontinuity and the fragments show a high horizontal velocity. On the other hand, when the glue is stronger (G2), the cracks generally extend beyond the first discontinuity, and the horizontal velocity appears to be lower (Chapter 3b –Figure 8).

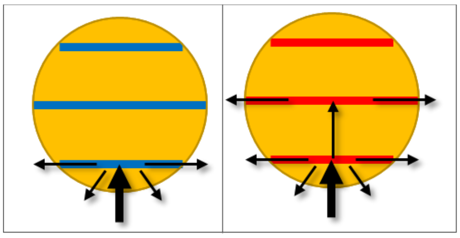

Chapter 3b - Figure 8 Sketch of the two models of anvil fracture pattern for D3: weaker glue (G1, left panel) constrains fractures to the first discontinuity while stronger glue (G2, right panel) allows for crack propagation beyond.

The maximum rebound heights (i.e, the maximum height reached by fragments exceeding 2 cm in length) achieved by the spheres and fragments during the tests is significantly different according to the fragmentation behavior, the strength of the glue and the orientation of discontinuities at impact. The greatest heights are achieved by intact spheres without any discontinuities (D0) and by sphere with one discontinuity, independently of the glue strength (Chapter 3b –Figure 9). On the other side, with three discontinuities, the strength of the glue seems more important, and the highest rebound are achieved with the stronger glue (Chapter 3b – Figure 9). Moreover, in general, we observe that the larger the angle of orientation of the discontinuities, the lower the rebound height (Chapter 3b – Figure 9).

As for the fragmentation mechanism, the anvil type shows the smallest heights, especially in contrast with the purely deformation behavior and the meridian (Chapter 3b –Figure 10).

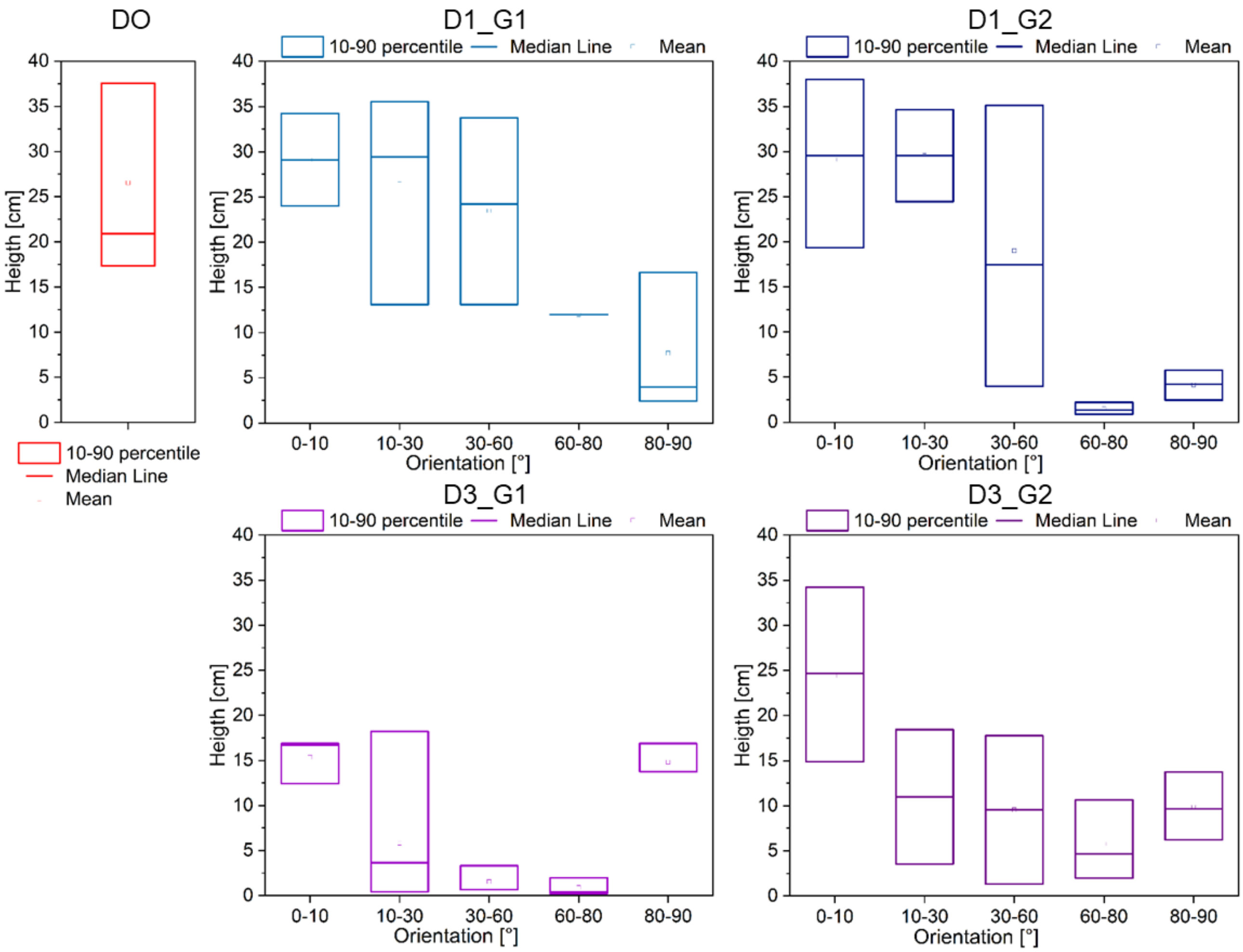

Chapter 3b - Figure 9 Heights reached by fragments in the tests, categorized by orientations of discontinuities relative to the slab at the time of impact, and organized in terms of sphere structure and composition.

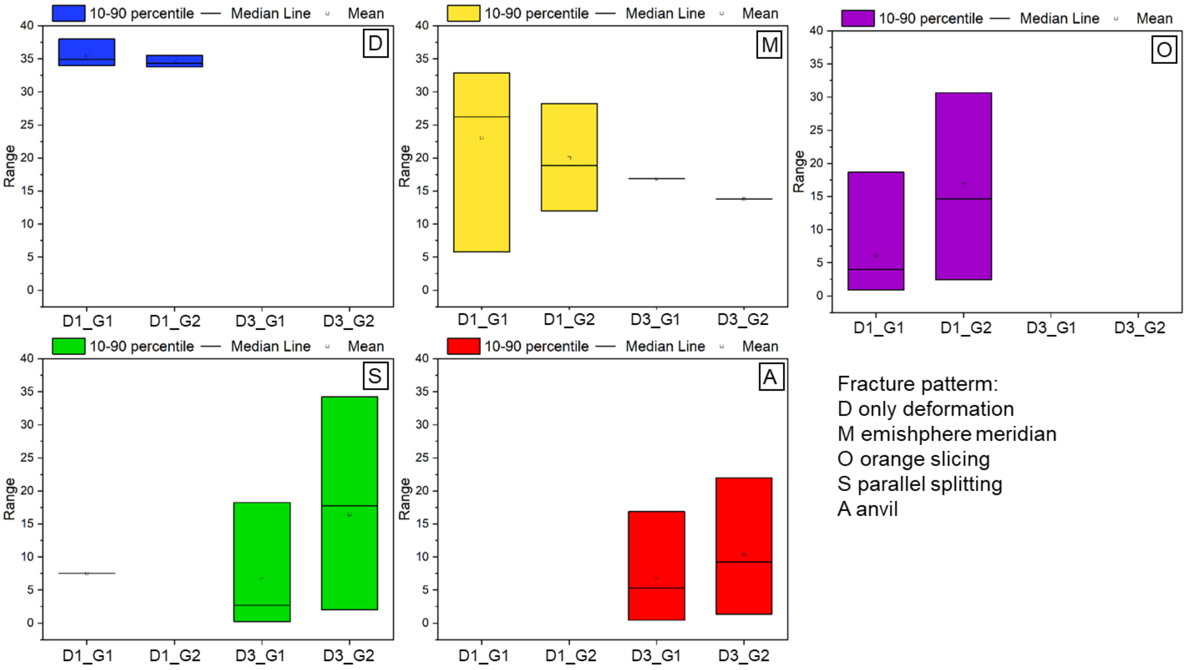

Chapter 3b - Figure 10 Heights reached by fragments in the tests, categorized by orientations of discontinuities relative to the slab at the time of impact, and organized in terms of fracture pattern.

Mass-frequency analysis

Chapter 3b – Figure 11 illustrates the cumulative mass frequency distributions for all sphere configurations (0, 1, and 3 discontinuities) impacted at all possible orientations, categorized into spheres filled with Glue 1 in panels (a, 1 discontinuity) and (b, 3 discontinuities), and those filled with Glue 2 in panels (c, 1 discontinuity) and (d, 3 discontinuities). Each curve represents a test that produced fragments, and each point corresponds to a single fragment. Spheres with three discontinuities produce more fragments compared to those with a single discontinuity, for all the impact orientation (Chapter 3b – Figure 11).

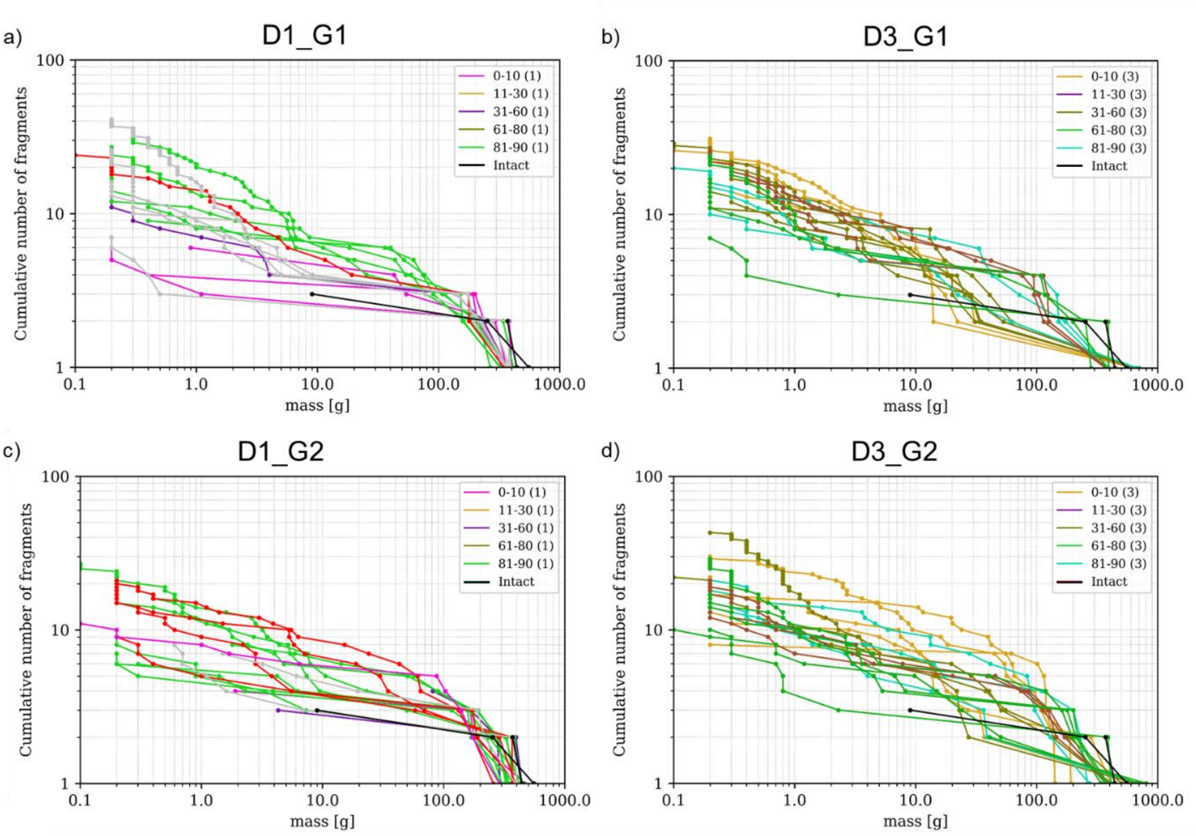

Chapter 3b - Figure 11 Cumulative number of fragments as function of the fragment mass. a) 1 discontinuity, glue 1; b) 3 discontinuities, glue 1; c) 1 discontinuity, glue 2; d) 3 discontinuities, glue 2.

The orientation classes where this effect is most evident are those between 0° and 30°, where the anvil fracture pattern occurs. In both the 0-10 and 11-30 orientation classes (Chapter 3b – Figure 12), fewer and larger fragments are observed, particularly when there is only 1 discontinuity compared to cases with 3 discontinuities. This effect is less pronounced for Glue 2 compared to Glue 1.

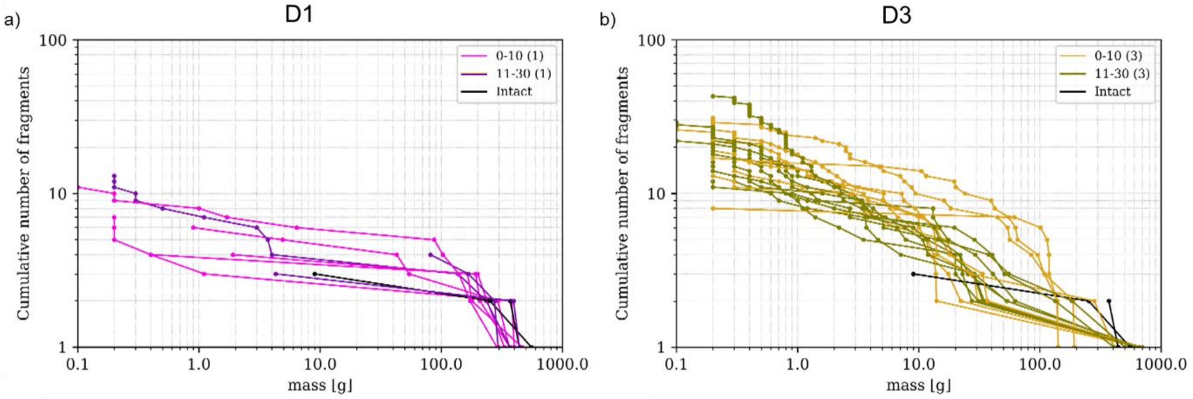

Chapter 3b - Figure 12 Cumulative number of fragments as function of the fragment mass. a) orientation classes 0-30°, 1 discontinuity; b) orientation classes 0-30°, 3 discontinuites.

Discussion

The analysis of fragmentation mechanisms reveals six main behaviors, that appears to be mainly controlled by the number of discontinuity and the orientation of the discontinuities at impact, and not significantly by the strength of the glue. Most of the observed behaviors have been already recognized in the literature (Guccione et al. 2023) for the spheres without discontinuities. The only behavior that seems to be specific of spheres with discontinuities is the anvil one, which occurs only with three horizontal or sub-horizontal discontinuities. This mechanism seems to be associated to the dissipation of shock-wave energy along the lower discontinuity (occasionally also along the median one), keeping intact the upper part of the sphere, which consequently acts as an hammer that crushes the lower part of the sphere. Interestingly, this behavior does not appear in case of only one discontinuity, because the first discontinuity is too far from the impact point to dissipate the shock-wave energy, generating vertical fractures that leads to meridian or orange patterns.

The explanation of the anvil behavior as a consequence of shock-wave dissipation, is supported by the fact that in cases of weaker glue (G1) that allows a more affective dissipation, the crushing of the lower part is limited to the lower discontinuity. On the contrary, for the stronger glue (G2), the shock wave is not enough dissipated in the lower discontinuity and propagates up to the median one, due to the higher strength of the glue.

In addition, the effective dissipation of energy along the discontinuities that characterizes the anvil behavior, is witnessed by much lower rebound heights compared to cases where spheres remaining entirely unbroken or with other patterns.

The strength of the glues does not affect the fragmentation mechanisms as much as the number of discontinues and the orientation angles at impact, but shows a significant effect on rebound heights in case of one discontinuity (Chapter 3b – Figure 9). This is related to the fact that the rebound is connected with the stiffness of the spheres which depends on the strength of the glue for spheres with discontinuities.

The analysis of the cumulative mass-frequency distribution of fragments allows to characterize the degree of comminution of the spheres due to fragmentation for the different configurations. As expected, the higher the number of discontinuity, the larger the comminution. However, this effect is significant only when the discontinuities are horizontal and sub-horizontal, and disappears when the discontinuities are vertical. This is probably related to the fragmentation behavior (e.g., meridian vs anvil), suggesting that the degree of comminution is the result of an interplay between the number of discontinuities, their orientation and the fragmentation behavior. Interestingly, the strength of the discontinuity (i.e., the glue strength) does not affect the degree of comminution significantly.

As discussed above, the behavior and degree of comminution during fragmentation depends on many factors that are interconnected. Therefore, in order to untangle the effect of the different factors, it is necessary to test numerous configurations. In this research, we tested around 90 spheres, probably still not sufficient for a comprehensive understanding of the problem. Nonetheless, the consistent results from these tests are encouraging.

Another point of discussion is the mechanical characterization of the materials. The Brazilian tests specifically refer to compression tests on a disc, and not a sphere. Moreover, the tests were conducted under quasi-static conditions, with an average time to failure of approximately 50 seconds for D45, which is markedly shorter than the impact time. The increase in strain rate between quasi-static and dynamic testing is assumed to be proportional to the ratio of loading times, with half of the impact time allocated to the compression phase and the other half to the rebound phase.

Conclusion

In this study, we conducted an assessment of the results by analyzing images captured during the tests. These images allowed us to observe fracture patterns, fragment distribution, and the overall mode of failure, providing qualitative insights into fragmentation mechanisms and fracture propagation within the spheres. We classified fracture mechanisms based on the type of impact. This classification included observations of deformation, chipping, hemisphere-meridian, orange-slicing, parallel splitting, and a previously unreported anvil pattern. The results reveal that the fracture behaviour depends primarily on the number and orientation of the discontinuities. Spheres with three horizontal and sub-horizontal discontinuities reveal a characteristic pattern of fragmentation that we defined as anvil. This fracture behavior exhibits two distinct patterns depending on glue strength, affecting the extent and location of fractures within the spheres. The degree of comminution seems to be the result of an interplay between the number of discontinuities, their orientation and the fragmentation behavior, while the strength of the discontinuity seems to be less significant.

References

Arbiter N, Harris CC, Stramboltzis GA. (1969). Single fracture of brittle spheres. Transaction of AIME 244:118-133

Einstein, H. H., & Hirschfeld, R. C. (1973). Model studies on mechanics of jointed rock. Journal of the Soil Mechanics and Foundations Division, 99(3), 229-248.

Giacomini, A., Buzzi, O., Renard, B., & Giani, G. P. (2009). Experimental studies on fragmentation of rock falls on impact with rock surfaces. International Journal of Rock Mechanics and Mining Sciences, 46(4), 708-715.

Gorham DA, Salman AD, Pitt MJ. (2003). Static and dynamic failure of PMMA spheres. Powder Technology 138:229-238. doi:https://doi.org/10.1016/j.powtec.2003.09.008

Gorham DA, Salman AD. (2005). The failure of spherical particles under impact. Wear 258:580-587. doi:https://doi.org/10.1016/j.wear.2004.09.012

Guccione, D. E., Giacomini, A., Thoeni, K., Fityus, S., & Buzzi, O. (2023). On the Dynamic Fragmentation of Rock-Like Spheres: Insights into Fragment Distribution and Energy Partition. Rock Mechanics and Rock Engineering, 56(2), 847-873.

Guccione, D. E., Thoeni, K., Fityus, S., Nader, F., Giacomini, A., & Buzzi, O. (2021). An experimental setup to study the fragmentation of rocks upon impact. Rock Mechanics and Rock Engineering, 54(8), 4201-4223.

Salman AD et al. (2004). Descriptive classification of the impact failure modes of spherical particles. Powder Technology 143-144:19-30. doi:https://doi.org/10.1016/j.powtec.2004.04.005

Schönert K. (2004). Breakage of spheres and circular discs. Powder Technology 143-144:2-18. doi:https://doi.org/10.1016/j.powtec.2004.04.004

Shipway PH, Hutchings IM. (1993). Attrition of brittle spheres by fracture under compression and impact loading. Powder Technology 76:23-30.

Tomas J, Schreier M, Gröger T, Ehlers S. (1999). Impact crushing of concrete for liberation and recycling. Powder Technology 105:39-51.

Final reflections

At the end of these three years of doctoral research, I managed to investigate various aspects of rockfall phenomena, delving into topics related to the volumes involved, their distribution, frequency of occurrence, and fragmentation. I find the work I have produced satisfying because I have successfully addressed the three objectives I had set before starting.

In the analysis of rockfall case studies, with a specific focus on examining block size distributions in the final rockfall deposit, I have made significant progress. I was able to demonstrate that a detailed characterization of rockfall deposits can substantially enhance our comprehension of rockfall processes. The observed reversal in the longitudinal distribution of block sizes within a rockfall deposit is an indicator of dynamic fragmentation during propagation. Notably, this shift from the typical longitudinal sorting of talus to inverse sorting indicates the occurrence of dynamic fragmentation.

Moreover, I identified two additional indicators of successful dynamic fragmentation. In cases of fragmentation, most of the case studies exhibited a second deviation from the power-law distribution for larger volumes, which we hypothesize as the effect of fragmentation of the largest blocks. Interestingly, this second rollover may indicate a characteristic size at which fragmentation becomes effective. Another key indicator is the alteration in typical rockfall mobility indices, such as the reach angle and lateral dispersion metrics. The reach angles of rockfalls known to have experienced fragmentation exceeded typical values reported in the literature, suggesting reduced mobility of the primary rockfall body. To compensate for this, a few small fragments were ejected beyond the main deposit body, highlighting the energy-consuming nature of the fragmentation process.

In my research related to the quantification and assessment of fragmentation in rockfall dynamics and hazard, through detailed modeling and analysis of real case studies, I have highlighted the role of block fragmentation in two distinct studies, both based on actual rockfall events. Specifically, I have demonstrated that if we do not explicitly simulate the fragmentation phenomenon, we tend to overestimate the hazard in terms of energy values. However, we simultaneously underestimate the spreading of blocks during these events. By explicitly simulating the fragmentation process, we can achieve more accurate hazard mapping, quantifying the improvement in precision. I have also emphasized the necessity of simulating a block distribution that accurately represents what has previously occurred, as this serves as the most likely scenario. This is crucial because the design of mitigation measures relies on the expected and simulated kinetic energies of the blocks.

The third objective of the thesis turned out to be the most complex of all. I aimed to conduct a detailed study of the physical fragmentation process through experiments conducted at different scales (both full scale and laboratory scale), with the hope of arriving at new conclusions regarding the dynamics accompanying the creation and ejection of fragments upon impact. This required a multitude of tests and extremely in-depth analyses in terms of load analysis, the redistribution of kinetic energy to the fragments, and the survival probability of the blocks. While I did not fully achieve this goal, I am satisfied with my investigation into rockfall fragmentation behaviors, and I have observed that the results obtained from experimental tests all point in the same direction. They confirm what I have observed in real-case deposits concerning rockfall dispersion, deposition, and mobility.

The investigation into the role of discontinuities and their impact on fragmentation has been a fascinating journey, and I am thankful for the opportunity to collaborate with the Australian research group. While we have not yet achieved comprehensive results, our study has unveiled a novel anvil-type fracture pattern observed in spheres with three discontinuities. This pattern indicates a significant dissipation of energy during the fracture process, resulting in reduced fragment heights and a more pronounced horizontal movement.

Furthermore, our work has emphasized the importance of comprehending the fundamental principles governing fragmentation to enhance existing models, laying foundation for future research.

I'm glad that the results of my thesis have practical significance, especially in the context of risk mitigation. They have implications for improving safety measures and could contribute to the development of more accurate models for understanding and predicting fragmentation processes in impact events.